Electric field induced modification of magnetic and structural properties in thin films

Md Golam Hafiz
University of Leeds
School of Physics and Astronomy

Submitted in accordance with the requirements for the degree of
Doctor of Philosophy
July, 2024

Intellectual Property Statement

The candidate confirms that the work submitted is his own and that appropriate credit has been given where reference has been made to the work of others.

The right of Md Golam Hafiz to be identified as Author of this work has been asserted by him in accordance with the Copyright, Designs and Patents Act 1988.

Acknowledgements

First and foremost, I extend my sincere gratitude to my supervisors, Prof. Gavin Burnell and Prof. Chris Marrows, for granting me the opportunity to contribute to this research project. Gavin's unwavering encouragement and invaluable guidance at every step of this project have been beneficial. His profound understanding of experimental physics, exceptional mentoring abilities, and insightful perspectives have made this study possible. I deeply appreciate his patience, motivation, and adeptness at simplifying complex physics to tackle challenging problems. I am thankful for his consistent availability and willingness to discuss problems and scientific matters.

I also express my appreciation to Dr. Mannan Ali for his enlightening discussions, assistance, and training. Furthermore, I extend my thanks to the academic staff, including Prof. Thomas Moore, Prof. Joseph Barker, Prof. Oscar Céspedes, Prof. Bryan Hickey, and Dr. Satoshi Sasaki, whose supportive discussions and suggestions have been invaluable. Dr. Philippa Shepley deserves special recognition for her training on material growth and exceptional guidance and support.

Acknowledgment is due to Dr. Nathan Satchell, Dr. Mark Rosamond, and Dr. Li Chen for their assistance and training in the cleanroom, as well as to Dr. Lin Huang for aiding in device fabrication. I am grateful for the initial training provided by Dr. Matthew Rogers, Dr. Craig Knox, Dr. Alexandra Jane Stacey, and Dr. Emily Rachel Darwin, whose assistance proved invaluable throughout my PhD journey.

I extend my gratitude to Dr. Zabeada Aslam and John Harrington, Dr. Andrew Britton, and Dr. H.B. Vasili for their contributions to TEM, XPS, and XAS measurements, respectively. Special thanks to Dr. Liza Herrera Diez, Professors Gianfranco Durin, Eloi Haltz, M. Belmeguenai, Dr. Yves Roussigne, Adriano, Rohit, Subhajit, and Mouad for their support during my secondments in Turin and Paris. I am also thankful to Clare Desplats and PIs from MagnEFi for their guidance, training, and lectures, as well as to my fellow ESRs from MagnEFi: Adithya, Giovanni, Mandy, Gyan, Cristina, Sreeveni, Beatrice, and Adrian.

Special thanks to my colleagues and friends, Jintao and Ahasan, and my neighbours little angle Diya and her parents Mr. and Mrs. Didar, Mr. and

Mrs. Rafid, and Mr. and Mrs. Sunon, whose presence has greatly enriched my experience in Leeds. Special appreciation goes to my friends Sunzida, Iftekhar, Ahad, Anu, and Almas, who have always patiently listened to me.

I gratefully acknowledge the support from the European Union's Horizon 2020 research and innovation programme for the Marie Sklodowska-Curie grant agreement No. 860060 "Magnetism and the Effect of Electric Field" (MagnEFi) project.

Last but not least, I am eternally thankful to my parents, my wife Jinia, my son Zayan, as well as my brothers Razib and Mutahar, and sisters Rupa and Ritu, for their support and encouragement throughout this journey.

Abstract

This experimental work focuses on modifying the characteristics of ultra-thin magnetic multilayers through electric field (E-field) driven migration of oxygen. We investigated thin film multilayers composed of Ta/Pt/CoB/Ir or Cu/Pt/HfO_2. In these systems, metal layers such as Ir and Cu are utilized to induce structural inversion asymmetry. The Pt gives rise to a strong perpendicular magnetic anisotropy (PMA), spin-orbit coupling (SOC), and the Dzyaloshinskii-Moriya Interaction (DMI). We conducted measurements of magnetic properties such as effective anisotropy and DMI, which are relevant for devices based on skyrmions or domain walls.

The modification of magnetic properties by ionic liquid gating (ILG) is explored as a promising technique in spintronics due to its room temperature application, non-volatility, energy efficiency, and reversibility. We have investigated the oxygen migration via ILG of structures within metallic layers, which provide flexibility in terms of material choice. With an applied negative voltage, oxygen migrates from the HfO_2 to the magnetic layer, changing the interfacial chemistry of the magnetic system. As a result, changes in coercive field, domain nucleation field and effective anisotropy. The oxygen migration process is almost fully reversible, and the migrated oxygen produces a nonvolatile effect for up to fifteen weeks.

The magneto-ionic modification of structural and interfacial properties was studied using X-ray photoelectron spectroscopy (XPS), scanning transmission electron microscopy (STEM), energy dispersive X-ray spectroscopy (EDX), and electron energy loss spectroscopy (EELS). The O-K edge and Co $L_{2,3}$ edges of XPS study predict the oxidization of the system during two growths. The XAS and XMCD studies shows the oxidization states are changing with applied voltage and it is therefore changing the magnetic moments. This data is also consistent with SQUID-VSM data. The Pt M_3 edge also confirms the oxidation of the Pt top layer in the as-grown sample, which changes with the applied voltage.

Additionally, interfacial magnetic properties were examined using Brillouin light scattering (BLS). This experimental work aims to understand the origin of DMI in the studied magnetic system. We found that the DMI contribution is significantly coming from top CoB/Heavy metal interface.

Applied voltage change the interface chemistry of this interface and changes the DMI, particularly for the Cu/Pt samples.

The magneto-ionic modulation in all metallic structure might be useful in spintronics device application, emphasizing domain wall-based and skyrmion-based spintronics devices. The modulated magnetic properties, in combination with nonvolatility and reversibility, allow for the possibility of field-programmable domain wall and skyrmion devices.

Contents

1 Introduction **1**

1.1 Introduction . . . 2

1.1.1 Domain wall and skyrmion based magnetic multilayer systems . 2

1.1.2 Electric fields gating of magnetic multilayers . . . 3

1.2 Thesis layout . . . 5

2 Theoretical Background and Literature Review **6**

2.1 Introduction . . . 7

2.2 Energies and interaction in ferromagnetic systems . . . 7

2.2.1 Exchange energy . . . 8

2.2.2 Anisotropy energy . . . 9

2.2.3 Dzyaloshinskii-Moriya interaction . . . 12

2.3 Magnetic spin textures . . . 14

2.3.1 Magnetic domain walls . . . 14

2.3.2 Magnetic skyrmions . . . 17

2.4 Manipulation of interfacial magnetic properties . . . 19

2.4.1 Interface engineering . . . 19

2.4.2 Electric field . . . 22

2.5 Summary . . . 28

3 Experimental Methods **29**

3.1 Introduction . . . 30

3.2 Thin film deposition techniques . . . 30

3.2.1 DC magnetron sputtering . . . 30

3.2.2 Atomic layer deposition (ALD) . . . 32

3.3 Structural characterisation techniques . . . 33
3.3.1 X-ray reflectivity (XRR) . . . 33
3.3.2 Atomic force microscopy (AFM) . . . 35
3.3.3 X-ray photoelectron spectroscopy (XPS) . . . 36
3.4 Scanning transmission electron microscopy (STEM) . . . 37
3.5 Superconducting quantum interference device for vibrating sample Magnetometry (SQUID-VSM) . . . 38
3.6 Wide-field Kerr microscopy . . . 40
3.7 Magneto-resistance (MR) measurement . . . 43
3.8 Brillouin light scattering (BLS) spectroscopy . . . 45
3.9 XAS and XMCD . . . 47
3.10 Ionic liquid and ionic liquid gating . . . 49
3.11 Device fabrication process . . . 51

4 Growth and Optimization 53
4.1 Introduction . . . 54
4.2 Thin film optimization . . . 54
4.3 Structural properties . . . 60
4.3.1 X-ray reflectivity (XRR) analysis . . . 60
4.3.2 Morphology . . . 62
4.4 Magnetic properties . . . 63
4.4.1 Effective anisotropy . . . 63
4.4.2 Exchange stiffness, A . . . 64
4.5 Measuring the Dzyaloshinskii-Moriya interaction (DMI) . . . 66
4.5.1 Domain wall velocity in the creep regime . . . 66
4.5.2 Measuring DMI in the creep regime . . . 67
4.6 Conclusions . . . 71

5 Effect of Electric Field on Ta/Pt/CoB/Ir/Pt/HfO2: Ionic liquid gating of magnetic multilayer with structural inversion asymmetry 73
5.1 Introduction . . . 74
5.2 Multilayer systems . . . 75
5.3 AHE hysteresis loops . . . 75
5.4 Kerr microscopy hysteresis loop and imaging . . . 79

5.5 Magnetic characterization . . . 81
5.5.1 Saturation magnetization . . . 81
5.5.2 Anisotropy field . . . 83
5.6 Reversibility . . . 85
5.7 Discussion . . . 85
5.8 Conclusion . . . 88

6 Electric Field Induced Structural and Interfacial Modification 89
6.1 Introduction . . . 90
6.2 Sample structures . . . 90
6.3 Structural properties . . . 92
6.3.1 X-ray photoelectron spectroscopy (XPS) . . . 92
6.3.2 Atomic level investigation of oxygen migration . . . 101
6.4 Magnetic properties . . . 104
6.4.1 Saturation magnetization and effective anisotropy . . . 104
6.4.2 Interfacial magnetic properties . . . 109
6.4.3 X-ray absorption spectroscopy (XAS) and X-ray magnetic circular dichroism (XMCD) measurements . . . 110
6.5 Discussion . . . 116
6.6 Conclusions . . . 121

7 Towards Devices 123
7.1 Introduction . . . 124
7.2 Micromagnetic simulations using Mumax3 . . . 124
7.3 Re-configurable domain wall device: a proof of principle . . . 129
7.4 Conclusions . . . 132

8 Conclusion and Outlook 133
8.1 Summary . . . 134
8.2 Future Work . . . 137

A Appendix1 139
A.1 Calculating damping constant from Brillouin light scattering (BLS) spectroscopy . . . 140

References 142

List of Figures

2.1 Interfacial DMI at the interface between a magnetic (red) and a non-magnetic (blue) layer. The resulting DMI vector D_{12} is perpendicular to the plane of the triangle [56]. 13
2.2 An example of magnetic domains in the Ta/Pt/CoB/Ir/Pt system was captured using a Kerr microscope, where white region indicates domains pointing down, while black regions indicate domains pointing up. A domain wall is the boundary region between two domains. These results are further discussed in Chapter 4. 14
2.3 Bloch and Néel types of domain walls in a PMA magnetic system, where the red arrow represents the clockwise (CW) and counterclockwise (CCW) directions as a guide for the eye [25]. 15
2.4 a) Domain wall velocity regimes as a function of driving force, f. b) domain wall flow regimes. Outside of Walker field the domain wall move without pinning. (b) The walker breakdown field (H_w) is marked between the steady state and precessional regimes [61]. 16
2.5 a) Néel-type skyrmion b) Bloch-type skyrmion [66]. 17
2.6 The saturation magnetization per unit area depends on the thickness of the Co layer (t_{Co}). The saturation magnetization was measured using a superconducting quantum interference device (SQUID) magnetometer. The Pt/Co/Pd film shows higher saturation magnetization then Pt/Co film, which gives an give an explanation of magnetic moment in Pd layer due to ferromagnetic proximity effect [28]. 19

2.7 Hysteresis loop of Au/Co/Au tri-layer at T=10 K with perpendicular ($\perp$) and parallel ($\|$) applied field (H) [77]. For a Ta/CoFeB/Pt/MgO/Ta magnetic system: (b) Dependence of DMI on the thickness t_{Pt} of the Pt layer: The red points are derived from the linear dependency of k_x and f_{DM} where k_x is the spin wave vector, and f_{DM} is the difference between the stock and anti-stock frequency. The black points are calculated using a fixed $k_x = 16.7$ rad/μm.(c) Saturation magnetization, M_S does not change with Pt thickness, and (d) Dependence of $4\pi M_{eff}$ on t_{Pt}, Black dots represent Brillouin light scattering (BLS) measurements, and red dots represent vibrating sample magnetometer (VSM) measurements. (Figure b-d are taken from the Figure 3 in reference [78].) 20

2.8 First-principles calculations were used to calculate the DMI in Co/Pt and Co/Ir interfaces, where the numbers represent the number of monolayers: a) DMI constant, D of Co/Pt_3 (red) and Co/Ir_3(blue).The Co atoms are placed between hcp and fcc sites of metallic layers. b) D of Co/Pt and Co/Ir against Co layer thickness [80]. 21

2.9 (a) The sample structure involves a polymer combined with an ionic liquid, used in the process of gold (Au) growth.(b) Perpendicular component of moment (m$\perp$)per area at different temperatures for Co thicknesses of 0.1 nm (A) and 0.19 nm (c). The inset shows the Hall resistance measurement at 10 K for Co 0.10 nm. The sample shows a square hysteresis loop at $\pm 2V$. (b) The difference between m$\perp$ at $\pm 2V$ as a function of temperature. For both samples, the data show linear relationships. Figure 2 and 3 in reference [28]. 23

2.10 (a) Applied negative voltage at FM/MO_x film and charge depletion at the interface (b) Voltage directly changes the electronic occupation of d orbitals [44] 24

2.11 (a) The effect of the E-field on DMI was studied using first-principles calculations. The microscopic DMI (d) and micromagnetic DMI (D) exhibit a linear dependence on the E-field. Microscopic DMI refers to the atomic-level interaction, whereas micromagnetic DMI describes the interaction on a continuum scale. Figure 5 in reference [15]. (b) Magneto-ionic modulation of DMI in the Pt/Co/HfO_2 system occurs when a gate voltage of -3 V is applied for up to 4 minutes. The migrated ions decouple the Pt/Co interface; therefore, the DMI decreases. The process is not reversible. Figure 2.10 in reference [40]; [83]. 25

2.12 Magneto-ionic modulation of the CoFeB/HfO_2 system with an applied voltage of a) -2 V changes the in-plane (In-P) magnetization to out-of-plane (OoP) magnetization. This change starts at 25 s, and the magnetization gradually rotates to OoP. b) The process is reversible. When -2 V is applied for an extended period of time, it goes back to In-P again. In this case, the CoFeB might be fully oxidized[40]. he Kerr microscopy hysteresis loop shows the effect of an applied voltage. The voltage was applied through a Polyimide (1500 nm)/ITO(100 nm) structure. With an applied $\pm 200V$ change the in plane sample to OoP, which is also reversible. Figure 3 in [84]. 26

2.13 (a) Nucleation and annihilation of an isolated skyrmion at 7.8 K in Ir/Fe bilayer. An applied voltage changes the exchange interaction, which nucleate skyemion (writing) [85]. (b) Nucleation and annihilation of a skyrmion bubble at 300 K in Pt/Co/AlO_x trilayer with ±20 V. When a negative voltage is applied, the skyrmion (white bubble) appears on the ITO electrode, which is annihilated by applying a positive voltage. [72]. 27

3.1 Schematic diagram of dc magnetron sputtering. Ar ions ejects required materials from the target, which form thin films on a substrate [11, 88]. 32

3.2 XRR data of a [CoB/Pt]x10/Pt calibration sample on a Si/SiO_2 substrate. The experimental data is fitted with GenX software. The thickness of each CoB layer is around 12 ±0.4 Å and the thickness of each Pt layer is around 20 ±0.3 Å. 33

3.3 A schematic representation of an AFM is shown in the left image [90]. The sample is attached to a piezoelectric scanner, which can move along the x and y directions. The vibration amplitude the tip affected by Van der Walls force provides the sample's morphology. An example of an AFM surface image is shown in the right image. 35
3.4 Experimental XPS data show the full spectral range. The sample was scanned with a photoelectron energy up to 1500 eV. Peak positions are shown according to their binding energy. C KLL and O KLL represent the emission of an electron (carbon or oxygen, respectively) from the K shell, with the resulting vacancy being filled by another electron from the L shell. 36
3.5 STEM require ultra thin (35-100 nm) sample. Preparation steps are: a) Ir/Pt cap deposition on the sample b) bulk removal c) under cut d) in-situ lift-out e) Attached to TEM grid f) the sample is transparent under e-beam. 38
3.6 Magnetic moment as a function of applied OoP field at room temperature. The image is also showing the diamagnetic background (violet), which is corrected by a straight-line subtraction. 39
3.7 The polar, transverse and longitudinal Kerr effect. The magnetization direction is shown by the small arrow. The large arrow is showing the incident and reflected light beam [51]. 40
3.8 The diagram shows the Kerr effect. The polarized light rotates after reflecting from a magnetic in-plane sample. The reflected light obtain a new vector K [51]. 41
3.9 a) A small bubble is nucleated with an applied OoP pulse and recorded. Outside of the bubble, the magnetization is pointing upward, indicating the initial position of the domain wall. b) A second OoP pulse is applied to nucleate another bubble and recorded. c) The difference between these two images can be used to calculate the domain wall velocity. . . . 42
3.10 An example of MR data, where Hall resistance is recorded as a function of the rotational angle, and the anisotropy field is calculated through parabolic fitting, is presented. The A_2 in Equation 3.7 is calculated from the parabolic part, as indicated in the figure. 43

3.11 A schematic diagram of scattering by photon spin wave interaction. Due to conservation of momentum magnon can be (a) created by the stokes process or (b) annihilated by anti-Stocks process, the figure is adapted from ref [40]. 45
3.12 The Damon-Eshbach geometry and the back scattering geometry, where θ is the wave vector, $-\mathrm{K}_{\mathrm{SW}}$ is the anti-Stocks spin wave and $+\mathrm{K}_{\mathrm{SW}}$ is the Stocks spin wave [25, 40]. 46
3.13 a) The sample is irradiated with a light beam, and the connected ammeter helps determine the total yield of electrons. b) The XMCD two-step diagram shows electrons in the core shells 2p3/2 and 2p1/2. Left (σ^-) and right (σ^+) circularly polarized light are used to eject electrons from the core shell, with the lines (perpendicular) indicating the expected transitions [114]. c) An example of XMCD data shows the $\mathrm{Co{-}L_{2,3}}$ absorption edge for left (blue) and right (magenta) circularly polarized light. The differences and averages are used to calculate the moment per atom in Chapter 6. 48
3.14 Geometry of ionic liquid gating with positive applied voltage. The applied voltage arrange ions in ionic liquid and form electric double layer. The distance between cations and anions is 1-2 nm [40]. 49
3.15 Structure of the electric double layer (colored) produced by an applied voltage. The double layer is predicted using a Landau-Ginzburg-type continuum theory, with parameters specific to the room-temperature ionic liquid $[\mathrm{bmpy}]^+[\mathrm{FAP}]^-$. (a) At low voltage, overscreening occurs. (b) At high voltage, an extended layer of countercharges leads to crowding [124]. 50
3.16 Chemical structure of the $[\mathrm{EMI}]^+[\mathrm{TFSI}]^-$ ionic liquid [123] 51
3.17 The fabrication process for the microchannel on the magnetic thin film involves several steps: Application of a bi-layer photoresist comprising LOR7B and S1813 using spin-coating. Exposure of the sample to UV light to transfer the desired pattern onto the photoresist. Development of the photoresist using Microposit 351 solution. Growth of $\mathrm{SiO_x}$ layer using DC magnetron sputtering. Removal of the photoresist to achieve the desired microchannel configuration. 52

4.1 Example of PMA of Pt/CoB(X)/Ir sample, where CoB 8 Åexhibits PMA. The CoB 20 Åmight be still PMA but the remanence is not full at zero field, and CoB 24 Åmight be in-plane sample. 55

4.2 M-H loop taken using Kerr microscope. The Green is Ta(5 Å)/Pt(7 Å)/CoB(8.5 Å)/Ir(5 Å)/Pt(14 Å) and the blue is representing Ta(5 Å)/Pt(14 Å)/CoB(8.5 Å)/Ir(5 Å)/Pt(14 Å). The M-H loop shows that the PMA can be tuned by changing the Pt layer thickness. 56

4.3 The thickness wedge of Ta and bottom Pt layers is shown here. A mask was used to cover the sample during the wedges' growth. 58

4.4 Domain morphology of Pt/CoB/Ir films. (a-c) Repeated samples are showing maze-type and tree-branch-type domain patterns, which might be due to a high demagnetizing field and shape anisotropy. (d-f) domain morphology with Ta layer thickness the isolated thin domain disappears from the bubble. However, the edge of the domain is still rough. (g-h) The domain morphology also depends on the CoB thickness. The 10 Å CoB shows isolated thin wall inside the bubble. In Section 4.5, we estimated the DMI from domain wall motion, which cannot be applied to maze-type domains. 59

4.5 AFM images showing surface morphology of as grown sample 5: Ta(12 Å)/Pt(19 Å)/CoB(7 Å)/Ir(3.5 Å)/Pt(6 Å), (a) 20μm × 20μm, (b)5μm × 5μm. 62

4.6 The left side image is showing normalized resistance data as a function of rotational angle. The right side image is showing the magnification of the polynomial fit. 63

4.7 Temperature dependent magnetization fitted with Bloch law thin film assumption. Samples: S2 = (Ta(8 Å)/Pt(12.5 Å)/CoB(5 Å)/ Ir(6 Å)/Pt(16.5 Å), S3 (Ta(8.5 Å)/Pt(12 Å)/CoB(5.5 Å)/Ir(6 Å)/Pt(17 Å), S4 Ta(7.5 Å)/Pt(12 Å)/CoB(5.5 Å)/Ir(6 Å)/Pt(17.5 Å), S5 Ta(12 Å)/Pt(19 Å)/CoB(7 Å)/Ir(3.5 Å)/Pt(6 Å). 65

4.8 Creep check of domain wall motion of S5 (Ta (12 Å)/Pt(19 Å)/CoB(7 Å)/Ir(3.5 Å)/Pt(6 Å)). (a) ln(v) as a function of the applied OOP field. (b) ln(V) as a function of $\mu_0\mathrm{H}^{-(1/4)}$. The linear behavior confirms that the velocity with the OOP field is in the Creep regime. 67

4.9 Bubble expansion of S5: (a) Symmetric bubble expansion. (b) Asymmetric bubble expansion. (c) The domain wall velocity of studied film as a function of applied in-plane field, nucleation field is 29 Oe. The left-hand side (LHS) and the right-hand side (RHS) indicate the negative and positive values of the in-plane field respectively. The error bars are standard deviation of 20 or more velocities. Due to the chirality of the domain wall, the in-plane field (denoted as H_x in the image) creates different domain wall energy ratios (domain wall energy due to in-plane field and with out in-plane field $\sigma_{DW}(H_{IP})/\sigma_{DW}(0)$ in Equation 4.6. Additionally, the left-hand side (LHS) and right-hand side (RHS) possess opposite DMI fields. Consequently, H_x+H_{DMI} varies with the applied in-plane field for LHS and RHS, leading to distinct energy profiles and resulting in different velocities. At the point where the domain wall velocity is minimized, the DMI opposes the IP field and effectively cancels it out [11]. 69

5.1 Typical sample structures in the E-field gating technique include: (a) W/CoFeB/HfO_2 [160] and (b) Pt/Co/HfO_2 [83]. These examples illustrate the magnetic layer positioned adjacent to the oxide layer. 74

5.2 (a) Ionic liquid EMI^+ $TFSI^-$ is applied on the sample, and an ITO glass electrode is used as a top electrode. (b) The M-H loops are shown for 0 V, -2.1 V, and +2.1 V. The applied voltage loops represent a mixture of gated and ungated signals. This effect is reversible and is discussed in Section 5.6. 76

5.3 (a) The 20% nucleation field and 80% saturation field under -1.5 V and -2.1 V as a function of gating time. A higher voltage for a longer time has a greater influence on the change than a lower voltage and/or a shorter time. (b) The 20% nucleation field and 80% saturation field under +4 V and +4.4 V as a function of gating time. Compared to a negative voltage, a larger positive voltage is required for a longer duration to observe any changes. 77

5.4 (a) The percentage change in 20% nucleation and 80% saturation at -2.1 V as a function of top Pt thickness. For the 2 Å Pt layer, an approximate 100% change indicates that the change in mT is roughly double. Conversely, an approximate 0% change indicates almost no change in mT. (b) The percentage change in 20% nucleation and 80% saturation at +4 V as a function of top Pt thickness. The change is significantly higher for 20% nucleation than for 80% saturation, with the exception of the 8 Å Pt layer. 78

5.5 (a) Kerr Microscopy hysteresis loop of 4 Å Pt top layer with -2.1 V for 120s, as grown and with +4 V for 300 s. Negative voltage increases the coercive field, and the Positive voltage decreases the coercive field. (b) Domain images were taken at +4 V for 300 s, including both G and U regions. After removing the liquid, the differences between the G and U regions became visually apparent. Consequently, a line was drawn on the microscopy image to delineate the boundary between the two regions. (c) Under -2.1 V for 120 s, a high field is required to nucleate domains. . 80

5.6 (a) SQUID-VSM hysteresis loop of a 4 Å Pt top layer at room temperature, measured at -2.1 V for 120 s, 0 V, and with +4 V for 300 s. The change in coercive field is consistent with the Kerr microscope measurement. (b) Magnetization as a function of the top Pt layer thickness. A positive voltage increases it, while a negative voltage decreases it. (c) The percentage change in magnetization varies with the thickness of the top Pt layer. Notably, a significant increase is observed for Pt thicknesses of 4 Å under a negative voltage. 82

5.7 Anisotropy field ($\mu_0\mathrm{H_k}$) and effective anisotropy ($\mathrm{K_{eff}}$) as functions of top Pt layer thickness, as an effect of -2.1 V for 120s , and +4 V for 300 s.The anisotropy field shows a trend of decreasing with Pt thickness: (a) $\mu_0\mathrm{H_k}$ and (b) percentage change in $\mu_0\mathrm{H_k}$, where the change is small with increasing Pt thickness, except for the 6 Å Pt layer. The $\mathrm{K_{eff}}$ was calculated using equation 3.7. The scattering in calculated values is due to variations in $\mathrm{M_s}$ values: (c) $\mathrm{K_{eff}}$ and (d) percentage change in $\mathrm{K_{eff}}$. . 84

5.8 Reversibility of the 4 Å Pt top layer as a function of cycle number, where black points indicate the starting position, red points indicate the percentage reversibility, and magenta points indicate the position along the x-axis after reversibility: (a) Center of the loop after applying -2.1 V for 120 s and +4 V for 300 s. The resistivity changes with an applied negative voltage and is fully reversible with a higher positive voltage. (b) Reversibility at 20% nucleation is almost fully reversible. (c) Reversibility at 80% saturation is also almost fully reversible. The field difference in the cases of 20% nucleation and 80% saturation might be due to a slight dislocation of the ITO electrode. 86

6.1 Kerr microscope M-H loops of as-grown and voltage-applied samples, where ±2.1 V were applied for 30 minutes. (a) The M-H loops of the Ir/Pt top layer: initial state, with an applied negative voltage, and with an applied positive voltage. The sample shows a similar effect as observed in Chapter 5. (b) The M-H loops of the Cu/Pt top layer: initial state, with an applied negative voltage, and with an applied positive voltage. The effect on the Cu/Pt samples is also the same as for Ir/Pt, though it is more pronounced here. 90

6.2 Non-volatility check of the Ir/Pt top layer: (a) As-grown sample after deposition, where no change was observed after 6 weeks. (b) -2.1 V for 30 minutes: After applying the voltage, no change was observed after 6 weeks. (c) +2.1 V for 30 minutes: After applying the voltage, no change was observed after 6 weeks. The Ir/Pt samples are very stable and do not change over time. 91

6.3 Non-volatility check of the Cu/Pt top layer: (a) As-grown sample after deposition, which changed significantly after 6 weeks. (b) -2.1 V for 30 minutes: After applying the voltage, no change or only minor changes were observed after 6 and 15 weeks. (c) +2.1 V for 30 minutes: After applying the voltage, the coercive field increased over time. The positive voltage pulls oxygen from the CoB layer, which may be re-oxidizing over time. 92

6.4 An example of XPS measurements. (a) Oxygen spectra displaying the metal oxide bond (Co-O-Fe) at approximately 530.4 eV and oxygen functional groups at around 531.2 eV. (b) The complex Co$-2\,p_{3/2}$ peak in $CoFe_2O_4$ attributed to contributions from both Co and CoO [176]. . . . 93

6.5 XPS spectra at the O 1s edge: (a-c) As-grown and voltage-applied Ir/Pt samples, and (d-f) As-grown and voltage-applied Cu/Pt samples. For both samples (Ir/Pt and Cu/Pt), the oxygen peaks represent a combination of metal oxides and hydroxyl groups, as illustrated in example Figure 6.4. 94

6.6 XPS spectra at the Cobalt $L_{2,3}$ edge: (a-c) As-grown and voltage-applied Ir/Pt samples, and (d-f) As-grown and voltage-applied Cu/Pt samples. All samples exhibit a complex Co peak, comprising metallic Co and CoO. As-grown and positively gated samples suppress the CoO peak, while negatively gated samples suppress the metallic Co peak. 96

6.7 XPS spectra of Ir in Ir/Pt and Cu in Cu/Pt samples: (a-c) Effect of applied voltage on Ir/Pt. Only slight or no changes were observed with applied voltages on Ir, indicating that higher energy is required to obtain information for Ir. (d-f) Effect of voltage on Cu/Pt. The negatively gated Cu/Pt sample shows a significant difference in oxidation. 98

6.8 XPS spectra of Pt 4f: (a-c) Samples with Ir/Pt, and (d-f) Samples with Cu/Pt. For both samples, little or no change was observed in Pt with applied voltages, indicating that higher energy is also required to obtain information for Pt, as shown in the XAS of Pt (Figure 6.18). 100

6.9 EDX mapping was performed on the as-grown samples The bright most region in the middle is the magnetic multilayer, the gray region on top of the magnetic layer is the HfO_2, dotted lines were added as a guide for the eye. All the elements in the sample can be distinguished separately. The red color represents the Si substrate, while blue indicates Ta. The light blue color shows Pt layers, with the double layer in Pt attributed to the re-sputtered TEM capping layer applied before sample preparation. Magenta corresponds to the Co layer, yellow represents Ir, and orange indicates Hf. The double layer in oxygen (green) is due to the presence of SiO_2 and HfO_2. The elements are presented individually due to noise caused by the limited resolution of the TEM system. 102

6.10 (a) EDX mapping of the as-grown sample. Different elements of the film are shown with color coding similar to the previous image. (b) EDX elemental mapping of Co and oxygen, showing high noise and difficulty in distinguishing other elements in a single image. (c-d) O-K EELS spectra at HfO_2 and the substrate, indicating that no oxygen can be detected within the metallic multilayer. (e-f) Co-$L_{2,3}$ EELS spectrum at the CoB layer, where (f) shows the as-grown sample and at -2.1 V. The Co spectra show no difference between the two conditions. 103

6.11 (a) The M_s values of the as-grown and gated samples (unadjusted M_s) are shown. The gated M_s values are aligned with the straight line fit, with the shift from the original positions calculated using the toy model described in Equation 6.1. (b) The goodness of fit using the toy model is evaluated by comparing the adjusted gated data points to the original linear fit of the as-grown samples. 105

6.12 The slab model assumed that negative voltage is decreasing the CoB thickness and increasing the CoO thickness. Nevertheless the positive voltage increases the CoB thickness and decreases the CoO thickness. . 106

6.13 H_K and K_{eff} of Ir/Pt and Cu/Pt samples: (a) H_K, b) K_{eff}. As observed in Chapter 5, the application of a negative voltage increases both the anisotropy field and and the effective anisotropy constant, whereas the application of a positive voltage results in a decrease in these parameters. However, Cu/Pt under +2.1 V is an exception. 107

6.14 (a) The averaged frequency difference between the Stokes and anti-Stokes peaks is used to calculate the DMI. (b) The effective DMI significantly changes with the application of a negative voltage. (c) The effective magnetization, $4\pi M_{eff}$, where the negative sign indicates high interfacial anisotropy. 110

6.15 XAS spectra in the vicinity of the $Co-L_{2,3}$ absorption edges. Data were taken with left and right circularly polarized light. The data has two characteristics peaks from $Co-2\,p_{3/2}$ and $Co-2\,p_{1/2}$. The difference due to the left and right circularly polarized photon is shown by the blue line. Ir/Pt samples at normal incident: (a) 0 V, (b) -2.1 V, (c) +2.1 V. And at grazing incident: (d) 0 V, (e) -2.1 V, (f) +2.1 V 111

6.16 XAS spectra of (a,b) Ir/Pt and (c,d) Cu/Pt samples show a negative voltage increasing the Co pre-peak (inset), indicating CoO formation is high. A reference sample Ta(14 Å)/Pt(23 Å)/CoB(8 Å)/Ir(2 Å)/Pt(6 Å)/Ta(10 Å). The Ta cap protects the sample from oxidation, indicating that the as-grown samples underwent oxidation between two growth. . . 113

6.17 XMCD spectra of (a) Ir/Pt and (b) Cu/Pt. Both samples (Ir/Pt and Cu/Pt) show low dichroism under negative voltage. However, under positive voltage, the Cu/Pt sample exhibits lower dichroism compared to the as-grown sample, possibly due to re-oxidation. 114

6.18 Magnetic moment of (a) Ir/Pt samples and (b) Cu/Pt samples. A negative voltage decreases the moment of Co. However, a positive voltage on the Cu/Pt sample is an exception. (c) Hysteresis loops of Ir/Pt samples: a negative voltage increases the coercive field, as observed under a Kerr microscope. XAS spectra at the $Pt-M_3$ absorption edge for (d) Ir/Pt and (e) Cu/Pt samples indicate a change in oxidation state under negative voltage, suggesting oxygen migration from the HfO_2 115

6.19 Summary of results presented in Chapter 6: (a) the predicted oxygen state of the as-grown sample, (b) oxygen diffusion at -2.1 V, c) oxygen diffusion at +2.1 V, d) summary of the effect of applied voltage. 122

7.1 Domain wall velocity of a uniform wire for two different anisotropy constants. Material parameters are taken from experiments and listed in Table 7.1. Field-driven domain wall: (a) Illustrates the domain wall velocity, where low anisotropy shows higher velocity compared to high anisotropy. The inset shows the Walker breakdown and Walker breakdown field. Current-driven domain wall: (b) Current-driven domain wall velocity. At a low anisotropy, the velocity increases significantly after . . 125

7.2 (a) Domain wall motion and pinning in a hypothetical device structure shown in Figure 7.2, using parameters derived from experimental work given in Table 7.1. (b-e) Magnetic field and spin-polarized current-driven domain wall motion and depinning. The initial images depict the simulated gated area, where white represents higher anisotropy compared to black. The arrows indicate that time is increasing compared to the previous images. (b) Domain wall pinning is observed until 22 mT. (c) Depinning of the domain wall occurs as it passes through the gated area at 24 mT. (d) The domain wall fails to pass through the gated area until a current density of 4×10^{11}A/m^2. (e) It begins to move with a current density of 5×10^{11}A/m^2 (no field applied). 127

7.3 (a) Displays the magnetisation component along the z-axis of skyrmion as a function of time (during the simulation, no parameters were changed). (b) Change of skyrmion radius with time. (c) Initial skyrmion radius. (d) Skyrmion radius after 0.1 ns. (e) Skyrmion radius after 0.2 ns. (f) Skyrmion radius after 0.3 ns. (g) Skyrmion radius after 0.4 ns. (h) Skyrmion radius after 0.5 ns. (i) Skyrmion radius after 0.6 ns. (j) Skyrmion transforms to donut shaped complex structure before annihilation. 128

7.4 A 1000 μm reconfigurable magnetic domain wall device (with top Pt 5 Å), (a) domain nucleation and saturation under positive voltage. (b) a negative voltage of -2.1 V delays domain nucleation with in the gate region130

7.5 A 50 μm track fabricated on a sheet film: (a) Initially, domain nucleation occurs on the track, and it propagates uniformly along the device. (b) Application of a negative voltage delays domain nucleation and saturation on the track. (c) The effect of the negative voltage is reversible with the application of a positive voltage 131

A.1 Change in damping constant α as a function of the reciprocal effective thickness of CoB. The Cu/Pt system shows a lower slope compared to Ir/Pt. The Cu/Pt samples show two regimes of α; however, only the linear part as a function of $1/\,\mathrm{t}_{\mathrm{eff}}$ is considered for the fitting. The linear fit gives α from the y-axis. The value of α is determined as $0.4 \pm 0.1 \times 10^{-3}$. We used the alpha = 0.005. 141

List of Tables

3.1 Properties of $[EMI]^+[TFSI]^-$ ionic liquid [40, 117, 118, 123, 127, 128] . . 51

4.1 The individual layer thicknesses of the metallic multilayer films were extracted from experimental data using GenX. The associated errors were also obtained from GenX. 61
4.2 H_{eff} has been extracted from a polynomial fit and $K_e$ff have been calculated using the Ms and H_{eff}. Samples: S2 = (Ta(8 Å)/Pt(12.5 Å)/CoB(5 Å)/ Ir(6 Å)/Pt(16.5 Å), S3 (Ta(8.5 Å)/Pt(12 Å)/CoB(5.5 Å)/Ir(6 Å)/Pt(17 Å), S4 Ta(7.5 Å)/Pt(12 Å)/CoB(5.5 Å)/Ir(6 Å)/Pt(17.5 Å), S5 Ta(12 Å)/Pt(19 Å)/CoB(7 Å)/Ir(3.5 Å)/Pt(6 Å). 64
4.3 H_{DMI}, A, and D for the sample S2 to S5. Samples: S2 = (Ta(8 Å)/Pt(12.5 Å)/CoB(5 Å)/ Ir(6 Å)/Pt(16.5 Å), S3 (Ta(8.5 Å)/Pt(12 Å)/CoB(5.5 Å)/Ir(6 Å)/Pt(17 Å), S4 Ta(7.5 Å)/Pt(12 Å)/CoB(5.5 Å)/Ir(6 Å)/Pt(17.5 Å), S5 Ta(12 Å)/Pt(19 Å)/CoB(7 Å)/Ir(3.5 Å)/Pt(6 Å). 71

6.1 XPS oxygen peaks were assigned using the CasaXPS elemental library. . 95
6.2 Co peaks were assigned using the CasaXPS element library. 97
6.3 Ir praks were assigned using the CasaXPS 99
6.4 Cu were assigned using the CasaXPS element library. 99
6.5 All elements were assigned using the CasaXPS element library, with additional reference to sources [178 to 200]. The magnitude of the residual standard deviation ranged from 0.77 to 0.96. 101
6.6 Calculated $\mu_0 H_k$ and K_{eff} using a M_s=750emu/cc for Ir/Pt and Cu/Pt samples. 108
6.7 XAS Peak Analysis of Ir/Pt, Cu/Pt, and Reference Samples. 112

6.8 Calculated $\mathrm{m_l/m_s}$ values for Co. The calculated values are with in the reported range. 118

7.1 Material properties are used in micromagnetic simulation. 125

8.1 Summary of results. All results show changes in material properties due to E-field induced oxygen migration, compared to as-grown samples. . . 135

Abbreviations

AHE	Anomalous hall effect
ALD	Atomic layer deposition
AFM	Atomic force microscopy
BLS	Brillouin light scattering
CoB	Cobalt(68%) Boron(32%)
DMI	Dzyaloshinskii-Moriya interaction
E-field	Electric fields
FM	Ferromagnetic
HM	Heavy metal
ILG	Ionic liquid gating
In-P	In plane field
ITO	Indium Tin oxide
MR	Magnetoresistance
OoP	Out of Plane Field
PMA	perpendicular magnetic anisotropy
STEM	Scanning transmission electron microscopy
SQUID	Superconducting quantum interference device
SOC	Spin-orbit coupling
STT	Spin transfer torque
VSM	Vibrating sample magnetometry
XAS	X-ray absorption spectra
XRR	X-ray reflectivity
XPS	X-ray photoelectron spectroscopy
XMCD	X-ray magnetic circular dichroism

Chapter 1

Introduction

1.1 Introduction

The control of nanomagnetism through electric fields (E-fields) holds significant technical importance in the development of compact, fast, and low-power electronic devices. Domain walls and skyrmions are being considered as potential candidates for data storage systems because of their microscopic size, magneto-electrical properties, and the minimal current required for their manipulation [1, 2]. These domain walls and skyrmions can be manipulated using an external magnetic field, spin-polarized current, or local heat [1–6]. To advance durable and robust technology, it is crucial to explore the E-field-controlled properties of domain walls and skyrmions.

1.1.1 Domain wall and skyrmion based magnetic multilayer systems

In 1974, Cronemeyer et al. [7] reported perpendicular magnetic anisotropy (PMA) in CoCd thin films. Three years later, Iwasaki et al. (1978) [8] proposed magnetic recording using PMA materials. Since then, PMA materials have been widely used in data storage technology. In contrast to in-plane magnetic systems, the PMA system is advantageous for high-density data storage. Moreover, the PMA storage system utilizing optical magnetization switching offers high-speed read, write, and access times [9, 10].

Magnetic thin films, such as Pt/Co/Pt, have high perpendicular magnetic anisotropy (PMA) due to spin-orbit coupling (SOC) and the intricate hybridization of orbitals at the interfaces. This characteristic proves valuable in domain wall and skyrmion-based memory devices [11, 12]. In such films, the Dzyaloshinskii-Moriya interaction (DMI) also arises from the ferromagnetic/heavy metal (FM/HM) interface through indirect exchange mechanisms, as presented in section 2.2.3. In 1980, Fert et al. [13] proposed that a magnetic multilayer system with a material possessing strong spin-orbit coupling produced DMI, where it arises due to the interaction between FM/HM layers. DMI in such films stabilizes Néel domain walls and skyrmions. Studies suggest that FM material with high spin-orbit coupling HM produces high DMI. Additionally, structural inversion asymmetry plays an important role here. Hrabec et al. (2014) [14] found that breaking inversion symmetry at the top Co/Pt interface by a HM increases the DMI significantly. In 2016, Yang et al. studied the Ir/Co/Pt and Pt/Co/Pt systems using first-principle calculations. They reported that the Co/Pt and Ir/Co interfaces produce DMI with opposite chirality. Therefore, the net DMI in the Ir/Co/Pt system is higher than in the Pt/Co/Pt systems [15].

PMA and DMI can be modified by changing growth parameters such as temperature and pressure [16–18], interface roughness, and inter-diffusion [19, 20], individual and total layer thickness [16, 21, 22], crystal structure [23], and oxidation [11, 24, 25]. However, some of these might not be useful due to complexity, which may lead to differences in film and interface quality. In this scenario, tuning these properties by changing materials and their layer thickness might be useful. Additionally, locally altering material properties using an electric field opens new possibilities in nanomagnetism; however, achieving reversible changes remains challenging.

1.1.2 Electric fields gating of magnetic multilayers

In 1960, the modulation of magnetic properties by E-fields was theoretically predicted, and this was first demonstrated by Ohno et al. in 2000 [26, 27]. They studied a semiconductor field-effect transistor of GaAs substrates/AlSb/(Al,Ga)Sb/InAs/(In,Mn)As, where a gate voltage was applied through a polyimide layer and a Cr/Au gate electrode. The applied gate voltage changed the 2D sub-band of the ultrathin magnetic layer. They observed that a positive voltage decreased the hole concentration and the ferromagnetic interaction between Mn ions, thereby reducing the Curie temperature.

Subsequently, E-fields have been utilized to manipulate fundamental material properties such as magnetic moment [28], perpendicular magnetic anisotropy (PMA) [29, 30], Dzyaloshinskii-Moriya interaction (DMI) [30–33], as well as domain wall motion [34, 35] and skyrmion manipulation [36, 37]. The E-field reduces the switching time in spin transfer torque (STT) and spin-orbit torque (SOT)-based voltage-controlled magnetic anisotropy (VCMA) devices [38–40]. Moreover, it (E-field) may reduce the current density required to switch magnetic tunnel junctions (MTJs) [41].

The E-field shifts the Fermi level and alters carrier density in FM, resulting in modulated magnetic properties. The E-field can accumulate or deplete charges at a ferromagnetic/oxide interface, as seen in Fe/Co/MgO, which changes the electronic occupation of orbitals. Consequently, this leads to hybridization of orbitals in the ferromagnetic layer, affecting magnetic properties such as magnetic anisotropy and magnetic moment. In addition to the charge effect, the E-field may lead to the migration of ions, such as oxygen or hydrogen, which in turn changes the magnetic properties.Magneto-ionic modulation provides a nonvolatile effect and is of great interest due to its significant magneto-electric effect, characterized by a large change in interfacial anisotropy ($\approx>$ 0.6erg/cm^{-}2 or 5000 fJ/Vm) [42, 43]. These two mechanisms can affect magnetic multilayers individually. On the other hand, the superimposition of the two mechanisms might produce a large change [28, 29, 44].

Although recent studies have already demonstrated the effect of E-fields in magnetic systems for spintronics device applications, most of the research has focused on investigating the magnetic layer adjacent to an oxide layer, primarily due to the short screening length in metals. The conduction electrons screen the E-field, making it challenging to modify magnetic properties without damaging the gate electrode. Therefore, this approach excludes a potential structure of FM/HM multilayers. On the other hand, magneto-ionic techniques offer advantages in resolving the E-field screening. Here, ions (i.e., oxygen ions) migrate as an effect of the electric field. Therefore, the thickness of the adjacent HM layer is crucial, because it may introduce another challenge: the penetration depth, which needs to be overcome by using an ultra-thin HM layer. Structural and interfacial magnetic properties play a key role in magnetic systems. Understanding the origin of PMA and DMI at a particular HM/FM/HM interface and its modulation is challenging. Additionally, the magnetoionic effect at the interface, states of oxygen ions, penetration depth, and its physical mechanisms limit its material-specific application. The chemical interaction between different metals and transported oxygen ions affects the durability of the nonvolatility effect.

The stability of domain wall and skyrmion-based devices depends on interfacial magnetic properties such as PMA and DMI. These parameters are crucial for controlling domain wall nucleation, domain wall dynamics, and skyrmion motion. Different studies have demonstrated the interfacial magnetic properties of Co/Pt interfaces. I have experimentally investigated into how the E-field modifies the properties of magnetic systems, such as anisotropy and DMI. Our focus lies in developing and optimizing different magnetic systems, specifically Ta/Pt/CoB/Ir/Pt, which are compatible with applying E-fields through gating structures (HfO_2) and the ionic liquid. Ultra-thin nonmagnetic layers are employed to reduce screening currents while ensuring that the material system has low magnetic pinning, thus preventing domain walls and skyrmions from being immobilized.

Additionally, we have explored the effect of E-fields on structural properties and have presented a proof-of-principle domain wall-based device.

1.2 Thesis layout

Chapter 2 discusses fundamental concepts, presenting magnetic interactions and energies in the studied system, followed by magnetic spin textures such as domain walls and skyrmions. This chapter concludes with a comprehensive literature review focusing on the manipulation of magnetic properties through material engineering and E-fields.

In Chapter 3 I present experimental techniques to understand the physical phenomena in this work and measures fundamental material properties before and after applying E-fields. Following this, Chapter 4 provides a comprehensive exploration of fundamental material properties (i.e., PMA) of magnetic thin films. Through this investigation, I emphasize the role of interface engineering in the behavior of magnetic multilayers, particularly in generating anisotropy energy and assist interactions within the thin film. Furthermore, the crucial role of DMI in stabilizing skyrmions and Néel domain walls within magnetic systems is highlighted.

The subsequent experimental results chapter (Chapter 5) demonstrates the effect of E-fields on the studied system, comparing anisotropy and magnetic moments before and after applying E-fields. Additionally, the chapter observes domain nucleation as an effect of applied E-fields and the reversibility of the system.

Chapter 6 concludes the principal results with the structural and interfacial magnetic properties and the effect of E-fields on them, including a discussion on the state of oxygen. The last chapter (Chapter 7) on results presents micromagnetic simulations of field- and current-driven domain wall devices. Skyrmion nucleation is conducted by current, and a proof-of-principle domain wall device is also presented in this chapter. Finally, the work is summarized, and future research directions are outlined in Chapter 8.

Chapter 2

Theoretical Background and Literature Review

2.1 Introduction

This chapter introduces fundamental concepts and presents a literature review, starting with the theoretical background essential for understanding this work. It draws from various sources, including books [45–48], a journal article [49], and PhD theses [11, 25, 50–52].

The first section, explores the energies and interactions related to magnetic thin films, such as exchange energy, magnetocrystalline anisotropy, shape anisotropy, perpendicular magnetic anisotropy, and the Dzyaloshinskii-Moriya interaction.

Section 2.3 discusses magnetic domain walls and skyrmions, covering domain wall motion regimes and material structures suitable for hosting stable skyrmions and domain walls.

The velocity of domain walls and the speed of skyrmions might be crucial for spintronics-based data storage systems. However, their significance depends on fundamental magnetic characteristics. Therefore, Section 2.4 reviews literature on controlling these fundamental magnetic properties through interface engineering and E-fields, which are also crucial for hosting skyrmions. Finally, the chapter is concluded with a summary.

2.2 Energies and interaction in ferromagnetic systems

Ferromagnetism is a property exhibited by specific materials like iron (Fe), nickel (Ni), and cobalt (Co). It is characterized by spontaneous magnetization, meaning these materials possess magnetic moments even in the absence of an external magnetic field. This phenomenon arises from the alignment of magnetic moments due to interactions between neighboring magnetic moments. The magnetic moment, a fundamental characteristic of ferromagnetism, originates from electron spin, angular momentum, and spin-orbit interactions.

Ferromagnetic materials align their magnetic moments with the direction of an applied magnetic field, exhibiting a positive susceptibility ($\chi_{\mathrm{FM}} = \frac{\delta \mathrm{M}}{\delta \mathrm{H}}$) typically ranging from 10^4 to 10^6. Weiss proposed that the interaction between neighboring atoms is mediated by a molecular field $\mathrm{H_m}$=λ_wM. The total effective magnetic field experienced by each atom is $\mathrm{H_{eff}} = \mathrm{H} + \lambda_\mathrm{w}\mathrm{M}$. The magnetic moments align due to this effective field, which leads to spontaneous magnetization. This spontaneous magnetization is temperature-dependent. Above the Curie temperature T_C, the thermal energy is high enough to overcome the interaction energy between neighboring atoms and the molecular field, resulting in the loss of spontaneous magnetization and the material exhibiting paramagnetic behavior. Curie-Weiss law can be written as, $\chi = \frac{C}{T-T_C}$, where λ_w is the Weiss constant, $T_C = \lambda_w C$, C is the Curie constant (SI unit m^3K/mol).

Different energy terms and types of interactions significantly influence the total energy within a ferromagnetic thin film, thereby governing its magnetization configuration and dynamics. Consequently, this discussion exclusively addresses energy and interactions relevant to thin films.

2.2.1 Exchange energy

The exchange interaction is a quantum mechanical effect. It describes the energy relationship between two neighboring particles and is directly connected to the Pauli exclusion principle.Fermions (i.e., electrons) with parallel spins tend to avoid the same spatial location due to Coulomb repulsion. This spatial separation reduces the electron-electron repulsion energy, resulting in an energy reduction associated with the parallel spin configuration. The rule arises because minimizing Coulomb repulsion leads to a lower energy state when electrons occupy different spatial orbitals with parallel spins, which is the basis for Hund's rule. The generalized Hamiltonian of the Heisenberg exchange interaction for a multi-electron lattice is represented by the following equation:

$$H_{ij} = -\sum_{i \neq j} (\mathcal{J}_{ij} \vec{S_i} . \vec{S_j}), \tag{2.1}$$

where, S_i and S_j represent the spin angular momentum of electrons and $\mathcal{J}_{ij}$ represent the exchange coupling strength between two electrons. When $\mathcal{J}$ is negative, the material exhibits antiferromagnetic properties, leading to antiparallel alignment of spins $\mathcal{J}$ results in parallel alignment of spins S_i and S_j. In contrast, a positive $\mathcal{J}$ results in parallel alignment of spins, indicating ferromagnetic behavior. Materials such as Co, Fe, Ni, and Gd are characterized by spontaneous magnetization due to ferromagnetic behavior. In the case of a 1-D spin chain, considering a angle ϕ_{ij} between two neighboring spins S_i and S_j, the exchange energy can be expressed as:

$$E_{ij} = -\mathcal{J} S^2 \sum_{i \neq j} (\cos(\phi_{ij})), \tag{2.2}$$

when the angle (ϕ_{ij}) between the spins of two neighboring atoms is small, the energy can be approximated as:

$$E_{ij} = -\mathcal{J}S^2(1 - \frac{\phi_{ij}^2}{2}) = \text{Const.} + \frac{\mathcal{J}S^2a^2}{2}(\frac{\delta\phi_{ij}}{\delta x})^2, \tag{2.3}$$

The exchange energy of continuous magnetization can be written by,

$$E_{ex} = \int_V A[(\bigtriangledown m_x)^2 + (\bigtriangledown m_y)^2 + (\bigtriangledown m_x)^2]dV, \tag{2.4}$$

where V represent the volume of material and m_x , m_y , m_z denote the magnetization components in different directions. Exchange stiffness A is approximately given by $\frac{JS^2Q}{a}$ erg/cm, a is lattice constant, and Q is the number of atoms in a unit cell.

2.2.2 Anisotropy energy

Magnetic anisotropy originates from spin-orbit coupling (SOC) and magnetic dipolar interaction. The SOC arises from the interaction between the electron's spin and its orbital motion. When considering a stationary electron, the motion of the nucleus around it generates an effective current loop, result in a magnetic field. Consequently, the electron's spin tends to align itself with this induced magnetic field, and the magnetic field is larger for heavier nuclei. This interaction, wherein the electron's spin aligns with the magnetic field induced by its orbital motion around the nucleus, is the SOC. The dipolar interaction is a long-range interaction dependent on the shape of the materials. In thin films, it favors in plane (In-P) magnetization. Spin-orbit interaction gives rise to magnetocrystalline anisotropy and interfacial anisotropy. Here, the electron's spin couples with its orbital motion, generating a small orbital momentum. The combination of orbital momentum and alignment with the crystal axes produces an energy known as magnetocrystalline anisotropy, which is determined by the orientation of magnetization relative to the crystalline axes. In the studied system, the ferromagnetic layer is amorphous and lacks magnetocrystalline anisotropy. However, it is discussed here for completeness.

Magnetocrystalline anisotropy

In a magnetic thin film, the internal energy or magnetocrystalline anisotropy energy depends on magnetization and crystalline direction, arising from the crystal-field effect and spin-orbit coupling. This internal energy drives the magnetization to align with a preferred direction, often referred to as the easy direction, while the opposite direction represents the maximum energy direction or hard axis. Depending on the shape of the lattice structure, anisotropy can be either uniaxial or cubic.

Cubic anisotropy occurs when a material exhibits easy axes in multiple directions. For example, Nickel possesses a face-centered cubic (FCC) structure, with easy axes along the $< 111 >$ directions, which include [111], $[11\bar{1}]$, $[1\bar{1}1]$ and $[\bar{1}11]$.The energy density for cubic anisotropy can be expressed as:

$$\epsilon_{\mathrm{AM}} = \mathrm{K}_0 + \mathrm{K}_1(\alpha_1^2\alpha_2^2 + \alpha_2^2\alpha_3^2 + \alpha_3^2\alpha_1^2) + \mathrm{K}_2(\alpha_1^2\alpha_2^2\alpha_3^2), \tag{2.5}$$

where, α represents the cosine of the angle between the crystal axis and the magnetization direction, and K is the anisotropy constant. The easy axis of a cubic crystal may change depending on the value of K; for instance, when $\mathrm{K} > 0$, the easy axis will be along $< 100 >$ axes.

Uniaxial anisotropy occurs when the magnetic anisotropy energy in a material is directed towards one easy axis, as seen in hexagonal crystals like cobalt (Co). For cobalt, the anisotropy energy can be expressed as:

$$\epsilon_{\mathrm{AM}} = \mathrm{K}_1 \sin^2\theta + \mathrm{K}_2 \sin^4\theta + ..., \tag{2.6}$$

where θ represents the angle between the easy axis and the magnetization direction, and K is the anisotropy constant. Higher-order terms in this equation can often be neglected due to their small values, resulting in a simplified expression such as:

$$\epsilon_{\mathrm{AM}} = \mathrm{K}_{\mathrm{u}} \sin^2\theta, \tag{2.7}$$

where K_{u} is the uniaxial anisotropy.

Shape anisotropy

Shape anisotropy depends on the shape of the sample and arises from magnetostatic interactions between magnetic dipoles. A magnetized sample generates magnetic poles at its surface due to the alignment of spins. This effect produces a stray field outside the sample that acts in the opposite direction to the original magnetization. A demagnetizing field is induced inside the sample, which attempts to reduce the stray field. The magnetization tends to align along directions that minimize the surface charge distribution to minimize the energy cost. The shape anisotropy can be expressed as:

$$\epsilon_{\mathrm{sh}} = -\frac{1}{2}\mu_0 \int_V \vec{\mathrm{H}_{\mathrm{d}}} \cdot \vec{\mathrm{M}} dV, \tag{2.8}$$

where, $\mathrm{H}_{\mathrm{d}} = -\mathbb{N}\vec{\mathrm{M}}$ is the demagnetization field with demagnetization factor or tensor $\mathbb{N}$, which depends on the shape of the magnetic system. For a thin film $\mathbb{N} = 1$ along the perpendicular direction, μ_0 is the vacuum permeability. The shape anisotropy energy per unit volume can be written as:

$$\epsilon_{\mathrm{sh}} = -\frac{1}{2}\mu_0 \mathrm{M}_{\mathrm{s}}^2 \cos^2\theta, \tag{2.9}$$

where, θ is the angle between the magnetization and easy axis and M_{s} is the saturation magnetization. The equation 2.9 favour In-P magnetization.

In order to minimize stray fields and demagnetizing energy, the sample will align magnetic moments in specific directions within small regions called domains. The boundaries between neighboring domains are known as domain walls. The formation of domains and domain walls reduces the overall demagnetization energy, and associated anisotropy energy.

Interfacial anisotropy

In a magnetic multilayer system, perpendicular magnetic anisotropy (PMA) originates from the spin-orbit coupling between the ferromagnetic layer and adjacent heavy metals. This coupling occurs due to the hybridization of the magnetic 3d electron orbitals with the 5d electron orbitals of the heavy metal. The strength and presence of PMA depend significantly on the growth conditions and structure of the heavy metal layer, as these factors influence the interface quality and the degree of orbital hybridization and the resulting magnetic anisotropy. The effective anisotropy in a magnetic system can be expressed as:

$$\epsilon_{\mathrm{i}} = \mathrm{K}_{\mathrm{eff}} \sin^2\theta, \tag{2.10}$$

$$\mathrm{K}_{\mathrm{eff}} = \mathrm{K}_{\mathrm{v}} + \frac{\mathrm{K}_{\mathrm{s}}}{\mathrm{t}_{\mathrm{FM}}}, \tag{2.11}$$

where, θ is the angle between easy axis and magnetization. Effective anisotropy, $\mathrm{K}_{\mathrm{eff}}$ = surface anisotropy (K_{s}) or interface anisotropy + volume anisotropy (K_{v}). The (K_{v}) = magnetocrystalline anisotropy (bulk) (K_{b})+shape anisotropy (K_{sh}), and t_{FM} is the thickness of the ferromagnetic layer.

When the interfacial anisotropy is positive, the effective anisotropy constant K_{eff} is also positive. In this case, the demagnetizing contribution is lower compared to the surface contribution. Consequently, the interfacial contribution overcomes the volume contribution, resulting in PMA, where the easy axis is perpendicular to the sample's surface. If the ferromagnetic layer is thick enough, the magnetization of the film aligns along the surface, resulting in a negative K_{eff}.

In this experimental work (Chapter 4 - 6), thin film multilayers of Pt/CoB/Ir and Pt/CoB/Cu were studied, where PMA originated from the Pt/CoB interface. The studied systems exhibit strong PMA at CoB = 0.5 nm, shifting to In-P at around 2.4 nm. PMA begins to decrease below 0.5 nm, possibly due to intermixing at the interface between ferromagnetic and heavy metals.

2.2.3 Dzyaloshinskii-Moriya interaction

DMI is an anisotropic exchange interaction produced by spin-orbital interaction in materials with low inversion symmetry. Dzyaloshinskii developed a model in 1958 to explain weak ferromagnetism, proposing an asymmetrical term based on symmetries. Later, in 1960, Moriya introduced the idea that spin-orbit coupling is responsible for this mechanism [53, 54]. Bulk magnetic systems, such as FeGe with B20 crystal orientation, produce DMI [55]. In 1980, A. Fert et.al. [13] proposed that DMI could be found in a material system with low inversion symmetry.

In thin film systems, inversion asymmetry is obtained through the combination of different materials such as ferromagnets (FM) and heavy metals (HM). Therefore, DMI originates from the FM/HM interfaces due to the interaction between neighboring FM spins influenced by a HM ion with large spin-orbit coupling. This interaction can be described by the equation:

$$E_{DMI} = -\vec{D_{12}}.(\vec{S_1} \times \vec{S_2}), \tag{2.12}$$

$S_{1,2}$ and D_{12} represent adjacent spins and the DMI vector, respectively. This interaction results in spin displacement or antisymmetric spin arrangements opposite to the exchange interaction, leading to a preference for orthogonal alignment. The sign of D_{12} vector depends on the materials in system and the clockwise/counterclockwise displacement from S_1 to S_2.

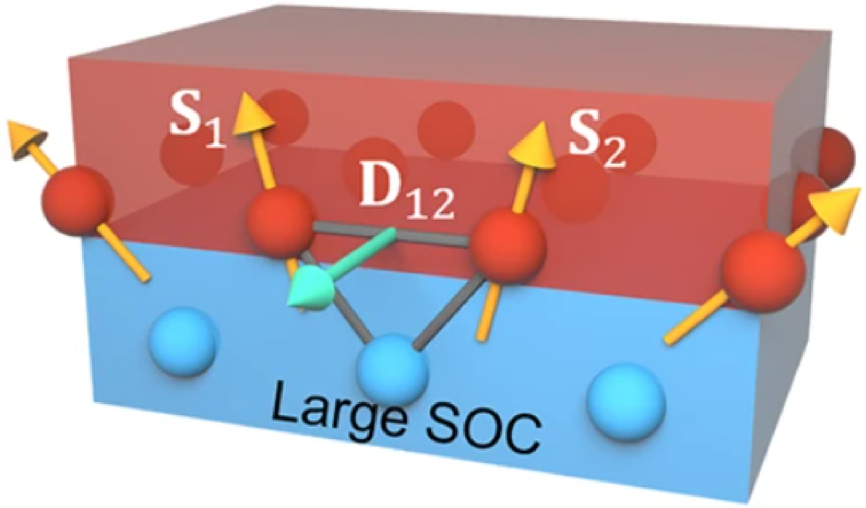

Figure 2.1: Interfacial DMI at the interface between a magnetic (red) and a nonmagnetic (blue) layer. The resulting DMI vector D_{12} is perpendicular to the plane of the triangle [56].

Figure 2.1 illustrates the schematic of DMI interaction between two adjacent spins of a FM and a HM ion, where the resulting DMI is perpendicular to the surface (or the $\vec{D}_{12}$ along the perpendicular direction) and the interaction occurs between a magnetic layer and a nonmagnetic layer.

Since it originates from the interface, DMI depends on interface quality, thin film deposition, and materials. Therefore, achieving the required DMI involves tailoring the FM/HM interfaces. In this experimental work, Pt/CoB/Ir/Pt and Pt/CoB/Cu/Pt systems were studied to investigate DMI and its response to applied E-fields. Previous studies indicate that the Co/Ir interface promotes clockwise and Co/Pt interface promotes counterclockwise spin rotation. However, Ir between the top Co/Pt interface increases DMI [57–60].

DMI stabilizes skyrmions and chiral domain walls in spintronic devices. Therefore, the next section briefly discusses magnetic textures such as domain walls and skyrmions.

2.3 Magnetic spin textures

2.3.1 Magnetic domain walls

The energies within a magnetic multilayer system play a crucial role in regulating the structure of magnetic domains. The magnetostatic energy within a ferromagnetic system is generated by the magnetization and the demagnetizing field. The magnetization represents the aligned magnetic moments within the material, while the demagnetizing field is an opposing internal field induced by the surface poles of the magnetized material. The interaction between these two factors results in the magnetostatic energy, which plays a crucial role in the magnetic behavior and stability of ferromagnetic systems. Magnetically easy axes or planes emerge from anisotropy energies. In order to minimize energy in a magnetic sample, aligning all moments along a magnetically easy axis may lead to the creation of a demagnetizing field, consequently resulting in domain formation. The so-called domain wall is the area separating two domains, where the magnetic moment changes direction. This process helps the magnetic system achieve energetically stable configurations and here the net magnetization is minimized. When magnetic moments are aligned in one direction, the magnetization is nonzero, indicating saturation. Figure 2.2 provides an example of domains and a domain wall. The system saturates with a large OoP applied field, and the domain is nucleated and driven using an opposite OoP magnetic field.

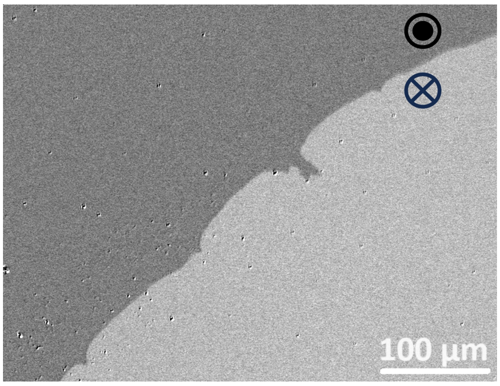

Figure 2.2: An example of magnetic domains in the Ta/Pt/CoB/Ir/Pt system was captured using a Kerr microscope, where white region indicates domains pointing down, while black regions indicate domains pointing up. A domain wall is the boundary region between two domains. These results are further discussed in Chapter 4.

Domain wall configuration depends on the energies discussed in previous sections. Exchange energy dominates uniform aligned moments, while dipole energy minimizes energy by splitting the system into domains. Anisotropy energy aligns magnetization to the easy axis. In a magnetic film, DWs are in general a combination of two types of DW. Figure 2.3 shows Néel and Bloch types of domain walls. A Bloch wall occurs when the magnetic moment rotates perpendicularly to the domain wall plane, while a Néel wall occurs when it rotates parallel to the domain wall plane. Bloch-type domain walls are more energetically stable compared to Néel walls because Néel-type walls process demagnetization energy. Large DMI energy can stabilize Néel-type domain walls.

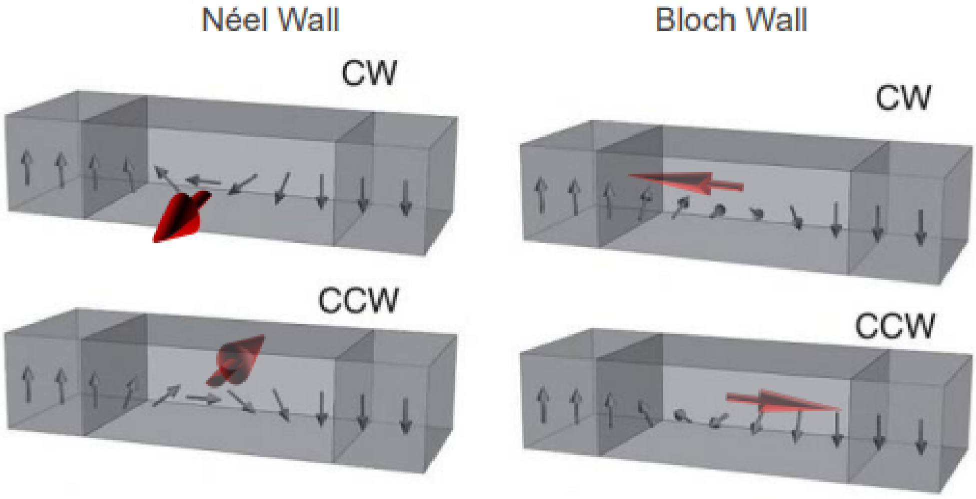

Figure 2.3: Bloch and Néel types of domain walls in a PMA magnetic system, where the red arrow represents the clockwise (CW) and counterclockwise (CCW) directions as a guide for the eye [25].

Domain wall motion

The domain wall may be considered as a 1-D elastic magnetization (along the z direction) that changes along a 2-D weakly disordered surface (along the x and y directions). The behavior of domain wall motion due to an applied magnetic field depends on the strength of the field and can be characterized as creep regime motion, depinning regime motion, and flow regime motion.

Domain wall motion occurs in different regimes depending on the applied conditions. In the creep regime, characterized by low driving forces and significant thermal energy, domain walls move gradually. When a higher driving force then creep regime, domain wall motion transitions into the depinning regime. Here, the influence of temperature diminishes, and in the subsequent flow regime, its effect is negligible. In the flow regime, domain wall motion is unaffected by pinning and is governed by the microscopic structure of the domain walls. Moreover, in this regime, the motion shows a linear relationship with the applied driving force.

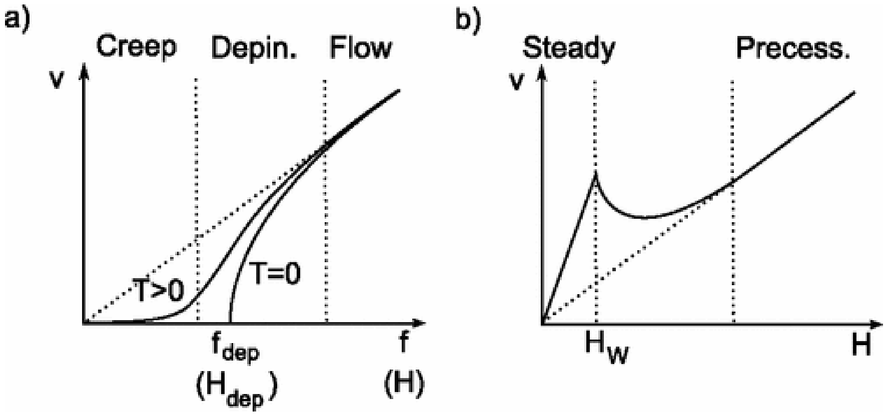

Figure 2.4: a) Domain wall velocity regimes as a function of driving force, f. b) domain wall flow regimes. Outside of Walker field the domain wall move without pinning. (b) The walker breakdown field ($\mathrm{H_w}$) is marked between the steady state and precessional regimes [61].

When the temperature is zero (T=0), the domain wall is affected by pinning below a threshold field $\mathrm{H_{dpin}}$, but above this threshold, it starts to move. On the other hand, when temperature is higher then zero ($T > 0$), the thermal energy overcome the depinning [61–63].

In this work the domain wall motion in creep regime is used to estimate the DMI, which can be written as:

$$\nu = \nu_0 \exp\left\{-\frac{\mathrm{U_c}}{\mathrm{K_B T}}\left(\frac{\mathrm{H_{dpin}}}{\mathrm{H}}\right)^{1/4}\right\}, \tag{2.13}$$

where $\mathrm{U_c}$ is the threshold energy for depinning, $\mathrm{k_B}$ is the Boltzmann's constant, H is the applied magnetic field. In the creep regime the $\ln(\nu)$ shows a linear behaviour with the $1/\mathrm{H}^{1/4}$.

Figure 2.4(a) shows domain wall motion regimes. Figure 2.4(b) shows two linear flow regimes and the Walker breakdown field (H_w) between them. Walker breakdown is a critical phenomenon in the dynamics of magnetic domain walls, characterized by a transition from stable to unstable motion as velocity increases. This transition occurs due to changes in the magnetization precession inside the domain wall, fundamentally altering its motion characteristics. The magnetization within the domain wall begins to precess, leading to complex internal dynamics and a breakdown of the linear velocity-field relationship [64, 65].

During the modeling of field-driven domain-wall devices, we have also observed the Walker breakdown, which is presented in Chapter 7

2.3.2 Magnetic skyrmions

Skyrmions are stable topological defects characterized by a chiral spin texture. The mathematical concept of skyrmions was first introduced by physicist Tony Skyrme in 1961 to describe the stability of hadrons in particle physics. This concept was later extended to condensed matter physics to explain similar chiral spin structures in magnetic materials [66, 67].

DMI is a relativistic effect that arises due to the combination of broken inversion symmetry and spin-orbit coupling, resulting in chiral magnetic structures. The DMI is an antisymmetric exchange interaction that promotes the formation of non-collinear spin structures, deviating from simple ferromagnetic alignment. This interaction is particularly significant in systems where inversion symmetry is broken, such as at the interfaces of multilayer structures.

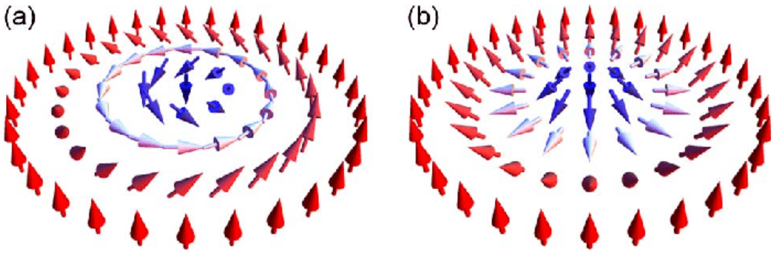

Figure 2.5: a) Néel-type skyrmion b) Bloch-type skyrmion [66].

In such multilayer systems, the combined effects of DMI and broken inversion symmetry give rise to chiral spin textures, such as skyrmions [68, 69]. These structures represent a twist in the magnetization that is topologically protected, meaning they cannot be easily unwound. The chirality of Néel walls, a specific type of domain wall, is determined by the sign of the DMI, which dictates the direction of spin rotation within the wall. Alongside the DMI, exchange and dipolar interactions are crucial in influencing the stability and chirality of skyrmions.

Skyrmion magnetic textures are usually considered to belong to one of three classes: Bloch-type, Néel-type skyrmions, and anti-skyrmions. Bloch-type and Néel-type skyrmions are the most common. Both involve the rotation of the moment from parallel outside to anti-parallel inside. In a Bloch skyrmion, the moment rotates in the plane perpendicular to the skyrmion radius, turning on tangential planes and perpendicular to the radial directions. Skyrmions can be nucleated by a magnetic field, current, and E-field [70–72]. Skyrmions can be defined by their topological or winding number, which can be written as:

$$\mathrm{W_{sk}} = \frac{1}{4\pi}\int(\vec{\mathrm{m}}.(\frac{\delta\vec{\mathrm{m}}}{\delta\mathrm{x}} \times \frac{\delta\vec{\mathrm{m}}}{\delta\mathrm{y}}))\mathrm{dxdy} = \pm 1, \tag{2.14}$$

where, $\vec{\mathrm{m}}$ is the normalized magnetization of the thin film. Figure 2.5 shows the Néel-type (a) and Bloch-type ($\mathrm{W_{sk}} = -1$) (b) skyrmions ($\mathrm{W_{sk}} = -1$). Skyrmion is a topologically protected quasi particle, because its stability and properties, such as its topological charge, are guaranteed by the non-trivial topology of the spin texture. Although skyrmions are not fundamental particles, they exhibit particle-like behaviors and can be manipulated and studied like particles. The topological number is a integer value ($\mathrm{W_{sk}} \neq 0$) resulting in skyrmion properties such as the topological Hall effect and low current density to move skyrmions. The topological number for Néel and Bloch type skyrmions is $\mathrm{W_{sk}} = \pm 1$. Recent studies show that for some materials, the topological numbers could be $\mathrm{W_{sk}} = 2$, in that case the topological texture is so-called biskyrmion [73, 74].

2.4 Manipulation of interfacial magnetic properties

Control of interfacial magnetism is an essential condition to build a spin-based device. Controlling fundamental magnetic properties such as magnetic moment, magnetic anisotropy, and DMI is important in spintronic devices. In recent years, several magnetic properties have been controlled by electric fields. Therefore, this section presents a brief discussion on controlling magnetic moment, magnetic anisotropy and DMI by tuning thin-film structure and E-field.

2.4.1 Interface engineering

Waller et al. (1993) [75] conducted a study on the OoP orbital magnetic moment of Co/Pt, Co/Ni, and Co/Pd thin films using X-ray magnetic circular dichroism (XMCD) spectroscopy. They observed a significant increase in the total magnetic moment in Co/Pt and Co/Pd films due to the intermixing of d-d orbitals (3d for Co, 4d for Pd, and 5d for Pt). The authors also performed theoretical calculations to validate their experimental results.

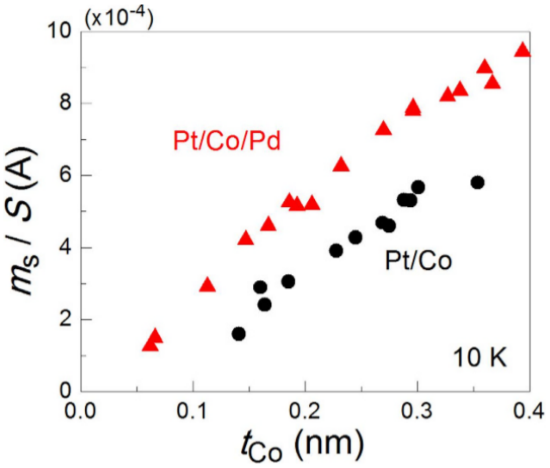

Figure 2.6: The saturation magnetization per unit area depends on the thickness of the Co layer (t_{Co}). The saturation magnetization was measured using a superconducting quantum interference device (SQUID) magnetometer. The Pt/Co/Pd film shows higher saturation magnetization then Pt/Co film, which gives an give an explanation of magnetic moment in Pd layer due to ferromagnetic proximity effect [28].

Wilhelm et al. (1999) [76] investigated magnetic moments in Ni/Pt multilayer samples using SQUID magnetometry. They utilized the XMCD technique to analyze the individual contributions of Ni and Pt layers. Their findings suggested that the total magnetization slightly depends on the Ni volume. Samples with an ultra-thin Pt layer of approximately two monolayers exhibited slightly higher magnetization.This implies that by using interface engineering techniques, it is possible to achieve tunable magnetization in magnetic thin films, which could enhance the performance and functionality of various spintronic devices.

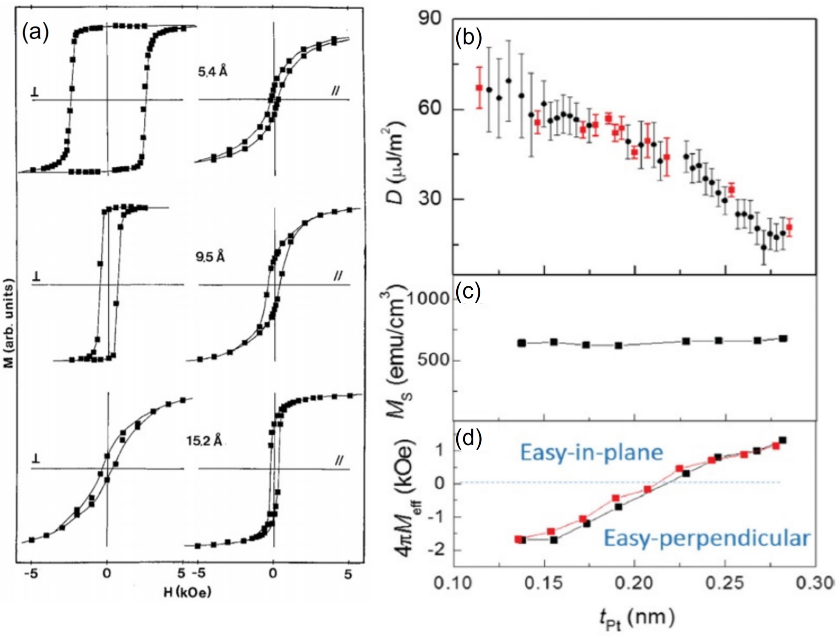

Figure 2.7: Hysteresis loop of Au/Co/Au tri-layer at T=10 K with perpendicular (⊥) and parallel (∥) applied field (H) [77]. For a Ta/CoFeB/Pt/MgO/Ta magnetic system: (b) Dependence of DMI on the thickness $\mathrm{t_{Pt}}$ of the Pt layer: The red points are derived from the linear dependency of $\mathrm{k_x}$ and $\mathrm{f_{DM}}$ where $\mathrm{k_x}$ is the spin wave vector, and $\mathrm{f_{DM}}$ is the difference between the stock and anti-stock frequency. The black points are calculated using a fixed $\mathrm{k_x} = 16.7\ \mathrm{rad}/\mu\mathrm{m}$.(c) Saturation magnetization, $\mathrm{M_S}$ does not change with Pt thickness, and (d) Dependence of $4\pi\mathrm{M_{eff}}$ on $\mathrm{t_{Pt}}$, Black dots represent Brillouin light scattering (BLS) measurements, and red dots represent vibrating sample magnetometer (VSM) measurements. (Figure b-d are taken from the Figure 3 in reference [78].)

Figure 2.6 illustrates the dependence of saturation magnetization on Co thickness. It demonstrates that saturation magnetization in Pt/Co/Pd films is remarkably higher than that in Pt/Co layers, which is attributed to the polarization of the Pd layer [28]. Similarly, Lau et al. (2019) investigated PMA in symmetric and asymmetric trilayers such as Pt/Co/Pt, Ir/Co/Ir, Ir/Co/Pt, and Pt/Co/Ir. They reported extremely high PMA of up to 10 T for Ir/Co/Pt system [79]. Therefore, the magnetization and anisotropy can be tune by changing the HM layer (i.e., Pt, Ir and Pd).

For ultra-thin films, surface anisotropy is more prominent compared to shape anisotropy contribution. Thus, shape and surface anisotropy can be controlled by adjusting the magnetic layer thickness. Figure 2.7a) presents the effective anisotropy of hcp Co thin films grown at room temperature on poly-crystalline Au (111). Experimental results show that Au/Co/Au films exhibit perpendicular magnetic anisotropy (PMA) when the Co thickness (t) is ≈ 12 Å or six monolayers. Ultra-thin Co films with PMA demonstrate large coercivity and the coercivity show a 1/t^2 dependence [77].

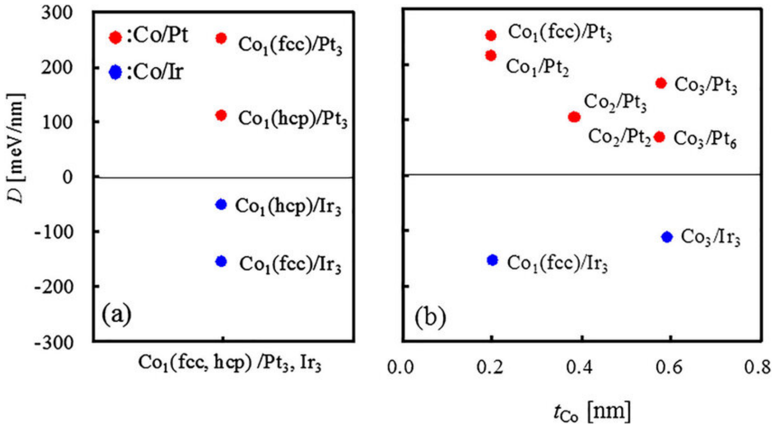

Figure 2.8: First-principles calculations were used to calculate the DMI in Co/Pt and Co/Ir interfaces, where the numbers represent the number of monolayers: a) DMI constant, D of Co/Pt$_3$ (red) and Co/Ir$_3$(blue).The Co atoms are placed between hcp and fcc sites of metallic layers. b) D of Co/Pt and Co/Ir against Co layer thickness [80].

HM on both sides of the FM layer creates an additive effect at the interfaces, resulting in a strong net DMI [15]. Figure 2.8 depicts the DMI parameters for metallic multilayer films studied by first principle calculations. Figure 2.8a) shows that the DMI for hcp Co is lower than for fcc Co, with positive DMI for Pt samples and negative DMI for Ir samples. Figure 2.8b) indicates that the DMI is negative for Ir samples, increasing with Co layer thickness for both Pt and Ir samples. The sign of DMI represent different chirality in the spin configuration of a magnetic material.

Ma et al. (2016) [78] studied the Ta/CoFeB/Pt(wedge)/MgO system using the BLS technique. They found that the DMI is high for 0.1 nm Pt thickness, which decreases with increasing with Pt thickness (Figure 2.7). The $4\pi M_{\mathrm{eff}}$ changes from negative to positive with increasing Pt thickness.

2.4.2 Electric field

The application of E-fields presents a versatile method for localized and dynamic control of interfacial magnetic properties. The magnetic moment arising from the ferromagnetic proximity effect when these materials are deposited on magnetic substrates (Figure 2.9), can rise with E-field. Obinata et al. (2015) [28] reported on E-field manipulation of magnetic moments in Pt/Co/Pd/MgO films at low temperatures (10 K), demonstrating tunable proximity-induced magnetic moments in Pd by applying an E-field. They placed a polymer with ionic liquid during the growth of the Au gate electrode using evaporation. The voltage was applied during magnetic moment measurement using SQUID magnetometry. A positive voltage increases the charge density at the Pd surface, resulting in a larger moment per area. The difference between positive and negative voltage effects increases linearly with decreasing temperature.

Kawabe et al. (2017) [29] investigated E-field-induced changes in the orbital moment in Fe/Co/MgO structures. Their XMCD study confirmed E-field modulation of the Co 3d state, with the orbital magnetic moment changing by 0.013 μB with an applied ± 2 V/nm E-field. This effect arises from charge accumulation or depletion at the magnetic and oxide interface under E-field, altering the electronic occupation of orbitals and resulting in ferromagnetic layer hybridization, directly influencing interfacial magnetic anisotropy

Figure 2.10 illustrates the mechanism of E-field effect. An applied E-field applied to a magnetic sample leads to charge accumulation or depletion at the FM/$\mathrm{MO_x}$ interface, which changes the electronic occupation of orbitals and results in ferromagnetic layer hybridization. The complex hybridization is directly related to interfacial magnetic anisotropy. Thus the applied E-field directly alter it, which may take up to a few second.

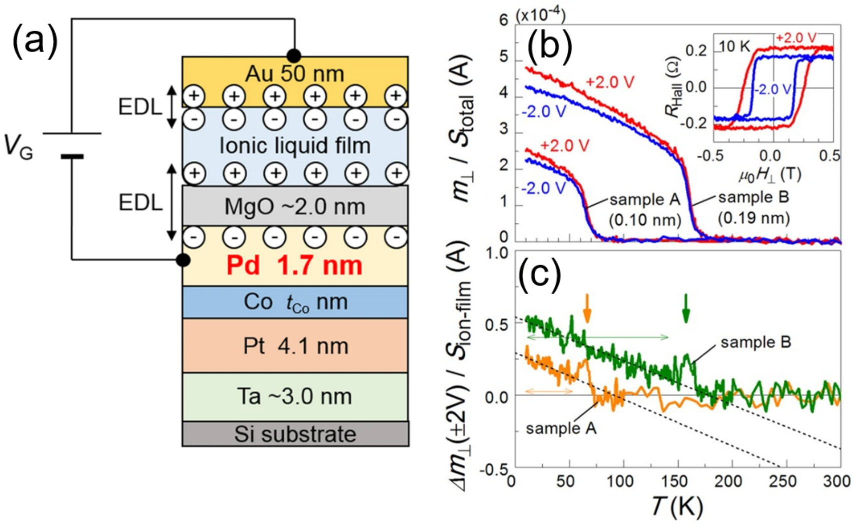

Figure 2.9: (a) The sample structure involves a polymer combined with an ionic liquid, used in the process of gold (Au) growth.(b) Perpendicular component of moment (m⊥)per area at different temperatures for Co thicknesses of 0.1 nm (A) and 0.19 nm (c). The inset shows the Hall resistance measurement at 10 K for Co 0.10 nm. The sample shows a square hysteresis loop at $\pm 2V$. (b) The difference between m⊥ at $\pm 2V$ as a function of temperature. For both samples, the data show linear relationships. Figure 2 and 3 in reference [28].

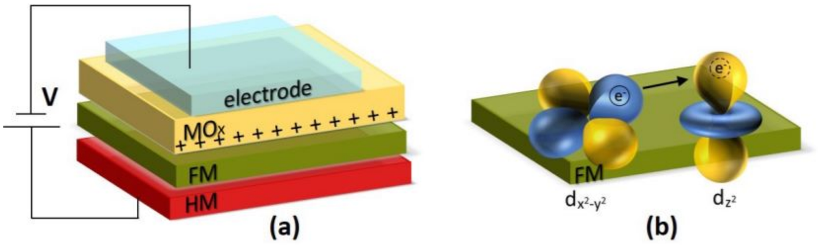

Figure 2.10: (a) Applied negative voltage at FM/MO$_x$ film and charge depletion at the interface (b) Voltage directly changes the electronic occupation of d orbitals [44]

E-field also induces ion migration, causing oxygen ions to migrate from the oxide layer to the FM/MOx interface. Superposition of two mechanisms might produce large changes. The ion (i.e., oxygen) migration occurs as an effect of the E-field, and it takes a long time (a few minutes to several hours). E-field also changes the M$_s$ and T$_c$ for ultra-thin (0.4-0.8 nm) FM layer. For ultra-thin films, interfacial magnetic properties are more prominent than bulk materials. Thus, it is sensitive to E-field [44].

Yang et al. (2018) [15] studied the effect of E-field using first principle calculation. Firstly, the authors prepared ferromagnetic and nonmagnetic layer structures, such as Pb/Co/Pt, with the aim of enhancing DMI. In this setup, they employed inversion geometry stacking from both sides of the magnetic layer to enhance the overall DMI. Secondly, they introduced a top layer of oxide, specifically MnO, to amplify the DMI. The interaction between the oxide and magnetic layer was crucial due to the Rashba effect. Finally, they proposed an approach to control DMI using a gate E-field, as illustrated in Figure 2.11. The microscopic DMI originates from the atomic level and represents the energy difference between clockwise and counterclockwise magnetic spiral configurations of a pair of atoms. The micromagnetic DMI is average of the microscopic DMI of many atoms, which is useful for micromagnetic simulation. The authors demonstrated that both microscopic and micromagnetic DMI increased with an increasing gate E-field. The E-field influences the interfacial spin-orbit coupling (SOC) and electron density at the Co/MgO interface, which then changes the magnetic properties, such as the DMI strength or anisotropy. Additionally, at the Fe/MgO interface, the E-field changes the relative occupancy of the 3d orbitals of Fe, resulting in the modulation of magnetic properties [81]. Therefore, an E-field can affect the band structure, specifically the minority-spin bands near the Fermi level, of a ferromagnetic layer. These changes may include both band hybridization and band splitting, potentially resulting in shifts in band positions as well as modifications in magnetic properties [82].

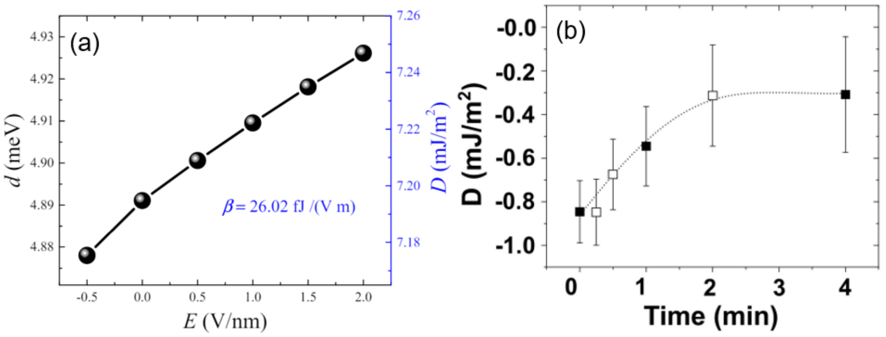

Figure 2.11: (a) The effect of the E-field on DMI was studied using first-principles calculations. The microscopic DMI (d) and micromagnetic DMI (D) exhibit a linear dependence on the E-field. Microscopic DMI refers to the atomic-level interaction, whereas micromagnetic DMI describes the interaction on a continuum scale. Figure 5 in reference [15]. (b) Magneto-ionic modulation of DMI in the Pt/Co/HfO_2 system occurs when a gate voltage of -3 V is applied for up to 4 minutes. The migrated ions decouple the Pt/Co interface; therefore, the DMI decreases. The process is not reversible. Figure 2.10 in reference [40]; [83].

Diez et al. investigated the magneto-ionic modulation of DMI at the Pt/Co interface. Figure 2.11(b) illustrates the change in DMI with gating time. The E-field facilitated the migration of oxygen from the HfO_2 layer, thereby altering the coupling between the HM and FM layers at the interface, resulting in lower DMI. Additionally, they observed a switching phenomenon from In-P magnetization to OoP magnetization. However, they only observed reversibility for a short gating time of up to 1 minute [83].

Pachat et al. (2023) [40] demonstrated the full spectrum (In-P to OoP to InP) of oxidation through ionic liquid gating. They began with an In-P magnetized CoB/HfO_2 system and applied voltage to induce a transition to OoP magnetization. This transition was fully reversible, as depicted in Figure 2.12(a-b). During the process they only applied a negative voltage for an extended amount of time. Throughout the process, they applied only a negative voltage for an extended period. Figure 2.12(c) depicts magnetization switching of an $Fe_{80}Co_{20}$ film at ±200 V, demonstrating that negative voltage induces perpendicular anisotropy, altering the easy axis from In-P to OoP.

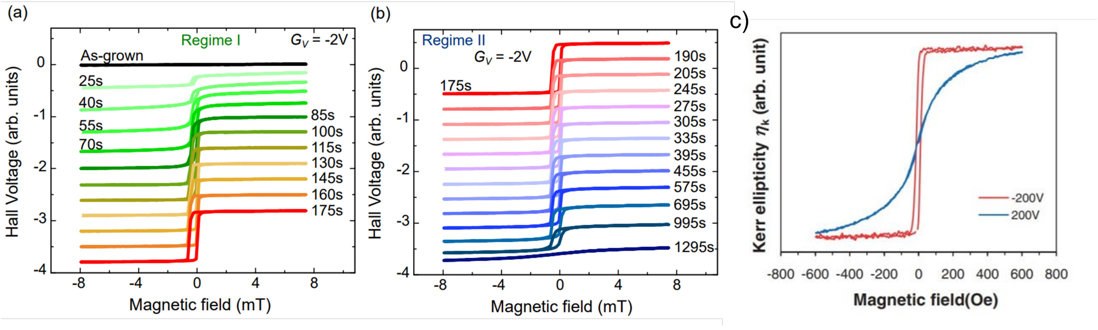

Figure 2.12: Magneto-ionic modulation of the CoFeB/HfO$_2$ system with an applied voltage of a) -2 V changes the in-plane (In-P) magnetization to out-of-plane (OoP) magnetization. This change starts at 25 s, and the magnetization gradually rotates to OoP. b) The process is reversible. When -2 V is applied for an extended period of time, it goes back to In-P again. In this case, the CoFeB might be fully oxidized[40]. he Kerr microscopy hysteresis loop shows the effect of an applied voltage. The voltage was applied through a Polyimide (1500 nm)/ITO(100 nm) structure. With an applied $\pm 200V$ change the in plane sample to OoP, which is also reversible. Figure 3 in [84].

Figure 2.13(a) shows the skyrmion nucleation (writing) and annihilation (deleting) of an Fe layer grown on an Ir substrate. With +3 V, a skyrmion is nucleated, and with -3 V, the skyrmion is annihilated. The voltage modifies the structure and charge at the Fe/Ir interfaces, which then affect the exchange interaction. They mentioned that a positive voltage increases the exchange interaction, which favors the ferromagnetic state. On the other hand, a negative voltage decreases the exchange interaction, which favors the skyrmion state [85]. Figure 2.13b) shows the skyrmion nucleation in the Pt/Co/oxide trilayer with -20 V. The voltage may affect the electron density of states in the Co, which changes the magnetic properties such as saturation magnetization and effective anisotropy. The authors observed the effect near Tc, which may be due to the voltage-induced modulation of magnetic properties.

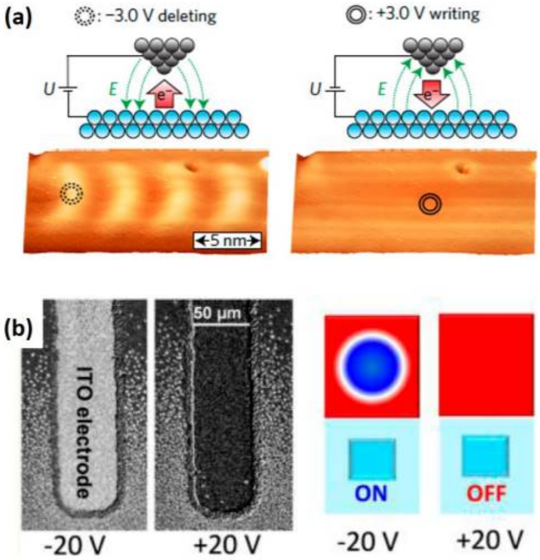

Figure 2.13: (a) Nucleation and annihilation of an isolated skyrmion at 7.8 K in Ir/Fe bilayer. An applied voltage changes the exchange interaction, which nucleate skyemion (writing) [85]. (b) Nucleation and annihilation of a skyrmion bubble at 300 K in Pt/Co/AlO_x trilayer with ±20 V. When a negative voltage is applied, the skyrmion (white bubble) appears on the ITO electrode, which is annihilated by applying a positive voltage. [72].

2.5 Summary

In this chapter, we have briefly discussed the fundamental material properties of PMA magnetic thin films. It's evident that in magnetic multilayers, interface engineering plays an important role as it gives rise to anisotropy energy and interactions within the thin film. PMA, facilitated by heavy metals like Pd, Pt, and Ir in combination with magnetic layers such as Co and CoB, offers significant advantages for high data density in spintronics devices.

Moreover, DMI emerges as a crucial factor in stabilizing skyrmions and Néel domain walls within magnetic systems [86], providing pathways for enhancing functionalities and applications. For devices based on skyrmions and domain walls for information storage and processing, effective manipulation is essential.

E-fields have emerged as a promising tool for modulating material properties, offering avenues for nucleating and controlling domain walls or skyrmions, thereby enabling precise control over their properties. Such advancements hold immense potential for the development of next-generation magnetic devices and technologies. However, the majority of work on E-field manipulation has been conducted on Hm/FM/oxide systems. However, there is potential to benefit from a wider choice of interfaces if one employs FM/metal interfaces and can make E-field gating effective within such structures.

CHAPTER 3

Experimental Methods

3.1 Introduction

This chapter presents a brief overview of methods used for growing and characterizing thin films in this project. The magnetic multilayer films were grown by dc magnetron sputtering within the Royce deposition chamber at the University of Leeds. We have studied structural properties using X-ray reflectivity (XRR), X-ray photon spectroscopy (XPS), transmission electron microscopy (TEM) and atomic force microscopy (AFM). XRR and AFM data are shown in section 4.3. XPS and TEM data are shown in section 6.3. The saturation magnetization and magnetic moments were estimated through vibrating sample magnetometry (SQUID VSM) measurements, which are shown in section 4.4.2, section 5.5, and section 6.4. Kerr microscopy was utilized to analyze domain patterns and domain wall velocity within the samples, which are presented in section 4.2 and section 4.5. The effective anisotropy constant K_{eff} was measured using anomalous Hall effect measurements, and the data are presented in section 4.4.1, section 5.5.2, and section 6.4. Dzyaloshinskii-Moriya interaction (DMI) constant were estimated using Kerr microscope and Brillouin light scattering (BLS), data were presented in section 4.5 and section 6.4.2, respectively. X-ray magnetic circular dichroism (XMCD) and X-ray absorption spectra (XAS) were carried out to investigate the state of oxygen, which is presented in section 6.4.3.

The BLS measurement was conducted at the Process and Material Sciences Laboratory (LSPM) in France. XMCD and XAS were performed at ALBA Synchrotron in Spain. All other measurements were carried out at the University of Leeds.

In our research group all these techniques were used to investigate magnetic thin films in order to find magnetic properties. Consequently, certain information and images have been adapted from the following references: [11, 25, 40, 51, 52, 87–90].

3.2 Thin film deposition techniques

3.2.1 DC magnetron sputtering

Magnetic multilayer systems were grown by dc magnetron sputtering, a physical vapour deposition (PVD) technique commonly used for depositing metallic thin films, including magnetic films and alloys, optical devices, semiconductor manufacturing, and disk drives. This technique utilizes high-energy particles to eject target material, depositing it onto a substrate within a high-vacuum chamber. The process involves the use of metal sources as target materials in the presence of inert gas, typically Ar. A negative voltage of approximately 250 V is applied between the anode and cathode to create Ar plasma. The voltage between the anode and cathode will establish an electric field between them. Therefore, the cathode attracts free electrons into the chamber (a small amount of free electrons will be present naturally). These free electrons will gain kinetic energy and collide with the Ar atoms due to their high velocity. During the collisions between the electrons and argon atoms, the argon atoms will lose one or more electrons. As a result, there will be positively charged Ar^+ ions and additional electrons. The newly created electrons will contribute to a chain reaction. Consequently, more Ar^+ ions and electrons will be created, forming a dense cloud of ions and free electrons. This dense cloud is the Ar plasma. These ions are accelerated towards the target, causing atoms to be ejected and free electrons to be released. The ejected atoms form a thin film on the substrate, while the free electrons contribute to sustaining the Ar plasma and thus Ar^+ formation. The magnetron sputtering technique is displayed on Figure 3.1. This method involves the use of permanent magnets positioned behind the target material. This setup allows for the interaction between electric and magnetic fields, effectively confining electrons onto the target. This confinement results in high plasma density and an high growth rate. Throughout the growth process, running water is employed to cool the target.

The Ta/Pt/CoB/Ir/Pt samples were deposited on a 36 × 36 mm Si substrate with 300 nm SiO_2 thermal oxide. Prior to deposition, the substrates went through a cleaning process in an ultrasonic water bath using acetone, isopropanol, and deionized (DI) water. Subsequently, they were baked at 110°C for one minute and then subjected to plasma ashing for an additional minute to remove organic condemnations. The oxygen plasma contains oxygen ions, radicals, and ozone. These species react with the organic condemnations and produce gases.

Our sputtering system, operates within an ultra-high vacuum environment with a base pressure of 10^{-9} mbar and a growth pressure of 10^{-3} mbar. This system is equipped with eight sputtering guns and six sample holders, offering a diverse range of material choices for deposition onto a single substrate. To achieve uniformity in the films, the substrate is rotated at 120°/s during the deposition process.

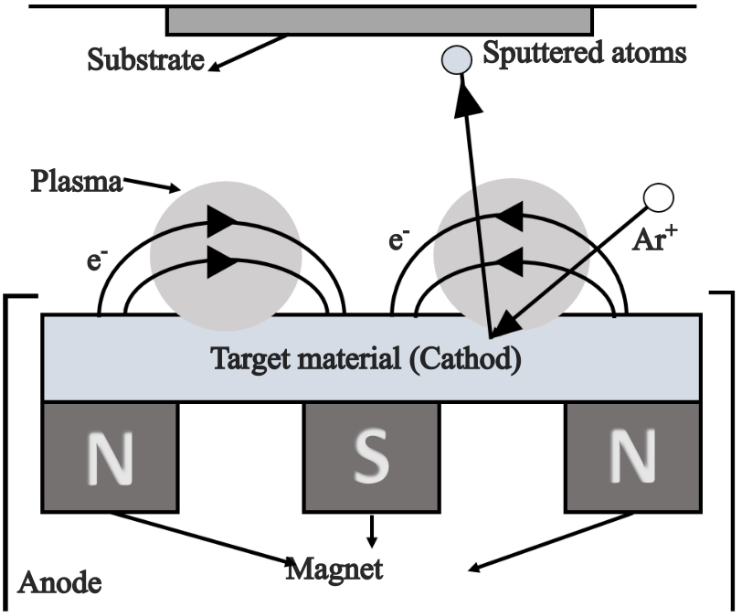

Figure 3.1: Schematic diagram of dc magnetron sputtering. Ar ions ejects required materials from the target, which form thin films on a substrate [11, 88].

3.2.2 Atomic layer deposition (ALD)

The gate oxide (HfO_2) on the magnetic multilayer was fabricated by Fiji F200 ALD tool. The precursor was Tetrakis(Dimethylamido)Hafnium $Hf(NMe_2)_4$. The precursor is composed of one hafnium atom connected to four dimethylamido ligands. Dimethylamido ligands are nitrogen atoms that are bonded to two methyl (CH3) groups [91]. ALD is a sequential, self-limiting surface reactions technique, where, reactant gases are introduced sequentially into the reaction chamber, preventing two gas-phase reactants from meeting within the chamber. Following the introduction of each reactant, an inert gas purges the reaction chamber, removing excess reactant gas and by-products. This process evacuates all molecules except those that have chemisorbed to the magnetic film surface. Consequently, deposition occurs in a self-limiting manner, ensuring the uniform growth of a thin layer with conformal coverage. Precise control over film thickness is achieved by repeating these reaction cycles [92]. During the Atomic Layer Deposition (ALD) process, the chamber is purged with inert nitrogen gas to remove any contaminants. Subsequently, a precursor gas is introduced into the chamber, where it chemisorbs onto the substrate (a metallic film in this case), forming a monolayer of

Hf. Nitrogen gas is then used to purge any excess precursor materials. Water vapor is subsequently introduced to oxidize the deposited Hf, resulting in the formation of HfO_2. Once again, nitrogen is employed to purge any excess water vapor. This sequential process gives a mono-layer of HfO_2, with a growth rate typically around 0.83 nm per ALD cycle. The ALD cycle is repeated until the desired film thickness ($\approx$ 2.5 nm) is achieved.

3.3 Structural characterisation techniques

3.3.1 X-ray reflectivity (XRR)

XRR is a highly effective characterization technique in thin-film technology, enabling precise analysis of thickness and roughness from the XRR data. In this project, XRR is used to estimate the deposition rates of sputter-grown films.

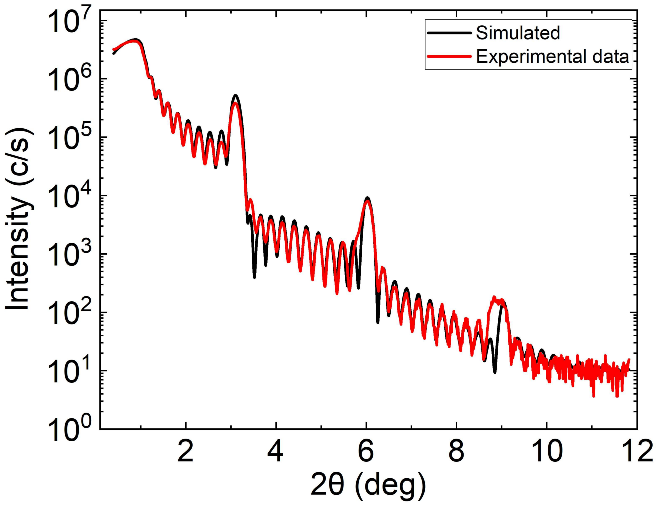

Figure 3.2: XRR data of a [CoB/Pt]x10/Pt calibration sample on a Si/SiO_2 substrate. The experimental data is fitted with GenX software. The thickness of each CoB layer is around 12 ±0.4 Å and the thickness of each Pt layer is around 20 ±0.3 Å.

X-rays are produced in a vacuum using a copper X-ray tube. Electrons are emitted through thermionic emission from a heated cathode. A copper target acts as the anode. When a high voltage (30 KV - 50 KV) is applied between the cathode and the anode, the thermionically emitted electrons accelerate towards the anode. These accelerated electrons have sufficient energy to eject an electron from the inner electron shells (K, L, or M) of the copper atoms in the anode. Specifically, an electron from the K shell can be ejected, creating a vacancy. This vacancy is subsequently filled by an electron transitioning from the L or M shell to the K shell. The electronic transition from the higher L or M shell to the lower-energy K shell results in the emission of characteristic X-ray radiation, known as Kα and Kβ X-rays, respectively. Subsequently, Cu Kα wavelength radiation is directed onto the sample surface at a low angle ($2\theta < 15^\circ$). The X-rays scatter from atoms at specific angles and produce interference from interfaces and the surface.

However, in XRR, there is a critical angle below which X-rays do not penetrate the film significantly, providing information about the top-most layer of the sample. Beyond that angle, X-rays penetrate the film, and interference between reflections from the top and bottom surfaces of the film is observed, causing constructive and destructive interference, which observed as Kiessig fringes (Figure 3.2). Additionally, due to the periodic structure (CoB/Pt multilayer here), constructive interference is enhanced at a specific angle, resulting in a sharp Bragg peak. From these fringes, we can extract the film thickness. In practice, the film needs to be 10-30 nm thick to obtain sufficient Kiessig fringes for accurate thickness determination. We calibrate very thin films with multilayer growth, where Bragg peaks appear (Figure 3.2) along with the Kiessig fringes, caused by Bragg reflection from the multilayer, which are analogous to Bragg reflections from atomic planes in X-ray diffraction (XRD). Figure 3.2 illustrates an example of XRR data fitting of a multilayer calibration sample, which shows Kiessig fringes and Bragg peak.

From the Bragg law (Equation 3.1 and Equation 3.2), we determine both the lattice parameter and various thin-film properties [88].

$$\mathrm{n}\lambda = 2\mathrm{d}(\sin\theta), \tag{3.1}$$

$$\mathrm{d} = \frac{\mathrm{a}}{\sqrt{\mathrm{h}^2 + \mathrm{k}^2 + \mathrm{l}^2}}, \tag{3.2}$$

where, the λ is the wavelength of the X-ray, d is the distance between two parallel atomic plane, θ is the angle of reflection, n is proportional to the order of reflection, a is the lattice constant, and h, k, l are the miller indices. The equation 3.2 can be used for finding lattice parameter form XRD.

3.3.2 Atomic force microscopy (AFM)

AFM is a surface topography measurement technique known for its nanometer-scale lateral resolution. In this work AFM is used to investigate the surface roughness of ultra thin films which is measured by Dr. L. Huang at the university of Leeds.

The AFM technique uses two methods to investigate the sample surface: contact mode and tapping mode. The cantilever tip directly scans the sample surface in contact mode, though this approach can potentially damage both the tip and the sample. Conversely, the tapping mode, also known as intermittent contact mode, involves tapping the sample surface at the resonance frequency of the oscillating cantilever to perform the scan. Figure 3.3 shows the schematic diagram of a sample being scanned using AFM. The sample is placed on a piezoelectric scanner, which moves precisely along two dimensions (x and y axes) with a scan size ranging from 15 nm to 90 μm. As the sample moves, the tip starts to oscillate, and the displacement of the cantilever is captured using laser light, which is used to investigate the sample topology. The image on the right shows an example of an AFM scan, which is further discussed in Chapter 4.

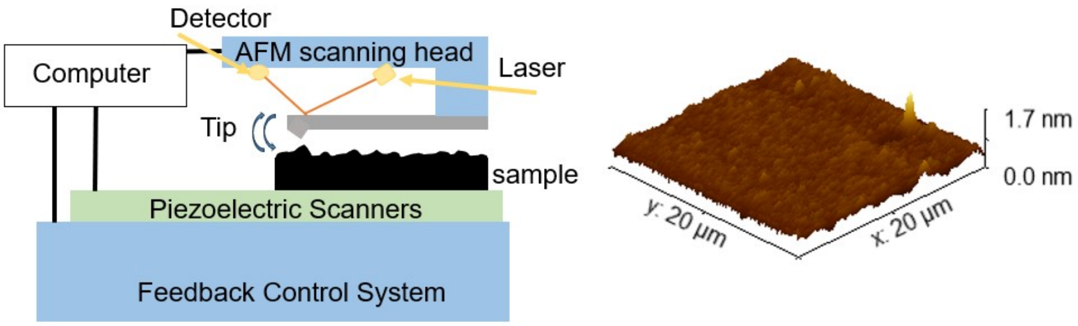

Figure 3.3: A schematic representation of an AFM is shown in the left image [90]. The sample is attached to a piezoelectric scanner, which can move along the x and y directions. The vibration amplitude the tip affected by Van der Walls force provides the sample's morphology. An example of an AFM surface image is shown in the right image.

3.3.3 X-ray photoelectron spectroscopy (XPS)

The XPS spectroscopic technique can be used to analyze the surface chemistry of thin-film, powder, gaseous samples, and ionic liquids [93]. The samples were measured at the Bragg Centre for Material Research at the University of Leeds, with the XPS device operated by Dr. A. Britton.

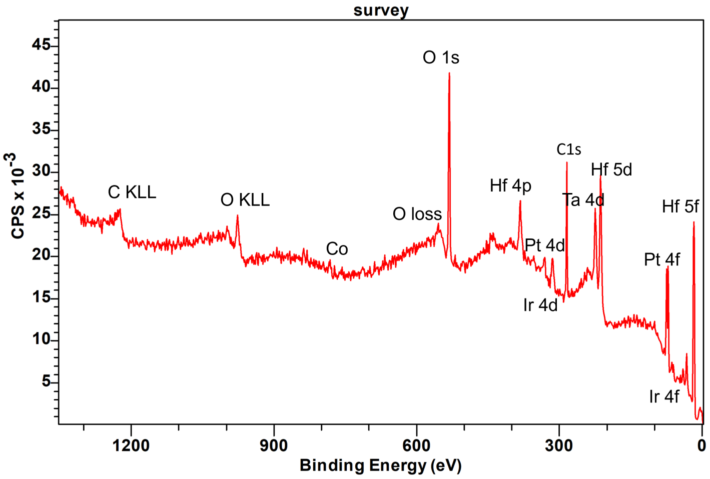

Figure 3.4: Experimental XPS data show the full spectral range. The sample was scanned with a photoelectron energy up to 1500 eV. Peak positions are shown according to their binding energy. C KLL and O KLL represent the emission of an electron (carbon or oxygen, respectively) from the K shell, with the resulting vacancy being filled by another electron from the L shell.

The technique utilizes the so-called photoelectric effect, which occurs when a material is exposed to X-ray photons with energies higher than the binding energy of its electrons. In this process, the material absorbs the photons and releases an electron. By analyzing the kinetic energy of the ejected electron, the binding energy of the electron can be identified, which provides atomic information about the material. Consequently, it is possible to investigate the elemental composition, oxidation states of the elements, and chemical bonds of organic molecules from the binding energy. The effect can be present as follows,

$$\mathrm{E_{KE}} = \mathrm{hf} - \mathrm{E_B} - \mathrm{W_f}, \tag{3.3}$$

where, E_{KE} is the kinetic energy, h is the Plank constant, E_B electron's binding energy, w_f is the work function (the energy ejected electron required to escape the solid), and f is the frequency of the X-ray photon [94, 95].

All the samples presented in this work were measured using a UHV XPS module with Al Kα radiation and a spot size of 500 μm × 500 μm. Twenty scans were performed at three positions on each sample and averaged. Raw data is shown in Figure 3.4 with the full spectrum range. The obtained data were analyzed using a software called Casa XPS. Lorentzian line shapes (line-shape of the Kα X-ray is also Lorentzian) were employed to fit the experimental data, and the Shirley background was subtracted to enhance the quality of the fitting.

3.4 Scanning transmission electron microscopy (STEM)

The structural properties of as grown films and applied voltage films were investigated using STEM cross-section analysis at the Leeds electron microscopy and spectroscopy (LEMAS) centre. The measurement technique requires ultra-thin sample slices, ranging between 50 nm to 100 nm in thickness, which were prepared by J. Harrington. The measurements were performed using the FEI Titan3 Themis 300, operated by Dr. Z. Aslam.

Figure 3.5 shows the STEM sample preparation. The sample was redeposited with Ir(30 nm)/Pt(40 nm) by ion beam deposition technique. Subsequently, a Ga ion beam current was utilized to section the sample, followed by thinning up to 1 µm thick sample using ion milling with a smaller current. The ultra-thin samples were detached using tweezers and affixed to the TEM grid using a Copper mesh. Finally, another step of the samples underwent ion milling is used for thinning down ranging between 35 nm to 100 nm to achieve transparency.

The prepared samples were used in the microscopy for imaging and elemental mapping. The measurement were conducted using e-beam, which was focused onto the sample. The transmitted beam allowed for the investigation of atomic structures. High-quality images were captured using a 46 mm camera lens. The EDX mapping process involved the detection of emitted electrons from the inner core of the sample materials. The emitted energy was captured and transformed into voltage pulses using a multichannel analyzer. This technique provides a resolution of up to 0.8 nm.

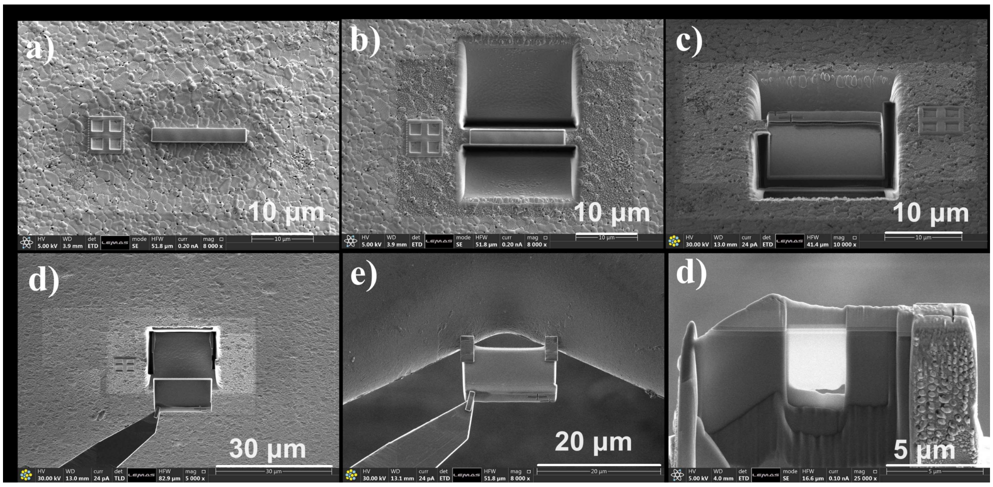

Figure 3.5: STEM require ultra thin (35-100 nm) sample. Preparation steps are: a) Ir/Pt cap deposition on the sample b) bulk removal c) under cut d) in-situ lift-out e) Attached to TEM grid f) the sample is transparent under e-beam.

3.5 Superconducting quantum interference device for vibrating sample Magnetometry (SQUID-VSM)

SQUID-VSM is an extremely sensitive technique to measure the absolute magnetization, which converts magnetic flux into voltage. In this work, the method is used to calculate saturation field (H_{sat}), saturation magnetization (Ms) and magnetic moment (m) at different temperature. In this work we used Quantum Design SQUID-VSM, which can measure samples between 2 K to 1000 K with applied magnetic field up to 6 T.

The technique combine two methods the VSM and a SQUID. The SQUID works as an extremely low noise magnetic flux to voltage amplifier, and due to be coupled to the second order gradiometer coils of the VSM, it converts and amplifies changes in the local magnetic moment to a voltage signal. SQUID-VSM measures the absolute magnetic moment of a sample and provides the hysteresis loop as a function of applied magnetic field. The magnetic properties such as H_c and H_{sat} can be determined from the hysteresis loop. Accordingly, the saturation magnetization can be calculated from moment/volume. Figure 3.6 shows an example of SQUID-VSM data obtained in OoP configuration. Silicon (Si) is a diamagnetic material with a susceptibility of $\chi = -4.1^{-6}$ (χ is unit less [96]).Consequently, the measurement exhibits diamagnetic behavior attributable to the substrate, in addition to the magnetic behavior of the CoB. The data (violet) includes diamagnetic behaviour from the substrate, which is then corrected by subtracting a straight line (blue) [46].

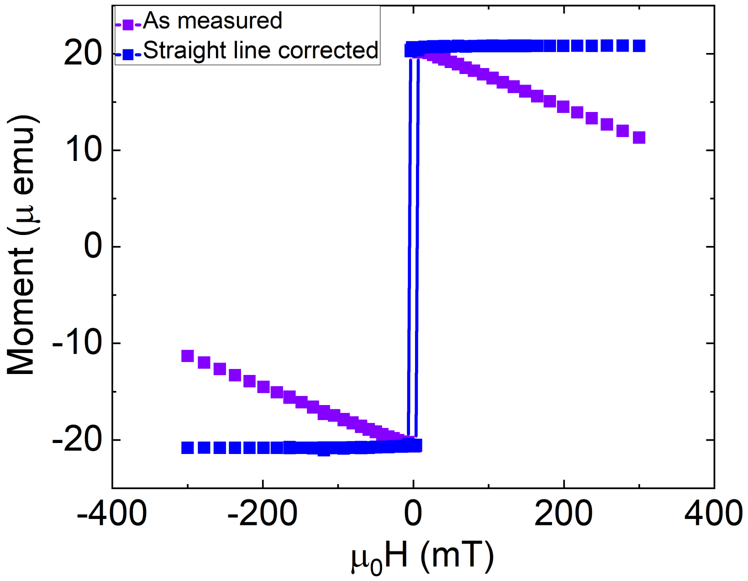

Figure 3.6: Magnetic moment as a function of applied OoP field at room temperature. The image is also showing the diamagnetic background (violet), which is corrected by a straight-line subtraction.

The measurement technique is highly dependent on the sample size and shape, as well as vibration amplitudes, which may result in errors between In-P and OoP measurement. Therefore, fill factors from reference [88], were used to correct the experimental data in Chapters 4 and 5.

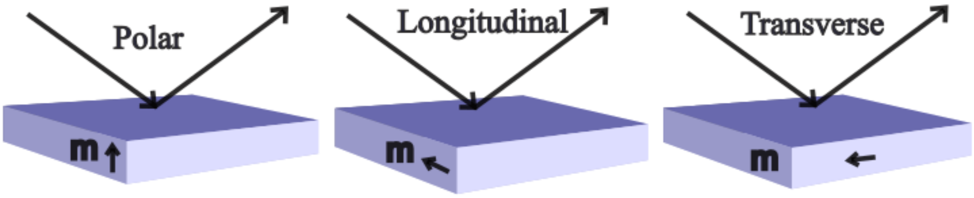

Figure 3.7: The polar, transverse and longitudinal Kerr effect. The magnetization direction is shown by the small arrow. The large arrow is showing the incident and reflected light beam [51].

3.6 Wide-field Kerr microscopy

The domain morphology and domain wall behavior are crucial in the development of domain wall-based storage devices. This study investigates domain formation, domain wall velocity, and the resultant hysteresis loop using a wide-field Kerr microscopy. The experimental technique operates based on the magneto-optic Kerr effect, which involves the rotation of a polarized light beam when interacting with a magnetic surface. This rotation arises due to the absorption coefficient of left and right circularly polarized light caused by the exchange and spin-orbital coupling. The Kerr microscopy produces the domain contrast from the reflected light, allowing simultaneous observation of the magnetization process and the resulting hysteresis loop. The Kerr rotation provides relative change of magnetization in the magnetic films and depending on the magnetization direction of the films, there are three types of Kerr effect geometry namely, polar, transverse and longitudinal Kerr effect. The Polar Kerr effect is observed when a sample exhibits perpendicular magnetization. The transverse and longitudinal Kerr effects are observed when the samples exhibit In-P magnetization. The longitudinal effect occurs when the magnetization is aligned parallel with the plane of incident. On the other hand, the transverse effects shows when the magnetization is perpendicular to the plane incident. The dielectric law can describe the Kerr rotation or Kerr effect [11, 25, 51, 89, 97],

$$\mathrm{D_i} = \vec{\epsilon}\mathrm{E} = \epsilon(\mathrm{E} + \mathrm{i}\mathrm{Q_v}\mathrm{m} \times \mathrm{E}), \tag{3.4}$$

$$\vec{\epsilon} = \begin{bmatrix} \epsilon & \epsilon_{12} & \epsilon_{23} \\ -\epsilon_{12} & \epsilon & \epsilon_{23} \\ -\epsilon_{13} & -\epsilon_{23} & \epsilon \end{bmatrix} \tag{3.5}$$

where, the D and E are the displacement vector and electrical vector respectively. $\vec{\epsilon}$ is the dielectric tensor. $\mathrm{Q_v}$ is the Voigt material constant. The m × E denotes the Lorentzian force. The off-diagonal components $(\epsilon_{1,2} and - \epsilon_{1,2})$ of the matrix are significant under an applied magnetic field. These components cause magneto-optical coupling and the rotation of reflected light. The surface electrons of a sample oscillate with the incident polarized light. Simultaneously, the surface magnetization produces the Lorentz force, which in turn rotates the polarization of reflected light.

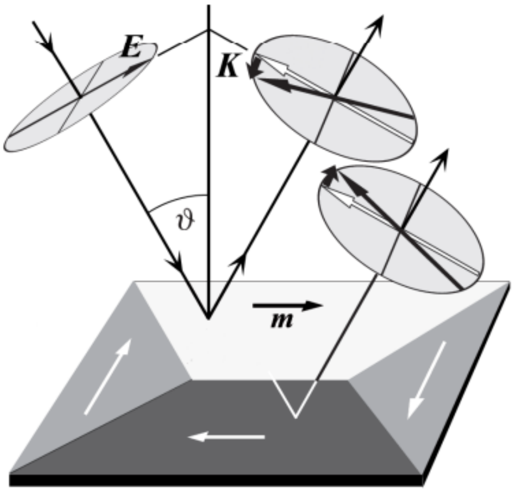

Figure 3.8: The diagram shows the Kerr effect. The polarized light rotates after reflecting from a magnetic in-plane sample. The reflected light obtain a new vector K [51].

The domain morphology was studied using a commercial wide-field Kerr microscopy system from Carl Zeiss AG. The system uses a Kepco power supply to magnetize the samples and a white LED light source for sample illumination. The reflected light is recorded using a CCD camera and a computer. It produces grayscale images as shown in the Figure 3.9(a-b) and the intensity depends directly on the magnetization of the domains within the sample. Additionally, a resultant hysteresis loop is produced due to the change in intensity of the domains. Domain wall energy and stability are affected by DMI. Therefore, the direction of domain wall velocity under an applied field can help estimate the DMI. To calculate the domain wall velocity displacement of bubble type domain is used. The formation of these domains relies on various factors, including the magnetic properties of the films, such as total film thickness, uniaxial anisotropy (Ku), exchange stiffness (A), and saturation magnetization (Ms), where, the $Q = 2\pi M_s^2$ should be lower than the Ku and the film thickness lower than $(A/K_u)^{1/2} \times (K_u/Q)$ [98–100]. Additionally, the thin film geometry, like Pt/FM and Ir/FM interfaces, which contributes to long-range dipole-dipole interaction, interlayer exchange coupling, and SOC, further influencing the appearance and stability of bubble-type domains [101–106].

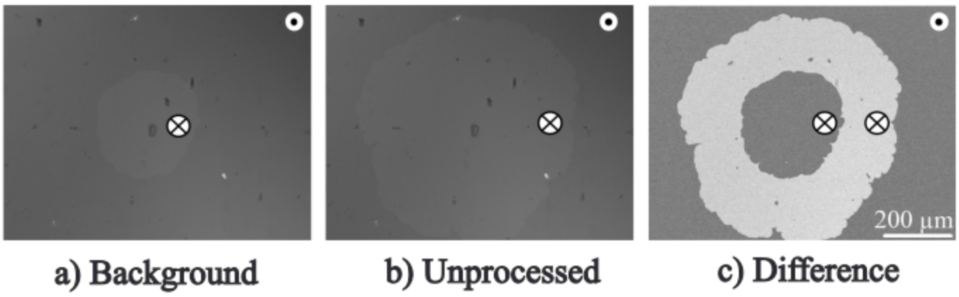

a) Background b) Unprocessed c) Difference

Figure 3.9: a) A small bubble is nucleated with an applied OoP pulse and recorded. Outside of the bubble, the magnetization is pointing upward, indicating the initial position of the domain wall. b) A second OoP pulse is applied to nucleate another bubble and recorded. c) The difference between these two images can be used to calculate the domain wall velocity.

An out of plane (OoP) field pulse is applied to nucleate a bubble type domain and an image is captured as a background (Figure 3.9(a)). Subsequently, A second OoP pulse is applied expand the domain, and captured another image (Figure 3.9(b)). The difference between two images indicates the domain wall displacement. The displacement is calculated using the formula: velocity = displacement / pulse time [11, 25, 47, 51].

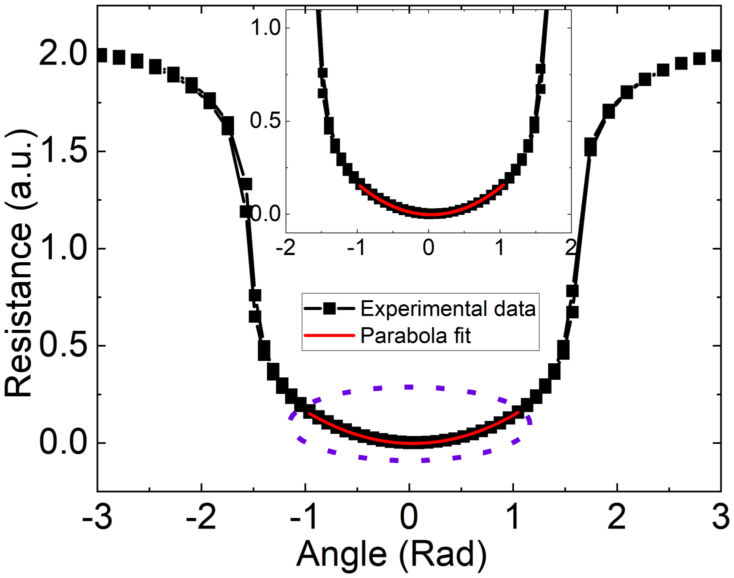

Figure 3.10: An example of MR data, where Hall resistance is recorded as a function of the rotational angle, and the anisotropy field is calculated through parabolic fitting, is presented. The A_2 in Equation 3.7 is calculated from the parabolic part, as indicated in the figure.

3.7 Magneto-resistance (MR) measurement

Anomalous Hall effect (AHE)

In 1879, Edward Hall made the groundbreaking observation of the Hall effect in normal metals [107]. This effect states that when a magnetic field is present, a current passing through a conductor generates a voltage that is perpendicular to the direction of the current flow. There are three types of hall effects (i) ordinary Hall effect: is observed in the non-magnetic or ordinary metals. (ii) anomalous Hall effect: is observed in magnetic metals and the effect is more pronounce than the non magnetic metals [108]. (iii) topological Hall effects: is observed with topological magnetic spin textures, such as antiskyrmions and skyrmions. In this work only AHE is used to obtain the M-H curve and anisotropy field.

During the Hall measurement a current is applied through the sample. The voltage drop is measured at a right angle to the direction of the current. The applied magnetic field is also perpendicular to the film, which aligns with both the conventional current direction and the measured voltage. The OoP magnetic field introduces the Lorentz force causes charge carriers to change there path. Charge carriers accumulate at the sides of the wire (or sample) as a result of electron scattering with fluctuating spins, a phenomenon influenced by both the magnetic properties inherent to the sample and the magnetic field applied externally. The measured Hall voltage can be converted to resistance [109],

$$\mathrm{R_H} = (\mathrm{R_oH_z} + \mathrm{R_AM_z}), \tag{3.6}$$

where, $\mathrm{R_o}$ is the ordinary Hall coefficient, $\mathrm{H_z}$ is the OoP magnetic field, $\mathrm{R_A}$ is the anomalous Hall coefficient, and $\mathrm{M_z}$ is the OoP magnetization. The total Hall resistance is the sum of ordinary Hall effect ($\mathrm{R_oH_z}$) and anomalous Hall effect ($\mathrm{R_AM_z}$). The anomalous Hall effect originates from the Berry's phase curvature, and SOC originated Side jump and Skew scattering mechanisms. To observe the AHE effect, a current is applied to the sample, and the voltage is measured while a constant magnetic field, typically greater than half a Tesla (arbitrary 518 mT), is applied perpendicular to the current direction. The sample is rotated through a range from $-180°$ to $+180°$, with the rotational angle being perpendicular to the measured voltage. The Hall voltage is converted to Hall resistance and recorded as a function of the rotational angle. The recorded data (shown in Figure 3.10) is then subjected to a parabolic fitting process to calculate $\mathrm{k_{eff}}$.

$$\mathrm{A_2} = \frac{\mathrm{H_z^2}}{2(\mathrm{H_z} + \mu_0\mathrm{H_k})^2}, \tag{3.7}$$

$$\mu_0\mathrm{H_K} = \frac{2\mathrm{K_{eff}}}{\mathrm{M_s}} = \mathrm{H} \times \frac{1 - \sqrt{\mathrm{A_2}}}{\sqrt{2\mathrm{A_2}}}, \tag{3.8}$$

where $\mathrm{K_{eff}}$= effective magnetic anisotropy constant, $\mathrm{M_s}$= saturation magnetization, $\mu_0\mathrm{H_k}$ = anisotropy field, $\mathrm{A_2}$ = quadratic term of the parabola [89].

In this thesis, the resistance measurements were carried out with a Keithley 2400 source meter and a 182 nano-voltmeter using a typical current of ±1 mA at room temperature. During these measurements, there was no evidence of Joule heating.

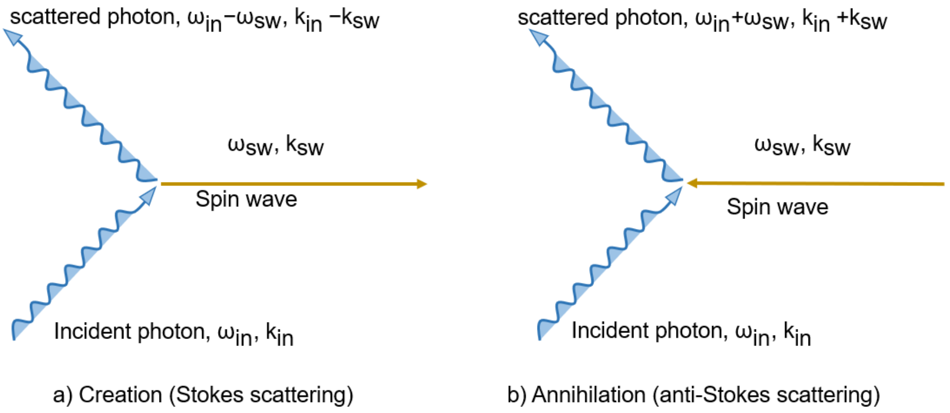

Figure 3.11: A schematic diagram of scattering by photon spin wave interaction. Due to conservation of momentum magnon can be (a) created by the stokes process or (b) annihilated by anti-Stocks process, the figure is adapted from ref [40].

3.8 Brillouin light scattering (BLS) spectroscopy

The BLS spectroscopic technique is used to estimate the DMI in magnetic thin films. The measurement were performed under supervision of Prof. M. Belmeguenai at the Process and Material Sciences Laboratory (LSPM), France.

In this work the BLS is employed to estimate the DMI from the scattering of phonon from the spin waves, which is shown on figure 3.11 [25, 40, 51, 110]. In a magnetic material, collective excitations of spins are known as spin waves, and magnons are considered the quantized particles of these spin waves. A laser beam of 532 nm wavelength and a 50 µm beam width, is used to irradiate the sample. As a result of conservation of moment a magnon can be created by the Stocks process and a magnon can be annihilated from the anti-Stocks process.

The BLS measurements were conducted according to the Damon-Eshbach geometry as shown in Figure 3.12a). In this geometry, the sample's magnetization is saturated along the sample plane, and the spin waves propagate non-reciprocally perpendicular to the direction of magnetization. Fabry-Pérot interferometers (FPI) measures the wavelength and intensity of light, making it suitable for detecting scattered beams owing to its high spectral resolution, tunable frequency range, and sensitive detection capability. Figure 3.12b) shows the geometry of the back scattered light beam. The wave vector is calculated from $K_{sw} = 4\pi \sin\theta/\lambda$, where θ represent the angle of incident.

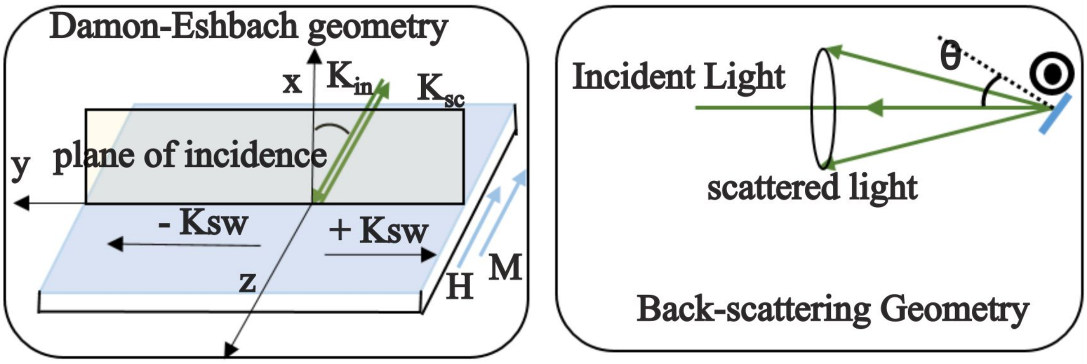

Figure 3.12: The Damon-Eshbach geometry and the back scattering geometry, where θ is the wave vector, $-\mathrm{K_{SW}}$ is the anti-Stocks spin wave and $+\mathrm{K_{SW}}$ is the Stocks spin wave [25, 40].

During this measurement the angle is changed from 0 °C to 60 °C. However, only 60 °C is used for the DMI measurement. Due to DMI, spin waves with different wave-vectors exhibit non-reciprocity, which can be observed as a difference between Stokes and anti-Stokes frequencies. The frequency difference can be express as [111, 112],

$$\Delta \mathrm{F} = \mathrm{F_S} - \mathrm{F_{AS}} = \frac{2\gamma}{\pi \mathrm{M_s}} \mathrm{D_{eff}} \mathrm{K_{sw}} = \frac{2\gamma}{\pi} \mathrm{K_{sw}} \frac{\mathrm{D_s}}{\mathrm{t_{FM}} \mathrm{M_s}}, \tag{3.9}$$

where, $\mathrm{K_{sw}} = 4\pi \sin\theta/\lambda$ represents the spin wave vector, γ stands for the gyromagnetic ratio (ratio between magnetic moment and angular momentum, unit rad/second/Tesla), $\mathrm{D_{eff}}$ stands for the effective DMI, and $\mathrm{t_{FM}}$ represents the thickness of the magnetic layer.

The $\mathrm{M_{eff}}$ is calculated using the following equation [111, 112],

$$\mathrm{F_{avg}} = \frac{\gamma}{2\pi} \sqrt{(\mathrm{H} + \frac{2\mathrm{A}}{\mathrm{M_s}} \mathrm{K_{sw}^2} + \mathrm{P}(\mathrm{K_{sw}} \mathrm{t_{FM}}) 4\pi \mathrm{M_s})(\mathrm{H} + \frac{2\mathrm{A}}{\mathrm{M_s}} \mathrm{K_{sw}^2} - \mathrm{P}(\mathrm{K_{sw}} \mathrm{t_{FM}}) 4\pi \mathrm{M_s}) + 4\pi \mathrm{M_{eff}}}, \tag{3.10}$$

$$P(K_{sw} t_{FM}) = 1 - \frac{1 - e^{-(K_{sw}) t_{FM}}}{K_{sw} t_{FM}} \tag{3.11}$$

where, $\mathrm{F_{avg}}$ represents the average between Stokes and anti-Stokes frequencies. A is the exchange constant, Ms is the saturation magnetization, $\mathrm{M_{eff}}$ is the effective magnetization, $\mathrm{t_F M}$ is the thickness of ferromagnetic layer, .

3.9 XAS and XMCD

The XAS and XMCD measurements were conducted by Dr. H.B.Vasili at the BL29-BOREAS beam line in ALBA synchrotron, Spain.

The XAS is a chemical state analysis-based measurement technique used to investigate solids, liquids, and gases. The technique utilizes absorption spectra to characterize a material, where the absorption edge changes significantly at specific binding energies. The absorption edge represents the energy required to move a core electron to a higher (unoccupied) excited state, which is studied within about 30 eV of the absorption edge and is known as X-ray Absorption Near Edge Structure (XANES). Beyond this region, up to several hundred eV from the absorption edge, the ejected photoelectron leads to oscillations in the absorption spectrum, which are analyzed in Extended X-ray Absorption Fine Structure (EXAFS) spectroscopy. The spectra can then provide information about the unoccupied state. In this experiment, the technique is used to investigate the oxidation state of the $\mathrm{Co{-}L_{2,3}}$. Therefore, the data at the X-ray absorption near edge structure is the most important, providing information about metallic Co and CoO.

The samples were measured in terms of total yield electrons (3.13a)). They were connected to an ammeter and illuminated with a circularly polarized light beam, which ejects electrons from core levels such as the 2p level (3.13b)). The ejected electrons create a charge imbalance within the sample. The ammeter helps to neutralize the sample by measuring the resulting current. The total yield of electrons then provides the absorption spectra. Figure 3.13c) shows an example of XAS data, which displays the $\mathrm{Co{-}L_{2,3}}$ absorption edge. The $\mathrm{Co{-}L_{2,3}}$ represent the transition of electron from core level 2p orbital to valence label 3d orbital, where $2\,\mathrm{p}_{3/2}$ correspond to L_2 and $2\,\mathrm{p}_{1/2}$ correspond to L_3 [113]. All the XAS data presented in Chapter 6.

XMCD measurement is also based on the XAS technique, where right-handed and left-handed circularly polarized light is used to conduct the measurement. The angular momentum of circularly polarized light is either parallel (for positive circular polarization) or anti-parallel (for negative circular polarization) to the direction of the light. The incident light transfers angular momentum to excite electrons. The absorption of left and right circularly polarized light will be different (3.13c). The average and difference of these absorption spectra are used to calculate the magnetic moment per atom. The XMCD study is presented in Chapter 6.

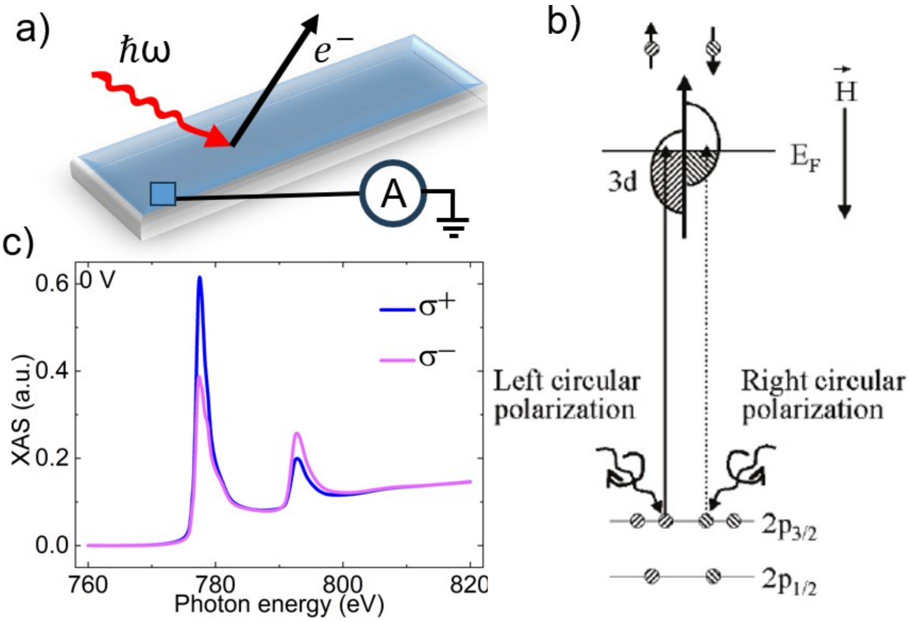

Figure 3.13: a) The sample is irradiated with a light beam, and the connected ammeter helps determine the total yield of electrons. b) The XMCD two-step diagram shows electrons in the core shells 2p3/2 and 2p1/2. Left (σ^-) and right (σ^+) circularly polarized light are used to eject electrons from the core shell, with the lines (perpendicular) indicating the expected transitions [114]. c) An example of XMCD data shows the Co$-$L$_{2,3}$ absorption edge for left (blue) and right (magenta) circularly polarized light. The differences and averages are used to calculate the moment per atom in Chapter 6.

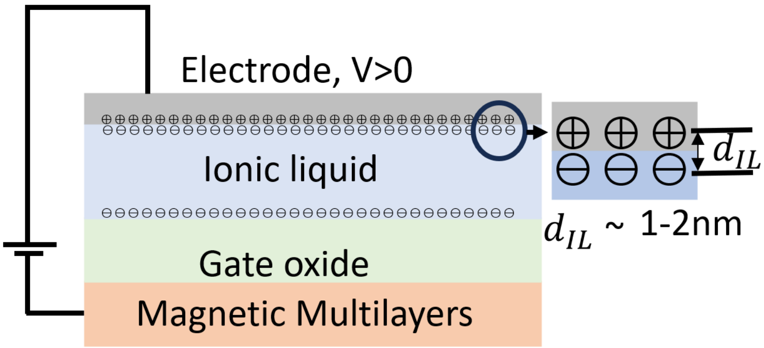

Figure 3.14: Geometry of ionic liquid gating with positive applied voltage. The applied voltage arrange ions in ionic liquid and form electric double layer. The distance between cations and anions is 1-2 nm [40].

3.10 Ionic liquid and ionic liquid gating

Ionic liquids are molten salts composed of anions and cations without any water at room temperature. They find applications in spintronics, medical science, and chemistry owing to their high capacitance, non-volatility, large temperature window, and low toxicity. Ionic liquids have an operational voltage upto 6.1 V, which depends on their electrochemical stability window[115–118].

The magneto-ionic technique enables the control of magnetic properties at room temperature by facilitating the migration of ions to or from the ferromagnetic layers, thereby altering their magnetic properties. With an applied voltage, ions from source materials such as HfO_2 and SiO_2 [119] migrate, and electrochemical reactions between the ions and ferromagnetic materials lead to changes the magnetic properties in the magnetic system.

Figure 3.14 depicts a schematic of the ionic liquid gating technique. The liquid is applied between the gate oxide and the top electrode. An applied voltage accumulates ions on the two electrodes, generating a large electric field. The accumulated ions act as a nano-capacitor, with the capacitance given by $\mathrm{C} = \epsilon \mathrm{A_{IL}}/\mathrm{d_{IL}}$, where $\mathrm{A_{IL}}$ represents the film surface covered by the ionic liquid or the gated area, ϵ is the dielectric permittivity, and $\mathrm{d_{IL}}$ is the distance between the electric double layer (EDL). The EDL depends on the ion size and typically ranges from 1 to 2 nm, which act as a nano capacitor [120–122]. As a result, a small voltage can produce a large capacitance of up to 170 μF/cm^2

at 0.1 Hz. A voltage of 1 V can lead to a carrier density of $5.3 \times 10^{14}/\mathrm{cm}^2$, which is 50 times higher than what a SiO_2 device can achieve [123]. Consequently, an electric field in the range of 10 MV/cm is generated at the interface of the ionic liquid and the gate oxide. Achieving the same effect in a SiO_X gate would destroy the gate.

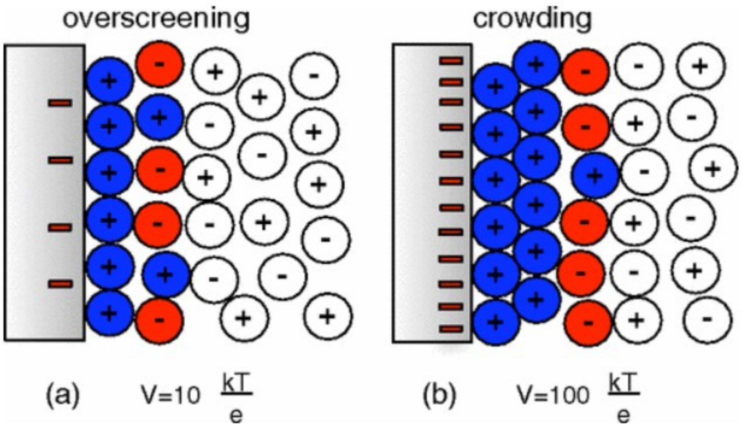

Figure 3.15: Structure of the electric double layer (colored) produced by an applied voltage. The double layer is predicted using a Landau-Ginzburg-type continuum theory, with parameters specific to the room-temperature ionic liquid $[\mathrm{bmpy}]^+[\mathrm{FAP}]^-$. (a) At low voltage, overscreening occurs. (b) At high voltage, an extended layer of countercharges leads to crowding [124].

Figure 3.15 illustrates the structure of the voltage-induced ionic liquid EDL. At low voltage, the liquid delivers more charges than the surface (i.e., gate oxide), resulting in a small amount of opposite charge at the second layer. This phenomenon is known as the overscreening state, which persists until it achieves an electroneutrality state. However, with a large voltage, the second layer of counterions appears and suppresses the overscreening state, a phenomenon known as crowding [124].

The anions and cations in the liquid are connected by relatively weak electrostatic interactions,and their size is approximately 2 nm. Theoretically there are more than a thousand types of ionic liquid is possible by chaining the functionality of ions [125, 126]. In this work a commercial ionic liquid 1-Ethyl-3-methylimidazolium bis(trifluoromethylsulfonyl)imide or $[\mathrm{EMI}]^+[\mathrm{TFSI}]^-$ is used for manipulating magnetic properties. Figure 3.16 shows the chemical structure of $[\mathrm{EMI}]^+[\mathrm{TFSI}]^-$ and Table 3.1 shows the properties of the $[\mathrm{EMI}]^+[\mathrm{TFSI}]^-$.

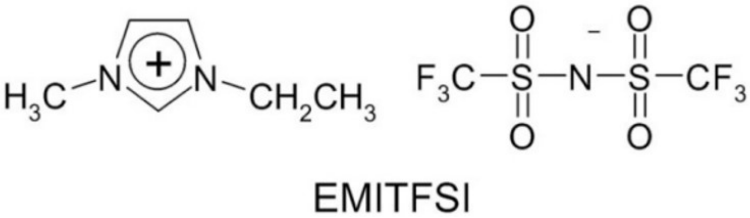

Figure 3.16: Chemical structure of the $[EMI]^+[TFSI]^-$ ionic liquid [123]

Properties	Values	Properties	Values
Anions size	0.23 nm^3	Cations size	0.16 nm^3
Density	1.53 g/cm^3	Electrochemical window	> 4 V
Freezing point	-16°C	Thermally stable	up to 400°C
Capacitance	11.4 $\mu F/cm^2$ at 0.1 Hz	EDL thickness	≈1 nm

Table 3.1: Properties of $[EMI]^+[TFSI]^-$ ionic liquid [40, 117, 118, 123, 127, 128]

3.11 Device fabrication process

Figure 3.17 illustrates the device fabrication process. The thin film multilayers are grown on thermally oxidised Si substrate with 300 nm SiO_2 by DC magnetron sputtering, and the gate electrode is deposited through ex-situ atomic layer deposition. Subsequently, the photoresist LOR7B is applied using spin coating and baked at 165°C for three minutes. Another layer of photoresist, S1813, is then applied and baked at 110°C for two minutes. We used a mask-less aligner (MLA) to expose the sample to UV light. It utilizes a virtual design (desired pattern) and a 375 nm laser to transfer the pattern onto the photoresist. Following exposure, the sample undergoes development in a Microposit 351:H_2O (3:1) solution for 50 seconds, which dissolves the exposed areas of the photoresist. The LOR7B is more soluble compared to S1813, creating an undercut. These undercuts are helpful to remove extra materials during the lift-off process. The photoresist pattern serves as a mask on the sample, facilitating the deposition of a 120 nm SiOx layer via DC magnetron sputtering. Finally, the lift-off of the photoresist completes the process, resulting in the desired microchannel formation on the magnetic multilayer.

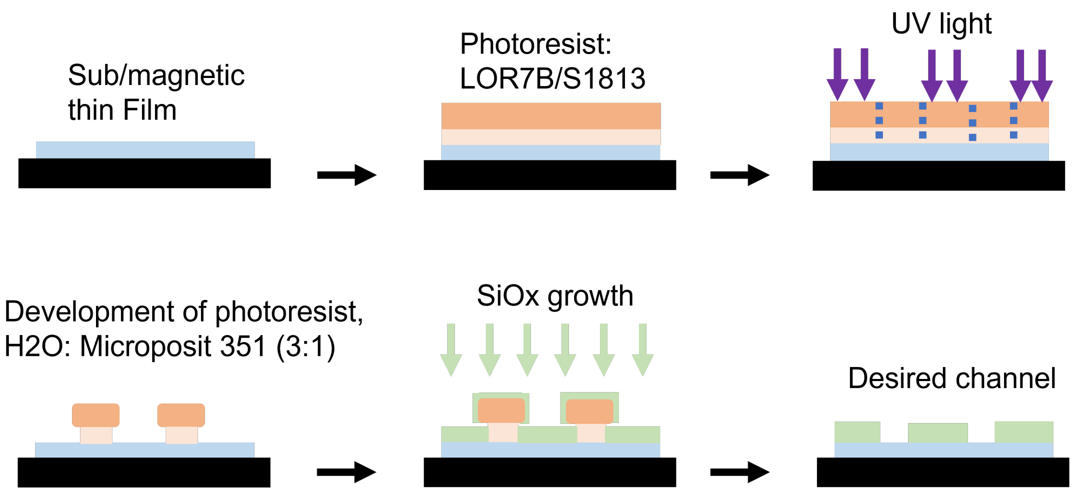

Figure 3.17: The fabrication process for the microchannel on the magnetic thin film involves several steps: Application of a bi-layer photoresist comprising LOR7B and S1813 using spin-coating. Exposure of the sample to UV light to transfer the desired pattern onto the photoresist. Development of the photoresist using Microposit 351 solution. Growth of SiO_x layer using DC magnetron sputtering. Removal of the photoresist to achieve the desired microchannel configuration.

CHAPTER 4

Growth and Optimization

4.1 Introduction

In recent years, magnetic multilayers with structural inversion asymmetry have been discussed in literature. These multilayers employ heavy metal layers to break the symmetry, driven by factors such as strong perpendicular magnetic anisotropy (PMA), strong spin-orbit coupling (SOC), and a significant Dzyaloshinskii-Moriya Interaction (DMI) [25, 71, 129, 130]. In this project, we have grown ultrathin multilayers comprising Ta/Pt/CoB/Ir/Pt for electric field (E-field) applications. These multilayers include a magnetic layer sandwiched between heavy metals Pt and Ir, maintaining the inversion asymmetry. Additionally, we conducted measurements of magnetic properties crucial for devices based on skyrmions or domain walls.

This chapter details the growth and optimization of ultrathin samples. Section two goes into the description of different thin-film tuning properties. Following this, section three explores the structural properties of the samples, followed by the magnetic properties such as effective anisotropy, and estimating the exchange stiffness in section four. Section five focuses on calculating the interfacial magnetic property DMI. The chapter concludes with a summary.

4.2 Thin film optimization

Fundamental material properties including PMA can be modified by material composition, interface engineering and deposition parameters. In magnetic multilayers, PMA arises from the electronic interaction at the interface between the heavy-metal (HM) layer and the ferromagnetic (FM) layer. Materials exhibiting PMA have a high energy barrier between magnetization states, which prevents thermal fluctuations from causing spontaneous flipping of the magnetization direction. This provides excellent magnetic stability essential for data encoding at room temperature, effectively overcoming the superparamagnetic limit. Additionally, the excellent room temperature stability of PMA magnetization is crucial for long-term data storage. These materials are expected to be easily manipulated using the spin transfer torque (STT), presenting potential advantages for STT-MRAM [131]. Spintronics devices based on domain walls; high anisotropy results in narrow domain walls, and increased data storage density. Low shape anisotropy facilitates having a single domain state, where all magnetic moments are aligned in the same direction. This alignment is advantageous for isolating skyrmions in skyrmion-based devices, as it stabilizes their formation and manipulation within the material [9, 10].

Figure 4.1 (blue) demonstrates full remanence at zero magnetic field due to strong PMA. However, the green loop, while potentially still indicative of PMA, does not exhibit full remanence at zero magnetic field.

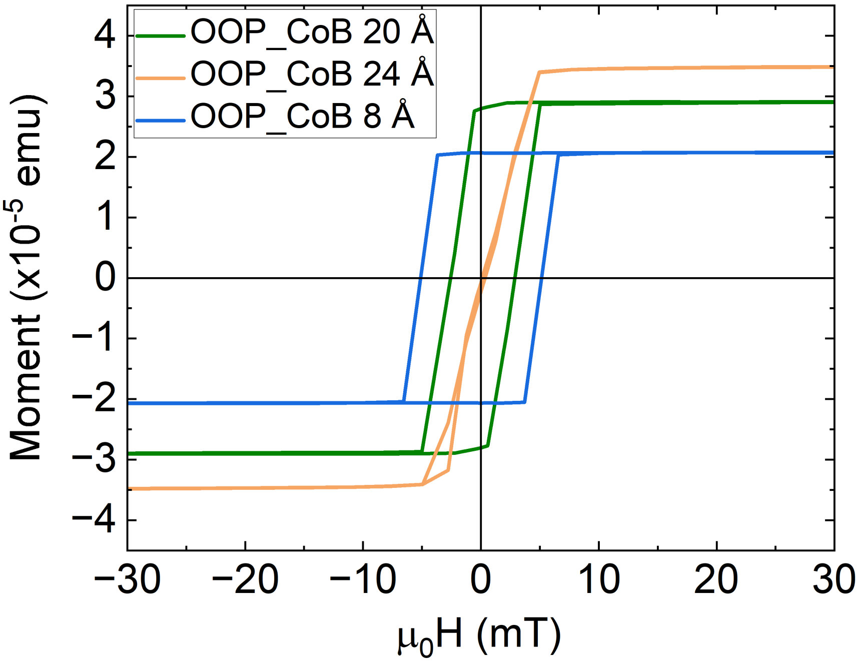

Figure 4.1: Example of PMA of Pt/CoB(X)/Ir sample, where CoB 8 Åexhibits PMA. The CoB 20 Åmight be still PMA but the remanence is not full at zero field, and CoB 24 Åmight be in-plane sample.

The PMA of a magnetic system can be modify by interface engineering. In a magnetic multilayer, the surface anisotropy arises from the HM/FM interfaces, while the FM layer contributes to the magnetocrystalline anisotropy, and the overall thickness introduces shape anisotropy. Therefore, strong PMA can be achieved by adjusting the FM thickness and HM/FM interfaces. The PMA in a Co/HM arises from the the SOC of Co and Pt [132–134]. Figure 4.2 shows the hysteresis loop obtained using Kerr microscopy with polar configuration. The blue loop shows PMA, while the green curve does not show any hysteresis loop, which due to the thickness of bottom Pt layer thickness. Hence, the PMA can be controlled by tuning individual layer thickness.

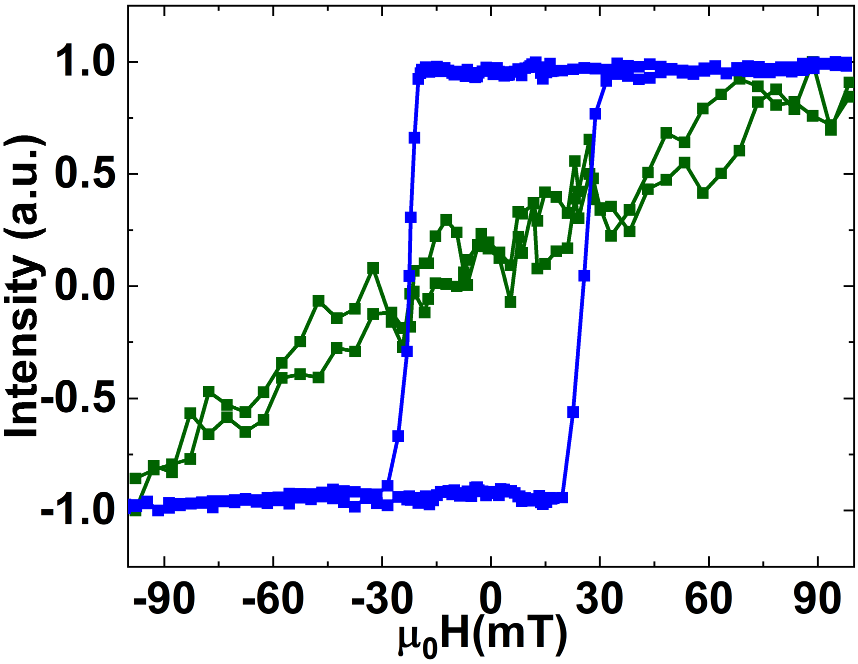

Figure 4.2: M-H loop taken using Kerr microscope. The Green is Ta(5 Å)/Pt(7 Å)/CoB(8.5 Å)/Ir(5 Å)/Pt(14 Å) and the blue is representing Ta(5 Å)/Pt(14 Å)/CoB(8.5 Å)/Ir(5 Å)/Pt(14 Å). The M-H loop shows that the PMA can be tuned by changing the Pt layer thickness.

Another approach for controlling magnetic properties by E-field dates back in 1960 [26, 135, 136]. Initially, the concept encountered uncertainty due to the material structure, the conduction electrons in metals typically screen the E-field with a short screening length, making it almost impossible to modify bulk ferromagnetic properties without disrupting the dielectric. However, Ohno et al. (2000) [27] first demonstrated the effect of the E-field on magnetic properties at low temperature.

In recent years, a large number of theoretical and experimental works have demonstrated the electric field effect on magnetism in order to build devices for applications. They have mostly investigated magnetic materials adjacent to an oxide layer. Table 4.1 shows that inversion symmetry is broken using heavy metals.

Since the E-field can not penetrate the bulk metal, the HM and FM layers must be ultra-thin (a few nm). For this experiment ultra-thin multilayers of Ta/Pt/CoB/Ir/Pt were grown by DC magnetron sputtering, with the total thickness of the films being 4 nm to 6 nm (Table 4.1). As a result of the exchange interaction in the FM layer, the screening charge is spin-dependent, which is a Coulomb interaction due to the total charge and a ferromagnetic interaction due to the up-spin and down-spin of electrons. The spin dependency produces a magnetoelectrical effect at the FM layer surface, which can change the orbital moment anisotropy of ferromagnetic atoms at the surface [137]. Here the Pt layer will be fully or partially oxidized as soon as it exposes to the environment, and the FM layer will polarize the Ir layer. Thus, the E-field-induced surface magnetoelectric effect might play a role in the Ir layer and CoB/Ir interface. As a result, the 3d and 5d orbital hybridization might change the interfacial anisotropy [138–140]. The thickness of individual layers were tailored from a comparatively thick OOP sample, for example Ta(30 Å)/[Pt(30 Å)/CoB(10 Å)/Ir(5 Å)/Pt(15 Å)]X5/Pt(15 Å). For initial studies we grew samples where we wedged Ta and bottom Pt layers as shown schematically in figure 4.3, and samples were selected depending on the total thickness, magnetization orientation (OOP) and domain morphology.

Magnetic multilayers with strong PMA often exhibit maze and bubble-type domains under an OOP magnetic field [99]. The magnetostatic energy originating form long range dipolar energy causes maze-type domain pattern, where the uniform magnetic state break into up and down domain pattern [141, 142]. On the other hand, the presence of the DMI, arising from asymmetric HM/FM interfaces, has the potential to induce Néel -type domain walls configuration in bubble domains.

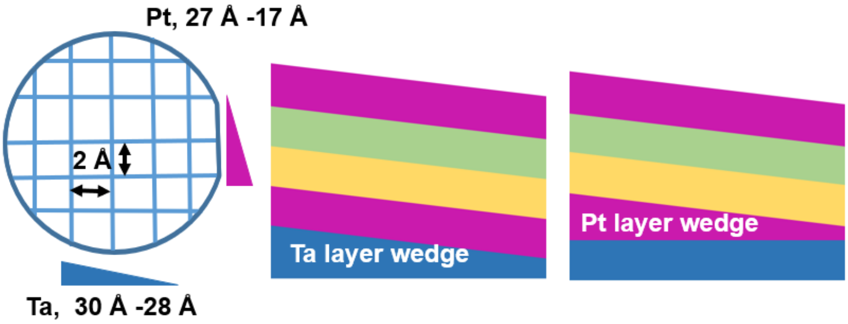

Figure 4.3: The thickness wedge of Ta and bottom Pt layers is shown here. A mask was used to cover the sample during the wedges' growth.

Initially, our plan was to investigate the DMI through asymmetric bubble expansion in the creep regime; therefore, the domain wall morphology is a crucial characteristic for further investigation. The technique is well established in our research group and it requires cheaper equipment and minimal sample preparation. A wide-field Kerr microscope configured in a polar setup was used to examine the magnetic domains. The in-plane magnetic field was produced with an in-plane electromagnet, and an in-house built OOP electromagnet produced the OOP magnetic field [11, 25, 51, 87, 88].

Figure 4.4 shows the domain morphology of the magnetic multilayer structures. The domain nucleates at the surface near abnormality or defect. Only an OOP magnetic field was applied to nucleate and propagate these domains. Figures 4.4a-c) depict the domain morphology for repeats samples, showing the changes in the domain structures corresponding to decreasing repeats. Figure 4.4(a) exhibits a maze type domain caused by the high perpendicular anisotropy. The total film thickness produces high shape anisotropy compared to the surface anisotropy, resulting in the formation of small domain walls within the maze-like domain configuration [89, 99, 141, 142]. Figures 4.4(b-c) also depict the maze type domain wall, however, the domain size is larger compared to the previous picture. As the sample thickness decreases, the domain size increases, manifesting as a combination of separate branches consisting of both reversed and unreversed domains. Domain wall roughness may depend on the difference between domain wall energy and magnetostatic energy, where thick films are dominated by magnetostatic energy and give rough domain walls.

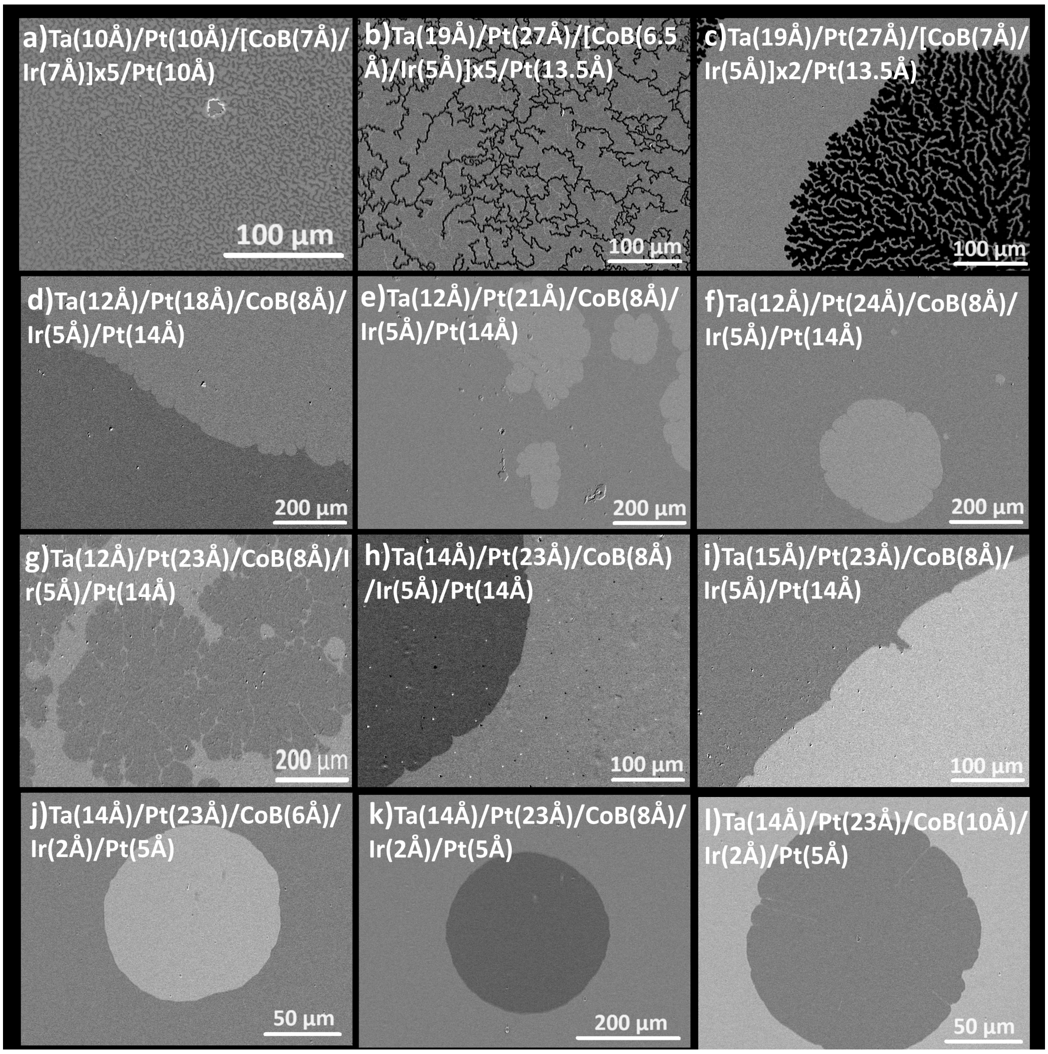

Figure 4.4: Domain morphology of Pt/CoB/Ir films. (a-c) Repeated samples are showing maze-type and tree-branch-type domain patterns, which might be due to a high demagnetizing field and shape anisotropy. (d-f) domain morphology with Ta layer thickness the isolated thin domain disappears from the bubble. However, the edge of the domain is still rough. (g-h) The domain morphology also depends on the CoB thickness. The 10 Å CoB shows isolated thin wall inside the bubble. In Section 4.5, we estimated the DMI from domain wall motion, which cannot be applied to maze-type domains.

A narrow domain pattern is observed in Figure 4.4(c), which nucleates and propagates as a bubble type domain. However, during its propagation, the domain wall experiences pinning at defect sites. Subsequently, it bend around these pinning sites, adopting a tree-branch like configuration as it requires lower energy compared to crossing the pinning sites. The pinning site process a high energy barrier that can be overcome by applying a large external field. These domains, stabilized by the DMI, exhibit stability and continue to grow, expanding and creating branches over time. Samples with multiple repetition cycles process a lot of nucleation site, resulting in smaller and narrower domain patterns.

Figures 4.4(d-f) show the relationship between domain patterns and the Ta layer and Figure 4.4(g-i) show the dependence of bottom Pt layer. For thinner layer thicknesses, the domain walls exhibit isolated bubble-type domains. However, in Figures 4.4(e,g), isolated ultra narrow unreversed domain pattern are observed within the bubble-type domains. These types of walls possess high energy barriers, making them difficult to annihilate. Another potential factor contributing to the thin domain wall could be the interfacial roughness within the FM/HM layer, as depicted in Figure 4.4(l). Conversely, Figures 4.4(j-l) exhibit circular bubble domains without roughness at the edges, whereas Figures 4.4(h-i) display roughness at the edge [51, 89, 143].

4.3 Structural properties

4.3.1 X-ray reflectivity (XRR) analysis

XRR technique is used to characterize the structural properties of the thin films, which is described in Chapter 3. The technique helps to determine total film thickness and individual layer thickness, material growth rate and density, and surface and interface roughness. All the samples were grown on highly doped n-type Si/SiO$_2$(300 nm). The samples consist of ultra-thin layers of Ta/Pt/CoB/Ir/Pt, which is chosen to host chiral domain walls and complex topological structures. Therefore, each layer planted to affect the structural and magnetic properties. The seed Ta (BCC 110) layer acts as a base for the whole structure and provides an approximately hexagonal atomic arrangement (It grows diagonally). It promotes Pt (111) growth, thereby facilitating the interaction of the 5d orbitals of Pt and the 3d orbitals of CoB, which are responsible for the magnetic properties. The Ir layer introduces broken symmetry, and the top Pt layer acts as the capping layer.

Broken inversion symmetry enhances the magnetic properties such as PMA and DMI. The asymmetry arises from factors such as the interfaces, interface roughness, inter-diffusion, growth conditions, and oxidation, each capable of individually altering interface quality and resulting in structural inversion asymmetry [24, 25, 144–148]. However, all the films under study in this project are produced by sputtering at room temperature. Therefore, comparing or reproducing results and comprehending the underlying physics at the interfaces, as well as DMI, becomes challenging. To address this challenge, controlling structural inversion asymmetry can be achieved by introducing HM layers on both sides of the FM layer. Therefore, the heavy metal Ir is used to preserves the inversion asymmetry and enhance the magnetic properties such as PMA and DMI.

The intended thickness for the individual layers are down to 2 Å, however, these thickness is difficult to identify from the low angle x-ray scans. Table 4.1 summarize some fitted data. The estimated roughness form the fitted data fitted data show high roughness for individual layers such as CoB roughness was up to 3.5±0.5 Å, Ta, Pt and Ir roughness was up to 5.0±0.5 Å, 5.0±0.5 Å, and 4.0±0.5 Å respectively. Therefore, only target thickness is listed for rest of the work in this thesis which is estimated from calibration samples (Section 3).

Properties	Ta	Pt	CoB	Ir	Pt	Sample ID
Thickness (Å)	17.0±0.3	30.0±0.6	9.0±0.7	7.0±0.3	17.0±0.3	S1
	8.0±0.5	12.5±0.6	5.0±0.3	6.0±0.4	16.5±0.6	S2
	8.5±0.6	12.0±0.6	5.5±0.6	6.0±0.5	17.0±0.9	S3
	7.5±0.5	12.0±0.5	5.5±0.4	6.0±0.5	17.5±0.6	S4
	12.0±0.6	19.0±0.4	7.0±0.6	3.5±0.4	6.0±0.2	S5

Table 4.1: The individual layer thicknesses of the metallic multilayer films were extracted from experimental data using GenX. The associated errors were also obtained from GenX.

We grew a series of samples with different individual layer thicknesses as shown in the Table 4.1. The samples in this chapter is selected based on the magnetization direction, domain images and total thickness. However, growing ultra-thin metal is a challenge due to surface roughness. When a film has high roughness domain wall and skyrmion stop moving [149, 150]. On the other hand, low roughness results in low pinning of the domain wall. Thus, to gain optimal roughness, domain wall motion and surface morphology were also considered essential characteristics in the sample selection process.

4.3.2 Morphology

Surface roughness is a critical factor for the application of E-fields through ionic liquid gating. High surface roughness might lead to unstable gating therefore the atomic force microscopy (AFM) measurement were carried out the identify the surface roughness. The measurement was conducted by Dr. L. Huang at the university of Leeds. The surface roughness was studied at different positions and different scan size.

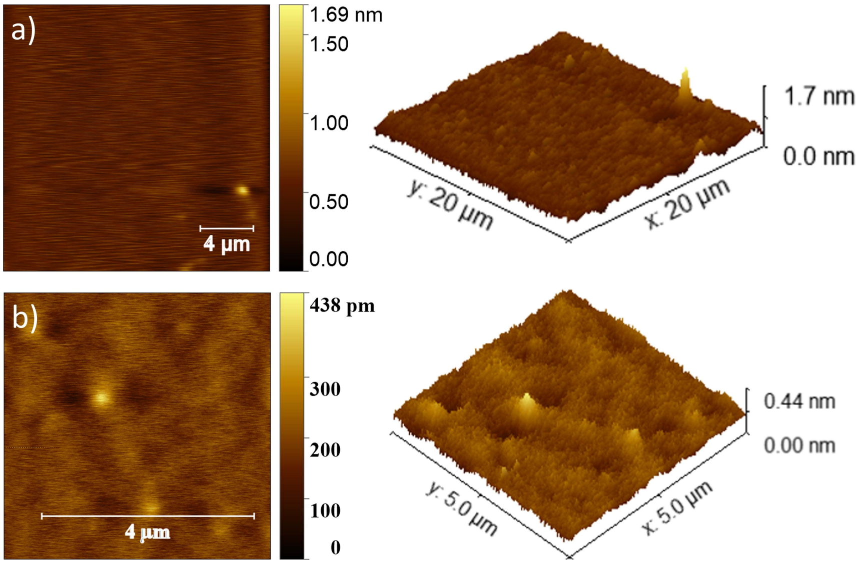

Figure 4.5: AFM images showing surface morphology of as grown sample 5: Ta(12 Å)/Pt(19 Å)/CoB(7 Å)/Ir(3.5 Å)/Pt(6 Å), (a) $20\mu m \times 20\mu m$, (b)$5\mu m \times 5\mu m$.

Figure 4.5 shows the 2d and 3d AFM images of a as grown sample at different position. Figure 4.5a) shows a surface roughness of 1.7 nm. It can be seen that the surface roughness is coming from the island type growth of metals. The AFM study shows that the studied ultra-thin films are processing low roughness compared to the XRR measurement. Therefore, the magnetic systems can be used for E-field application.

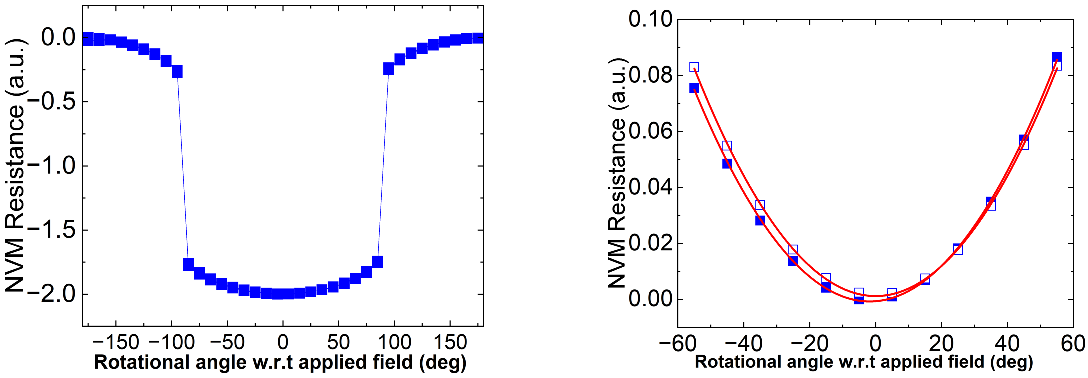

Figure 4.6: The left side image is showing normalized resistance data as a function of rotational angle. The right side image is showing the magnification of the polynomial fit.

4.4 Magnetic properties

4.4.1 Effective anisotropy

This section presents magnetic anisotropy measurement of Ta/Pt/CoB/Ir/Pt samples. The magneto-resistance measurement is adapted from the extraordinary Hall effect (EHE) to determine magnetic states under the influence of a magnetic field. The samples are wire-bonded at four points, and are positioned between electromagnetic pole pieces, and rotated from $\Phi = -180^0$ to $+180^0$. Where Φ is the rotational angle of the applied magnetic field. Current is passed through the sample while it placed in a constant perpendicular field of 518 mT (arbitrary). The applied magnetic field alters the magnetization direction, resulting in a voltage drop known as the Hall voltage. Figure 4.6, shows the experimental data on the left where resistance is recorded as a function of Φ, and the corresponding parabolic fitting on the right side. Normalized data is utilized for fitting a parabola, and $\mu_0 \mathrm{H_K}$ is calculated using the following equation [89, 151],

$$\mathrm{H_K} = \frac{2\mathrm{K_{eff}}}{\mathrm{M_s}} = \mathrm{H}\frac{1-\sqrt{\mathrm{A_2}}}{\sqrt{2\mathrm{A_2}}}, \tag{4.1}$$

where $\mathrm{K_{eff}}$ is the effective magnetic anisotropy, H denotes the applied magnetic field (518 mT), and $\mathrm{A_2}$ is the quadratic term of the parabola. The determination of the anisotropy field relies on the anomalous Hall effect (AHE), as described in the theory section. From the anisotropy field, the effective anisotropy K_{eff} is calculated, which is shown in Table 4.2. Alshammari et al. (2021) [89] calculated the effective anisotropy field ranging from around 450 mT to 900 mT for CoB multi-layers. Additionally, Tan et al. (2021) investigated the K_{eff} for $Co_{80}B_{20}$ (2 nm)/Ir. They found K_{eff} values between $0.1\,MJ/m^3$ to $0.2\,MJ/m^3$, which are slightly lower than the values we observed. The reason might be that the CoB composition is different.

$\mu_0 H_K$(T)	M_s(emu/cc)	K_{eff}(MJ/m^3)	samples
0.8 ± 0.1	590±20	0.3±0.1	S2
0.9 ± 0.1	610±20	0.3±0.2	S3
0.7 ± 0.1	670±30	0.2±0.1	S4
1.2 ± 0.1	910±30	0.5±0.2	S5

Table 4.2: H_{eff} has been extracted from a polynomial fit and K_{eff} have been calculated using the Ms and H_{eff}. Samples: S2 = (Ta(8 Å)/Pt(12.5 Å)/CoB(5 Å)/ Ir(6 Å)/Pt(16.5 Å), S3 (Ta(8.5 Å)/Pt(12 Å)/CoB(5.5 Å)/Ir(6 Å)/Pt(17 Å), S4 Ta(7.5 Å)/Pt(12 Å)/CoB(5.5 Å)/Ir(6 Å)/Pt(17.5 Å), S5 Ta(12 Å)/Pt(19 Å)/CoB(7 Å)/Ir(3.5 Å)/Pt(6 Å).

4.4.2 Exchange stiffness, A

This section focuses on measuring the magnetization of CoB multilayer films with temperature variations, aimed to determine the exchange stiffness (A). Ferromagnetism is limited at the Curie temperature due to thermal fluctuations overcoming the exchange interactions that align spins. At lower temperatures, the reduced thermal energy leads to a smaller population of spin wave excitations (magnons). This decreased spin wave population allows for better alignment of spins, resulting in an increase in the saturation magnetization (Ms) [88, 89]. The Bloch law describes the temperature dependent magnetization. Below Curie temperature the magnetization decreases with increasing temperature. Therefore the reduced magnetization can be fitted with Bloch law.

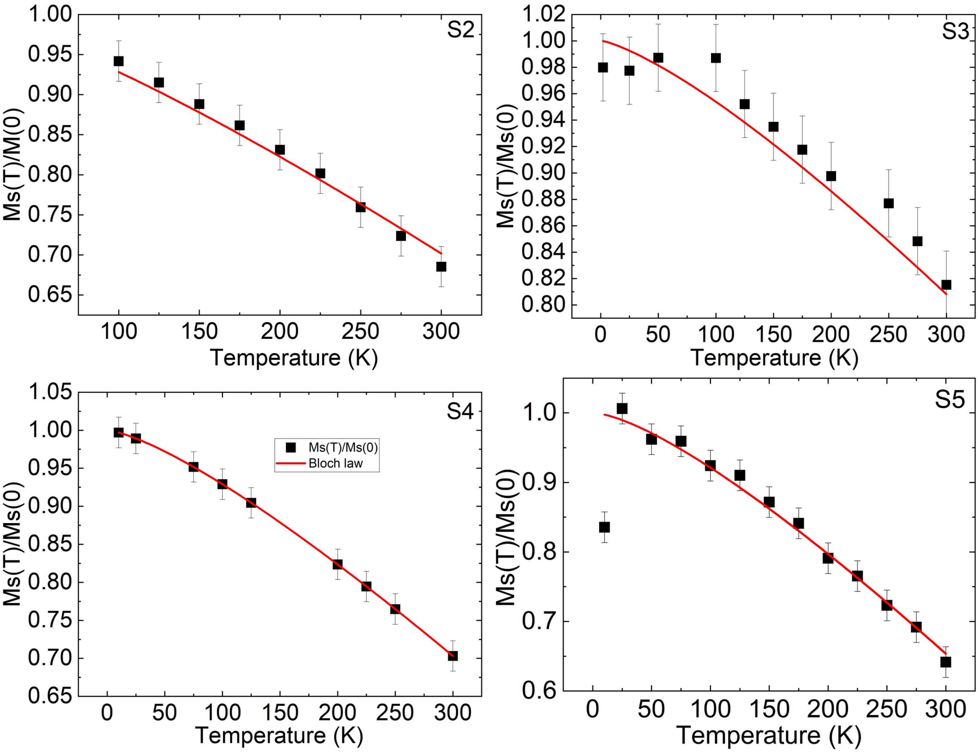

Figure 4.7: Temperature dependent magnetization fitted with Bloch law thin film assumption. Samples: S2 = (Ta(8 Å)/Pt(12.5 Å)/CoB(5 Å)/ Ir(6 Å)/Pt(16.5 Å), S3 (Ta(8.5 Å)/Pt(12 Å)/CoB(5.5 Å)/Ir(6 Å)/Pt(17 Å), S4 Ta(7.5 Å)/Pt(12 Å)/CoB(5.5 Å)/Ir(6 Å)/Pt(17.5 Å), S5 Ta(12 Å)/Pt(19 Å)/CoB(7 Å)/Ir(3.5 Å)/Pt(6 Å).

The hysteresis loop is measured from 2 K to 300 K in the OOP configuration. A Python code is used to fit the saturation magnetization according to the Bloch law's thin film approximation, which considers the motion of spin waves in two dimensions (2D) [88, 89, 152],

$$\frac{\mathrm{M_s(T)}}{\mathrm{M_s(0)}} = 1 + \frac{\mathrm{V_{ws}}}{\mathrm{S}}.\frac{1}{4\pi \mathrm{a_z}}.\frac{\mathrm{K_B T}}{2\mathrm{D_{sw}}}\sum_{\mathrm{n=0}}^{\mathrm{n_2}}\log\Big(1 - \mathrm{e}^{-(\mathrm{D_{sw}}(\frac{\mathrm{n}\pi}{\mathrm{n_z a_z}})^2+\hbar \mathrm{w_0})/\mathrm{K_B T}}\Big), \tag{4.2}$$

where, $\mathrm{M_s(T)}$ is the temperature dependent saturation magnetization, n_z is the number of atomic layer along z direction, a_z is the distance between atomic layer in z direction. $\hbar\omega_0 = g\mu_0\mu_B(H_k - H_{damg})$, where g is the g is gyromagnetic ratio, H_k is the anisotropy field and H_{dmag} is the demagnetizing field. The magnetization at zero kelvin temperature is determined from the intercept of the straight line obtained by plotting $\mathrm{M_s}$ vs $\mathrm{T^{3/2}}$. $\mathrm{V_{ws}}$ is the Wigner-Seitz volume, $\mathrm{D_{sw}}$ is the spin-wave stiffness, S is the spin quantum number. Additionally, $K_B = 1.3807 \times 10^{-23}$ J/K is the Boltzmann constant.

The spin wave stiffness D_{sw} can be calculated from

$$D_{sw} = \frac{2AV_{sw}}{S}, \tag{4.3}$$

$$V_{ws} = \frac{\pi r^2 h M_{Co_2B}}{2m}, \tag{4.4}$$

where the r is the radius of the CoB target, h is the height of the CoB target, m is the mass of the CoB target, and M_{Co_2B} is the mass of CoB. CoB does not have a well-defined lattice, so V_{ws} is calculated from the CoB target density, where V_{ws} represents the volume per magnetic moment.

Figure 4.7 shows the temperature dependent magnetization fitted with Bloch law in equation 4.4.2. The exchange stiffness A can be obtained from the Bloch law fit and above equations. Sample S2 exhibits an exchange stiffness of 3.3 ± 0.1 pJ/m,while sample S3 has a higher value of 4.8 ± 0.2 pJ/m. Sample S4 shows an exchange stiffness of 3.4 ± 0.1 pJ/m, pJ/m, and sample S5 has the lowest value at 2.6 ± 0.2 pJ/m. The error is taken from the fitting. Kona et. al. (1994) [153] reported a range of exchange stiffness values for different CoB compositions, ranging between 3.4 pJ/m to 9.8 pJ/m. Kuzmin et al. (2007) determined A as 4.4 pJ/m specifically for Co_2B [154]. Alshammari et.al. [89] using thin film approximation, calculated A within the range of 3.9 ± 1.7 pJ/m to 4.8 ± 1.6 pJ/m.

4.5 Measuring the Dzyaloshinskii-Moriya interaction (DMI)

DMI stabilizes domain walls and complex structures, i.e. skyrmions in thin films. Moreover, DMI delays walker breakdown, which increases Domain wall velocity. Thus, it is essential to investigate DMI in the system for further applications. This section is written following references [11, 51].

4.5.1 Domain wall velocity in the creep regime

This section observed the domain wall velocity regime of CoB multilayer samples. The DMI is calculated from the field-driven domain wall motion in the creep regime. Therefore, prior to calculating DMI, it is essential to verify that the domain-wall-driven fields are in the creep regime. Domain wall velocity was calculated for the

OOP pulses applied to the sample to study the motion regimes. The domain wall displacement with applied pulses was calculated from Kerr microscope images, where the Velocity, $\mathrm{v} = \mathrm{displacement/Pulsetime}$ [11, 25, 51]. Figure 4.8 shows ln(v) as a function of the applied OOP field and ln(v) as a function of $\mu_0\mathrm{H}^{-(1/4)}$. When $\ln(\mathrm{v}) \propto \mu_0\mathrm{H}^{-(1/4)}$, a linear behavior is observed in plot, confirming that the velocity is within the creep regime [11, 25, 51]. However, we could not analyze the images before 27 Oe due to low contrast and high pinning. Additionally, after 31 Oe, the high velocity of the domain wall suggested that it might be entering the flow regime.

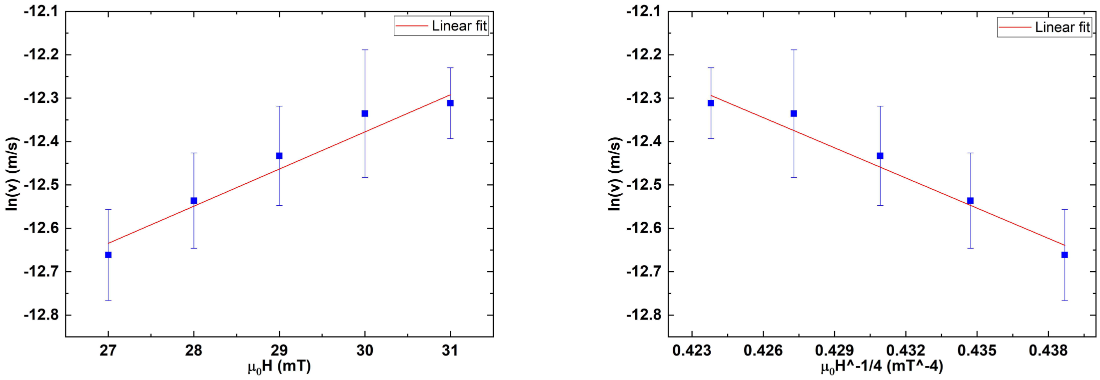

(a) ln(v) vs applied OOP field

(b) ln(v) vs $\mu_0\mathrm{H}^{-(1/4)}$

Figure 4.8: Creep check of domain wall motion of S5 (Ta (12 Å)/Pt(19 Å)/CoB(7 Å)/Ir(3.5 Å)/Pt(6 Å)). (a) ln(v) as a function of the applied OOP field. (b) ln(V) as a function of $\mu_0\mathrm{H}^{-(1/4)}$. The linear behavior confirms that the velocity with the OOP field is in the Creep regime.

4.5.2 Measuring DMI in the creep regime

In this section, the calculation of DMI was conducted using the bubble domain expansion technique. This method involves manipulating the energy degeneracy within domain walls by applying an in-plane magnetic field, allowing us to estimate the DMI strength. This technique, require a step-by-step process. Initially, an OOP field is applied to saturate the sample. Subsequently, an opposing pulse similar to the coercive field is employed to nucleate a domain bubble. The bubble typically forms at local energy minima or near defects within the film. Thus, the magnetic state is meta-stable. The bubble also experiences an effective magnetic field, referred to as the DMI field

(H_{DMI}) along the film surface. The DMI affects the domain wall locally, and the H_{DMI} preserves radial symmetry with the nucleation point parallel to the applied OOP field. The radial symmetry is broken with an applied in-plane field parallel or anti-parallel to H_{DMI}. As a result, the bubble expands in one direction while suppressing expansion in another direction. Figure 4.9(b) shows an example of asymmetric bubble expansion, demonstrating how the in-plane field (H_x) break symmetry. Consequently, the bubble expands in one direction due to the combined effect of $H_x + H_{DMI}$ while suppressing expansion in another due to $H_x - H_{DMI}$ [11, 14, 25, 51, 87, 155].

A plot of domain wall velocity as a function of the applied in-plane field is presented in Figure 4.9. As mentioned before, the velocity is calculated from the Kerr-Microscope images, which was performed using a Python script [156, 157] that involved slicing an image horizontally at its midpoint and measuring the displacement in pixels. This pixel displacement was then converted to meters per second. The process was repeated at fifteen positions to minimize errors, and velocities were calculated for various OOP pulse times for further averaging. The velocity plots for the right-hand side (RHS) and left-hand side (LHS) displacements exhibit similar trends. The minimum velocity value is shifted from zero. The movement of the axis of symmetry in opposite directions away from zero in-plane field indicates the influence of the DMI field (H_{DMI}). This suggests that at this specific location, the in-plane field seemingly has no effect and vanishes the H_{DMI} field, effectively measuring the in-plane field as the H_{DMI}. The model is adapted and modified from the Creep model, which includes the effect of the in-plane field and DMI on the energy of the domain wall. The Creep law states that the applied OOP field induces exponential changes in domain wall velocity [11, 25, 51, 62, 87, 155, 158]. The Creep law can be written as,

$$\nu = \nu_0 \exp\Big\{-\zeta(\mu_0 H_{OOP})^{\frac{1}{4}}\Big\}, \tag{4.5}$$

where, ν is the domain wall velocity and ν_0 characteristics velocity. $\mu_0 H_{OOP}$ is the OOP field. The scaling coefficient ζ is,

$$\zeta = \zeta_0[\sigma_{DW}(H_{IP})/\sigma_{DW}(0)]^{\frac{1}{4}}, \tag{4.6}$$

where ζ is the scaling constant. σ_{DW} is the energy of the domain wall. $\sigma_{DW}(0)$ is the domain wall energy density.

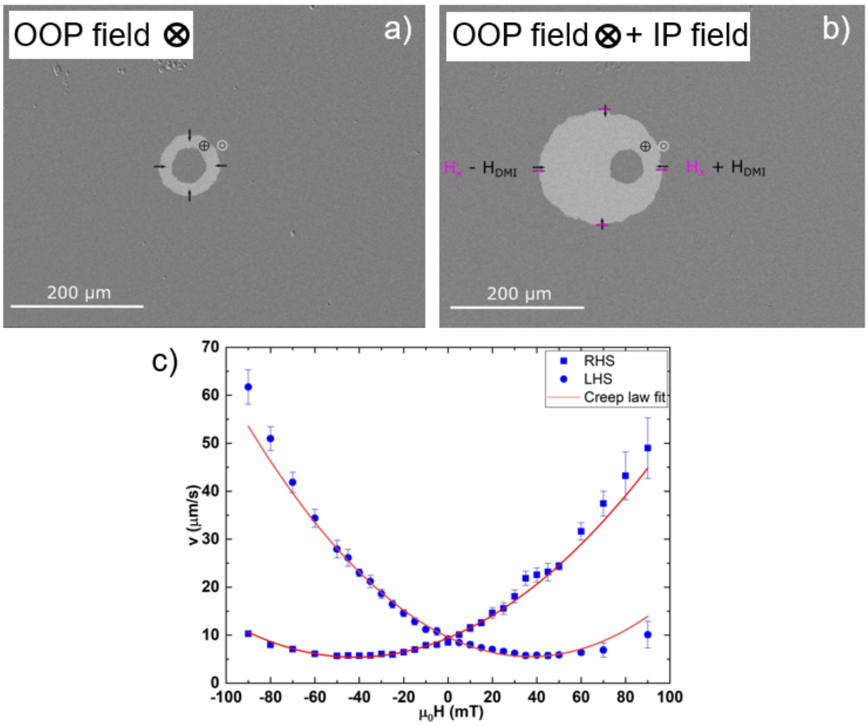

Figure 4.9: Bubble expansion of S5: (a) Symmetric bubble expansion. (b) Asymmetric bubble expansion. (c) The domain wall velocity of studied film as a function of applied in-plane field, nucleation field is 29 Oe. The left-hand side (LHS) and the right-hand side (RHS) indicate the negative and positive values of the in-plane field respectively. The error bars are standard deviation of 20 or more velocities. Due to the chirality of the domain wall, the in-plane field (denoted as $\mathrm{H_x}$ in the image) creates different domain wall energy ratios (domain wall energy due to in-plane field and with out in-plane field $\sigma_{\mathrm{DW}}(\mathrm{H_{IP}})/\sigma_{\mathrm{DW}}(0)$ in Equation 4.6. Additionally, the left-hand side (LHS) and right-hand side (RHS) possess opposite DMI fields. Consequently, $\mathrm{H_x}$+$\mathrm{H_{DMI}}$ varies with the applied in-plane field for LHS and RHS, leading to distinct energy profiles and resulting in different velocities. At the point where the domain wall velocity is minimized, the DMI opposes the IP field and effectively cancels it out [11].

Domain wall energy density = Bloch wall energy density + shape anisotropy energy density + DMI energy density + in-plane field energy density [11, 25, 51, 87]. The energy of a domain wall (considering H_{DMI} and in-plane field) can be written as [11],

$$\sigma_{\mathrm{DW}} = \sigma_{\mathrm{DW}}((0)) + 2\Delta \mathrm{K}_{\mathrm{DW}} \cos^2\theta - \mathrm{D}\pi \cos\theta - \mu_0 \mathrm{M_s} \pi \Delta \mathrm{H_{IP}} \cos\theta, \tag{4.7}$$

Where, $\sigma_{\mathrm{DW}}(0)$ is the Bloch wall energy density $= 4\sqrt{\mathrm{AK_{eff}}}$, A is the exchange stiffness and $\mathrm{K_{eff}}$ is the effective anisotropy $\mu_0 \mathrm{H_K M_s}/2$, $\mu_0\mathrm{H_K}$ is the anisotropy field and $\mathrm{M_s}$ is the saturation magnetization. The domain wall width Δ is calculated as $\Delta = \sqrt{\mathrm{A/K_{eff}}}$, where A denotes the exchange stiffness. The domain wall anisotropy is given by $\mathrm{K_{DW}} = (\mathrm{M_{demag}}\mu_0\mathrm{M_s^2})/2$, with $\mathrm{M_{demag}}$ as the domain wall demagnetization factor. θ denotes the angle between the in-plane magnetization and the x-axis, and D stands for DMI constant [11, 25, 51, 87].

The equation 4.7 could gives two energy solutions: if the in-plane field changes the domain wall to Néel s type, D will be $\mathrm{D} > \Delta\mathrm{K_{DW}}/\pi$, the energy density can be written according to the equation 4.8, Otherwise, there will be some component of Bloch wall (Bloch-Néel wall configuration), where D will be $\mathrm{D} < \Delta\mathrm{K_{DW}}/\pi$ and the energy density can be written as equation 4.9 [11],

$$\sigma_{\mathrm{DW,N}} = \sigma_{\mathrm{DW(0))}} + 2\mathrm{K_{DW}}\Delta - \mu_0\mathrm{M_s}\pi\Delta|\mathrm{H_{IP}} + \mathrm{H_{DMI}}| \tag{4.8}$$

$$\sigma_{\mathrm{DW,NB}} = \sigma_{\mathrm{DW(0))}} - (\mu_0^2\mathrm{M_s^2}\pi^2\Delta/8\mathrm{K_{DW}}) - (\mathrm{H_{IP}} + \mathrm{H_{DMI}})^2 \tag{4.9}$$

The Creep law fitting of experimental data is shown in Figure 4.9, with fitting parameters including velocity v, ζ_0, and $\mathrm{H_{DMI}}$. Extracted from these fits, $\mathrm{H_{DMI}}$ enables the subsequent calculation of the DMI constant using the formula, $\mathrm{D} = \mu_0\mathrm{H_{DMI}M_s}\Delta$ [11, 25, 51, 87, 145]. The calculated DMI values are presented in table 4.3.

Alshammari et. al. (2021) [89] reported the D of Pt/CoB/Ir multilayers ranging between $0.27\mathrm{mJ/m^2}$ to $0.43\mathrm{mJ/m^2}$, higher than our calculated D. Conversely, Lucassen et al. (2020) [159] calculated D of around $0.44\mathrm{pJ/m^2}$ for a Pt/CoB/Ir SAF system. Additionally, Zeissler et al. (2020) [130] conducted investigations using BLS and found $\mathrm{D} = -1.1 \pm 0.1\mathrm{mJ/m^2}$. Darwin et al. (2023) [88] presented an extended study of DMI using different techniques. They observed that DMI varies between 0.1 $\mathrm{mJ/m^2}$ and 0.7 $\mathrm{mJ/m^2}$ for different techniques and different labs, where Brillouin Light Scattering (BLS) shows the highest DMI and Bubble Expansion shows the lowest DMI. These contrasting values highlight the diversity and complexity in determining DMI across various experimental methodologies.

H_{DMI}(mT)	A (pJ/m)	K_{eff}(MJ/m^3)	D(mJ/m^2)	samples
10 ± 1	3.3 ± 0.1	0.3 ± 0.1	0.02 ± 0.01	S2
12 ± 3	4.8 ± 0.1	0.3 ± 0.2	0.03 ± 0.01	S3
15 ± 3	3.4 ± 0.1	0.2 ± 0.1	0.04 ± 0.01	S4
39 ± 1	2.6 ± 0.1	0.5 ± 0.2	0.08 ± 0.01	S5

Table 4.3: H_{DMI}, A, and D for the sample S2 to S5. Samples: S2 = (Ta(8 Å)/Pt(12.5 Å)/CoB(5 Å)/ Ir(6 Å)/Pt(16.5 Å), S3 (Ta(8.5 Å)/Pt(12 Å)/CoB(5.5 Å)/Ir(6 Å)/Pt(17 Å), S4 Ta(7.5 Å)/Pt(12 Å)/CoB(5.5 Å)/Ir(6 Å)/Pt(17.5 Å), S5 Ta(12 Å)/Pt(19 Å)/CoB(7 Å)/Ir(3.5 Å)/Pt(6 Å).

In our magnetic system, maintaining the bubble on some samples was challenging due to high velocity, while other films exhibited high pinning. The calculated DMI was found to be significantly lower than the reported value for the CoB system. This suggests that the bubble expansion technique may not be suitable for our system. Therefore, in Chapter 6, BLS is employed to calculate DMI.

4.6 Conclusions

In this chapter, the investigation centered around the development and analysis of ultra-thin magnetic multilayers composed of Ta/Pt/CoB/Ir/Pt, primarily focusing on the magnetic and structural properties. The excellent stability of perpendicular magnetic anisotropy (PMA) at room temperature has advantages for long-term data storage, particularly in STT-MRAM devices. High perpendicular anisotropy in domain wall-based spintronics facilitates narrower domain walls, thereby increasing data storage density. Moreover, PMA materials play a crucial role in isolating skyrmions within skyrmion-based devices, a characteristic achieved in the studied system through the SOC of Co-Pt.

In order to study the magnetoelectric effect at the surface of the FM layer surface, the total thickness of the film as well as individual layers were produces as ultra thin. The structural properties were investigated by XRR and AFM. The AFM analysis revealed that the film exhibits low surface roughness. The effective magnetic anisotropy is investigated using AHE and yielded the following results: S2 = 0.3 ± 0.1 MJ/m^3, S3 = 0.3 ± 0.1 MJ/m^3, S4 = 0.2 ± 0.1 MJ/m^3, S5 = 0.5 ± 0.1 MJ/m^3.

The exchange stiffness (A) was determined using the temperature-dependent magnetization and Bloch law thin film approximation. For ultra-thin CoB multilayers, the calculated values for the exchange stiffness are as follows: S2 = 3.3 ± 0.1 pJ/m, S3 = 4.8 ± 0.2 pJ/m, S4 = 3.4 ± 0.1 pJ/m, and S5 = 2.6 ± 0.2 pJ/m.

The study also focused into exploring the DMI by examining asymmetric bubble expansion within the creep regime, with a focus on domain wall morphology as a crucial characteristic parameter. Samples exhibited different domain structures such as maze-like domains, and isolated bubble-type domains, corresponding to different film thicknesses. Key observations included domain nucleation, bubble formation, and characteristics of domain wall motion, highlighting the influence of film geometry and interfacial roughness on domain morphology. The DMI value obtained was significantly smaller (ranging from 0.02 to 0.08 mJ/m^2) than the reported values for CoB systems, so we did not to utilize these values for further experiments and simulations. Instead, the exchange stiffness value is employed for Mumax3 simulations in Chapter 7.

CHAPTER 5

Effect of Electric Field on Ta/Pt/CoB/Ir/Pt/HfO2: Ionic liquid gating of magnetic multilayer with structural inversion asymmetry

5.1 Introduction

In this chapter, we present measurements on devices using several techniques and explain them within a single framework of ion migration. The first section discusses the change in the anomalous Hall effect (AHE) hysteresis loop as an effect of gating, which is followed by the Kerr microscopy images and resultant hysteresis loop. Subsequently, the modification of magnetic properties are presented along with an exploration of reversibility. All these data can be understood in terms of oxygen ion migration. Finally, we interpret our findings within the framework of oxygen ion migration and conclude with final remarks.

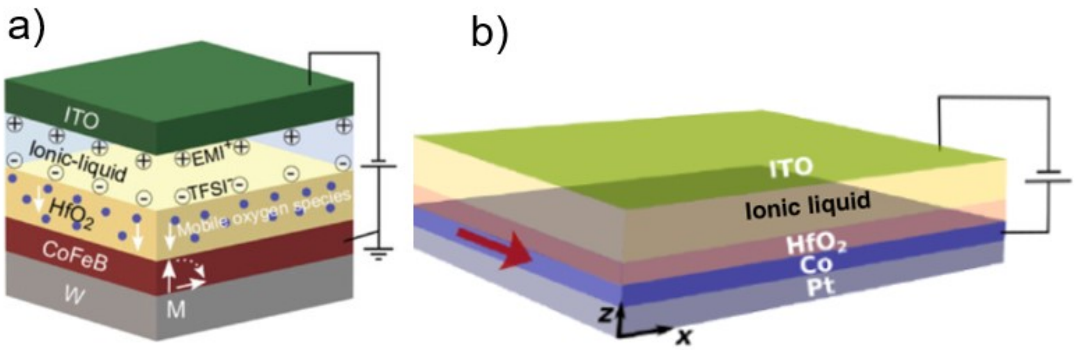

Figure 5.1: Typical sample structures in the E-field gating technique include: (a) W/CoFeB/HfO_2 [160] and (b) Pt/Co/HfO_2 [83]. These examples illustrate the magnetic layer positioned adjacent to the oxide layer.

As we introduced in Chapter 1, E-field modification of magnetic properties by ionic liquid gating (ILG) is a promising technique in spintronics due to its room temperature application, nonvolatility, energy efficiency, and reversibility [160, 161]. The technique has already proven its ability to modulate spin orientation and anisotropy in perpendicular magnetic anisotropy (PMA) materials [43, 160, 162–164]. All these examples show that oxygen is migrating from an oxide layer adjacent to the magnetic layer, similar to the structure shown in Figure 5.1. However, general PMA structures often include metallic layers on both sides of the ferromagnetic layer [11, 25, 51, 71, 89, 130, 165]. In this experimental work, we have investigated oxygen migration by ionic liquid gating of a material structure with metallic layers between ferromagnetic and oxide layers. This type of structure provides more flexibility in terms of material choice.

I received the training on ILG at the Centre for Nanosciences and Nanotechnologies (C2N), Paris under supervision of Dr. L. Herrera Diez. However, all the data presented in this chapter were taken at the University of Leeds.

5.2 Multilayer systems

The magnetic multilayer system studied here consists of Ta (1 nm)/Pt (2.3 nm)/$Co_{68\%}B_{32\%}$ (0.8 nm)/Ir (0.2 nm)/Pt(X nm), where X = 0.2, 0.4, 0.5, 0.6, 0.8. The magnetic multilayers are grown on a Si/SiO_2 (300 nm) substrate by dc magnetron sputtering at room temperature. Cobalt exhibits a polycrystalline or nanocrystalline state and the addition of Boron transforms it into nearly an amorphous state. This transformation reduces grain boundaries, resulting in low pinning of domain walls (DWs) and skyrmions. The narrow DWs, attributed to high PMA, coupled with the reduced pinning caused by Boron, position the Pt/CoB/Pt structure as a potential candidate for skyrmion and DWs-based spintronic devices [166]. The ultra-thin Iridium layer preserves the structure inversion asymmetry. Due to the broken symmetry, the DMI contribution arises from both interfaces of the CoB, resulting in a large net DMI. The thickness of the top Platinum layer varies from 0.2 nm to 0.8 nm to observe the effect of E-field-induced ion migration. As described in Chapter 3, a 2.5 nm layer of HfO_2 was grown for the E-field application by ex-situ atomic layer deposition.

5.3 AHE hysteresis loops

The gate voltage is applied between the film, which acts as a bottom electrode, and an Indium Tin Oxide (ITO)coated glass substrate, serving as a top electrode. The ITO-coated glass is used to carry out optical measurements on the sample whilst applying the E-field. The electric conductivity between the ITO glass electrode and the gate oxide is maintained using an ionic liquid. Specifically, the ionic liquid [EMI^+][$TFSI^-$] or 1-Ethyl-3-methylimidazolium bis (trifluoromethanesulfonyl)imide is used to apply voltage across all the samples presented in this thesis. The voltage is applied over an area of around 25 mm^2. During voltage application, a transient leakage current less than 1.5 μA was considered acceptable. This applied voltage causes nonvolatile [43, 167] modification of magnetic state; hence, all measurements were taken after turning off the gate voltage. In Chapter 6 we will show the results confirming nonvolatility of this changes. Details of the magneto-resistance measurement techniques are discussed in Chapter 3.

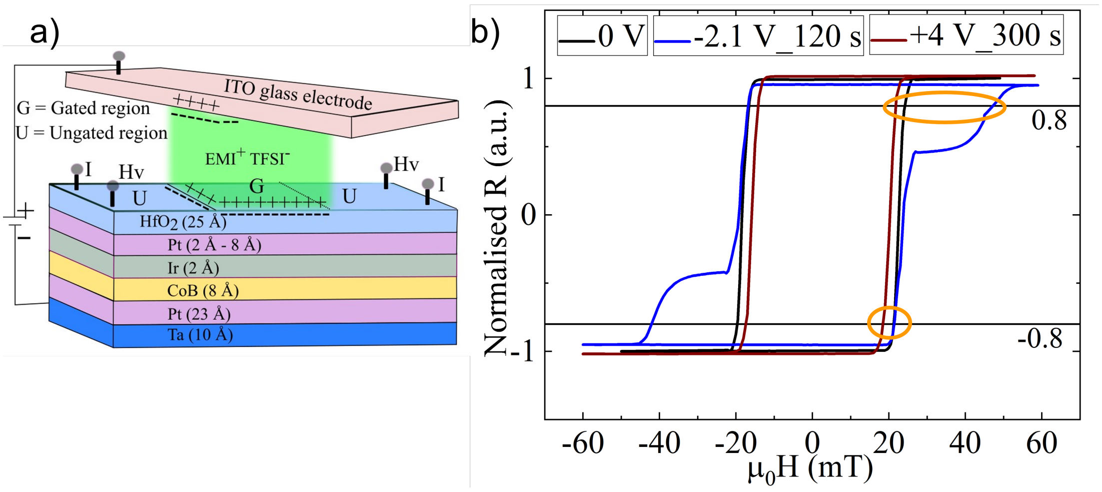

Figure 5.2: (a) Ionic liquid EMI$^+$ TFSI$^-$ is applied on the sample, and an ITO glass electrode is used as a top electrode. (b) The M-H loops are shown for 0 V, -2.1 V, and +2.1 V. The applied voltage loops represent a mixture of gated and ungated signals. This effect is reversible and is discussed in Section 5.6.

Figure 5.2(a) shows the sample structure and the electrical connections. When a gate voltage is applied, ions within the liquid gate move toward the opposite polarity, forming electric double layers. The distance between two the positive and negative ions in a double layer is ≈1 nm [43, 168], creating a nanocapacitor with a large capacitance of around 100 μF/cm^2. Therefore, a small applied voltage produces a large E-field effect, altering the carrier density by an order of magnitude, from 10^{14}/cm^2 to 10^{15}/cm^2, at the ionic liquid and oxide interface [169]. Moreover, in our devices, the voltage is applied at the middle of the sample, while the anomalous Hall voltage is measured outside of the gated region. As a result, the M-H loop with applied voltage is a mixture of gated (G) and ungated (U) regions (Figure 5.2(b)). However, The multilayer systems studied here show remanence/saturation magnetization ≈ 1 indicating retention PMA, even for samples where voltage had been applied. Figure 5.2(b) shows the M-H curve of initial stage, with an applied negative voltage and an applied positive voltage. The shape of the M-H curve changes under different gate voltages due to the E-field-induced relocation of oxygen ions within the sample structure: A positive gate voltage reduce the domain nucleation field, while a negative gate voltage increases the saturation field. It is assumed that the data can be decomposed into components that are symmetric and antisymmetric with respect to the magnetic field. Thus, the antisymmetric part, identified as R_{xy}, is considered the Hall signal. The symmetric part, which remains constant with the magnetic field, is denoted as R_{xx}. However, negative gate voltage increases it, while positive voltage decreases it.

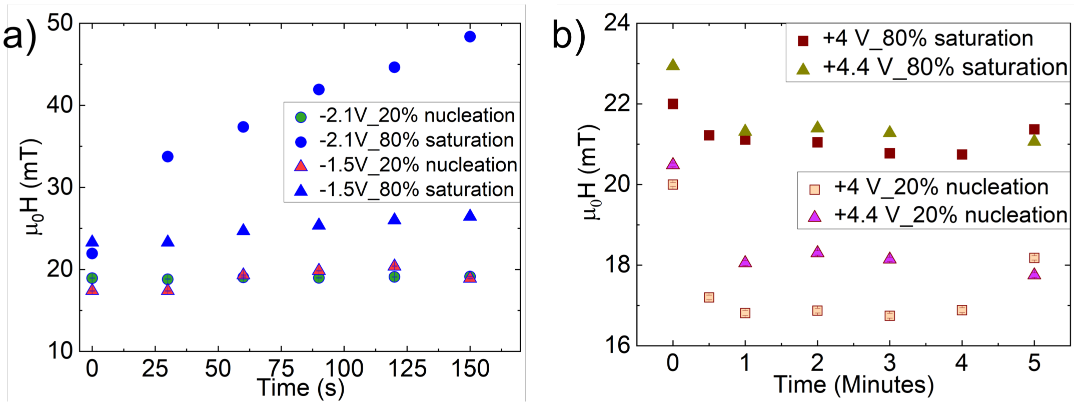

Figure 5.3: (a) The 20% nucleation field and 80% saturation field under -1.5 V and -2.1 V as a function of gating time. A higher voltage for a longer time has a greater influence on the change than a lower voltage and/or a shorter time. (b) The 20% nucleation field and 80% saturation field under +4 V and +4.4 V as a function of gating time. Compared to a negative voltage, a larger positive voltage is required for a longer duration to observe any changes.

The changes observed in Figure 5.2(b) may be attributed to change in anisotropy caused by the applied electric field. Under a negative voltage, the curvature represents the final stage of sample saturation, whereas under a positive voltage, part of the sample reverses more quickly than the rest. To quantify these effects, we use a convenient metric: the magnetic field at which the device reaches 80% saturation (indicated on the Figure 5.2(b)), representing the state just before full saturation, and the field at which 20% of the sample has switched (indicated on the Figure 5.2(b)), indicating the initial stage of domain nucleation and motion.

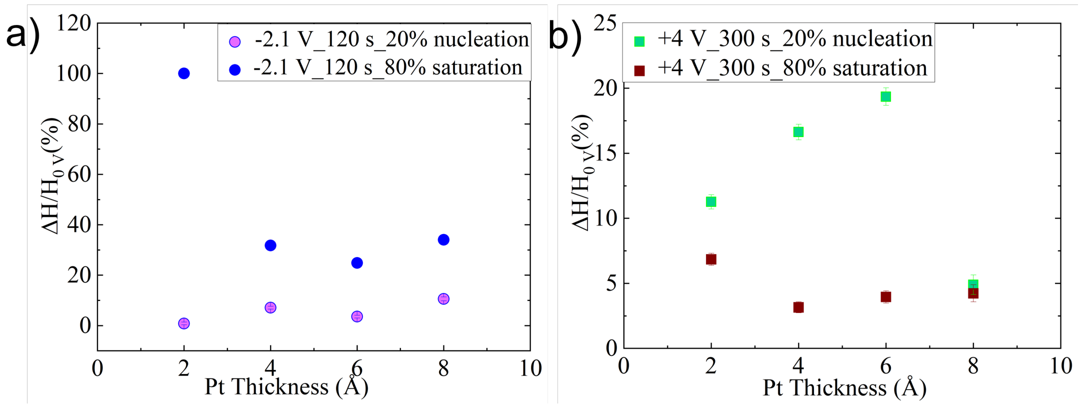

Figure 5.4: (a) The percentage change in 20% nucleation and 80% saturation at -2.1 V as a function of top Pt thickness. For the 2 Å Pt layer, an approximate 100% change indicates that the change in mT is roughly double. Conversely, an approximate 0% change indicates almost no change in mT. (b) The percentage change in 20% nucleation and 80% saturation at +4 V as a function of top Pt thickness. The change is significantly higher for 20% nucleation than for 80% saturation, with the exception of the 8 Å Pt layer.

Figure 5.3(a) shows the 20% nucleation field and 80 % saturation field at -1.5 V and -2.1 V as a function of time. The negative voltage showed a higher effect on saturation compared to nucleation, where the effect is more prominent at -2.1 V with 150 s gating time. Figure 5.3(b) shows shows the 20% nucleation field and 80 % saturation field at +4 V and +4.4 V as a function of time. This data suggests that manipulating the system requires a higher positive voltage and longer gating time compared to the negative voltage. The observed discrepancies may be attributed to changes in the sample's chemistry due to oxygen migration, with a negative voltage having a significantly greater influence than a positive voltage. As observed, the effect of ionic liquid gating depends on the applied voltage and gating time. Applying -2.1 V for 120 s is sufficient to observe the induced changes. Higher positive voltages are required for longer durations; however, this may induce electrochemical reactions, potentially degrading the liquid or film. Although the chemical window for the ionic liquid is reported to be between 4.1 V to 6.1 V [118], we apply up to +4 V for further study in this work.

Figure 5.4(a) shows the change in 80% saturation and 20% nucleation for the -2.1

V with a gating time of 120 s as a function of top Pt layer thickness. The negative voltage significantly increases the saturation field for the 0.2 nm Pt sample, this can be approximately doubled. However, here the 20% nucleation changes monotonically. The 80% saturation undergoes a sharp decline from Pt 2 Å to Pt 4 Å however after that it changes monotonically.

Figure 5.4(b) shows the effect of applied voltage at the 80% saturation and 20% nucleation at +4 V as a function of the top Pt thickness. With increasing Pt thickness, the positive voltage increases nucleation significantly, except for the 8 Å thickness, which is an exception. In this instance, the 80% saturation experiences a sharp decline from 2 Å Pt to Pt 4 Å and subsequently follows a monotonic trend. Consequently, these observations indicate the potential to manipulate the magnetic state by adjusting the thickness of the top Pt layer.

5.4 Kerr microscopy hysteresis loop and imaging

The AHE measurement were conducted across a wide area including both gated and ungated regions. To comprehend the local modifications or the localized E-field effects, the samples were measured using a Kerr microscope. This enabled the investigation of the gated and ungated regions individually.

The voltage is applied on 10 × 5 mm sheet film (Figure 5.2). Subsequently, upon turning off the voltage, the ITO glass electrode is detached, and the sample is washed with acetone to clean away the ionic liquid. The nonvolatile nature of the ILG technique maintains the E-field-modified magnetic state unchanged [43]. Figure 5.5 shows the effect of an applied voltage on a 4 Å Pt top layer sample. Figure 5.5 (a) presents the out of Plane (OoP) M-H loop at the initial state (black curve). It shows full remanence at 0 mT, so the film has PMA, although the loop exhibited curvature in the middle due to the Faraday effect in the microscope lenses. This was corrected by subtracting the quadratic term from a parabolic fit. Under a negative voltage of -2.1 V for 120 s the coercive field increases by 42%±5% (the percentage error is calculated from the applied field steps), signifying an increase in domain nucleation and saturation field. Conversely, a positive voltage of +4 V applied for 300 s reduces the coercive field by 20%±5%. This decrease indicates a reduction in domain nucleation and saturation field due to the positive voltage.

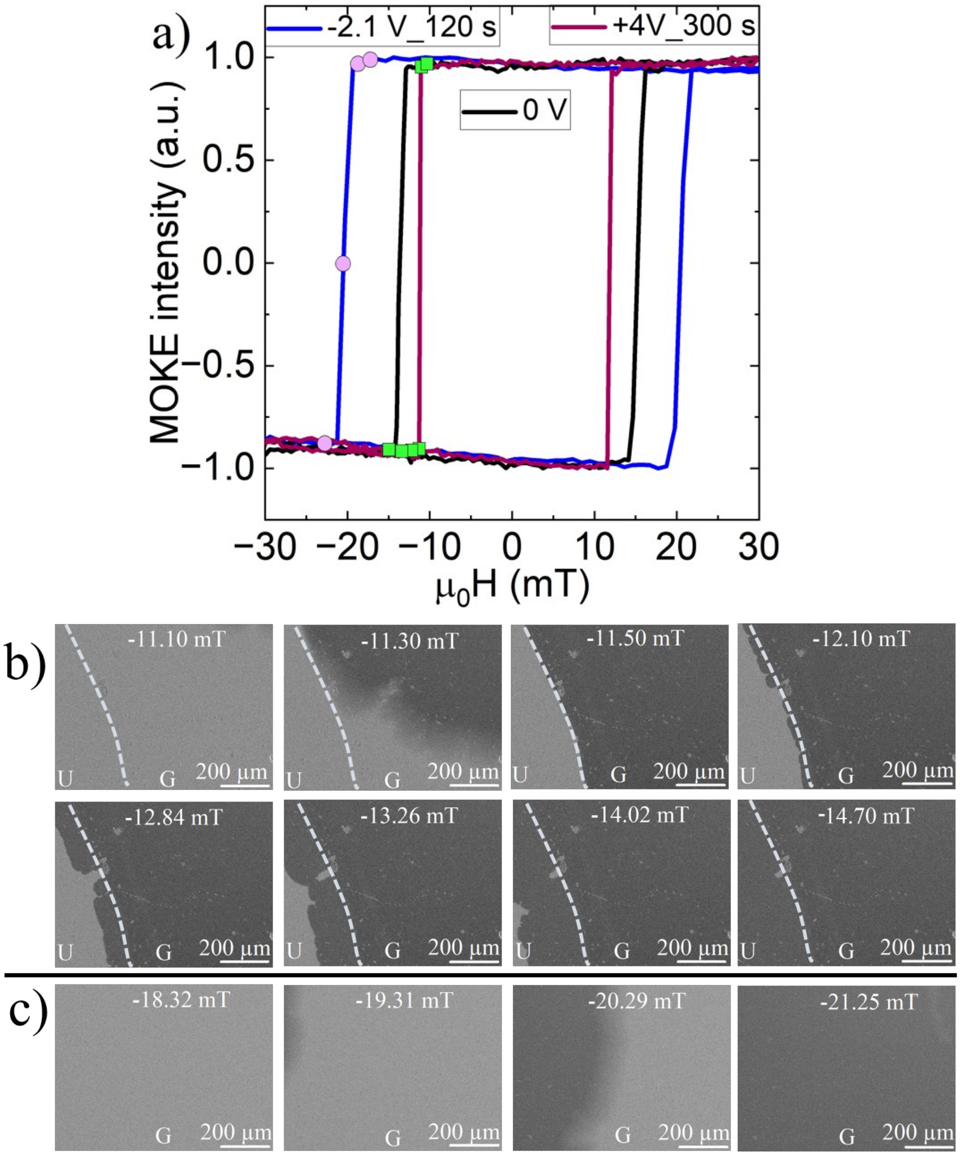

Figure 5.5: (a) Kerr Microscopy hysteresis loop of 4 Å Pt top layer with -2.1 V for 120s, as grown and with +4 V for 300 s. Negative voltage increases the coercive field, and the Positive voltage decreases the coercive field. (b) Domain images were taken at +4 V for 300 s, including both G and U regions. After removing the liquid, the differences between the G and U regions became visually apparent. Consequently, a line was drawn on the microscopy image to delineate the boundary between the two regions. (c) Under -2.1 V for 120 s, a high field is required to nucleate domains.

It worth mentioning that an applied voltage does not eliminate PMA in the system studied; rather, it alters DWs motion as a gating effect, evident in domain images of the samples. However, Diez's group observed that -2.1 V in turn changes the magnetization direction from In plane (In-P) to OoP, with longer gating time, the magnetization direction changes back to In-P [40, 83].

Figure 5.5(b) shows the Kerr microscope images of the gated and ungated region. The white line is indicating the boundary between two regions. Under a positive voltage, domain nucleation occurs within the gated region at an external field of approximately -11.30 mT, slowly expanding into the ungated area. In contrast, Figure 5.5 (c) shows the negative gated area, where the domain nucleates at around -18.32 mT, which is significantly higher than the positive voltage. At the same time compared to the positive voltage it also increases the saturation field by approximately 44.56%±5%. This delay indicates a significant effect on both domain nucleation and saturation due to the negative voltage.

5.5 Magnetic characterization

5.5.1 Saturation magnetization

This section presents the evolution of the magnetic moment and saturation magnetization under the influence of an E-field. The Kerr Microscopy hysteresis loop only provides the relative magnetization orientation, instead of absolute magnetization. Therefore, SQUID-VSM measurement were perform to study precise and accurate changes in magnetization. To avoid the mixed signal from gated and ungated regions (Figure 5.2(b)), only the gated area was selected and measured for magnetic moment measurements. The magnetic moment is measured at the room temperature (300 K) in the OoP configuration. Details of the experimental techniques are discussed in Chapter 3.

In Figure 5.6(a), the M-H loop of 4 Å Pt top layer at 0 V, -2.1 V for 120 s, and +4 V for 300 s are displayed. The magnetic moment and coercive field change significantly with applied voltage. From the Kerr microscopy data above (Section 5.4), we also observed similar changes in the coercive field. Under a negative voltage, the magnetic moment decreases while the coercive field increases. On the other hand, a positive voltage increases the magnetic moment and reduces the coercive field.

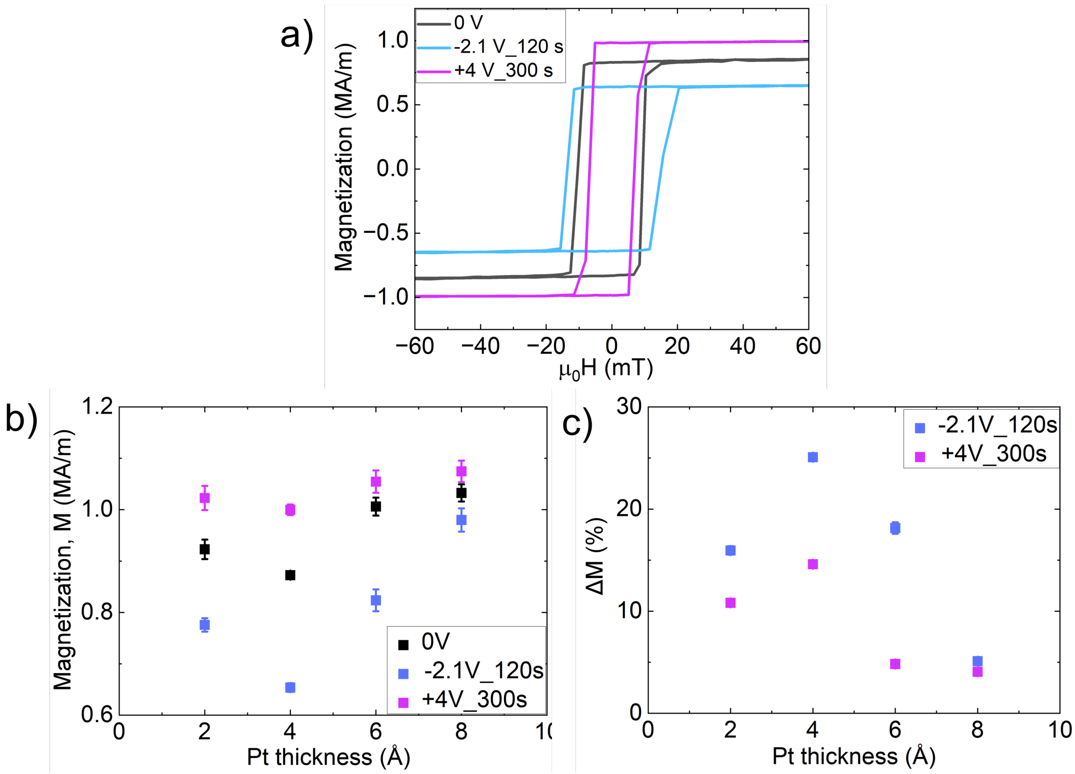

Figure 5.6: (a) SQUID-VSM hysteresis loop of a 4 Å Pt top layer at room temperature, measured at -2.1 V for 120 s, 0 V, and with +4 V for 300 s. The change in coercive field is consistent with the Kerr microscope measurement. (b) Magnetization as a function of the top Pt layer thickness. A positive voltage increases it, while a negative voltage decreases it. (c) The percentage change in magnetization varies with the thickness of the top Pt layer. Notably, a significant increase is observed for Pt thicknesses of 4 Å under a negative voltage.

Figure 5.6(b) demonstrates the magnetic moment as a function of top Pt thickness. With a negative voltage, moments decrease, whereas with a positive voltage, they increase. The magnetic moment generally increases with increasing Pt thickness, except for Pt 4 ÅȦt the same time, the E-field effect decreases with increasing Pt thickness, with the Pt 4 Å showing a larger effect when exposed to -2.1 V. Figure 5.6(c) presents the percentage change in magnetic moment with applied -2.1 V for 120 s and +4 V for 300 s. The change with a negative voltage is higher than the positive voltage, as further discussed in section 5.7. The moment is linearly decreasing with increasing Pt thickness, except for the 2 Å Pt, which shows an exception. For Pt 4 Å the negative voltage decreases it by approximately 26%. In contrast, the positive voltage increases it by around 13%. The images distinctly indicate the significant E-field evolution of the magnetic moment.

5.5.2 Anisotropy field

The anisotropy field is measured by the AHE technique, which is discussed in 3. The sample were rotated from -180° to +180° within a constant OoP field of 518 mT. The external magnetic field changes the sample's magnetization direction which result in a voltage drop (Hall voltage). The Hall voltage is recorded as a function of the angle. The data was fitted with a parabolic curve, as outlined in references [89, 151]. This fitting process provided the anisotropy field along with its associated error. The derived value of $\mu_0 \mathrm{H_k}$ was then used to calculate the effective anisotropy constant using Equation 3.7. Figure 5.7(a) shows the $\mu_0 \mathrm{H_k}$ as a function of top Pt layer thickness. The anisotropy field exhibits an increase with negative voltage and a decrease with positive voltage. The Figure 5.7 (b) shows the percentage anisotropy field as a function of top Pt layer thickness. For the Pt 8 Å Pt, the change in anisotropy field ($\mu_0 \mathrm{H_k}$) is smaller compared to the thin Pt. The percentage change of effective anisotropy constant $\mathrm{K_{eff}}$ is shown in the Figure 5.7(c). The anisotropy constant can be changed significantly with an applied voltage.

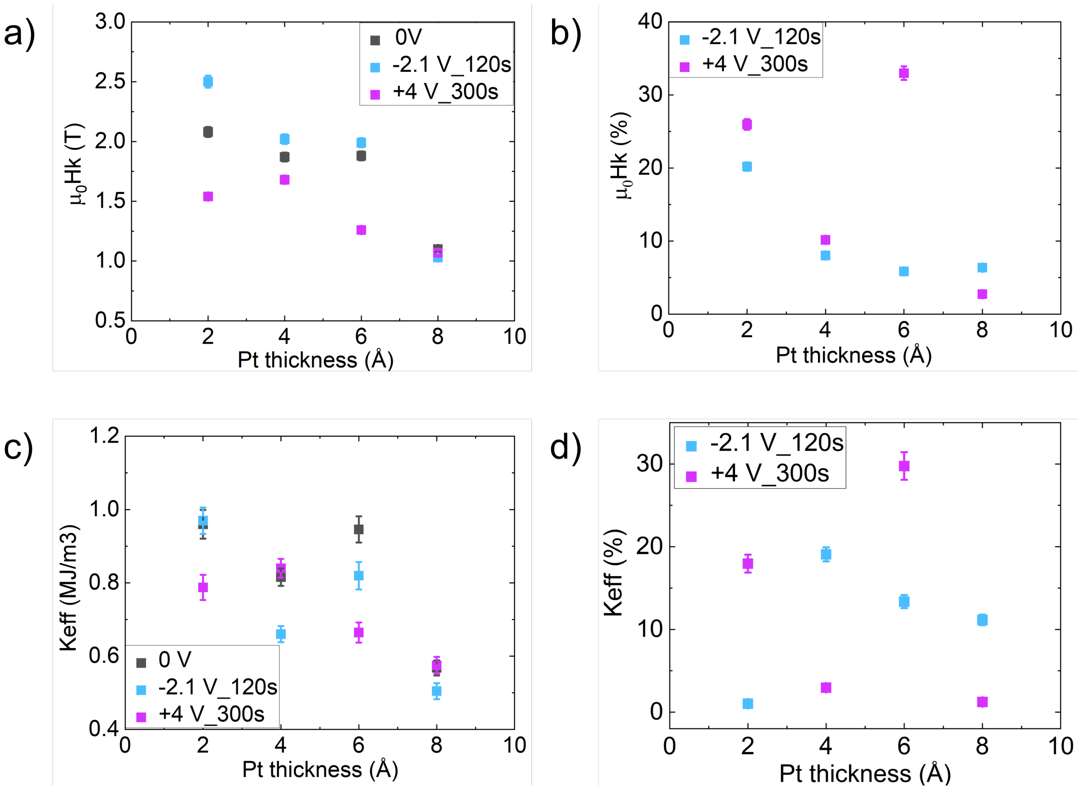

Figure 5.7: Anisotropy field ($\mu_0\mathrm{H_k}$) and effective anisotropy ($\mathrm{K_{eff}}$) as functions of top Pt layer thickness, as an effect of -2.1 V for 120s , and +4 V for 300 s.The anisotropy field shows a trend of decreasing with Pt thickness: (a) $\mu_0\mathrm{H_k}$ and (b) percentage change in $\mu_0\mathrm{H_k}$, where the change is small with increasing Pt thickness, except for the 6 Å Pt layer. The $\mathrm{K_{eff}}$ was calculated using equation 3.7. The scattering in calculated values is due to variations in $\mathrm{M_s}$ values: (c) $\mathrm{K_{eff}}$ and (d) percentage change in $\mathrm{K_{eff}}$.

5.6 Reversibility

We investigated the number of times a sample could be reversed. We repeated the application of positive and negative voltages over a series of cycles to gain an idea of this as a typical measurement for the samples. We selected a Pt thickness of 4 Å which is in the middle of the range. As it has already seen that, in the studied multilayer systems, the negative voltage has a larger effect than the positive voltage. Thus, a positive voltage has been applied to test the reversibility of the effects of applying negative gate voltage. The negative voltage increases and the positive voltage decreases resistivity. Figure 5.8a) illustrates the centre of the M-H loop at the initial position, where an applied -2.1 V for 120s increases the resistance sequentially at each cycle. Similarly, it also changes the shape of the M-H loop in Figure 5.2b). In the case of cycle 1, the system was reversed with an applied +4 V for 60 s, while a longer exposure time was required for the following cycles. At the tenth cycle, +4 V was applied for 35 minutes. Figures 5.8(b) and 5.8(c) show reversibility at 20% nucleation and 80% saturation, respectively. For both cases, the system is almost entirely reversible. However, cycle eight is an exception where a short exposure time results in low reversibility. The reversibility is calculated with the reference of the previous cycle, which can be seen from the position plotted on the right axis of Figure 5.8(b-c). Therefore, after cycle eight the system is again fully reversible.

5.7 Discussion

Recent studies show that E-field moves the mobile oxygen in a magnetic multilayer system [43, 160, 164, 170, 171]. Therefore, we interpret our results as an effect of oxygen migration. The oxygen ions move towards the CoB layer with an applied negative voltage, which changes the oxidation state of the sample. The oxygen species remain at the new position after removing the gate voltage. It is worth mentioning that the PMA is conserved in the sample, although it modifies the domain nucleation and saturation. Manchon et al. (2008) showed that an optimally oxidized magnetic layer promotes PMA. Due to the charge transfer between cobalt and oxygen at the Co/oxide interface, the 3d band of cobalt becomes asymmetric, creating an energy difference between the in-plane and out-of-plane d orbitals.

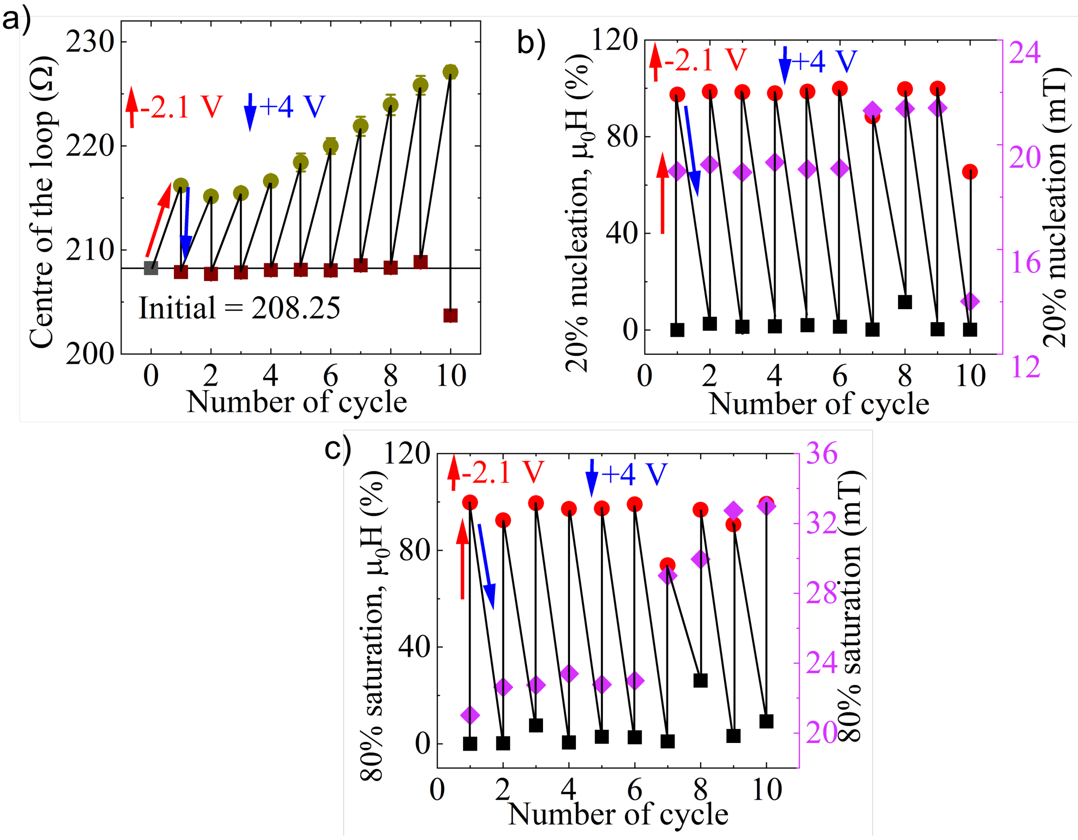

Figure 5.8: Reversibility of the 4 Å Pt top layer as a function of cycle number, where black points indicate the starting position, red points indicate the percentage reversibility, and magenta points indicate the position along the x-axis after reversibility: (a) Center of the loop after applying -2.1 V for 120 s and +4 V for 300 s. The resistivity changes with an applied negative voltage and is fully reversible with a higher positive voltage. (b) Reversibility at 20% nucleation is almost fully reversible. (c) Reversibility at 80% saturation is also almost fully reversible. The field difference in the cases of 20% nucleation and 80% saturation might be due to a slight dislocation of the ITO electrode.

This strong spin splitting mitigates the effect of the low spin-orbit coupling of oxygen atoms, resulting in PMA. However, in our system, due to the presence of heavy metals (HM) on both sides of the ferromagnetic (FM) layer, the spin-orbit coupling (SOC) is stronger at the interface. Consequently, the oxidation alone is insufficient to eliminate the PMA from the bottom Pt/CoB interface (Section 6.3.2 study the oxygen penetration depth) . Contrariwise, with a positive voltage, the oxygen ions travel away from the CoB layer. Besides, due to ex-situ fabrication of the HfO_2 layer, in our structure, the Pt layer might be partially or fully oxidized as soon as it is exposed to the environment; therefore, under a gate voltage, we can remotely control the oxygen species in the Pt layer along with the oxygen species in HfO_2.

We observed that a negative voltage increases the coercive field. Li et al. (2017) [172] studied the Co/SrCoO interface and observed a change in coercive field. They attributed this change to Co-3d and O-2p hybridization. Here, we also observe that the magnetic moment and the anisotropy field are changing significantly [42, 43, 173, 174]. The change in magnetic moment suggests that oxygen ions are forming CoO, which is antiferromagnetic, thereby reducing the moment under negative voltage. Previous studies have also suggested that the bonding of oxygen with Co alters the magnetization [83, 160, 164]. However, there might be two scenarios; firstly, the ions are moving towards the magnetic layer with a negative voltage and changing the interfacial chemistry between the CoB/Ir layers. Hence, the interfacial anisotropy and the Ir polarization are also changing, which results in the modified anisotropy and the magnetic moment. Secondly, the ions migrate up to the magnetic layer, forming a thin CoO layer. It is possible that Boron is also oxidized. However, our measurements are not sensitive to it. In Chapter 6, we present further data on the chemical nature of the changes within Co and CoO. However, we can rule out the bulk oxidization of the magnetic layer, as the effect is observed in a system where the magnetic layer is adjacent to the oxide layer [83, 175]. Moreover, in this case, the system is not fully reversible, whereas our system is almost fully reversible. The reversibility is calculated based on the previous cycle. Following the eighth cycle, the position of 20% nucleation and 80% saturation is higher compared to the previous cycles. The top electrode, connected loosely with silver paste on the top of the ionic liquid. Therefore, the top electrode experienced slight shifts due to vibrations, resulting in minor unchanged areas. This issue could potentially be resolved by restricting the movement of the top electrode.

The total resistance increases gradually at each cycle 5.8(a), which might be due to disorder caused by oxygen migration, leading to increased surface roughness and higher resistivity. A longer exposure with the positive voltage decreases the resistance to around 203 Ohm.

We also observed that the system is not symmetric in gate voltage. It could be due to bonding in Co-O so that reducing the bond takes more energy than oxidising (with a positive voltage). On the other hand, it could be the ionic liquid itself is asymmetric as the positive and negative charged parts of the molecule are different. The changes in reversibility might be down to the cyclability of the ionic liquid, or might be down to progressive changes in the same due to repeated motion of oxygen ions.

5.8 Conclusion

In this chapter, we have presented measurements of magnetic moments, anisotropy fields, and Kerr microscopy images before and after the application of gate voltages. All the results presented here can be explained with a model of oxygen migration. The oxygen ions migration towards or away from the CoB layer under negative or positive voltages respectively alters the oxidation state of the magnetic films, affecting PMA while conserving the magnetic layer's properties. The E-field impacts magnetic moments and anisotropy fields significantly, potentially modifying interfacial chemistry and leading to individual magnetic responses. The reversibility of the technique and adjacent metallic layers offers remote magnetization control. Kerr microscopy images shows that, negative voltages delay domain nucleation and positive voltage promotes domain nucleation, likely due to changes in CoB/Ir interface oxidation states, which also changes the anisotropy and spin-orbit torque. While all the magnetic properties we have measured can be explained by the hypothesis that the oxygen ion bonds with Co to form CoO, fully understanding this requires a direct examination of the chemistry and structural changes at the interface. In the next chapter (Chapter 6), we will focus on this aspect.

CHAPTER 6

Electric Field Induced Structural and Interfacial Modification

6.1 Introduction

Following the argument in the previous chapter, in this chapter the structural and interfacial properties of the thin films studied as a function of magneto ionic modification. In order to understand the changes in material properties with applied voltage the X-ray photo electron spectroscopy (XPS), Scanning transmission electron microscopy (STEM), Energy Discursive X-ray Spectroscopy (EDX) and Electron Energy Loss Spectroscopy (EELS) measurements were carried out. These techniques collectively allow the understanding of elemental composition and their changes due to magneto ionic effect. Additionally, the investigation of interfacial magnetic properties was conducted through the use of the Brillouin light scattering (BLS) technique.

6.2 Sample structures

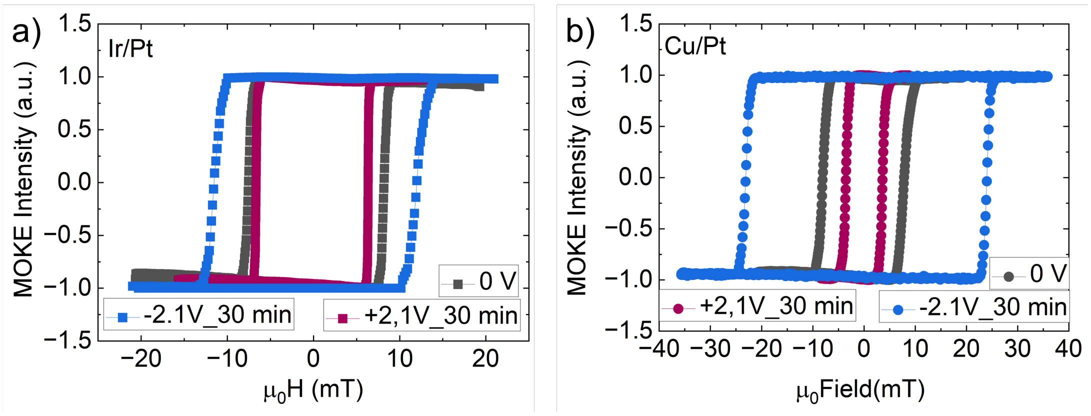

Figure 6.1: Kerr microscope M-H loops of as-grown and voltage-applied samples, where ±2.1 V were applied for 30 minutes. (a) The M-H loops of the Ir/Pt top layer: initial state, with an applied negative voltage, and with an applied positive voltage. The sample shows a similar effect as observed in Chapter 5. (b) The M-H loops of the Cu/Pt top layer: initial state, with an applied negative voltage, and with an applied positive voltage. The effect on the Cu/Pt samples is also the same as for Ir/Pt, though it is more pronounced here.

The metallic multilayers investigated in this chapter are Ta(14 Å)/Pt(23 Å)/CoB(8 Å)/Ir(2 Å)/Pt(6 Å) and Ta(14 Å)/Pt(23 Å)/CoB(8 Å)/Cu(2 Å)/Pt(6 Å). The samples were grown on a Si wafer with 300 nm SiO_x by magnetron sputtering at the University of

Leeds. In order to apply the electric field (E-field), 25 Å of HfO_2 was deposited using the ex-situ Atomic layer deposition (ALD) technique. All as-grown samples exhibit PMA. For the application of the E-field, a commercial ITO glass electrode with 70 nm Indium Tin Oxide (ITO) was connected using an ionic liquid, whereby the film acted as a bottom electrode. In this chapter, voltage and time parameters were chosen to maximize the observable effects during ILG gating. Specifically, a voltage of ±2.1V and a duration of 30 minutes were used to induce the largest possible changes in the sample.

The measurements were conducted using a Kerr microscope in a polar configuration, employing an out-of-plane (OoP) magnetic field. The M-H loops obtained from the Kerr microscope are averages of two to three positions and are presented in Figure 6.1 to Figure 6.3.

Figure 6.1a) shows the effect of applied voltage on Ir/Pt samples. Similar to the previous results (Chapter 5) with applied -2.1 V the coercive field increases and with +2.1 V the coercive field decreases. Figure 6.1b) shows the similar effect for Cu/Pt samples, but it is significantly higher than the Ir/Pt samples. However, both Ir/Pt and Cu/Pt maintain full remanence.

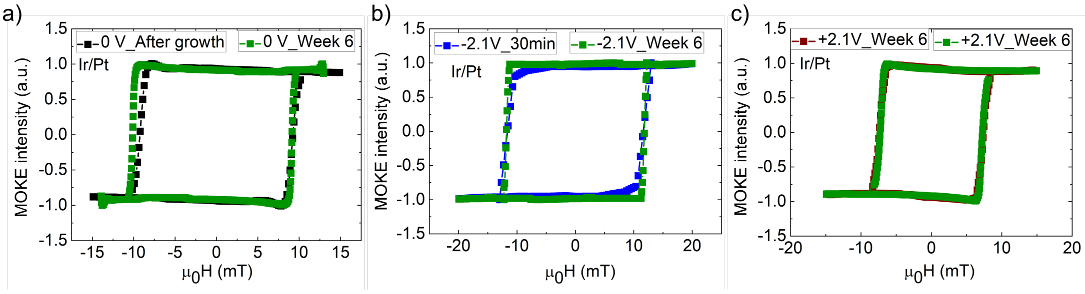

Figure 6.2: Non-volatility check of the Ir/Pt top layer: (a) As-grown sample after deposition, where no change was observed after 6 weeks. (b) -2.1 V for 30 minutes: After applying the voltage, no change was observed after 6 weeks. (c) +2.1 V for 30 minutes: After applying the voltage, no change was observed after 6 weeks. The Ir/Pt samples are very stable and do not change over time.

Figure 6.2 shows the nonvolatility effect of Ir/Pt samples after six weeks and all the samples are non-volatile. Figure 6.3 shows the nonvolatility effect of Cu/Pt samples after six weeks and fifteen weeks. Figure 6.3a) shows the as grown samples measured one week after the deposition and Six week after the first measurement. The image reveals significant changes in remanence during the second measurement of the as-grown samples. The black curve indicates full remanence, signifying magnetization directed out of the plane, while the red curve's remanence decreases by approximately 83%.

Figures 6.3b) and 6.3c) demonstrate the effect of negative and positive voltage, respectively, after applying voltage, at week six, and week fifteen. In the case of a negative voltage the change is smaller compared to the duration of the measurement. However, a significant change is observed with positive voltage, initially reducing the coercive field but later increasing it with time.

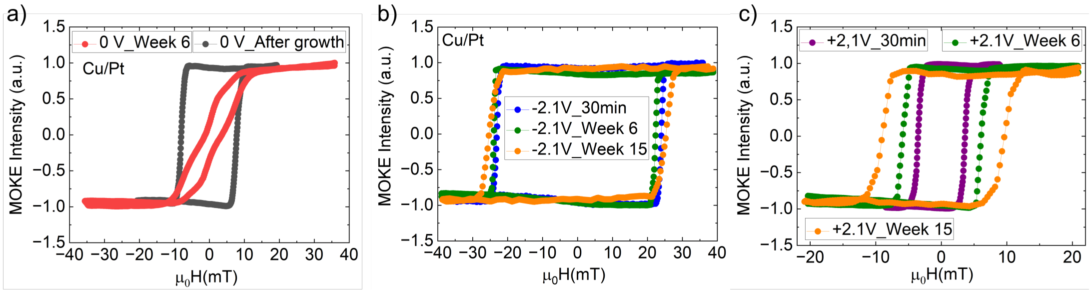

Figure 6.3: Non-volatility check of the Cu/Pt top layer: (a) As-grown sample after deposition, which changed significantly after 6 weeks. (b) -2.1 V for 30 minutes: After applying the voltage, no change or only minor changes were observed after 6 and 15 weeks. (c) +2.1 V for 30 minutes: After applying the voltage, the coercive field increased over time. The positive voltage pulls oxygen from the CoB layer, which may be re-oxidizing over time.

6.3 Structural properties

6.3.1 X-ray photoelectron spectroscopy (XPS)

This section focuses on XPS measurements conducted to understand the observed magnetoionic effect in our samples. XPS is a powerful technique for investigating the elemental composition and chemical states of materials within a surface-sensitive depth. Our XPS measurements reveal that the oxidation of Co is significantly higher in samples subjected to negative gating. This increased oxidation likely plays a crucial role in the magnetoionic effect observed in these samples.

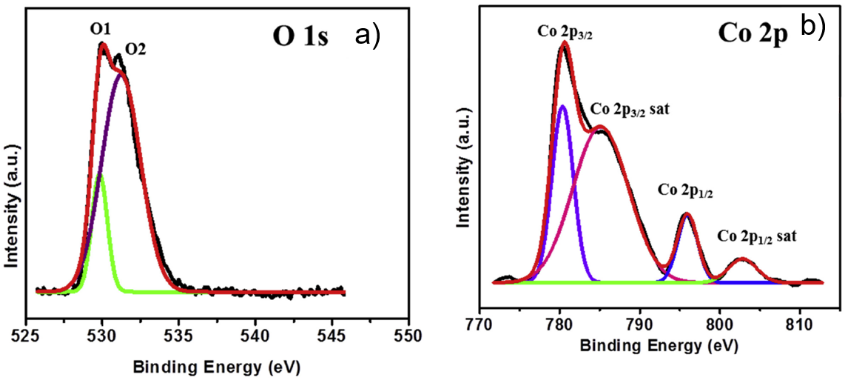

Figure 6.4: An example of XPS measurements. (a) Oxygen spectra displaying the metal oxide bond (Co-O-Fe) at approximately 530.4 eV and oxygen functional groups at around 531.2 eV. (b) The complex $\mathrm{Co}-2\,\mathrm{p}_{3/2}$ peak in $CoFe_2O_4$ attributed to contributions from both Co and CoO [176].

The technique facilitates elemental analysis within the depth range of 35 Å to 40 Å from the surface top. The measurement were conducted with the help of Dr. A. Britton at the University of Leeds. All XPS data presented in this chapter are averages derived from more than twenty scans. An initial scan was perform on the data using the carbon 1s peak, which help to identify the elemental region with background. Only material-specific spectra are shown in this chapter, with a typical dataset illustrating the full spectrum range provided in Section 3.3.3.

The experimental data were analyzed using CasaXPS software, where elemental peaks were fitted and analysed with the help of reference [177–183]. The Co, Pt, Ir and oxygen spectra give a strong indication of surface chemistry and interfacial oxidization. Figure 6.5 shows the oxygen peaks (O 1s) of Ir/Pt (6.5a-c) and Cu/Pt (6.5d-f) samples. All the samples exhibit two separate oxygen peaks. For the as grown samples, two peaks are at the $\approx$ 531.12 eV and $\approx$529.64 eV. Acharya et. al. (2020) [176] studied the CoFeO composition by XPS and founds two peaks at 530.4 eV, considered as metal oxide bond (Co-O-Fe), and at 531.2 eV, considered as oxygen functional group (6.4). Eslam et. al. (2018) [184] studied the CoO with XPS. They identified two peaks as metal oxide at 530 eV and a hydroxyl group at 530.9 eV. Sayeed et. al. [185] studied the $Au/Co(OH)_2$ electrode and observed the splitting of O 1s at 531.3 eV and 529.4 eV.

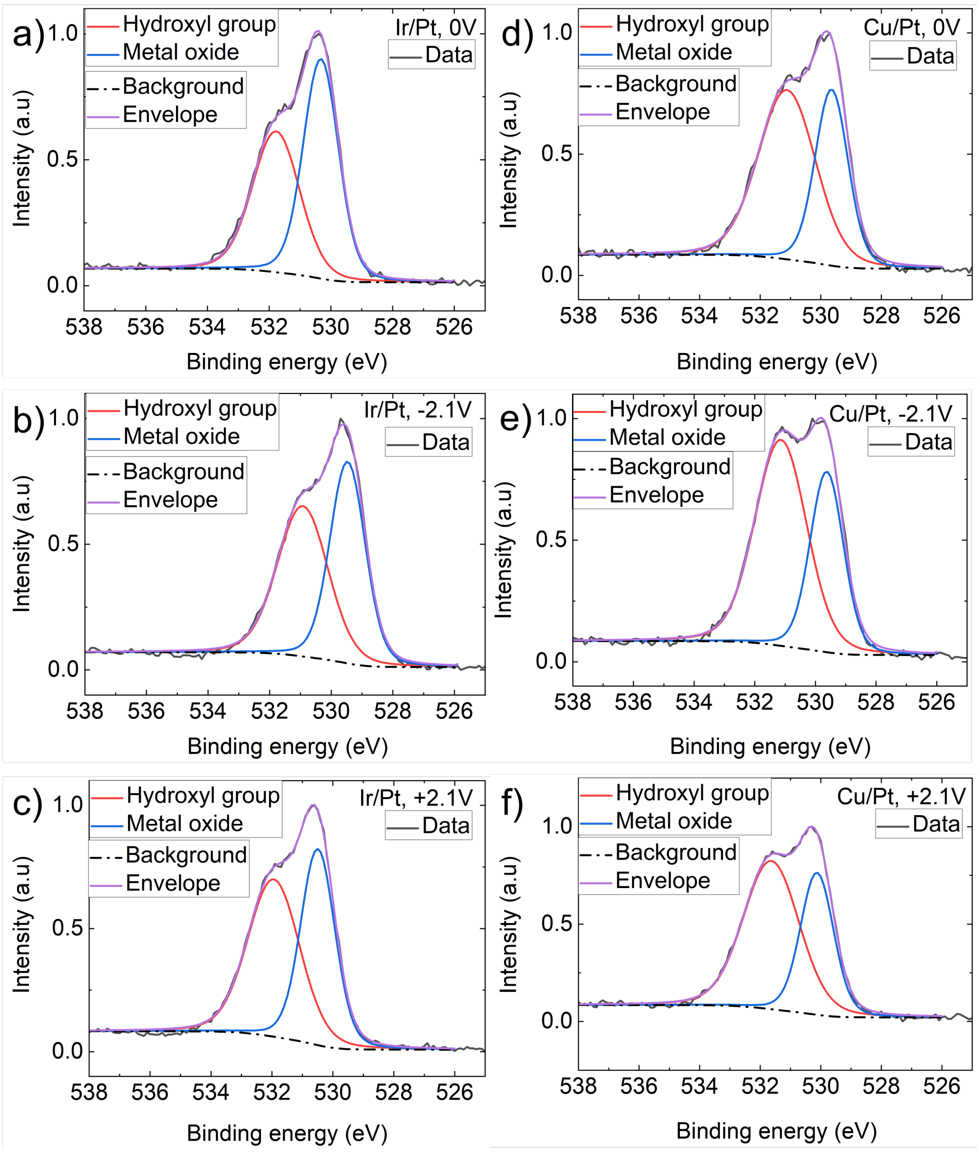

Figure 6.5: XPS spectra at the O 1s edge: (a-c) As-grown and voltage-applied Ir/Pt samples, and (d-f) As-grown and voltage-applied Cu/Pt samples. For both samples (Ir/Pt and Cu/Pt), the oxygen peaks represent a combination of metal oxides and hydroxyl groups, as illustrated in example Figure 6.4.

Following the examples above, we have identified the peak at ≈530 eV as metal oxide such as CoO and oxygen functional group at ≈ 532 eV. For both two samples the O 1s peak experiences a shift towards lower energy, with the shift being higher for the Ir/Pt sample. On the other hand, with positive voltage, it shifts towards the higher energy level. The observed shift in the oxygen peak might be attributed to changes in the chemical environment, specifically indicating that the oxygen is in a reduced state. This suggests the possible formation of CoO, which has a lower binding energy, from the Co2+ or Co3+ states [186–188].

Samples	oxides	0V	-2.1 V	+2.1V
Ir/Pt	Metal oxide	530 eV	529.5 eV	530 eV
	OH group	532 eV	531 eV	532 eV
Cu/Pt	Metal oxide	530 eV	529.5 eV	530 eV
	OH group	532 eV	531 eV	532 eV

Table 6.1: XPS oxygen peaks were assigned using the CasaXPS elemental library.

The splitting of the O 1s peak indicates the presence of oxides associated with the metals. Therefore, the complex Co-2P peak could be attributed to the oxide. Figure 6.6 shows the Co XPS data at 0 V (a and d), -2.1 V (b and e), and +2.1 V (c and f). The Ir/Pt as grown sample (0 V) shows two peak at 778 eV and 781.5 eV. On the other hand, the Cu/Pt as grown sample shows three major peaks at 778 eV, 781 eV, and 785 eV, with an additional small peak at 776 eV.

Grosvenor et al. (2005) [183] studied bonding in binary transition metals, identifying a Co metal peak at 778 eV and two satellite peaks at higher energy levels, which were attributed to interactions between photoelectrons and valence electrons on the surface. Yang et al. (2010) [181] investigated various cobalt compounds using XPS and found that Co oxides exhibit binding energies ranging from 779.9 eV to 790.7 eV. They noted that the proximity of the Co metal peak complicates data fitting.

Zhao et al. (2019) [189] studied electrochemical oxygen evolution in np$-$Ir$_{70}$Ni$_{15}$Co$_{15}$, identifying a Co metal peak at 777.5 eV and oxidized Co peaks at 781.2 eV and 785.5 eV. Feng et al. (2020) examined the effects of Co interface oxidation in Pt/Co/AlO$-$x trilayers. They observed that with decreasing AlO$-$x thickness, a high-energy shoulder at 780.7 eV appeared, indicating partial CoO formation alongside metallic Co.

Zhang et al. (2020) investigated perpendicular magnetic anisotropy (PMA) in SrTiO$_3$/Co/Pt, systems, focusing on oxygen diffusion from a CaTiO$_3$ spacer layer. They found the Co-2p$_{3/2}$ peak at 792.5 eV and the CoO-2p$_{3/2}$ peak at 781.1 eV. Similarly, Gweon et al. (2018) studied MgO dependent PMA in Pt/Co/MgO trilayers and observed that oxygen penetration influenced the PMA, with Co metal and CoO peaks appearing at 778.4 eV and 780.9 eV, respectively.

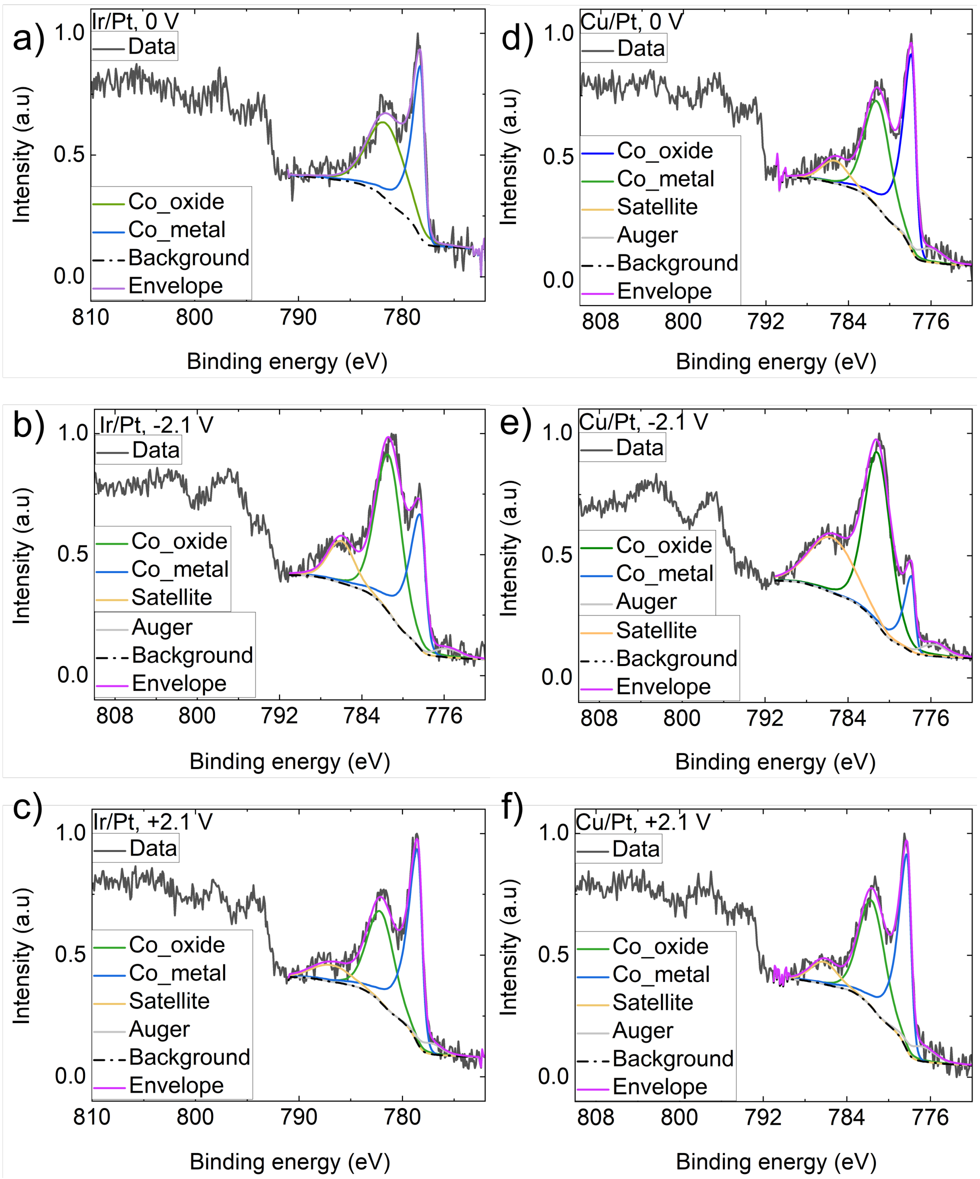

Figure 6.6: XPS spectra at the Cobalt $L_{2,3}$ edge: (a-c) As-grown and voltage-applied Ir/Pt samples, and (d-f) As-grown and voltage-applied Cu/Pt samples. All samples exhibit a complex Co peak, comprising metallic Co and CoO. As-grown and positively gated samples suppress the CoO peak, while negatively gated samples suppress the metallic Co peak.

All these examples illustrate the binding energies of Co and CoO, with the Co peak typically appearing near 778 eV and Co oxides at higher energy levels. The formation of CoO and the associated shift to higher energy levels help to understand the oxidation states and chemical environment of Co. Additionally, the chemical state and thickness of adjacent layers can significantly influence the formation of CoO. The diffusion of oxygen into the Co layer and changes in the chemical state can modify the PMA in multilayer systems. Therefore, after reviewing the above information and consulting the XPS analysis, all these peaks shown in Figure 6.6 were identified using the CasaXPS software elemental library. The peak at 778 eV was identified as the Co metal peak, while the peak at 781 eV was attributed to CoO. The peak at 785 eV was identified as a satellite peak. The small peak at 776 eV, slightly above the background and adjacent to the primary Co peak, has been identified as the Co Auger peak [190, 191]. In XPS, the interaction of X-ray photons with atoms leads to the ejection of electrons from the core levels (e.g., K shell). This ejection creates a vacancy in the core level. Electrons from higher energy levels (e.g., L and M shells) will then fill this vacancy. During this transition, the upper shell electrons release energy, which can excite nearby electrons. Some of these excited electrons may be scattered within the atom. This process can also excite conduction electrons. The excited electrons that are emitted in this process produce peaks known as Auger peaks. Figures 6.6 (b-f) were also analyzed similarly, revealing the presence of the Co oxide peak positioned between the Co metal and the satellite peaks.

Elements	Metal peak	Oxide peak	Satellite peak	Auger peak
Co	778 eV	781 eV	785 eV	776 eV

Table 6.2: Co peaks were assigned using the CasaXPS element library.

Figure 6.7a-c) are showing the Ir as grown, with applied -2.1 V and +2.1 V respectively. Park et. al. (2020) [192] studied the oxygen evolution reaction of IrO_2/Ti electrode under acidic conditions. After analysing XPS spectra they two Major peak as the Ir $4\,f_{5/2}$ at 65.1 eV and the Ir $4\,f_{7/2}$ at 62.1 eV, corresponding Ir^{3+} state. Additionally, Ir $4\,f_{5/2}$ at 66.4 eV and the Ir $4\,f_{7/2}$ at 63.5 eV, corresponding Ir^{4+} state.

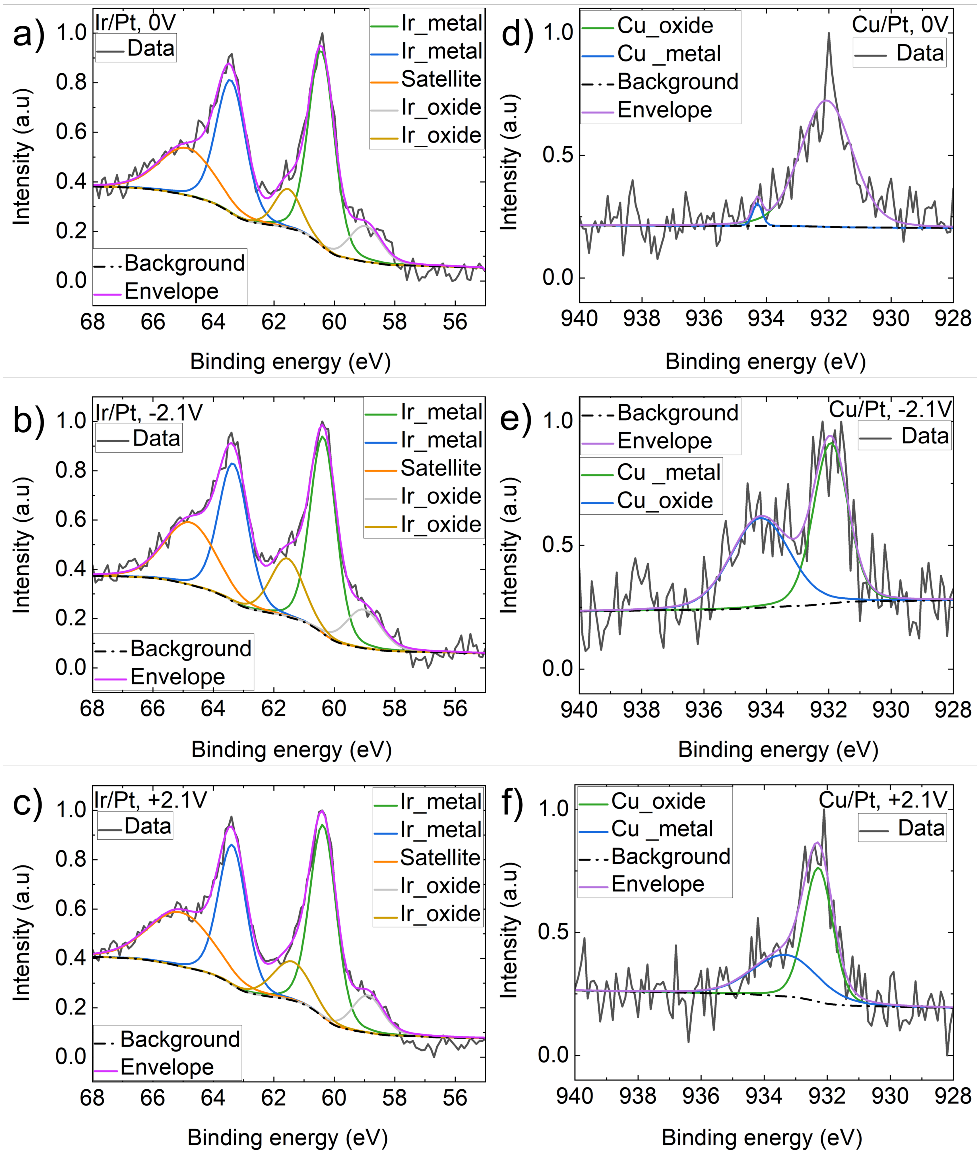

Figure 6.7: XPS spectra of Ir in Ir/Pt and Cu in Cu/Pt samples: (a-c) Effect of applied voltage on Ir/Pt. Only slight or no changes were observed with applied voltages on Ir, indicating that higher energy is required to obtain information for Ir. (d-f) Effect of voltage on Cu/Pt. The negatively gated Cu/Pt sample shows a significant difference in oxidation.

Choe et. al. [193] proposed the IrO_2/Ti as an efficient oxygen electrode at high temperature. They fitted peaks with Gaussian line profile and observed the Ir $4\,f_{5/2}$ and Ir $4\,f_{7/2}$ at the 65.1 eV and 62.2 eV respectively. They considered the Ir^{4+} at the

65.1 eV and 62.1 eV. The Ir XPS spectra on the Figure 6.7a-c) change slightly with appled voltage. The two Major peak are assumed to be Ir $4\,f_{7/2}$ and $4\,f_{5/2}$. The minor peaks at ≈ 58 eV and 61 eV are considered as represents Ir $4\,f_{7/2}$ and $4\,f_{5/2}$ respectively, representing the Ir^{4+} states. The peak at the higher energy level of 65 eV is considered as the satellite peak.

Elements	Metal peak	Oxide peak	Satellite peak	Auger peak
Ir	60 eV and 63 eV	58 eV and 61 eV	65 eV	-

Table 6.3: Ir praks were assigned using the CasaXPS

Figure 6.7d-f) shows the Cu XPS measurement of as grown sample (d), with applied -2.1 V (e) and with +2.1 V (f). Using the CasaXPS elemental library, two peaks were assigned at ≈ 932 eV and ≈ 934 eV. Kazak et. al. [194] synthesise of copper oxide/carbon nanocomposite and mentioned that the $Cu^{-}2\,p_{3/2}$ peak at 932.2 to 932.8 eV due to Cu_2O and 933.5 to 934.0 eV due to CuO. Sljukic et. al. [195] shows the $Cu^{-}2\,p_{3/2}$ peak at 933.8 eV for CoO/graphite composite. Ivanova et. al. (2020) [196] showed two peaks at 934.3 eV and 932.6 eV for Cu^{+2} ($Cu^{-}2\,p_{1/2}$) and Cu^{+1} ($Cu^{-}2\,p_{3/2}$) respectively.

Elements	Metal peak	Oxide peak	Satellite peak	Auger peak
Cu	332 eV	334eV	-	-

Table 6.4: Cu were assigned using the CasaXPS element library.

Figure 6.8 shows the Pt 4f XPS spectra of Ir (a-c) and Cu (d-f) samples at 0 V(a,d), -2.1 V(b, e), and +2.1 V(c, f). Using the CasaXPS elemental library four peaks were assigned at ≈ 71.2 eV, ≈ 74.5 eV, ≈ 72.2 eV, and ≈ 75.5 eV. Sofa et. al. (2019) [197] studied the Pt nanotube. They deconvoluted and fitted two Pt peaks for $Pt-4\,f_{7/2}$ and $Pt-4\,f_{5/2}$. They claimed metallic Pt (Pt 0) and Pt^{+2} peaks at the 70.9 eV and 72.6 eV respectively. However, Sen et. al. (2007) [198] found the Pt(0) at 71.2 eV and 74.3 eV, and the Pt(OH) at 72.2 eV and 75.5 eV.

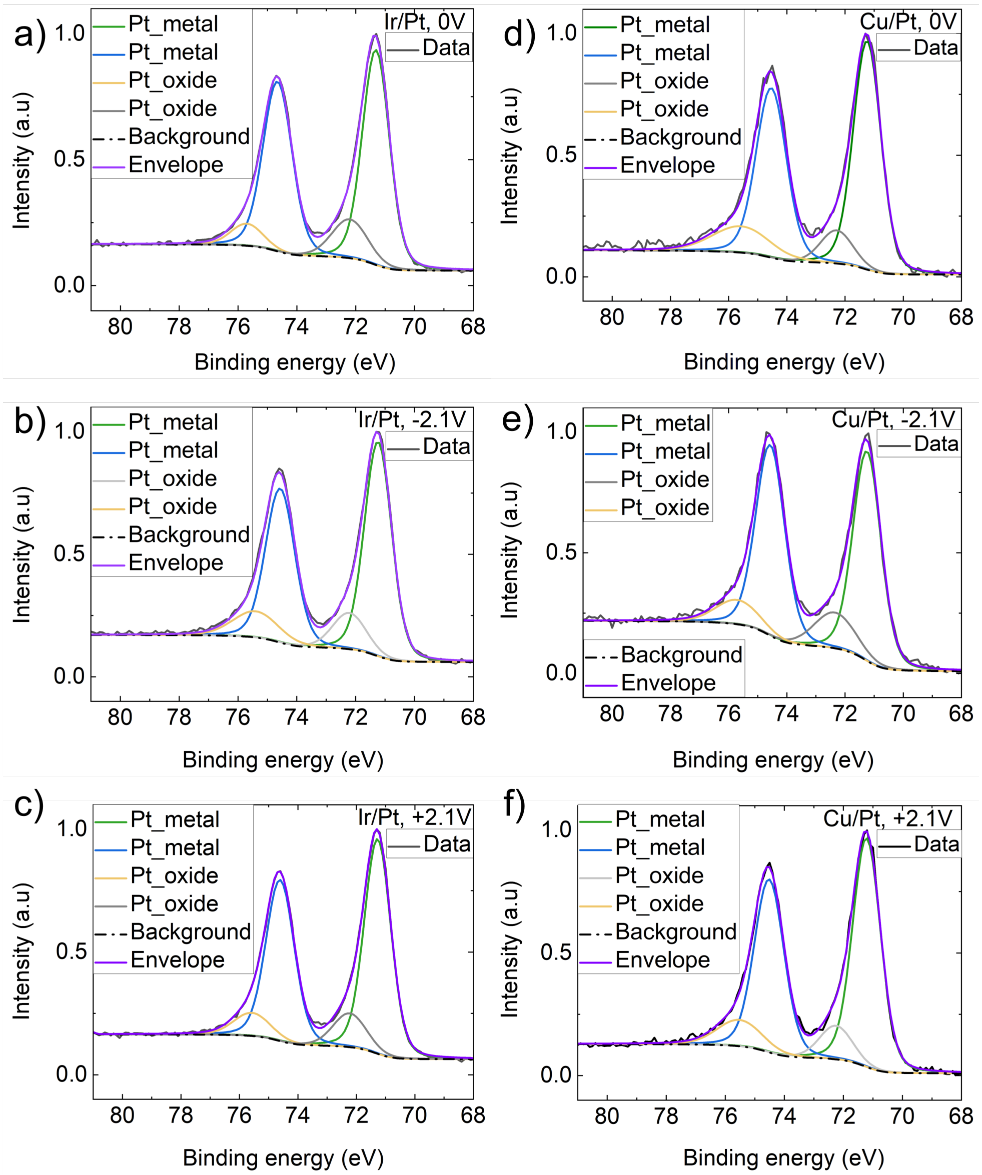

Figure 6.8: XPS spectra of Pt 4f: (a-c) Samples with Ir/Pt, and (d-f) Samples with Cu/Pt. For both samples, little or no change was observed in Pt with applied voltages, indicating that higher energy is also required to obtain information for Pt, as shown in the XAS of Pt (Figure 6.18).

In summary, the XPS spectra of Co, Pt, Ir, Cu, and oxygen provide strong indications of surface chemistry and interfacial oxidation. All the samples exhibit two separate oxygen peaks. The O 1s peak experiences a shift towards lower energy, with the shift being higher for the Ir/Pt sample. The splitting of the O 1s peak indicates the presence of oxides associated with the metal interfaces. Therefore, the complex Co 2P peak could be attributed to the oxide. The peak at 778 eV is designated as the Co metal peak, while the peak at 781 eV is attributed to CoO. All assigned peak are listed in the Table 6.5 below,

Elements	Metal peak	Oxide peak	Satellite peak	Auger peak
Co	778 eV	781 eV	785 eV	776 eV
Ir	60 eV and 63 eV	58 eV and 61 eV	65 eV	-
Cu	332 eV	334eV	-	-
Pt	71 eV and 74.5 eV	72 eV and 75.5 eV	-	-

Table 6.5: All elements were assigned using the CasaXPS element library, with additional reference to sources [178 to 200]. The magnitude of the residual standard deviation ranged from 0.77 to 0.96.

6.3.2 Atomic level investigation of oxygen migration

The scanning transmission electron microscopy (STEM) scan was performed to investigate the effect of applied voltage at the interface of the magnetic systems. The STEM samples were prepared by J. Harrington, while the data acquisition was carried out by Dr. Z. Aslam at the Leeds Electron Microscopy and Spectroscopy Centre (LEMAS), university of Leeds.

Figure 6.9 shows the high-angle annular dark-field (HAADF) imaging and energy dispersive x-ray spectroscopy (EDX) elemental mapping. All the indicated elements are present in the samples. Due to limited resolution, the interface is not visible at the HAADF image. For the as grown samples, the Ir/Pt was deposited as a STEM capping layer 3.4. Thus, The Pt and the Ir is showing double layers. The composition profile of elements are showing in the Figure 6.10a). In Figure 6.10b) is the combination of Co and Oxygen are shown. The Ir, Co, and Pt peaks are located between ≈ 15 nm and 18 nm, and they are distinct/separated. Therefore, from all these figures it is a evident that the Co is not diffusing with the top (Ir) and bottom (Pt) layers.

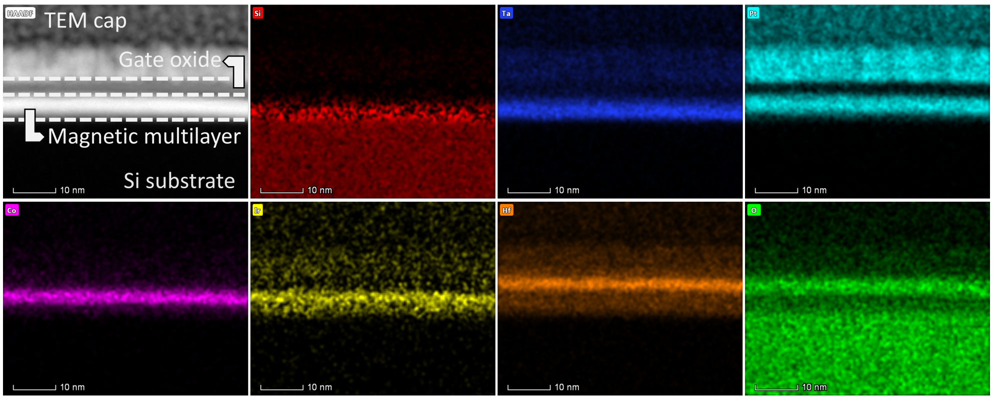

Figure 6.9: EDX mapping was performed on the as-grown samples The bright most region in the middle is the magnetic multilayer, the gray region on top of the magnetic layer is the HfO_2, dotted lines were added as a guide for the eye. All the elements in the sample can be distinguished separately. The red color represents the Si substrate, while blue indicates Ta. The light blue color shows Pt layers, with the double layer in Pt attributed to the re-sputtered TEM capping layer applied before sample preparation. Magenta corresponds to the Co layer, yellow represents Ir, and orange indicates Hf. The double layer in oxygen (green) is due to the presence of SiO_2 and HfO_2. The elements are presented individually due to noise caused by the limited resolution of the TEM system.

The minimum in the oxygen peak at the Co peak suggests that the Co layer either lacks oxygen or contains less oxygen compared to the surrounding layers. The Pt layer exhibits a double peak near the Co peak, and the oxygen contacts the Pt layer, suggesting the presence of oxygen in the Pt cap layer. The Co peak is around 1 nm, which might be accurate, but it broadens with a shoulder-type behavior over 2 nm. The Hf central peak is approximately correct, at around 3 nm, but it has a background on both sides. The Ir shows a small peak just before the Co peak. We know that the Si substrate should be the sharpest due to its smoothness, but it decays over 5 nm. STEM EDX mapping confirms the expected layer structure of the sample. The analysis verifies that the layers are well-defined and consistent with the anticipated design and the XPS data.

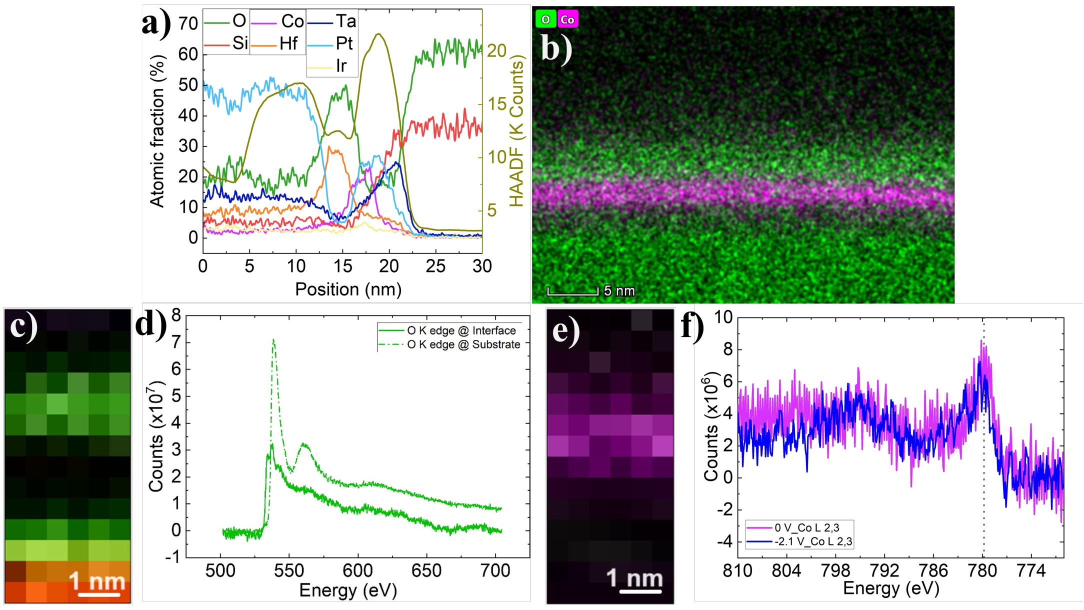

Figure 6.10: (a) EDX mapping of the as-grown sample. Different elements of the film are shown with color coding similar to the previous image. (b) EDX elemental mapping of Co and oxygen, showing high noise and difficulty in distinguishing other elements in a single image. (c-d) O-K EELS spectra at HfO_2 and the substrate, indicating that no oxygen can be detected within the metallic multilayer. (e-f) Co-$L_{2,3}$ EELS spectrum at the CoB layer, where (f) shows the as-grown sample and at -2.1 V. The Co spectra show no difference between the two conditions.

To obtain the EELS spectrum, we did perform a pixel-by-pixel scan across the cross-section, starting from the HfO_2 overlayer to the SiO_2 substrate layer. The O-K absorption edge EELS spectra in Figure 6.10c-d) hint at different spectral fingerprints as expected. The solid line is representing the top oxide layer or gate oxide, where the dotted line is presenting the substrate oxide (SiO_2). However, the Co-L EELS data shown in Figure 6.10e-f) were not well resolved because the instrumental resolution is insufficient to probe the CoB layer to a sub-nanometer thickness ($\approx$ 0.8 nm). Two bright color bands in Figure 6.10e represent the Co layer. Away from these bright bands, some pixels show intensity due to electrical noise. Figure 6.10f displays the $CoL_{2,3}$ edge spectra for both the as-grown (magenta) and the -2.1 V gated samples.

When investigating the oxygen distribution within the film, the limitations of the system become apparent. Although it is evident that oxygen does not penetrate completely through the film, the technique lacks the spatial resolution required to distinguish between the gated and ungated regions. This constraint prevents accurate quantification of the oxygen incorporated during the gating process. Consequently, it can be seen that gating does not move of oxygen throughout the entire film, or it does not lead to the saturation of the sample with oxygen.

To fully understand how oxygen moves under gating, sub-nanometer level resolution is essential. This high-resolution requirement sets a limit on the length scale that must be achieved for precise analysis. To overcome these limitations and obtain a more detailed understanding of oxygen dynamics, an electron microscopy-based technique with better than one nanometer resolution is necessary. Utilizing such advanced techniques would require access to more sophisticated facilities, such as SuperSTEM, which offer the enhanced resolution and capabilities needed to thoroughly investigate the oxygen distribution and behavior during gating.

6.4 Magnetic properties

6.4.1 Saturation magnetization and effective anisotropy

In order to estimate the saturation magnetization (M_s) of the CoB, a series of Ta(1.4 nm)/Pt(2.3 nm)/CoB(X nm)/Ir(0.2 nm)/Pt(0.6 nm) layers was grown, where X = 0.5, 1.2, 1.5, 1.8, 2.0, 2.2, 2.4, and 2.8 nm. There for here these samples information is used to determine the the room temperature magnetization of CoB using SQUID VSM. Figure 6.11a) shows the moment per cm^2 as a function of CoB thickness. To determine the saturation magnetization (M_s), the data was fitted with a straight line. The gradient of the fitted line yielded an M_s value of 750 +/- 20 emu/cc with the Boron concentration of 32 %.

The M_s depends on the CoB concentration, they also can be influenced on how the proximity of the Pt is treated. This is significant when the layer thickness is very thin (below 1 nm). In our research group, Satchell et al. (2021) [199] calculated the M_s as 760 +/- 90 emu/cc for CoB/Pt from the y-axis intercept, where the Boron concentration was 32 %. They observed a down-turned trend in M_s from a CoB thickness of 0.6 nm. Darwin et. al. (2023) [88] values between 300 emu/cc and 330 emu/cc for CoB/HM (such as CoB/Pt, CoB/Ir, and CoB/Ta) interfaces, with a boron concentration of 48%. This is significant when the layer thickness is very thin (below 1 nm).

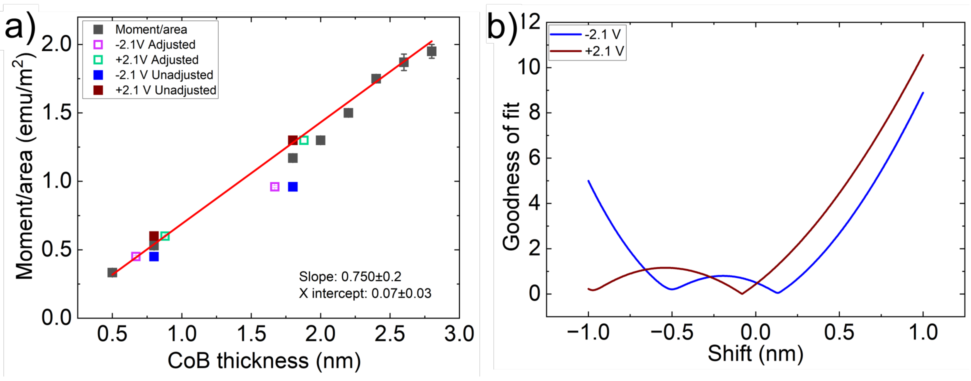

Figure 6.11: (a) The M_s values of the as-grown and gated samples (unadjusted M_s) are shown. The gated M_s values are aligned with the straight line fit, with the shift from the original positions calculated using the toy model described in Equation 6.1. (b) The goodness of fit using the toy model is evaluated by comparing the adjusted gated data points to the original linear fit of the as-grown samples.

In our research group, Satchell et al. (2021) [199] calculated the M_s as 760 +/- 90 emu/cc for CoB/Pt from the y-axis intercept, where the Boron concentration was 32 %. They observed a down-turned trend in M_s from a CoB thickness of 0.6 nm. Darwin et. al. (2023) [88] CoB/HM (such as CoB/Pt, CoB/Ir, and CoB/Ta) interfaces reporting the M_s between 300 emu/cc and 330 emu/cc for 48% boron concentration. Dusas group studied the temperature dependent magnetization of amorphous CoB with 20-30% of Boron. They claimed that the magnetization of CoB depends on the Boron concentration and found the M_s between 0.917 T to 3.353 T (917 A/m - 3353 A/m) at 0 K [153]. Lavrijsen et. al. [200] also presented the M_s of different Boron concentration for Pt/CoB/Pt films and measuring between 1030 kA/M to 1420 kA/M (1030 emu/cc - 1420 emu/cc). The straight-line method we used to calculate M_s assumes that the fit goes through the origin, implying the absence of any dead layer within the system. However, the figure illustrates that the straight line does not intersect the zero on the y-axis; instead, it extends beyond zero. Consequently, the sample exhibits a magnetic dead layer, with a calculated thickness of 0.7 ÅṖrevious literature has also mentioned the presence of a dead layer at the FM/HM interfaces. Tan et. al. (2021) [201] reported M_s of 0.8 MA/m to 1.2 MA/m (800 emu/cc - 1200 emu/cc) for the CoB/HM (20 % Boron) interfaces with dead layer of 4 Å to 6 Å.

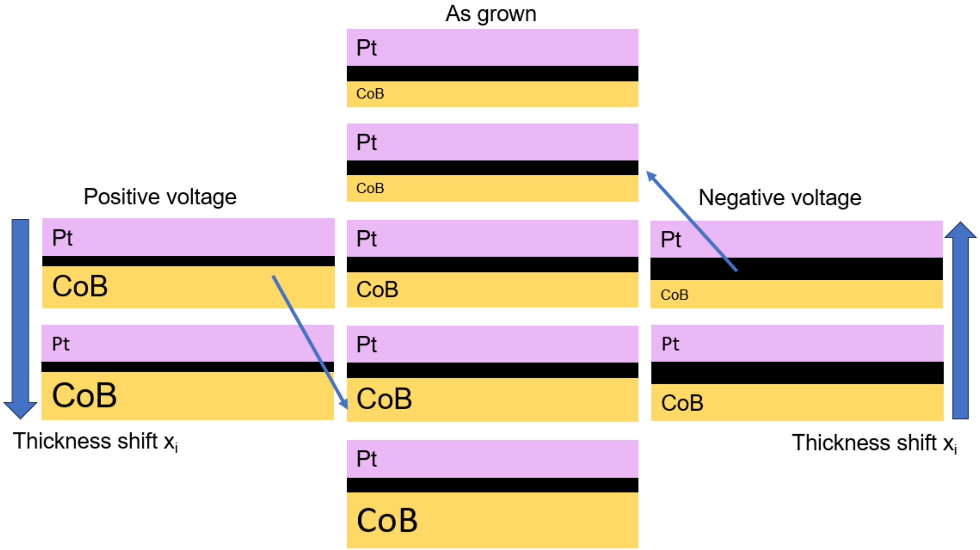

Figure 6.12: The slab model assumed that negative voltage is decreasing the CoB thickness and increasing the CoO thickness. Nevertheless the positive voltage increases the CoB thickness and decreases the CoO thickness.

One might expect the dead layer thickness different in the two gated samples. However, we do not have sufficient data across the full range of thicknesses to achieve statistically significant independent fittings. To work around this we used a toy model (Equation 6.1) where the samples have a slab of 'bulk like' CoB and a slab of oxidized CoB with effectively no moment. Figure 6.12 illustrates the model's assumptions.

Magnetometry measurements do not provide direct evidence of CoO formation. However, XPS (Section 6.3) and XAS (Section 6.4.3) are capable of identifying CoO. It is important to note that all these experiments were conducted at room temperature. Despite this, XPS and XAS do not offer insights into the energy scale associated with oxidation or reduction processes. Literature indicates that ionic liquid gating exhibits temperature dependence, with an increase in electrochemical reactions at higher temperatures [202]. However, distinguishing between ion migration and chemical reactions in such experiments remains challenging.

In the slab model, we assumed that negative voltage increases the CoO content by oxidizing the Co layer, while a positive voltage extracts oxygen from CoO, thereby increasing the metallic Co layer. Consequently, a positive voltage enhances the total magnetic moment, whereas a negative voltage diminishes it. We then displace the points corresponding to the gated samples sideways, calculating a goodness of fit of both the as-grown and shifted gated samples to the original linear fit of the as-grown samples. In this way we estimate what change in oxidised CoB slab thickness would be necessary to make the gated sample points fit the as-grown trend (figure 6.11(b)). Within the limits of this model, this suggest that the negative gated sample has a thicker dead layer 0f 0.88 Å and the positive gated sample has a thinner dead layer of 0.62 Å compared to the as-grown sample.

$$\mathrm{F(shift)} = [(\frac{\mathrm{m_0 - m_i}}{\mathrm{m_0}})^2 + (\frac{\mathrm{x_0 - x_i}}{\mathrm{x_0}})^2]^{1/2} \tag{6.1}$$

Where $\mathrm{m_i}$ is the shifted slope, $\mathrm{m_0}$ is the original slope, $\mathrm{x_0}$ is the original thickness and $\mathrm{x_i}$ is the shifted thickness. The model gives us a 0.8 Å shift for the positive voltage and 1.3 Å for the negative voltage.

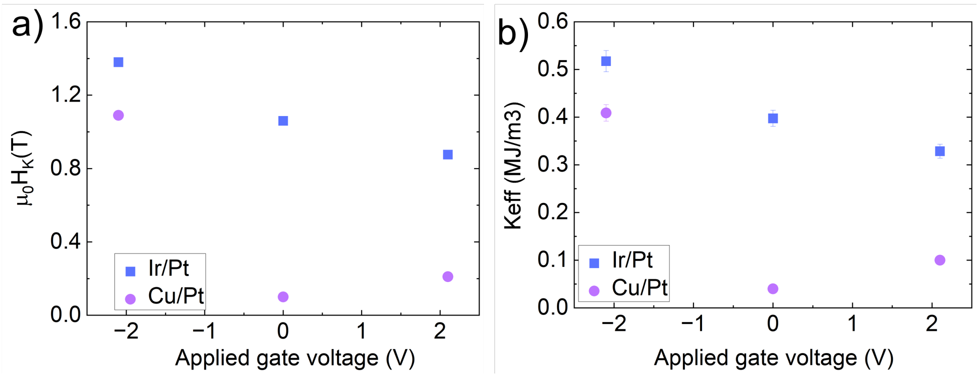

Figure 6.13: $\mathrm{H_K}$ and $\mathrm{K_{eff}}$ of Ir/Pt and Cu/Pt samples: (a) $\mathrm{H_K}$, b) $\mathrm{K_{eff}}$. As observed in Chapter 5, the application of a negative voltage increases both the anisotropy field and and the effective anisotropy constant, whereas the application of a positive voltage results in a decrease in these parameters. However, Cu/Pt under +2.1 V is an exception.

Figure 6.13 shows the anisotropy field ($\mu_0\mathrm{H_k}$) as a function of applied voltage and calculated effective anisotropy ($\mathrm{K_{eff}}$). $\mu_0\mathrm{H_k}$ is measured using AHE techniques by rotating samples (±180°) in a constant applied field of more than half a Tesla (in this case, an arbitrary 518 mT). The resulting Hall voltage is recorded as a function of angle. The parabolic part of the data is fitted with parabola function, gives the anisotropy field [89, 151]. The obtained $\mu_0\mathrm{H_k}$ is then used to calculate the effective anisotropy constant using Equation 3.7. From the figure, the Ir/Pt samples arepossessing significantly higher effective anisotropy than the Cu/Pt samples. The negative voltage increases the effective anisotropy for both Ir/Pt and Cu/Pt samples, while the positive voltage decreases it for Ir/Pt sample, but increases it for Cu/Pt. However, the transition from the as-grown sample to the negatively gated sample is higher for the Cu/Pt samples, while the shift from the as-grown to the positively gated sample is slightly low for the Ir/Pt samples. It is noteworthy that the anisotropy of the as-grown Cu/Pt sample is lower than that observed under positive voltage conditions. Table 6.6 shows the calculated μ_0H$_k$ and K$_{eff}$,

Samples	Gate Voltage (V)	μ_0H$_k$(T)	K$_{eff}$ MJJ/m^3	M$_s$(emu/cc)
Ir/Pt	0 V	1.06±0.01	0.40±0.02	750
	-2.1 V	1.38±0.01	0.52±0.02	
	+2.1 V	0.88±0.01	0.33±0.01	
Cu/Pt	0 V	0.10±0.01	0.04±0.01	
	-2.1 V	1.09±0.01	0.41±0.02	
	+2.1 V	0.21±0.01	0.0.08±0.01	

Table 6.6: Calculated μ_0H$_k$ and K$_{eff}$ using a M$_s$=750emu/cc for Ir/Pt and Cu/Pt samples.

6.4.2 Interfacial magnetic properties

The bubble expansion techniques works by utilizing the bubble domain wall velocity created using the OoP and In-P magnetic fields, which is than use to calculate the Dzyaloshinskii-Moriya interaction (DMI). In the studied systems, it was challenging to nucleate isolated bubble and control the domain wall velocity. Therefore, in addition to the bubble expansion technique, BLS technique is employed to study the DMI. The measurements and calculations were conducted during a secondment in LSPM (Process and Material Sciences Laboratory) under supervision of Professor M. Belmeguenai.

The BLS technique exploits the non-reciprocal propagation of spin waves (SWs) induced by DMI in magnetic films. Consequently, the DMI can be calculated from the averaged frequency mismatch, ΔF, between the Stokes and anti-Stokes frequency peaks obtained from the measurements. In Figure 6.14a), examples of BLS data for Cu/Pt samples are presented, where the frequency difference is indicated by red dotted lines. The measurement for DMI is only taken to the highest wave vector $\mathrm{K_{sw}} = 20.45\ \mu\mathrm{m}^{-1}$, which corresponds to the incident angle of 60° for positive and negative magnetic field (field applied along hard axis, Section 3.8). The effective DMI is calculated using the equation 3.8, which is shown in the Figure 6.14b). Figure 6.14 shows that the Ir/Pt samples are showing the positive DMI and the Cu/Pt samples are showing negative DMI. Cu/Pt samples arepossessing higher DMI than that of Ir/Pt samples. With applied negative voltage the DMI of Cu/pt sample decreasing significantly, while with positive voltage it the DMI is the same. With applied voltages the Ir/Pt samples are showing higher DMI than as grown sample. The surface constant ($\mathrm{D_s}$) can be calculated from effective DMI, where $\mathrm{D_s} = \mathrm{DMI_{eff}}/\mathrm{t_{CoB}}$, which is shown on 6.14c). The $\mathrm{D_s}$ shows the similar trend as effective DMI.

Figure 6.14d) shows the effective magnetization calculated from Equation 3.8.The effective magnetization is negative and higher for the Ir/Pt samples compared to the Cu/Pt sample. This difference may arise from the strong spin-orbit coupling at the heavy metal interfaces in the Ir/Pt samples, whereas in the Cu/Pt samples, it originates only from the bottom interface. The applied negative voltage decreases the effective magnetization, where changes it significantly for the Cu samples. Similarly, the positive voltage is also decreasing the effective magnetization.

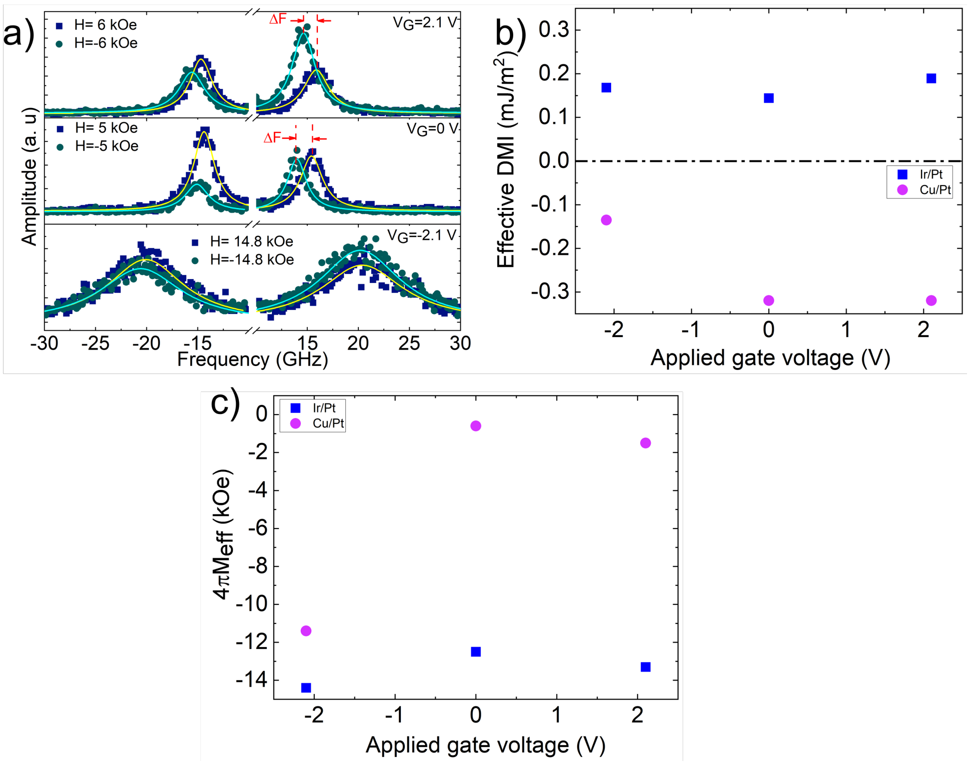

Figure 6.14: (a) The averaged frequency difference between the Stokes and anti-Stokes peaks is used to calculate the DMI. (b) The effective DMI significantly changes with the application of a negative voltage. (c) The effective magnetization, $4\pi M_{\text{eff}}$, where the negative sign indicates high interfacial anisotropy.

6.4.3 X-ray absorption spectroscopy (XAS) and X-ray magnetic circular dichroism (XMCD) measurements

This section presents a material-specific comprehensive study of magneto ionic effect on Pt and Co is performed using XAS and XMCD measurements. The data were acquired by Dr. H.B. Vasili at the BOREAS beamline of the ALBA synchrotron in Spain, and all analyses were conducted with his assistance.

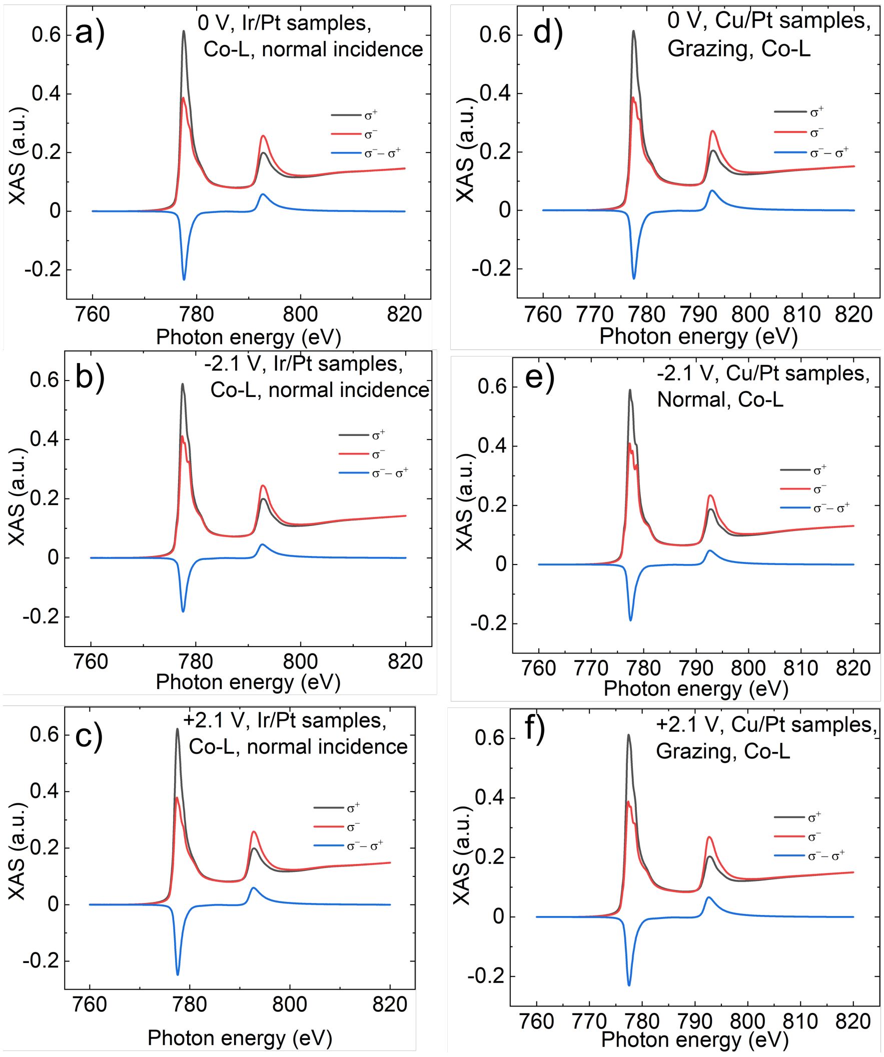

Figure 6.15: XAS spectra in the vicinity of the Co$-$L$_{2,3}$ absorption edges. Data were taken with left and right circularly polarized light. The data has two characteristics peaks from Co$-2\,$p$_{3/2}$ and Co$-2\,$p$_{1/2}$. The difference due to the left and right circularly polarized photon is shown by the blue line. Ir/Pt samples at normal incident: (a) 0 V, (b) -2.1 V, (c) +2.1 V. And at grazing incident: (d) 0 V, (e) -2.1 V, (f) +2.1 V

X-ray photon was generated using an Apple-II-type undulator, with 70% circularly polarized light employed for measurements in reflection geometry. The samples were saturated with an applied magnetic field of approximately 60 kOe. X-ray beams with energy similar to the Co Co$L_{2,3}$ absorption edge and Pt M absorption edge, including pre-edge and post-edge intensity, were used for the measurements. Figure 6.15 displays the XAS measurement of Ir/Pt and Cu/Pt samples at normal incident conditions, The black curve represents the right circularly polarized beam, the red curve represents the left circularly polarized beam, and the difference is indicated by the blue line. Both sets of data show two major peaks around 777.5 eV and 793 eV. In the Ir/Pt samples, a shoulder is observed at around 778.5 eV, the negative applied voltage sample showing a more prominent shoulder compared to the positive and as-grown samples. For the Cu/Pt samples, the shoulder is more pronounced than in the Ir/Pt samples. Additionally, the Cu/Pt samples with negative voltage display an additional shoulder between 777.5 eV and 778.5 eV.

Samples	Gate voltage (V)	Co-L_3 (eV)	Shoulder (eV)	Comments
Reference sample	0 V	$\approx$ 777.5	none	Metallic Co
Ir/Pt	0 V	$\approx$ 777.5	$\approx$776	CoOformation
	-2.1 V	$\approx$ 777.5	$\approx$776	CoOformation
	+2.1 V	$\approx$ 777.5	$\approx$776	CoOformation
Cu/Pt	0 V	$\approx$ 777.5	$\approx$776	CoOformation
	-2.1 V	$\approx$ 777.5	$\approx$776	CoOformation
	+2.1 V	$\approx$ 777.5	$\approx$776	CoOformation

Table 6.7: XAS Peak Analysis of Ir/Pt, Cu/Pt, and Reference Samples.

Figure 6.16 presents the XAS spectra of Ir/Pt samples (a,b) and the Cu/Pt samples (c,d), with insets are showing the Co metallic edge. Initially, discerning changes with applied voltage is challenging. However, upon magnification near 776 eV, differences become apparent between the as-grown, negative voltage, and positive voltage samples. All Ir/Pt and Cu/Pt samples exhibit a pre-shoulder behavior in this region, more pronounced in the Cu/Pt samples. For both types of samples the negative voltage is increasing the shoulder compared to the as grown samples. Negative voltage increases the shoulder for both sample types.

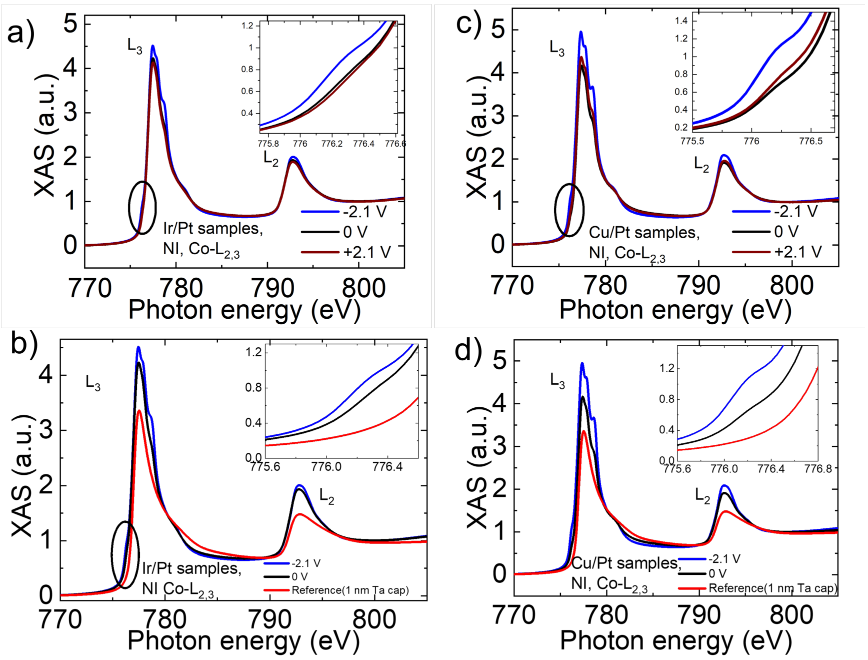

Figure 6.16: XAS spectra of (a,b) Ir/Pt and (c,d) Cu/Pt samples show a negative voltage increasing the Co pre-peak (inset), indicating CoO formation is high. A reference sample Ta(14 Å)/Pt(23 Å)/CoB(8 Å)/Ir(2 Å)/Pt(6 Å)/Ta(10 Å). The Ta cap protects the sample from oxidation, indicating that the as-grown samples underwent oxidation between two growth.

Under a positive voltage the Ir/Pt sample decreases the shoulder, while for Cu/Pt samples, it has the opposite effect. In the Figure 6.16 b,d), a sample with a Ta cap is used as a reference, with Ta helping to protect the sample from oxidation. The reference spectrum shows a smooth edge compared to the as-grown samples. Hence, it is evident that the as-grown samples deviate significantly from this reference.

Figure 6.17 illustrates the XMCD spectra of Ir/Pt samples (a) and the Cu/Pt samples (b) at normal incident conditions. Both types of samples exhibit two major peak at around 777.5 eV and 793 eV. For Ir/Pt samples, the peak decreases with applied negative voltage and increases with positive voltage compared to the as-grown samples. On the other hand, Cu/Pt samples show a decrease in peak intensity for both negative and positive voltages compared to the as-grown samples.

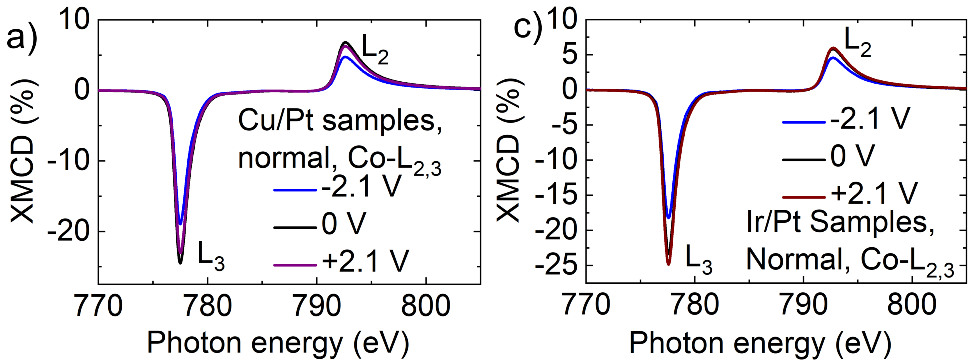

Figure 6.17: XMCD spectra of (a) Ir/Pt and (b) Cu/Pt. Both samples (Ir/Pt and Cu/Pt) show low dichroism under negative voltage. However, under positive voltage, the Cu/Pt sample exhibits lower dichroism compared to the as-grown sample, possibly due to re-oxidation.

Figure 6.18(a,b) presents the hysteresis loop of Ir/Pt, as grown and with -2.1 V samples, under normal and grazing incident conditions. The coercive field of the negative voltage sample is significantly increased compared to the as-grown sample. In Figure 6.18c,d), the magnetic moment of Ir/Pt and Cu/Pt samples, respectively, is displayed under normal and grazing incident conditions. All samples exhibit a higher moment under normal incident conditions. Cu/Pt samples have at least 10% higher magnetic moment than Ir/Pt samples. For Ir/Pt samples, the moment decreases significantly with negative voltage and increases significantly with positive voltage. Conversely, for Cu/Pt samples, positive voltage also decreases the magnetic moment. However, at grazing incident conditions, the moments of as-grown and positive voltage samples are the same. Figure 6.18 shows the XMCD measurement of Pt M absorption edge of Ir/Pt (c) and Cu/Pt (d) samples. For both types of samples, peaks are observed at 2654 eV. The negative voltage sample shows a higher peak compared to both the positive voltage and as-grown samples.

The measurements are consistent. Hysteresis loops obtained from Kerr imaging, SQUID-VSM, and XMCD demonstrate that negative voltage amplifies the coercive field. The XPS and XMCD measurements show an increase in Co oxide with negative gate voltage (see Figure 6.16 and Figure 6.6), which is supported by SQUID-VSM data indicating lower saturation magnetization for negatively gated samples.

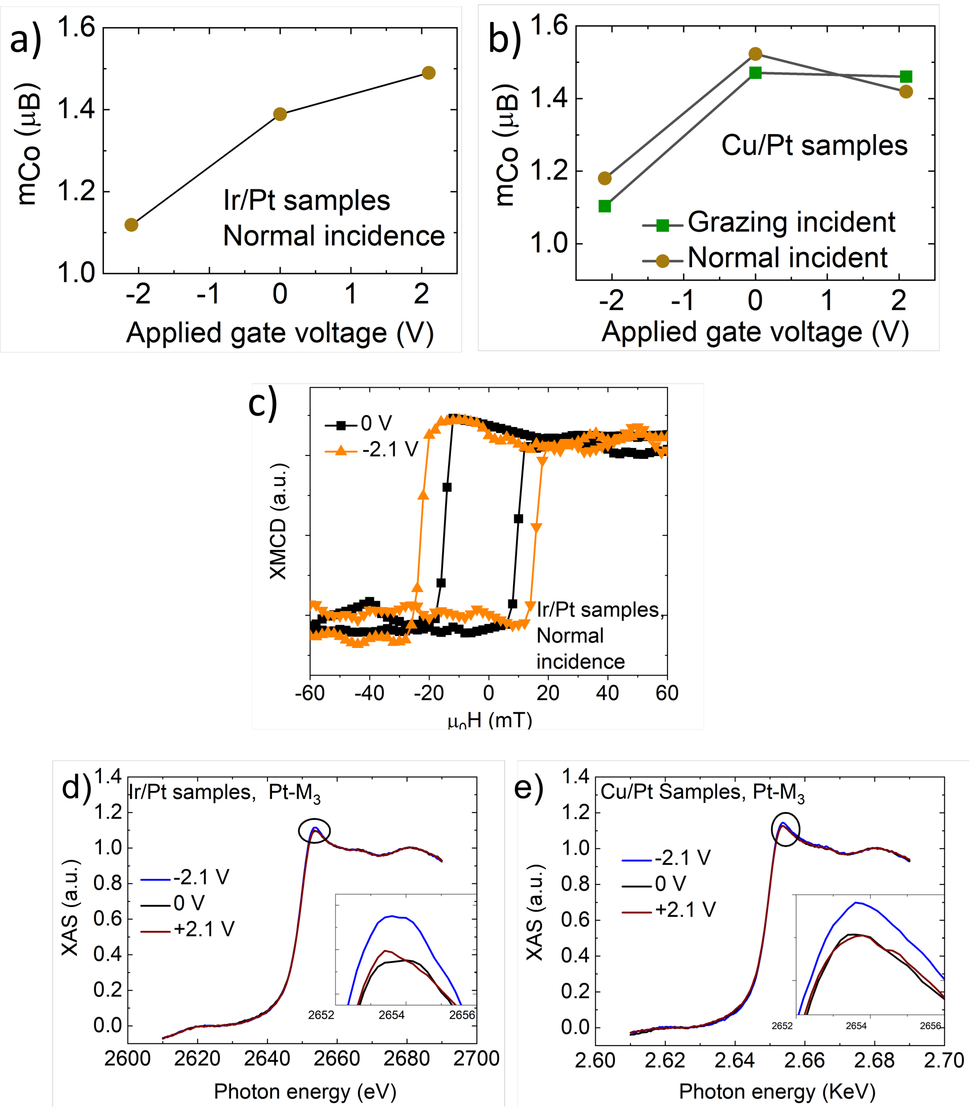

Figure 6.18: Magnetic moment of (a) Ir/Pt samples and (b) Cu/Pt samples. A negative voltage decreases the moment of Co. However, a positive voltage on the Cu/Pt sample is an exception. (c) Hysteresis loops of Ir/Pt samples: a negative voltage increases the coercive field, as observed under a Kerr microscope. XAS spectra at the Pt$-$M$_3$ absorption edge for (d) Ir/Pt and (e) Cu/Pt samples indicate a change in oxidation state under negative voltage, suggesting oxygen migration from the HfO$_2$

6.5 Discussion

This chapter presents the effect of ion migration (E-field induced) on the structural and interfacial magnetic properties of CoB/Ir/Pt samples. Additionally, we studied CoB/Cu/Pt samples, which exhibit a different DMI interaction due to a more pronounced asymmetry in the structure compared to CoB/Ir/Pt samples.

In Chapter 5, we demonstrated the effect of oxygen migration on the magnetic properties of CoB/Ir/Pt samples. We observed that oxygen ions move to the CoB layer under a negative voltage, decreasing the M_s and increasing the coercive field. The evidence presented here, based on XAS studies of the CoB/Ir/Pt samples, is consistent with our interpretation in Chapter 5.

The results from the CoB/Cu/Pt samples in this chapter show a similar effect. However, the effect on DMI, as measured by BLS, is more pronounced.

We assume that negative voltage drives oxygen to the magnetic layer, while positive voltage removes oxygen from the magnetic layer. The samples exhibit non-volatility, for Cu/Pt samples stable even after fifteen weeks with negative voltage. However, as-grown Cu/Pt samples experience changes in remanence magnetization over time, suggesting that the negatively gated samples are chemically more stable compared to the as-grown sample. This might be due to the formation of CoO at a negative voltage, which protects the sample from further oxidation. Copper, known for its quick oxidation behavior [203, 204], can oxidize within a few nanometers in a couple of days. This rapid oxidation may be attributed to the inability of the native oxide to protect against oxidation. Therefore, there might be oxidation due to ex-situ HfO_2 growth, subsequently altering the oxidation state of the Cu layer in Cu/Pt samples. Samples with applied positive voltage also undergo significant changes, possibly related to re-oxidation. The applied voltage moves oxygen ions from the CoB layers, but over time, the oxidation level changes, affecting the coercive field.

The oxidation of the samples between growth is confirmed by the XPS characterization, The O-K absorption edge exhibits multiple peaks, indicating the presence of metal oxides at around 513.12 eV and functional oxide groups at approximately 529.64 eV [176, 184, 185]. Co $L_{2,3}$ spectra of the as-grown samples show a CoO peak at around 781 eV along with a Co metal peak at around 778 eV [181, 183, 189, 205–207]. With applied negative voltage, the oxide peak at 781 eV increases, suppressing the Co metal peak at 778 eV. Conversely, with positive voltage, the metal peak increases, suppressing CoO. These results suggest that negative voltage drives oxygen to the magnetic layer, while positive voltage drives oxygen away from the magnetic layer. Additionally, XPS peaks for Ir, Pt, and Cu also suggest the oxidation of Ir, Pt, and Cu layers. In Ir XPS spectra, the major peaks around 60.4 eV and 63.4 eV represent Ir $4\,f_{7/2}$ and $4\,F_{5/2}$, respectively. Minor peaks at approximately 58 eV and 61 eV correspond to Ir^{4+} states, while the peak at a higher energy level of 65 eV is considered a satellite peak [192, 193, 208, 209]. The Cu XPS spectra indicate the Cu_2O at $\approx$ 332 eV and CuO at $\approx$ 334 eV [194–196]. The Cu XPS spectra indicate Cu_2O at approximately 332 eV and CuO at around 334 eV [194–196]. With applied voltage, the Cu XPS spectra exhibit significant changes, with both peaks undergoing substantial changes (6.7). The Pt XPS spectra show metallic Pt peaks at around 71.2 eV and 74.5 eV, with additional oxide peaks at 72.2 eV and 75.5 eV [198, 210, 211].

The XAS and XMCD study also suggests the oxidization of the as grown samples between two growths (sputtering and ALD). The XAS data show a peak at 777.5 eV with a high-energy shoulder at 781 eV, possibly indicating the ${Co_3}^+$ line shape, with the shoulder attributed to the primary ${Co_3}^+$ valence state [212]. Additionally, a prominent shoulder at 778.5 eV, more noticeable in the Cu/Pt samples, is observed. Negative voltage increases it, while positive voltage decreases it, indicating variations in oxidation states with applied voltage. An additional shoulder around 776 eV, before the Co metallic peaks, might be associated with the pre-peak of ${Co_2}^+$ [212], and it also changes with applied voltage, suggesting alterations in oxidation states in the systems. The magnetic moment from the metallic Co and the transition of Co valance between ${Co_3}^+$ and ${Co_2}^+$ might be due to the oxygen migration effect [212]. However, the shoulder between 777.5 eV and 781 eV can also be described as a multiplet structure due to a small background absorption, observed because of oxides related to photoelectron excitations into continuum states. This originates from the more confined nature of 3d orbitals in oxides, representing discreet transitions of 2p to 3d. This is considered a distinctive characteristic of the confined 3d orbitals associated with cobalt ions [213].

The coercive field of Ir/Pt samples is in good agreement with microscopy measurements, where negative voltage increases it. The XMCD data reveals the largest dichroism for the positively gated (Ir/Pt) and as grown (Cu/Pt) samples, indicating they have the highest magnetic moment [175]. This is consistent with the magnetic moment of Ir/Pt and Cu/Pt samples. It is worth mentioning that the Cu positively gated sample at normal incident shows a lower magnetic moment. However, with a grazing incident the moment is same as as grown sample.

The total magnetic moment is calculated from the orbital (m_l) and spin (m_l) magnetic moments, which depend on the number of holes in the Co 3d states, posing challenges for prediction and suggesting potential effects from electric polarization. The m_l/m_s ratio for the Ir/Pt as-grown sample is 0.15 at normal incident, compared to 0.12 for the Cu/Pt sample. Under a negative voltage of -2.1 V, the ratio for the Ir/Pt sample decreases to 0.13, while for Cu/Pt, it is 0.14. At a positive voltage of +2.1 V, the ratio increases to 0.15 for the Ir/Pt sample, whereas for Cu/Pt, it is 0.12. Ueno et al. (2015) calculated the ratio for Co in Pt/Co (0.2-1.7 nm)/AlO_x to be between 0.11 and 0.27 [214], and for Pt/Co (0.2-1.4 nm)/Pt to be approximately 0.1. Chen et al. [215] calculated the ratio for Co (5-7 nm) to be approximately 0.01. Gambardella et al. calculated the value to be 0.15 for the Co/Pt system [216]. These calculated values (Table 6.8) are within the range reported for Co.

Samples	0V	-2.1 V	+2.1V
Ir/Pt	0.15	0.13	0.15
Cu/Pt	0.12	0.14	0.12

Table 6.8: Calculated m_l/m_s values for Co. The calculated values are with in the reported range.

The Pt M_3 peak at 2646 eV shows oxidation behavior in as-grown samples [217]. A negative voltage significantly increases the oxidation, suggesting that oxygen from HfO_2 pushes the oxygen in Pt towards the CoB layer. The changes between as-grown and positively gated samples are negligible.

All this evidence suggests that the applied voltage is causing the movement of oxygen within the films, and the Co is forming CoO. However, the penetration depth of oxygen is not clear from these results. Therefore, a STEM study was conducted. Due to limitations in lateral resolution, the penetration depth could not be confirmed. However, it confirms that the oxygen does not reach the bottom Pt/CoB interface.

The magnetic moment of the samples changes with applied voltage; negative voltage causes oxygen to migrate to the magnetic layer, resulting in a decrease in magnetic moment, while positive voltage leads to an increase in moment as oxygen moves away from the magnetic layer. The magnetic moment of CoB is extracted from a series of Ir/Pt samples, revealing a 0.7 Å dead layer. This region suggests that heavy atoms of iridium might have slightly diffused with the CoB atoms [218]. Alternatively, there may already be some oxygen present at the interface before the gate voltage is applied.

An investigation into magnetic anisotropy indicates that Cu/Pt samples have lower effective anisotropy than Ir/Pt samples. Benguettat et al. (2020) studied the anisotropy of Co/Ir and Co/Cu interfaces, observing lower anisotropy in Co/Cu samples, mainly originating from the bottom layer. In our system, it's evident that applied voltage changes effective anisotropy, suggesting contributions from both the bottom and top interfaces. The top interface changes due to applied voltage, influencing the total effective anisotropy. Additionally, strong interlayer coupling of Ir may contribute to increased anisotropy [219, 220]. The E-field's effect is more pronounced on Cu/Pt films, possibly because Cu and Ir might have different grain sizes due to different surface diffusion rates and so the number of grain boundaries as well as their local chemical environments will be different [221]. To clarify this further, a detailed study of the oxidation states of the two layers would be required. However, this is technically challenging given the 2 Å layer thickness.

Interfacial magnetic properties, such as DMI and effective magnetization, are investigated using the BLS technique. The DMI and the effective magnetization also depend on the top interfaces, such as the CoB/Ir and CoB/Cu interfaces. DMI strength is influenced by the magnitude of spin-orbit torque (SOT) and the inversion asymmetry of the system, achievable by engineering the material interfaces. Here, we used Ir and Cu to break symmetry. It is established that heavy metals and adjacent ferromagnetic layers exhibit high DMI [57, 222].

It is observed that the Ir samples exhibit positive DMI, suggesting a left-handed or counterclockwise chirality [223]. Chen et al. (2015) also reported positive DMI for Co/Ir samples [224]. However, the sign of DMI is not an intrinsic property of material interfaces; rather, it depends on the quality of the interfaces [225]. The Ir/Pt samples are possessing lower DMI compared to the Cu/Pt samples. Copper does not contribute to the DMI, so the DMI primarily originates from the bottom interface. However, since Ir generates the same DMI as platinum, the overall DMI remains low. The DMI of Ir/Pt samples is higher than reported values. With the application of voltage, the DMI of the Ir/Pt interface does not change significantly. The calculated value of Cu/Pt DMI is also higher than reported values. Diez et al. (2019) studied the magneto-ionic effect on the Dzyaloshinskii-Moriya interaction (DMI) in a Pt/Co/HfO_2 structure, structure. They observed a reduction in DMI with oxygen ion migration, and the effect was not reversible. The oxygen traveled up to the Pt/Co interface and decoupled it, thereby reducing the DMI. We have also observed a reduction in the DMI of Cu/Pt samples. The reason might be the effect of the top Pt layer, where the oxygen is decoupling the Cu atoms. Therefore, the Pt is interacting with the CoB, resulting in a decrease in the total DMI. The applied voltage changes the top interface, changing the strength of DMI [218, 222, 226]. On the other hand, since Ir and Pt generate the same DMI, decoupling the Ir does not affect the total DMI. These findings also indicate that oxygen does not reach the bottom Pt/CoB layer, which is consistent with the STEM results.

6.6 Conclusions

In conclusion, this chapter has demonstrated that negatively gated samples exhibit more oxidation compared to as-grown and positively gated samples. This nonvolatile effect persists for up to 15 weeks in the Cu/Pt samples. Positively gated samples show a reduction in CoO content compared to as-grown samples. Evidence of these effects can be observed in the XPS peaks discussed in Section 6.3. The study also confirms the oxidation of samples during growth, indicating that Ir, Cu, and Pt are oxidizing. The XAS study provides stronger evidence of Pt oxidation (Figure 6.18(a,b)), alongside CoO formation. This suggests that oxygen from the HfO_2 layer is migrating into Pt and subsequently into the CoB layer. Furthermore, this study shows that the migration of oxygen (negatively gated) and CoO formation significantly alter the magnetic moment, as observed in magnetometry measurements. Conversely, the magnetic moment increases in positively gated samples due to the reduction of CoO and the presence of more metallic Co.

The controlled oxygen migration also affects the interfacial magnetic properties (Section 6.4.2). The DMI of the Cu/Pt samples decreases with negatively gated samples, suggesting an impact on the top CoB/Cu/Pt interfaces. The DMI of as-grown samples primarily originates from the bottom Pt/CoB interface. A negative voltage suppresses the Cu atoms and reduces the asymmetry effect, allowing Pt to establish exchange interactions with Co. This supports contributions from the top interface and leads to a decrease in net DMI. Additionally, the study shows that the effective anisotropy is negative, indicating that interfacial anisotropy is dominant in the structure. This finding is in good agreement with the AHE Hall effect measurements (Section 6.4). All the results concluded in this chapter are shown in Figure 6.19.

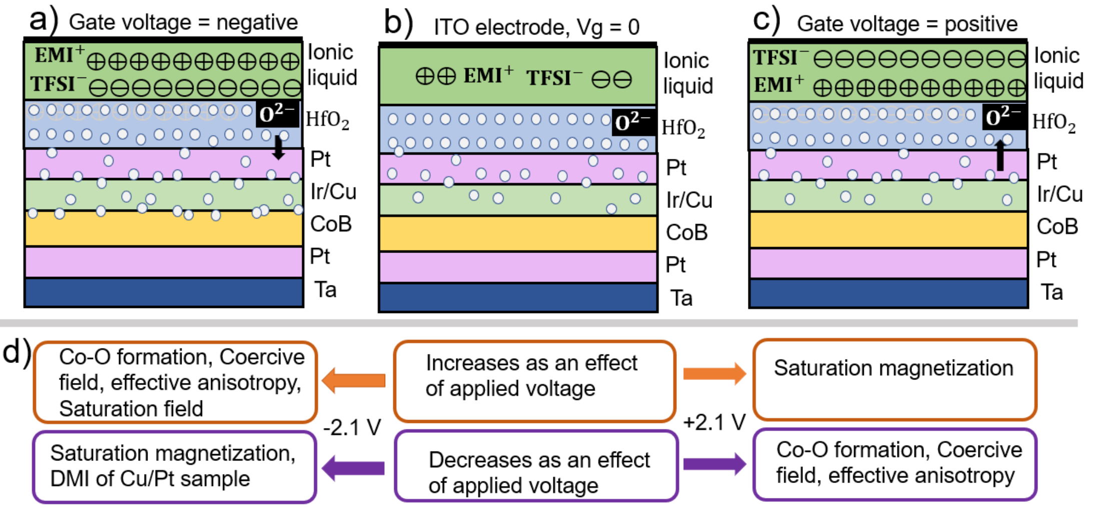

Figure 6.19: Summary of results presented in Chapter 6: (a) the predicted oxygen state of the as-grown sample, (b) oxygen diffusion at -2.1 V, c) oxygen diffusion at +2.1 V, d) summary of the effect of applied voltage.

Chapter 7

Towards Devices

7.1 Introduction

One of the aims of this research is to explore the feasibility of making field-programmable, reconfigurable domain wall/skyrmion devices. The previous chapters have focused on determining the magnetic properties and their E-field evolution. The next logical question is whether these changes are significant enough to influence the performance of spintronics devices. While addressing this question is beyond the immediate scope of this thesis, we can predict their potential in spintronics devices through micromagnetic simulations based on the parameters we have identified and by fabricating proof-of-principle devices. These steps will help bridge the gap between understanding the fundamental magnetic property changes and their practical application in spintronics devices.

The first section considers domain wall-based spintronics devices. Mumax3 simulations [227–229] were performed to understand the field- and current-driven domain wall (DW) motion, where all material parameters were taken from the experiments presented in the preceding Chapters 4 and Chapter 6. In the second section, a skyrmion device is simulated using Mumax3, where the skyrmion is nucleated using spin-polarised current. Finally, a reconfigurable DW-based device is presented as proof of principle.

7.2 Micromagnetic simulations using Mumax3

Domain wall based devices

The simulation of DW-based devices concentrates on the modulation of magnetic anisotropy by an electric field. To conduct the simulation, a grid size of $256 \times 32 \times 1$ is chosen, with a tetragonal cell size of $4\text{nm} \times 4\text{nm} \times 0.8\text{nm}$, which result in a device size of $1024 \times 128 \times 0.8$ nm as shown in Figure 7.2. The change in magnetic anisotropy affects both the motion and dynamics of the DW. Figure 7.2 illustrates such a device, wherein the anisotropy in the middle is increased by 25%, attributed to a magneto-ionic effect of -2.1 V. This configuration allows for the observation of both field-driven and current-driven DW velocities. In computing the PMA of the sample, a uniaxial anisotropy is considered along the z-axis. Table 7.1 list parameters used in this simulation.

Materials properties	Reference
$M_s = 750 \times 10^3 A/m$	Section 6.4
Exchange stiffness, $A = 5 \times 10^{-12}$ J/m	Section 4.4.2
$D = -0.3 \times 10^{-3} J/m^2$	Section 6.4.2
$\alpha = 0.05$	Figure A.1
$K_{u,1} = 0.4 \times 10^6 J/m^3$	Section 6.4
$K_{u,2} = 0.6 \times 10^6 J/m^3$	arbitrary 25% change of $K_{u,1}$
Easy axis = Vector (0,0,1)	-

Table 7.1: Material properties are used in micromagnetic simulation.

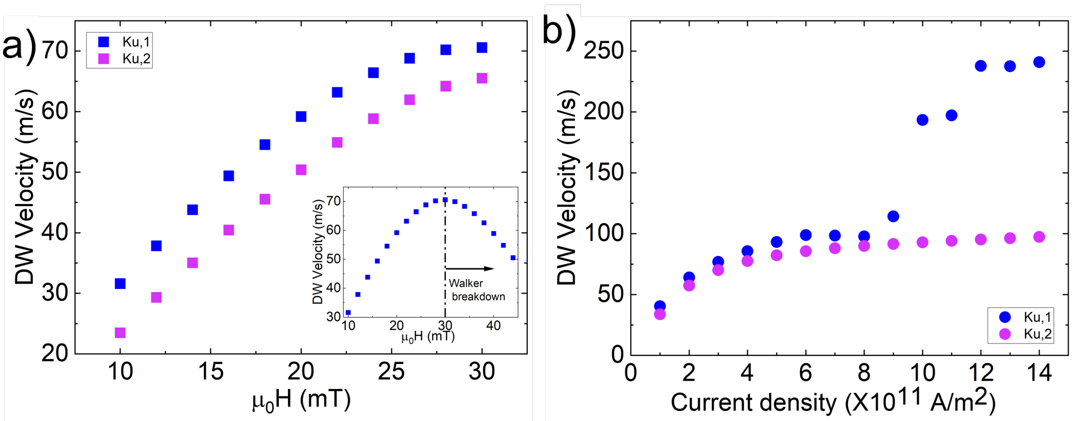

Figure 7.1: Domain wall velocity of a uniform wire for two different anisotropy constants. Material parameters are taken from experiments and listed in Table 7.1. Field-driven domain wall: (a) Illustrates the domain wall velocity, where low anisotropy shows higher velocity compared to high anisotropy. The inset shows the Walker breakdown and Walker breakdown field. Current-driven domain wall: (b) Current-driven domain wall velocity. At a low anisotropy, the velocity increases significantly after

Figure 7.1 shows the domain wall velocity for two different anisotropies. In the case of field-driven domain wall motion (Figure 7.1(a)), the low anisotropy has a high velocity, and the difference in velocity between the two anisotropies remains almost constant. However, in the case of current-driven domain wall motion, after $8 \times 10^{11} A/m^2$, the velocity shows a significant difference. In both scenarios, the reduced velocity for high anisotropy wires is due to the higher anisotropy energy of the wires. This example of a uniform hypothetical device provides evidence that both anisotropies can be used for further simulation.

An example of a hypothetical domain wall motion device includes a gate applied in the middle to create a localized pinning site (Figure 7.2). Figure 7.2(a) shows the device structure. The wire is simulated using ungated parameters, except for the middle section, which is assumed to change due to the effect of a negative voltage that alters the anisotropy by 25% (as a result of -2.1 V). All these parameters are derived from previous chapters (Table 7.1). The design of the device helps to observe the effect at the interface formed by the gating effect. Figures 7.2(b-e) show the domain wall motion. In each case, the initial images depict the presence of anisotropy variation or a gated area, highlighted by the white portion indicating high anisotropy. However, in the rest of the images, black and white represent the domain up and down, as indicated in Figure 7.2(a). Figures 7.2(f-g) provide a quantitative picture of domain wall pinning due to the gating effect and unpinning with a high applied field and current.

The motion controlled by the applied field exhibits a swinging type of motion, suggesting potential pinning effects (Figure 7.2(b-c)). Figures 7.2(f-g) display the magnetization component along the z-axis during domain wall motion under applied field and applied current, respectively. The negative and positive values of the z-component represent the up and down domains, respectively. The time-dependent component exhibits pinning behavior until a field of 24 mT and a current density of $5 \times 10^{11}\,\mathrm{A/m^2}$.

This will allow the creation of a domain wall device where one can turn on (and off) pinning sites where the domain wall will be stopped. Additionally, it also shows the range of field and current where the domain wall can be held. The advantage of this is that the pinning site can be reversible (as seen in Section 5.6 and also shown in 7.3). Moreover, it will help to deterministically introduce pinning sites for the domain wall, remove the pinning sites, and then place them in other locations since the device will be reconfigurable.

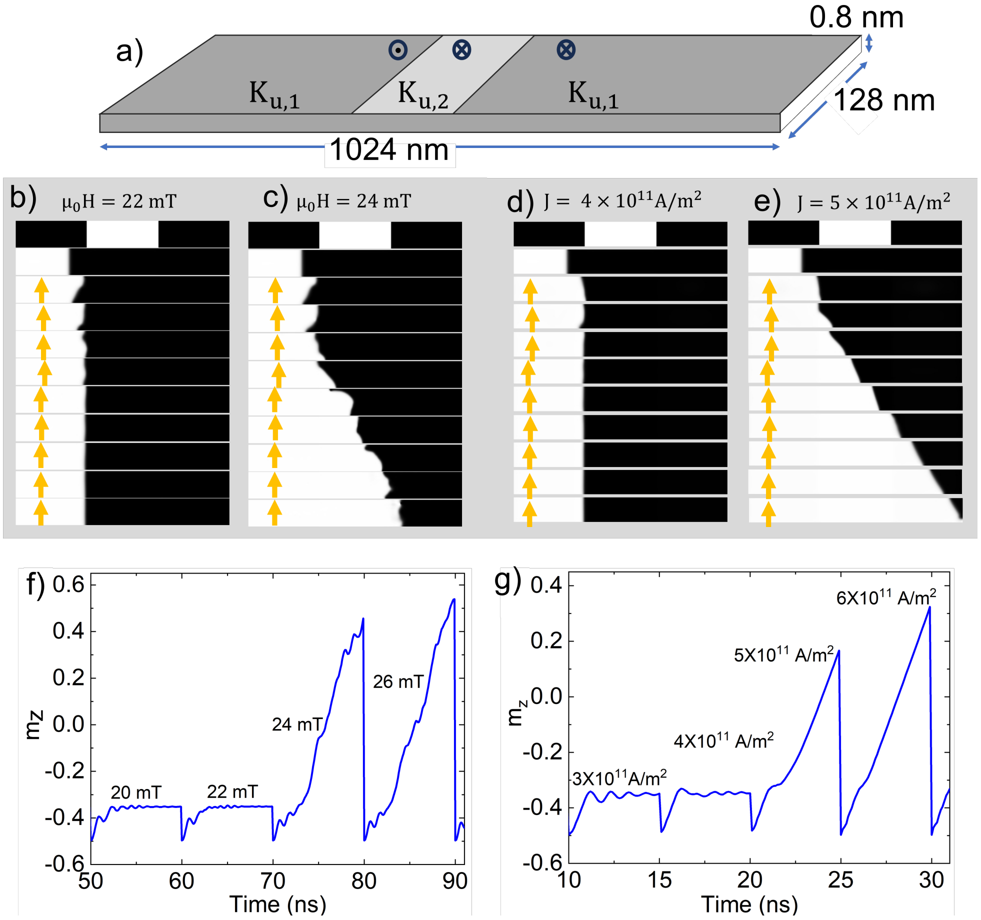

Figure 7.2: (a) Domain wall motion and pinning in a hypothetical device structure shown in Figure 7.2, using parameters derived from experimental work given in Table 7.1. (b-e) Magnetic field and spin-polarized current-driven domain wall motion and depinning. The initial images depict the simulated gated area, where white represents higher anisotropy compared to black. The arrows indicate that time is increasing compared to the previous images. (b) Domain wall pinning is observed until 22 mT. (c) Depinning of the domain wall occurs as it passes through the gated area at 24 mT. (d) The domain wall fails to pass through the gated area until a current density of $4 \times 10^{11}\text{A/m}^2$. (e) It begins to move with a current density of $5 \times 10^{11}\text{A/m}^2$ (no field applied).

Skyrmion nucleation using spin current

The prototype magnetic memory devices initially utilized domain wall structures. Recently, there has been significant interest in exploring whether skyrmion-based devices offer better performance. This study presents simulations of skyrmion-based devices using the parameters identified in our research. Unfortunately, skyrmions are not stable. To conduct the simulation studies, a grid size of $256 \times 64 \times 1$ is chosen, with tetragonal a cell size of $0.8 \times 0.8 \times 0.8$ nm. All material parameters remain consistent with those of the DW device.

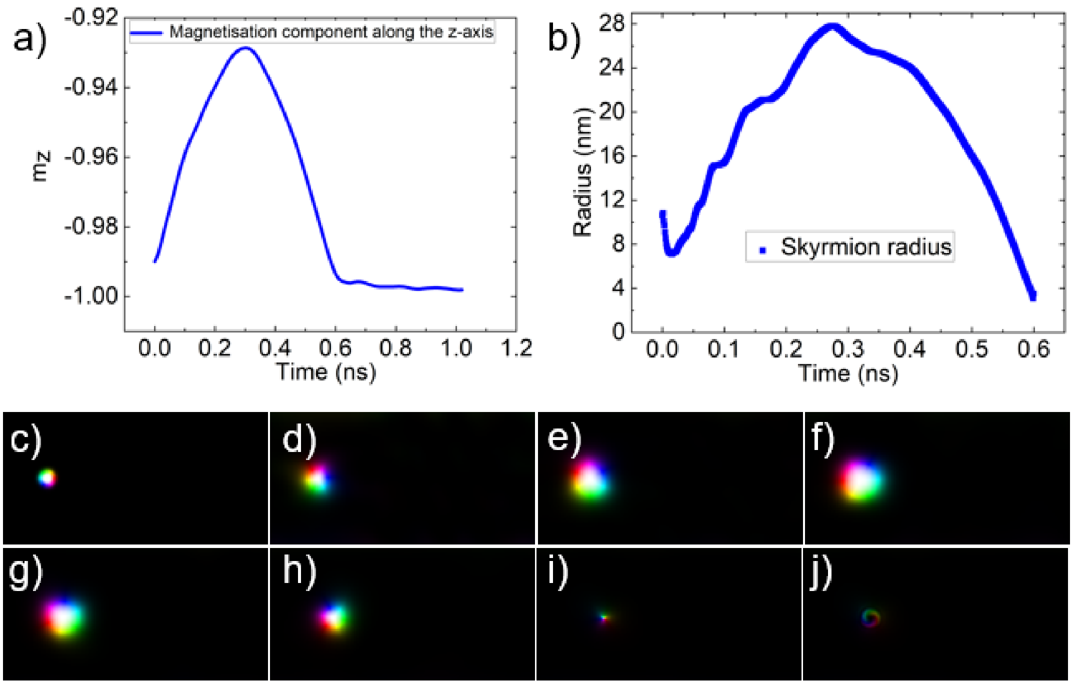

Figure 7.3: (a) Displays the magnetisation component along the z-axis of skyrmion as a function of time (during the simulation, no parameters were changed). (b) Change of skyrmion radius with time. (c) Initial skyrmion radius. (d) Skyrmion radius after 0.1 ns. (e) Skyrmion radius after 0.2 ns. (f) Skyrmion radius after 0.3 ns. (g) Skyrmion radius after 0.4 ns. (h) Skyrmion radius after 0.5 ns. (i) Skyrmion radius after 0.6 ns. (j) Skyrmion transforms to donut shaped complex structure before annihilation.

In magnetic thin films, skyrmions are stabilized by DMI. In our studied system, the DMI value is approximately -0.3 mJ/m^2. Skyrmion is studied using micromagnetic simulation in references [37, 229], where a DMI of 2.5 mJ/m^2 to 4 mJ/m^2 was used for a Co/Pt-based systems. It is important to note that when the DMI value falls below 2.5 mJ/m^2, the relaxed state of the system does not exhibit skyrmionic behavior. A stable skyrmion nucleation depends on the competition between direct exchange (FM) and indirect exchange (DMI) [229, 230]. In the relaxed state, the system shows a FM state. Therefore, for this simulation study, we have not considered the relaxation state of the system.

Figure 7.3 (a, b) depicts the magnetization along the z-axis and the skyrmion radius, respectively. PMA controls the radius of a skyrmion, which can be modified with an applied current [231]. Therefore, a spin current with a density of $1 \times 10^{12} A/m^2$ is applied during the simulation.

Figure 7.3(c-j) show the top view of skyrmion at different simulation time. The radius is initially increasing and then starting to decrease after approximately 0.3 ns. This decrease may be due to low damping value (0.05), the skyrmion started to annihilate as discussed in [231]. By around 0.6 ns, the skyrmion annihilates itself.

7.3 Re-configurable domain wall device: a proof of principle

One question regarding ILG is its scalability as a technology. In this section, we demonstrate that we can scale down devices to the micrometer range.

Previously, the gating effect was examined on a sheet film, applying the E-field over an area of 25 mm^2. As a starting point, we defined a gating region of similar scale, 1 mm in width. Additionally, we observed that the domain nucleation field remains high under negative voltage, consistent with previous samples 5.2. In order to do that reshaped the ITO electrode into a needle-shaped electrode (1 mm in width).

Figure 7.4 showcases microscope images of the needle electrode, with the gated area presented by the middle of the dotted lines. In Figure 7.4(a), +4 V (following the protocol outlined in Chapter 5) charge is applied for 30 minutes, resulting in domain nucleation within the gated region. As the applied magnetic field increases, the domain wall extends across the film. Conversely, Figure 7.4(b) illustrates the application of -2.1 V for 5 minutes, where domain nucleation occurs outside of the gated region. At 24 mT, the area beyond the gated region is entirely covered by the domain before expanding along the gated region.

a) +4V, 30min

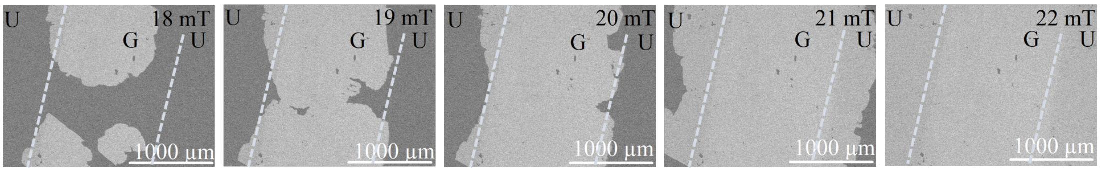

b) -2,1V, 5min

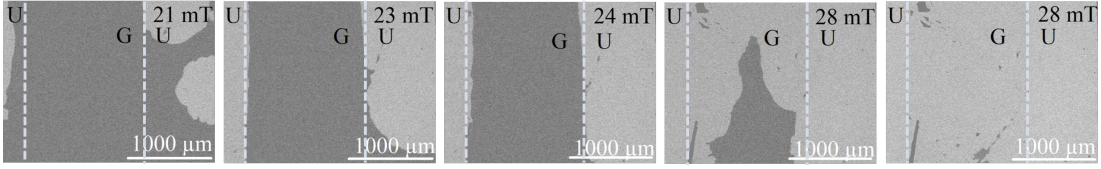

Figure 7.4: A 1000 μm reconfigurable magnetic domain wall device (with top Pt 5 Å), (a) domain nucleation and saturation under positive voltage. (b) a negative voltage of -2.1 V delays domain nucleation with in the gate region

In order to design a domain wall or skyrmion based device, the gating area must be in the micrometer to nanometer range. Extremely small component sizes facilitate fast switching and low energy consumption. Additionally, smaller component sizes increase the device density on a chip, thereby enabling the production of high-density devices on a single chip [232]. This process requires complex lithography techniques, which is shown in Section 3.11. We have scaled down the device fabrication to 50 μm as a proof-of-principle for a reconfigurable DW-based device. The device is fabricated on a sheet film using lithography techniques.

The ionic liquid is applied to the sample, and the ITO glass electrode is connected for voltage application. The SiO_x layer acts as a barrier, ensuring that the liquid contacts only the channel. Initially, the as-fabricated samples were measured. Subsequently, a negative voltage was applied to observe its effect, followed by the application of a positive voltage to reverse the effect of the negative voltage. After each voltage application, the ITO electrode and the ionic liquid were removed, and the samples were washed with acetone. Consequently, it was not possible to measure exactly the same position of the wire. The images presented here are representative of the entire wire.

Figure 7.5 depicts a 50 μm reconfigurable domain wall device. In its as-grown state (Figure 7.5a), when a magnetic field is applied, domains nucleate and propagate uniformly.

Upon application of -2.1 V for 3 minutes (Figure 7.5b), domains nucleate outside of the track and saturate it. As the field increases, domain nucleation on the track occurs at around 26 mT, saturating it at approximately 36.53 mT.

The process is reversed with an applied voltage of +3.5 V for 15 minutes (Figure 7.5c). In this case, the domains propagate both outside and on the track, saturating the entire device at around 19.46 mT.

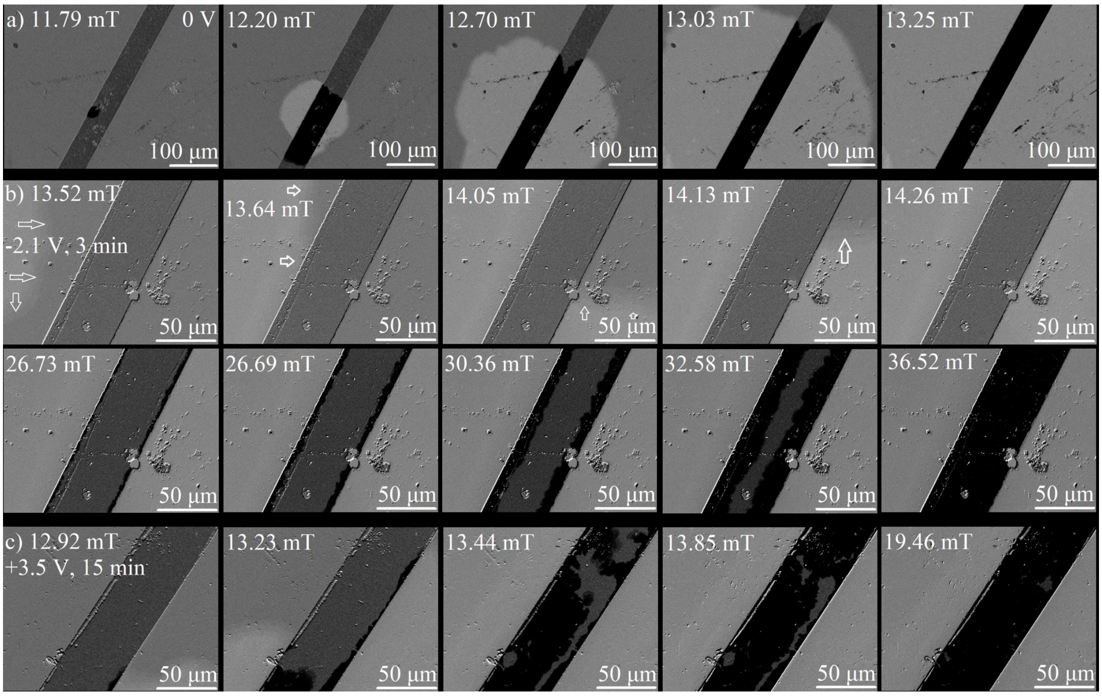

Figure 7.5: A 50 μm track fabricated on a sheet film: (a) Initially, domain nucleation occurs on the track, and it propagates uniformly along the device. (b) Application of a negative voltage delays domain nucleation and saturation on the track. (c) The effect of the negative voltage is reversible with the application of a positive voltage

7.4 Conclusions

In this chapter, we address whether our ability to change magnetic properties through gating can be applied to devices. Using micromagnetic simulations with the parameters we identified, we confirm that domain wall devices are functioning well. We investigated the dynamics of domain wall motion, pinning, and depinning phenomena under applied current and field, understanding their mechanisms and potential applications. However, we were not able to stabilize skyrmions in these structures. Many studies show that skyrmions require large DMI, and most experimental studies use multiple repeats in multilayers.

We have also built a proof-of-principle device that demonstrates our ability to fabricate a micro-scale device by defining a micro-scale track in a sheet film. This approach represents a potential method for producing a domain wall device through localized ionic liquid gating.

CHAPTER 8

Conclusion and Outlook

8.1 Summary

In this work, we investigated the effect of oxygen migration driven by an electric field(E-field) on all metallic magnetic multilayers. The aim of this study was to explore the magnetic properties and their response to an E-field, which might be useful for designing spintronics devices. Initially, an introduction to the work was presented, followed by the theoretical background and literature review, with a focus on this study. The results were categorized based on the experimental techniques and investigations.

The first necessary step for this study was to fabricate PMA thin films with ultra-thin layers, where ions can be transported and magneto-ionic driven changes can be observed. Chapter 4 focuses on the processing of these thin film structures. In this chapter, our investigation centered around the development and analysis of ultra-thin multilayers comprising Ta/Pt/CoB/Ir/Pt, with a primary focus on their magnetic and structural properties. The study revealed excellent stability of perpendicular magnetic anisotropy (PMA) at room temperature, which is useful for long-term data storage.

We estimated the exchange stiffness (A) from temperature-dependent magnetization and the Bloch law thin film approximation, which is used in micromagnetic simulations in Chapter 7. Additionally, we explored the Dzyaloshinsky-Moriya interaction (DMI) by examining asymmetric bubble expansion within the creep regime. However, we found that this technique was not useful for our systems. Therefore, we used the Brillouin light scattering (BLS) technique (Chapter 6) for estimating DMI. A smooth surface is essential for applying ionic liquid gating, and atomic force microscopy (AFM) revealed minimal roughness in the film, which is beneficial for this purpose. Overall, our findings provide valuable insights into the sample structures, facilitating further research on oxygen ion migration and its effects on magnetic properties.

In Chapter 5, our investigation illuminated the E-field induced magneto-ionic effect on the magnetic properties of thin films. The migration of oxygen ions towards or away from the CoB layer under negative or positive voltages, respectively, alters the oxidation state of the layers. The applied voltage affects the hysteresis loops, indicating that a positive voltage reduces the coercive field (Sections 5.5 and 5.4), while a negative voltage increases it. Additionally, observations from Kerr microscopy images (Section 5.4)) reveal that negative voltages delay domain nucleation. This change may be due to the variation in oxygen concentration within the film, with a negative voltage inducing pinning through oxygen migration within the overall structure.

		Ir/Pt		Cu/Pt		
Techniques	Properties	-2.1 V	+2.1V	-2.1 V	+2.1V	Sections
XPS	CoO	↑	↓	↑	↓	6.3
XAS	M_s	↓	↑	↓	↑	6.4.3
	Hc	↑	↓	↑	↓	
	CoO	↑	↓	↑	↓	
	Pt oxide	↑	-	↑	-	
SQUID	M_s	↓	↑	↓	↑	6.4, 5.5
	H_c	↑	↓	↑	↓	
Kerr Microscopy	H_c	↑	↓	↑	↓	5.4
AHE	K_{eff}	↑	↓	↑	↑	6.4, 5.5
BLS	M_{eff}	negative	negative	negative	negative	6.4.2
	DMI	similar	similar	↓	same	

Table 8.1: Summary of results. All results show changes in material properties due to E-field induced oxygen migration, compared to as-grown samples.

The magneto-ionic technique significantly impacts magnetic moments (Sections 5.5), which decrease with a negative voltage, suggesting the formation of CoO (antiferromagnetic), while a positive voltage removes oxygen, increasing metallic Co (ferromagnetic). Furthermore, these changes affect anisotropy (Sections 5.5) as well as spin-orbit interactions. To examine this hypothesis (CoO formation), we investigated the system's chemistry and structural changes (Section 6). Importantly, the system is almost fully reversible (Section 5.6), which opens possibilities for designing reconfigurable devices.

Chapter 6 delves into the structural and interfacial magnetic properties of E-field driven oxygen migration. In this chapter, we extend our study to CoB/Cu/Pt samples as well as CoB/Ir/Pt samples. We found that the magnetoionic modulation of magnetic properties is nonvolatile; when a negative voltage is applied, it remains nonvolatile up to fifteen weeks in Cu/Pt top layer samples. This nonvolatility may be due to the formation of CoO, which then protects the samples.

The XPS study (Section 6.3) suggests that the samples are partially oxidized during two growth processes: sputtering and ex-situ ALD. Analyzing the Co $L_{2,3}$ spectra, we found Co metal and CoO peaks at 778 eV and 781 eV, respectively. A negative voltage increases the oxidation of Co, resulting in an increase in the CoO peak. On the other hand, a positive voltage increases the metallic Co peak. This finding is also consistent with the XAS investigation (Section 6.4.3). At the edge of the metallic Co peak, a shoulder-type behavior is observed at 776 eV, which is higher for negatively gated samples compared to as-grown and positively gated samples. This pre-peak indicates the formation of CoO. Additionally, it shows that the coercive field of Ir/Pt samples increases with a negative voltage, which is consistent with Kerr microscopy and SQUID measurements (Section 5.5, 5.4). Moreover, the XMCD measurement (Section 6.4.3) shows a large dichroism for Ir/Pt (positive gate) and Cu/Pt (0 V), indicating they have high magnetic moments. The SQUID measurement (Section 6.4) also shows a high moment for the positively gated Ir/Pt sample.

The Ir/Pt samples have higher anisotropy than Cu/Pt samples because the interfacial contribution for Cu/Pt samples comes from the bottom interface 6.4. The ionic liquid gating modifies the top interface, affecting the total anisotropy of the samples. Additionally, Cu/Pt samples show higher DMI than Ir/Pt samples 6.4.2, with negative voltage significantly decreasing DMI (Cu/Pt sample), supporting the contribution from the top interface.

All the results are listed in Table 8.1, which can be interpreted as a consequence of oxygen ions being driven onto and off the interface with the CoB. The negative voltage forces the oxygen in HfO_2 toward the CoB layer, where they modify the magnetic properties of the layer and, hence, of the overall thin film in a controllable and reversible way.

Chapter 7 explores the potential of E-field controlled magnetic properties in magnetic multilayers for spintronics applications, focusing on domain wall devices. Through simulations and experiments, we investigate domain wall motion dynamics and propose new domain wall-based spintronics devices. Finally, we have fabricated proof-of-principle domain wall devices, where localized ionic liquid gating controls domain wall nucleation. The effect is reversible and reveals a potential method for domain wall-based devices.

8.2 Future Work

In order to build effective and stable spintronics devices, it is crucial to continue this intriguing project and delve deeper into several key aspects, particularly regarding penetration depth of oxygen (i.e., how far oxygen migrates into the magnetic layer) and device fabrication.

Sample Structure

As we showed in Chapter 7, using micromagnetic simulations, we could not stabilize skyrmions in our systems. Therefore, exploring thicker magnetic layers may enhance DMI. This would be further work on developing the magnetic structure, which would allow us to apply magnetic ionic gating and be able to host skyrmions at the ground state. The distinct magnetic and structural properties exhibited by ferromagnetic adjacent layers (such as Ir and Cu) suggest a significant contribution from the top interface. Investigating other heavy materials for comparison could provide valuable insights (for example Bismuth). Additionally, repeating the sample structure two or three times may yield exceptionally high DMI.

Characterization

The magneto-ionic technique alters magnetic, structural, and interfacial properties through oxygen ion migration. However, due to the ultra-thin layers, observing oxygen penetration depth using scanning transmission electron microscopy (STEM) was challenging. Utilizing techniques such as superSTEM, which has higher resolution, might be useful for locating the position of oxygen, and magnetic holography could help interpret it.

We conducted reversibility testing for a single thickness, which is from the middle of the thickness range we studied. Extending this study to include additional thicknesses and longer cycle periods would be advantageous.

Spintronics devices

In the majority of spintronics devices, the behavior is engineered during fabrication and cannot be changed afterward. Using ionic liquid gating, we can change the behavior of a device after fabrication. This could be useful in designing field-programmable domain wall devices, reconfigurable domain wall devices, or post-fabrication programmable domain wall devices. While we proposed a proof-of-principle domain wall-based device, further studies on efficiency, durability, and size (nanoscale) should be considered and optimized.

Micro-magnetic simulation

Similar to the domain wall-based devices, designing skyrmion-based reconfigurable devices will depend on the stability of the skyrmions. Therefore, conducting micro-magnetic simulations focused on skyrmion stability under varying conditions such as temperature, E-field, spin current, and system disorder could provide crucial insights.

Continuing research in these areas will advance our understanding and pave the way for the development of practical and efficient spintronics devices, such as reconfigurable domain wall or skyrmion devices.

APPENDIX A

Appendix1

A.1 Calculating damping constant from Brillouin light scattering (BLS) spectroscopy

The value of Alpha is calculated using BLS (Section 3.8) data that we collected at the same time as the data in Section 6.4.2. The calculation was performed by Professor M. Belmeguenai, and in this work, we have used the value obtained. The damping constant α can be calculated using the following equation [112, 233],

$$\delta F = 2\alpha \frac{\gamma}{2\pi} \mathrm{H} + \delta F_0, \tag{A.1}$$

where, δF is the full width half maxima from stock and anti-stock frequency, δF_0 extrinsic line-width contribution, γ stands for the gyromagnetic ratio, H is the applied field. For the Cu/Pt samples, we observe two different regimes. Similar to PMA and DMI, alpha also depends on interface quality. Additionally, PMA can be affected by interfacial roughness or strain [222]. Therefore, the reason might be the presence of two anisotropy regions in this sample, where residual strain originates from the Pt/CoB interface. It is considered that the total α is $\alpha_{CoB} + \alpha_{Pt}$ (where $\alpha_{CoB}= \alpha$ of CoB and $\alpha_{Pt} = \alpha$ of Pt), and only the linear regime versus $1/\,\mathrm{t_{eff}}$ is used for the calculation.

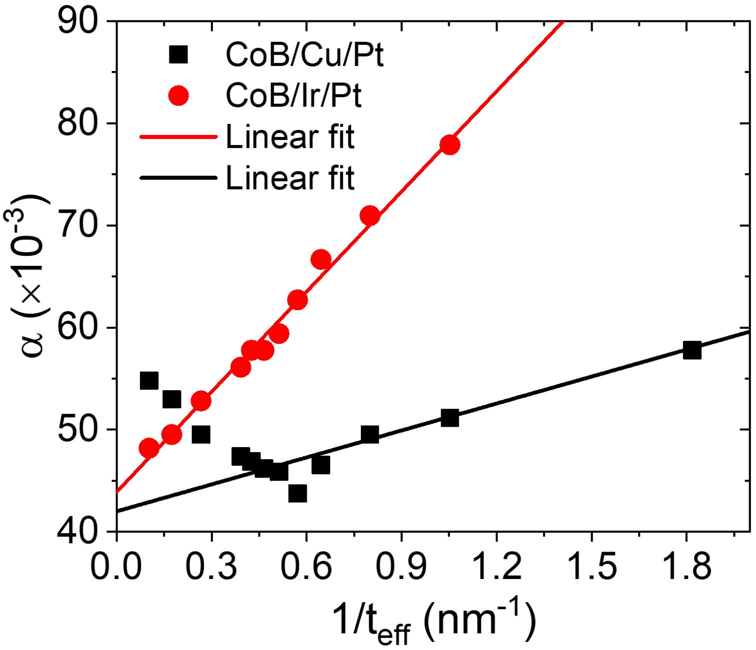

Figure A.1: Change in damping constant α as a function of the reciprocal effective thickness of CoB. The Cu/Pt system shows a lower slope compared to Ir/Pt. The Cu/Pt samples show two regimes of α; however, only the linear part as a function of $1/\,\mathrm{t_{eff}}$ is considered for the fitting. The linear fit gives α from the y-axis. The value of α is determined as $0.4 \pm 0.1 \times 10^{-3}$. We used the alpha $= 0.005$.

BIBLIOGRAPHY

[1] Albert Fert, Vincent Cros, and Joao Sampaio. Skyrmions on the track. *Nature Nanotechnology*, 8(3):152–156, 2013.

[2] Ioan Mihai Miron, Thomas Moore, Helga Szambolics, Liliana Daniela Buda-Prejbeanu, Stephane Auffret, Bernard Rodmacq, Stefania Pizzini, Jan Vogel, Marlio Bonfim, Alain Schuhl, and Gilles Gaudin. Fast current-induced domain-wall motion controlled by the Rashba effect. *Nature Materials*, 10(6):419 –423, 2011.

[3] Geoffrey S.D. Beach, Corneliu Nistor, Carl Knutson, Maxim Tsoi, and James L. Erskine. Dynamics of field-driven domain-wall propagation in ferromagnetic nanowires. *Nature Materials*, 4(10):741–744, 2005.

[4] S. L. Zhang, W. W. Wang, D. M. Burn, H. Peng, H. Berger, A. Bauer, C. Pfleiderer, G. Van Der Laan, and T. Hesjedal. Manipulation of skyrmion motion by magnetic field gradients. *Nature Communications*, 9(1):2115, 2018.

[5] Eleonora Raimondo, Elias Saugar, Joseph Barker, Davi Rodrigues, Anna Giordano, Mario Carpentieri, Wanjun Jiang, Oksana Chubykalo-Fesenko, Riccardo Tomasello, and Giovanni Finocchio. Temperature-Gradient-Driven Magnetic Skyrmion Motion. *Physical Review Applied*, 18(2):024062, 2022.

[6] Simone Moretti, Victor Raposo, Eduardo Martinez, and Luis Lopez-Diaz. Domain wall motion by localized temperature gradients. *Physical Review B*, 95(6): 064419, 2017.

[7] D C Cronemeyer. Perpendicular Anisotropy in Gd1-xCox Amorphous Films Prepared by RF Sputtering. *AIP Conference Proceedings*, 18(1):85–89, 3 1974.

[8] Shun ichi Iwasaki and Kazuhiro Ouchi. Co-Cr recording films with perpendicular magnetic anisotropy. *IEEE Transactions on Magnetics*, 14(5):3169 – 3171, 1978.

[9] Bharati Tudu and Ashutosh Tiwari. Recent Developments in Perpendicular Magnetic Anisotropy Thin Films for Data Storage Applications. *Vacuum*, 146:329–341, 2017.

[10] C. W. Chen. Fabrication and characterization of thin films with perpendicular magnetic anisotropy for high-density magnetic recording - Part II a review. *Journal of Materials Science*, 26(12):1705– 1728, 1991.

[11] Philippa M.' 'Shepley. *Effect of piezoelectric strain on the magnetic properties of Pt/Co thin films.* PhD thesis, University of Leeds, Leeds, 2015.

[12] Min He, Tiankuo Xu, Yang Gao, Chaoqun Hu, Jianwang Cai, and Ying Zhang. Mixed-Type Skyrmions in Symmetric Pt/Co/Pt Multilayers at Room Temperature. *Materials*, 15(22):8272, 2022.

[13] A. Fert and Peter M. Levy. Role of anisotropic exchange interactions in determining the properties of spin-glasses. *Physical Review Letters*, 44(23):1538, 1980.

[14] A. Hrabec, N. A. Porter, A. Wells, M. J. Benitez, G. Burnell, S. McVitie, D. McGrouther, T. A. Moore, and C. H. Marrows. Measuring and tailoring the Dzyaloshinskii-Moriya interaction in perpendicularly magnetized thin films. *Physical Review B - Condensed Matter and Materials Physics*, 90(2):020402, 2014.

[15] Hongxin Yang, Olivier Boulle, Vincent Cros, Albert Fert, and Mairbek Chshiev. Controlling Dzyaloshinskii-Moriya Interaction via Chirality Dependent Atomic-Layer Stacking, Insulator Capping and Electric Field. *Scientific Reports*, 8(1): 12356, 2018.

[16] M. S. Pierce, J. E. Davies, J. J. Turner, K. Chesnel, E. E. Fullerton, J. Nam, R. Hailstone, S. D. Kevan, J. B. Kortright, Kai Liu, L. B. Sorensen, B. R. York, and O. Hellwig. Influence of structural disorder on magnetic domain formation in perpendicular anisotropy thin films. *Physical Review B - Condensed Matter and Materials Physics*, 87(18):184428, 2013.

[17] Jin Hong Kim and Sung Chul Shin. Interface roughness effects on the surface anisotropy in Co/Pt multilayer films. *Journal of Applied Physics*, 80(5):3121–3123, 1996.

[18] A. P. Mihai, A. L. Whiteside, E. J. Canwell, C. H. Marrows, M. J. Benitez, D. McGrouther, S. McVitie, S. McFadzean, and T. A. Moore. Effect of substrate temperature on the magnetic properties of epitaxial sputter-grown Co/Pt. *Applied Physics Letters*, 103(26):262401, 2013.

[19] Adam W.J. Wells, Philippa M. Shepley, Christopher H. Marrows, and Thomas A. Moore. Effect of interfacial intermixing on the Dzyaloshinskii-Moriya interaction in Pt/Co/Pt. *Physical Review B*, 95(5):054428, 2017.

[20] R. Lo Conte, E. Martinez, A. Hrabec, A. Lamperti, T. Schulz, L. Nasi, L. Lazzarini, R. Mantovan, F. Maccherozzi, S. S. Dhesi, B. Ocker, C. H. Marrows, T. A. Moore, and M. Kläui. Role of B diffusion in the interfacial Dzyaloshinskii-Moriya interaction in Ta/Co20 Fe60 B20/MgO nanowires. *Physical Review B - Condensed Matter and Materials Physics*, 91(1):014433, 2015.

[21] Jacob Torrejon, Junyeon Kim, Jaivardhan Sinha, Seiji Mitani, Masamitsu Hayashi, Michihiko Yamanouchi, and Hideo Ohno. Interface control of the magnetic chirality in CoFeB/MgO heterostructures with heavy-metal underlayers. *Nature Communications*, 5:4655, 2014.

[22] R. Lavrijsen, P. P.J. Haazen, E. Murè, J. H. Franken, J. T. Kohlhepp, H. J.M. Swagten, and B. Koopmans. Asymmetric Pt/Co/Pt-stack induced sign-control of current-induced magnetic domain-wall creep. *Applied Physics Letters*, 100(26), 2012.

[23] Fernando Ajejas, Viola Křižáková, Dayane De Souza Chaves, Jan Vogel, Paolo Perna, Ruben Guerrero, Adrian Gudin, Julio Camarero, and Stefania Pizzini. Tuning domain wall velocity with Dzyaloshinskii-Moriya interaction. *Applied Physics Letters*, 111(20):202402, 2017.

[24] Dong Soo Han, Nam Hui Kim, June Seo Kim, Yuxiang Yin, Jung Woo Koo, Jaehun Cho, Sukmock Lee, Mathias Kläui, Henk J.M. Swagten, Bert Koopmans, and Chun Yeol You. Asymmetric hysteresis for probing Dzyaloshinskii-Moriya interaction. *Nano Letters*, 16(7):4438–4446, 2016.

[25] Kowsar Shahbazi. *Dzyaloshinskii-Moriya Interaction and Domain Wall Motion in Polycrystalline and Epitaxial Magnetic Multilayers.* PhD thesis, University of Leeds, University of Leeds, 2018.

[26] S' 'Methfessel. Methfessel, S. Potential application of magnetic rare earth compounds. *IEEE Trans. Magn.*, 1:144–155, 1965.

[27] H. Ohno, D. Chiba, F. Matsukura, T. Omiya, E. Abe, T. Dietl, Y. Ohno, and K. Ohtani. Electric-field control of ferromagnetism. *Nature*, 408(6815):944–946, 2000.

[28] Aya Obinata, Yuki Hibino, Daichi Hayakawa, Tomohiro Koyama, Kazumoto Miwa, Shimpei Ono, and Daichi Chiba. Electric-field control of magnetic moment in Pd. *Scientific Reports*, 5:14303, 2015.

[29] Takeshi Kawabe, Kohei Yoshikawa, Masahito Tsujikawa, Takuya Tsukahara, Kohei Nawaoka, Yoshinori Kotani, Kentaro Toyoki, Minori Goto, Motohiro Suzuki, Tetsuya Nakamura, Masafumi Shirai, Yoshishige Suzuki, and Shinji Miwa. Electric-field-induced changes of magnetic moments and magnetocrystalline anisotropy in ultrathin cobalt films. *Physical Review B*, 96(22):220412, 2017.

[30] Dongxing Yu, Yonglong Ga, Jinghua Liang, Chenglong Jia, and Hongxin Yang. Voltage-Controlled Dzyaloshinskii-Moriya Interaction Torque Switching of Perpendicular Magnetization. *Physical Review Letters*, 130(5):056701, 2023.

[31] Tomohiro Koyama, Yoshinobu Nakatani, Junichi Ieda, and Daichi Chiba. Electric field control of magnetic domain wall motion via modulation of the Dzyaloshinskii-Moriya interaction. *Science Advances*, 4(12):0265, 2018.

[32] Titiksha Srivastava, Marine Schott, Romeo Juge, Viola Křižáková, Mohamed Belmeguenai, Yves Roussigné, Anne Bernand-Mantel, Laurent Ranno, Stefania Pizzini, Salim Mourad Chérif, Andrey Stashkevich, Stephane Auffret, Olivier Boulle, Gilles Gaudin, Mairbek Chshiev, Claire Baraduc, and Helene Béa. Large-Voltage Tuning of Dzyaloshinskii-Moriya Interactions: A Route toward Dynamic Control of Skyrmion Chirality. *Nano Letters*, 18(8):4871–4877, 2018.

[33] Marine Schott, Laurent Ranno, Helene Béa, Claire Baraduc, Stephane Auffret, and Anne Bernand-Mantel. Electric field control of interfacial Dzyaloshinskii-

Moriya interaction in Pt/Co/AlOx thin films. *Journal of Magnetism and Magnetic Materials*, 520:167122, 2021.

[34] A. Bernand-Mantel, L. Herrera-Diez, L. Ranno, S. Pizzini, J. Vogel, D. Givord, S. Auffret, O. Boulle, I. M. Miron, and G. Gaudin. Electric-field control of domain wall nucleation and pinning in a metallic ferromagnet. *Applied Physics Letters*, 102(12):122406, 2013.

[35] Y. T. Liu, S. Ono, G. Agnus, J. P. Adam, S. Jaiswal, J. Langer, B. Ocker, D. Ravelosona, and L. Herrera Diez. Electric field controlled domain wall dynamics and magnetic easy axis switching in liquid gated CoFeB/MgO films. *Journal of Applied Physics*, 122(13):133907, 2017.

[36] Yifan Zhou, Rhodri Mansell, and Sebastiaan van Dijken. Voltage control of skyrmions: Creation, annihilation, and zero-magnetic field stabilization. *Applied Physics Letters*, 118(17):172409, 2021.

[37] Wang Kang, Yangqi Huang, Chentian Zheng, Weifeng Lv, Na Lei, Youguang Zhang, Xichao Zhang, Yan Zhou, and Weisheng Zhao. Voltage controlled magnetic skyrmion motion for racetrack memory. *Scientific Reports*, 6:23164, 2016.

[38] Eva Grimaldi, Viola Krizakova, Giacomo Sala, Farrukh Yasin, Sebastien Couet, Gouri Sankar Kar, Kevin Garello, and Pietro Gambardella. Single-shot dynamics of spin-orbit torque and spin transfer torque switching in three-terminal magnetic tunnel junctions. *Nature Nanotechnology*, 15(2):111–117, 2020.

[39] B. Dieny, I. L. Prejbeanu, K. Garello, P. Gambardella, P. Freitas, R. Lehndorff, W. Raberg, U. Ebels, S. O. Demokritov, J. Akerman, A. Deac, P. Pirro, C. Adelmann, A. Anane, A. V. Chumak, A. Hirohata, S. Mangin, Sergio O. Valenzuela, M. Cengiz Onbasli, M. d Aquino, G. Prenat, G. Finocchio, L. Lopez-Diaz, R. Chantrell, O. Chubykalo-Fesenko, and P. Bortolotti. Opportunities and challenges for spintronics in the microelectronics industry. *Nature Electronics*, 3(8): 446–459, 2020.

[40] Rohit Pachat. *Magneto-ionics in CoFeB based systems.* PhD thesis, University of Paris-Saclay, Paris, 2023.

[41] Wei Gang Wang, Mingen Li, Stephen Hageman, and C. L. Chien. Electric-field-assisted switching in magnetic tunneljunctions. *Nature Materials*, 11(1):64–68, 2012.

[42] Uwe Bauer, Lide Yao, Aik Jun Tan, Parnika Agrawal, Satoru Emori, Harry L. Tuller, Sebastiaan Van Dijken, and Geoffrey S.D. Beach. Magneto-ionic control of interfacial magnetism. *Nature Materials*, 14(2):174–181, 2015.

[43] R. Pachat, D. Ourdani, J. W. van der Jagt, M. A. Syskaki, A. Di Pietro, Y. Roussigne, S. Ono, M. S. Gabor, M. Cherif, G. Durin, J. Langer, M. Belmeguenai, D. Ravelosona, and L. Herrera Diez. Multiple magneto-ionic regimes in Ta/Co20Fe60B20/HfO2. *Physical Review Applied*, 15:064055, 5 2021.

[44] Evgeny Y. Tsymbal. Spintronics: Electric toggling of magnets. *Nature Materials*, 11(1):12–13, 2012.

[45] Olivier Fruchart. *LECTURE NOTES ON Nanomagnetism.* SPINTEC (Universite Grenoble Alpes, CNRS & CEA), Grenoble, 10 2018. URL `http://fruchart.eu`.

[46] Charles Kittel. *Introduction to solid state physics*, volume 8. Wiley, New York, 1996.

[47] Rudolf Schäfer. Investigation of Domains and Dynamics of Domain Walls by the Magneto-optical kerr-effect. In Kronmüller Helmut, editor, *Handbook of Magnetism and Advanced Magnetic Materials*, volume 1. John Wiley & Sons, Ltd, 2007.

[48] Stephen Blundell and David Thouless. Magnetism in Condensed Matter. *American Journal of Physics*, 71(1):94–95, 2003.

[49] M. T. Johnson, P. J.H. Bloemen, F. J.A. Den Broeder, and J. J. De Vries. Magnetic anisotropy in metallic multilayers. *Reports on Progress in Physics*, 59(11): 1409, 1996.

[50] Titiksha Srivastava. *Engineering and dynamical control of interfacial properties in ultra-thin films to tune magnetic spin textures.* PhD thesis, Université Grenoble Alpes, Grenoble, France, 8 2019.

[51] Risalat Amir Khan. *Chiral Spin Textures in Magnetic Nanostructures.* PhD thesis, University of Leeds, Leeds, 2018.

[52] Alexandra Jane Stacey. *Topological Hall Effect due to Skyrmions in Magnetic Multilayers.* PhD thesis, University of Leeds, Leeds, 2023.

[53] I. Dzyaloshinsky. A thermodynamic theory of ”weak” ferromagnetism of antiferromagnetics. *Journal of Physics and Chemistry of Solids*, 4(4):241–255, 1958.

[54] Tôru Moriya. Anisotropic superexchange interaction and weak ferromagnetism. *Physical Review*, 120(1):91–98, 1960.

[55] Nicolas Josten, Thomas Feggeler, Ralf Meckenstock, Detlef Spoddig, Marina Spasova, Ke Chai, Iliya Radulov, Zi An Li, Oliver Gutfleisch, Michael Farle, and Benjamin Zingsem. Dynamic unidirectional anisotropy in cubic FeGe with antisymmetric spin-spin-coupling. *Scientific Reports*, 10(1):2861, 2020.

[56] Jia Mian Hu, Tiannan Yang, and Long Qing Chen. Strain-mediated voltage-controlled switching of magnetic skyrmions in nanostructures. *npj Computational Materials*, 4(1):62, 2018.

[57] A. Hrabec, J. Sampaio, M. Belmeguenai, I. Gross, R. Weil, S. M. Chérif, A. Stashkevich, V. Jacques, A. Thiaville, and S. Rohart. Current-induced skyrmion generation and dynamics in symmetric bilayers. *Nature Communications*, 8:15765, 2017.

[58] Bertrand Dupé, Markus Hoffmann, Charles Paillard, and Stefan Heinze. Tailoring magnetic skyrmions in ultra-thin transition metal films. *Nature Communications*, 5:4030, 2014.

[59] Hongxin Yang, AndrAndré Thiaville, Stanislas Rohart, Albert Fert, and Mairbek Chshiev. Anatomy of Dzyaloshinskii-Moriya Interaction at Co/Pt Interfaces. *Physical Review Letters*, 115(26):267210, 2015.

[60] Sarah Schlotter, Parnika Agrawal, and Geoffrey S.D. Beach. Temperature dependence of the Dzyaloshinskii-Moriya interaction in Pt/Co/Cu thin film heterostructures. *Applied Physics Letters*, 113(9):092402, 2018.

[61] P. J. Metaxas, J. P. Jamet, A. Mougin, M. Cormier, J. Ferré, V. Baltz, B. Rodmacq, B. Dieny, and R. L. Stamps. Creep and flow regimes of magnetic domain-wall motion in ultrathin Pt/Co/Pt films with perpendicular anisotropy. *Physical Review Letters*, 99(21):217208, 2007.

[62] S. Lemerle, J. Ferré, C. Chappert, V. Mathet, T. Giamarchi, and P. Le Doussal. Domain wall creep in an ising ultrathin magnetic film. *Physical Review Letters*, 80(4):849, 1998.

[63] J. Gorchon, S. Bustingorry, J. Ferré, V. Jeudy, A. B. Kolton, and T. Giamarchi. Pinning-dependent field-driven domain wall dynamics and thermal scaling in an ultrathin Pt/Co/Pt magnetic film. *Physical Review Letters*, 113(2):027205, 2014.

[64] Rubén M. Otxoa, P. E. Roy, R. Rama-Eiroa, J. Godinho, K. Y. Guslienko, and J. Wunderlich. Walker-like domain wall breakdown in layered antiferromagnets driven by staggered spin-orbit fields. *Communications Physics*, 3(1):190, 2020.

[65] Joon Moon, Jaesung Yoon, Kitae Kim, Seong Hyub Lee, Dae Yun Kim, and Sug Bong Choe. Multiple Walker breakdowns in magnetic multilayers. *Scientific Reports*, 12(1):2307, 2022.

[66] Albert Fert, Nicolas Reyren, and Vincent Cros. Magnetic skyrmions: Advances in physics and potential applications. *Nature Reviews Materials*, 2:17031, 2017.

[67] Naoto Nagaosa and Yoshinori Tokura. Topological properties and dynamics of magnetic skyrmions. *Nature Nanotechnology*, 8(12):899–911, 2013.

[68] A.R. Fert. Magnetic and Transport Properties of Metallic Multilayers. *Materials Science Forum*, 59-60:439–480, 1991.

[69] Jeong-Heon Park. *Magnetoresistive Devices with Perpendicular Magnetic Anisotropy for Spin-Torque Driven Applications.* PhD thesis, Carnegie Mellon University Pittsburgh, Pennsylvania, 2010.

[70] Katharina Zeissler, Simone Finizio, Kowsar Shahbazi, Jamie Massey, Fatma Al Ma'Mari, David M. Bracher, Armin Kleibert, Mark C. Rosamond, Edmund H. Linfield, Thomas A. Moore, Jörg Raabe, Gavin Burnell, and Christopher H. Marrows. Discrete Hall resistivity contribution from N\'eel skyrmions in multilayer nanodiscs. *Nature Nanotechnology*, 13(12):1161–1166, 2018.

[71] Simone Finizio, Katharina Zeissler, Sebastian Wintz, Sina Mayr, Teresa Wessels, Alexandra J. Huxtable, Gavin Burnell, Christopher H. Marrows, and Jörg Raabe. Deterministic Field-Free Skyrmion Nucleation at a Nanoengineered Injector Device. *Nano Letters*, 19(10):7246–7255, 2019.

[72] Marine Schott, Anne Bernand-Mantel, Laurent Ranno, Stefania Pizzini, Jan Vogel, Helene Béa, Claire Baraduc, Stephane Auffret, Gilles Gaudin, and Dominique Givord. The Skyrmion Switch: Turning Magnetic Skyrmion Bubbles on and off with an Electric Field. *Nano Letters*, 17(5):3006–3012, 2017.

[73] S. L. Zhang, G. Van Der Laan, and T. Hesjedal. Direct experimental determination of the topological winding number of skyrmions in Cu2OSeO3. *Nature Communications*, 8:14619, 2017.

[74] Xichao Zhang, Yan Zhou, Kyung Mee Song, Tae Eon Park, Jing Xia, Motohiko Ezawa, Xiaoxi Liu, Weisheng Zhao, Guoping Zhao, and Seonghoon Woo. Skyrmion-electronics: Writing, deleting, reading and processing magnetic skyrmions toward spintronic applications. *Journal of Physics Condensed Matter*, 32(14): 143001, 2020.

[75] D. Weller, Y. Wu, J. Stöhr, M. G. Samant, B. D. Hermsmeier, and C. Chappert. Orbital magnetic moments of Co in multilayers with perpendicular magnetic anisotropy. *Physical Review B*, 49(18):12888, 1994.

[76] F. Wilhelm, P. Poulopoulos, G. Ceballos, H. Wende, K. Baberschke, P. Srivastava, D. Benea, H. Ebert, M. Angelakeris, N. K. Flevaris, D. Niarchos, A. Rogalev, and N. B. Brookes. Layer-resolved magnetic moments in Ni/Pt multilayers. *Physical Review Letters*, 85(2):413, 2000.

[77] P. Bruno and J. P. Renard. Magnetic surface anisotropy of transition metal ultrathin films. *Applied Physics A Solids and Surfaces*, 49(5):499–506, 1989.

[78] Xin Ma, Guoqiang Yu, Xiang Li, Tao Wang, Di Wu, Kevin S. Olsson, Zhaodong Chu, Kyongmo An, John Q. Xiao, Kang L. Wang, and Xiaoqin Li. Interfacial control of Dzyaloshinskii-Moriya interaction in heavy metal/ferromagnetic metal thin film heterostructures. *Physical Review B*, 94(18):180408, 2016.

[79] Yong Chang Lau, Zhendong Chi, Tomohiro Taniguchi, Masashi Kawaguchi, Goro Shibata, Naomi Kawamura, Motohiro Suzuki, Shunsuke Fukami, Atsushi Fujimori, Hideo Ohno, and Masamitsu Hayashi. Giant perpendicular magnetic anisotropy in Ir/Co/Pt multilayers. *Physical Review Materials*, 3(10):104419, 2019.

[80] Kento Yamamoto, Abdul Muizz Pradipto, Kenji Nawa, Toru Akiyama, Tomonori Ito, Teruo Ono, and Kohji Nakamura. Interfacial Dzyaloshinskii-Moriya interaction and orbital magnetic moments of metallic multilayer films. *AIP Advances*, 7(5):056302, 2017.

[81] Manish K. Niranjan, Chun Gang Duan, Sitaram S. Jaswal, and Evgeny Y. Tsymbal. Electric field effect on magnetization at the Fe/MgO(001) interface. *Applied Physics Letters*, 96(22):222504, 2010.

[82] K. Nakamura, T. Akiyama, T. Ito, M. Weinert, and A. J. Freeman. Electric field-induced modification of magnetocrystalline anisotropy in transition-metal films and at metal-insulator interfaces. *Journal of Magnetics*, 16(2):161–163, 2011.

[83] L. Herrera Diez, Y. T. Liu, D. A. Gilbert, M. Belmeguenai, J. Vogel, S. Pizzini, E. Martinez, A. Lamperti, J. B. Mohammedi, A. Laborieux, Y. Roussigné, A. J. Grutter, E. Arenholtz, P. Quarterman, B. Maranville, S. Ono, M. Salah El Hadri, R. Tolley, E. E. Fullerton, L. Sanchez-Tejerina, A. Stashkevich, S. M. Chérif, A. D. Kent, D. Querlioz, J. Langer, B. Ocker, and D. Ravelosona. Nonvolatile Ionic Modification of the Dzyaloshinskii-Moriya Interaction. *Physical Review Applied*, 12(3):034005, 2019.

[84] Yoichi Shiota, Takuto Maruyama, Takayuki Nozaki, Teruya Shinjo, Masashi Shiraishi, and Yoshishige Suzuki. Voltage-assisted magnetization switching in ultrathin Fe80Co20 alloy layers. *Applied Physics Express*, 2(6):063001, 2009.

[85] Pin Jui Hsu, Andre Kubetzka, Aurore Finco, Niklas Romming, Kirsten Von Bergmann, and Roland Wiesendanger. Electric-field-driven switching of individual magnetic skyrmions. *Nature Nanotechnology*, 12(2):123–126, 2017.

[86] M. Kuepferling, A. Casiraghi, G. Soares, G. Durin, F. Garcia-Sanchez, L. Chen, C. H. Back, C. H. Marrows, S. Tacchi, and G. Carlotti. Measuring interfacial

Dzyaloshinskii-Moriya interaction in ultrathin magnetic films. *Reviews of Modern Physics*, 95(1):015003, 2023.

[87] Adam William John Wells. *Interface morphology and Dzyaloshinskii-Moriya interaction in Pt/Co thin films.* PhD thesis, University of Leeds, Leeds, UK, 2017.

[88] Emily Rechel Darwin. *Tuning Synthetic Antiferromagnetic and Ferromagnetic Multilayers for Hosting Skyrmions.* PhD thesis, University of Leeds, Leeds, 2023.

[89] Khulaif Alshammari. *Temperature and strain dependence of the magnetic properties of multilayers with interfacial DMI.* PhD thesis, University of Leeds, Leeds, UK, 2021.

[90] Lin Huang. *Magnetisation Texture Motion Driven by Spin Currents: Simulation and Measurement.* PhD thesis, University of Leeds, Leeds, 2024.

[91] Mahesh C. Karunarathne, Joseph W. Baumann, Mary Jane Heeg, Philip D. Martin, and Charles H. Winter. Synthesis, structural characterization, and volatility evaluation of zirconium and hafnium amidate complexes. *Journal of Organometallic Chemistry*, 847:204–212, 2017.

[92] Steven M. George. Atomic layer deposition: An overview. *Chemical Reviews*, 110 (1):111–131, 2010.

[93] Ekaterina Gousseva, Scott D. Midgley, Jake M. Seymour, Robert Seidel, Ricardo Grau-Crespo, and Kevin R.J. Lovelock. Understanding X-ray Photoelectron Spectra of Ionic Liquids: Experiments and Simulations of 1-Butyl-3-methylimidazolium Thiocyanate. *Journal of Physical Chemistry B*, 126(49): 10500–10509, 2022.

[94] D. Nanda Gopala Krishna and John Philip. Review on surface-characterization applications of X-ray photoelectron spectroscopy (XPS): Recent developments and challenges, 2022.

[95] G. Greczynski and L. Hultman. X-ray photoelectron spectroscopy: Towards reliable binding energy referencing. *Progress in Materials Science*, 107:100591, 2020.

[96] John Michael David Coey and Karsten Rode. Dilute Magnetic Oxides and Nitrides. In *Handbook of Magnetism and Advanced Magnetic Materials*. John Wiley & Sons, 2007.

[97] John Kerr. On reflection of polarized light from the equatorial surface of a magnet. *The London, Edinburgh, and Dublin Philosophical Magazine and Journal of Science*, 5(30):161–177, 1878.

[98] J. A. Cape and G. W. Lehman. Magnetic domain structures in thin uniaxial plates with perpendicular easy axis. *Journal of Applied Physics*, 42(13):5732–5756, 1971.

[99] Alex Hubert and Rudolf Schäfer. *Magnetic domain: Magnetic Domains: The Analysis of Magnetic Microestructures*. Springer, 2009.

[100] S. A. Montoya, S. Couture, J. J. Chess, J. C.T. Lee, N. Kent, D. Henze, S. K. Sinha, M. Y. Im, S. D. Kevan, P. Fischer, B. J. McMorran, V. Lomakin, S. Roy, and E. E. Fullerton. Tailoring magnetic energies to form dipole skyrmions and skyrmion lattices. *Physical Review B*, 95(2):024415, 2017.

[101] Andrii S. Savchenko, Vladyslav M. Kuchkin, Filipp N. Rybakov, and Nikolai S. Kiselev. Magnetic bubbles with alternating chirality in domain walls. *Frontiers in Physics*, 11:1223609, 2023.

[102] A.P. Malozemoff and J.C. Slonczewski. Resume of Classical Magnetism and Bubble Domain Statics. In *Magnetic Domain Walls in Bubble Materials*. Elsevier Inc., 1979.

[103] T. T. Wang, W. Liu, Z. M. Dai, X. T. Zhao, X. G. Zhao, and Z. D. Zhang. Magnetic bubbles and domain evolution in Fe/Gd multilayer nanodots. *Journal of Magnetism and Magnetic Materials*, 451:660–664, 2018.

[104] A. A. Thiele. The Theory of Cylindrical Magnetic Domains. *Bell System Technical Journal*, 48(10):3287 – 3335, 1969.

[105] Karine Chesnel, Andrew S. Westover, Carson Richards, Brittni Newbold, Matthew Healey, Lauren Hindman, Berg Dodson, Kelsey Cardon, David Montealegre, Jeremy Metzner, Tobias Schneider, Benny Böhm, Fabian Samad, Lorenzo Fallarino, and Olav Hellwig. Morphological stripe-bubble transition in remanent

magnetic domain patterns of Co/Pt multilayer films and its dependence on Co thickness. *Physical Review B*, 98(22):224404, 2018.

[106] Gong Chen, Tianping Ma, Alpha T. N'Diaye, Heeyoung Kwon, Changyeon Won, Yizheng Wu, and Andreas K. Schmid. Tailoring the chirality of magnetic domain walls by interface engineering. *Nature Communications*, 4:2671, 2013.

[107] E. H. Hall. On a New Action of the Magnet on Electric Currents. *American Journal of Mathematics*, 2(3):287–292, 1879.

[108] E.H. Hall. On the "Rotational Coefficient" in nickel and cobalt. *The London, Edinburgh, and Dublin Philosophical Magazine and Journal of Science*, 12(74): 325, 1881.

[109] Naoto Nagaosa. Anomalous hall effect - A new perspective. *Journal of the Physical Society of Japan*, 75(4):042001, 2006.

[110] Leon Brillouin. Diffusion de la lumière et des rayons X par un corps transparent homogène. Influence de l'agitation thermique. *Ann. Phys. (Paris)*, 17(21):88–122, 1922.

[111] Mohamed Belmeguenai, Jean Paul Adam, Yves Roussigné, Sylvain Eimer, Thibaut Devolder, Joo Von Kim, Salim Mourad Cherif, Andrey Stashkevich, and Andre Thiaville. Interfacial Dzyaloshinskii-Moriya interaction in perpendicularly magnetized Pt/Co/AlOx ultrathin films measured by Brillouin light spectroscopy. *Physical Review B - Condensed Matter and Materials Physics*, 91(18):180405, 5 2015.

[112] H. Bouloussa, R. Ramaswamy, Y. Roussigné, A. Stashkevich, H. Yang, M. Belmeguenai, and S. M. Chérif. Pt concentration dependence of the interfacial Dzyaloshinskii-Moriya interaction, the Gilbert damping parameter and the magnetic anisotropy in Py/Cu1-xPtx systems. *Journal of Physics D: Applied Physics*, 52(5):055001, 2019.

[113] Gary Ledger. *X-ray Magnetic Circular Dichroism and Scanning Tunnelling Microscopy applied to Molecular Spintronics Supervised at the Diamond Light Source by.* PhD thesis, University of Liverpool, Liverpool, 10 2017.

[114] Stefania Pizzini, Jan Vogel, Marlio Bonfim, and Alain Fontaine. Time-Resolved X-Ray Magnetic Circular Dichroism A Selective Probe of Magnetization Dynamics on Nanosecond Timescales. In *Spin Dynamics in Confined Magnetic Structures II*, pages 157–187. Springer, 2007.

[115] Michel Armand, Frank Endres, Douglas R. MacFarlane, Hiroyuki Ohno, and Bruno Scrosati. Ionic-liquid materials for the electrochemical challenges of the future, 2009.

[116] R. Martel, V. Derycke, C. Lavoie, J. Appenzeller, K. K. Chan, J. Tersoff, and Ph Avouris. Ambipolar electrical transport in semiconducting single-wall carbon nanotubes. *Physical Review Letters*, 87(25):256805, 2001.

[117] Maan Hayyan, Farouq S. Mjalli, Mohd Ali Hashim, Inas M. AlNashef, and Tan Xue Mei. Investigating the electrochemical windows of ionic liquids. *Journal of Industrial and Engineering Chemistry*, 19(1):106–112, 2013.

[118] Kallidanthiyil Chellappan Lethesh, Ahmed Bahaa, Mariam Abdullah, Musbaudeen O. Bamgbopa, and Rahmat Agung Susantyoko. Temperature-Dependent Electrochemical Stability Window of Bis(trifluoromethanesulfonyl)imide and Bis(fluorosulfonyl)imide Anion Based Ionic Liquids. *Frontiers in Chemistry*, 10: 859304, 2022.

[119] Julius de Rojas, Alberto Quintana, Aitor Lopeandia, JoaquÃn Salguero, Jose L. Costa-Krämer, Llibertat Abad, Maciej O. Liedke, Maik Butterling, Andreas Wagner, Lowie Henderick, Jolien Dendooven, Christophe Detavernier, Jordi Sort, and Enric Menéndez. Boosting Room-Temperature Magneto-Ionics in a Non-Magnetic Oxide Semiconductor. *Advanced Functional Materials*, 30(36):2003704, 2020.

[120] Julius de Rojas, Alberto Quintana, Aitor Lopeandía, Joaquin Salguero, Beatriz Muniz, Fatima Ibrahim, Mairbek Chshiev, Aliona Nicolenco, Maciej O. Liedke, Maik Butterling, Andreas Wagner, Veronica Sireus, Llibertat Abad, Christopher J. Jensen, Kai Liu, Josep Nogués, Jose L. Costa-Krämer, Enric Menendez, and Jordi Sort. Voltage-driven motion of nitrogen ions: a new paradigm for magneto-ionics. *Nature Communications*, 11(1):5871, 2020.

[121] Zheng Ma, Laura Fuentes-Rodriguez, Zhengwei Tan, Eva Pellicer, Llibertat Abad, Javier Herrero-Martín, Enric Menéndez, Nieves Casañ-Pastor, and Jordi Sort. Wireless magneto-ionics: voltage control of magnetism by bipolar electrochemistry. *Nature Communications*, 14(1):6486, 2023.

[122] Benjamin I. Weintrub, Yu Ling Hsieh, Sviatoslav Kovalchuk, Jan N. Kirchhof, Kyrylo Greben, and Kirill I. Bolotin. Generating intense electric fields in 2D materials by dual ionic gating. *Nature Communications*, 13(1):6601, 2022.

[123] S. Ono, K. Miwa, S. Seki, and J. Takeya. A comparative study of organic single-crystal transistors gated with various ionic-liquid electrolytes. *Applied Physics Letters*, 94(6):063301, 2009.

[124] Martin Z. Bazant, Brian D. Storey, and Alexei A. Kornyshev. Double layer in ionic liquids: Overscreening versus crowding. *Physical Review Letters*, 106(4): 046102, 2011.

[125] Patricia C. Marr and Andrew C. Marr. Ionic liquid gel materials: Applications in green and sustainable chemistry. *Green Chemistry*, 18(1):105–128, 2015.

[126] Takuya Fujimoto and Kunio Awaga. Electric-double-layer field-effect transistors with ionic liquids, 2013.

[127] A. Cimini, O. Palumbo, E. Simonetti, M. De Francesco, G. B. Appetecchi, S. Fantini, R. Lin, A. Falgayrat, and A. Paolone. Decomposition temperatures and vapour pressures of selected ionic liquids for electrochemical applications. *Journal of Thermal Analysis and Calorimetry*, 142(5):1791–1797, 2020.

[128] Takahiro Ampo and Takahide Oya. Development of paper actuators based on carbon-nanotube-composite paper. *Molecules*, 26(5):1463, 2021.

[129] Grazvydas Ziemys, Valentin Ahrens, Simon Mendisch, Gyorgy Csaba, and Markus Becherer. Speeding up nanomagnetic logic by DMI enhanced Pt/Co/Ir films. *AIP Advances*, 8(5):056310, 2018.

[130] Katharina Zeissler, Simone Finizio, Craig Barton, Alexandra J. Huxtable, Jamie Massey, Jörg Raabe, Alexandr V. Sadovnikov, Sergey A. Nikitov, Richard Brearton, Thorsten Hesjedal, Gerrit van der Laan, Mark C. Rosamond, Edmund H.

Linfield, Gavin Burnell, and Christopher H. Marrows. Diameter-independent skyrmion Hall angle observed in chiral magnetic multilayers. *Nature Communications*, 11(1):428, 2020.

[131] Andrew D. Kent. Spintronics: Perpendicular all the way. *Nature Materials*, 9(9): 699–700, 2010.

[132] Xiangqian Wang, Yurui Wei, Kaizhou He, Yueyue Liu, Yi Huang, Qingfang Liu, Jianbo Wang, and Genliang Han. Effect of the repeat number and Co layer thickness on the magnetization reversal process in [Pt/Co(x)]N multilayers. *Journal of Physics D: Applied Physics*, 53(21):215001, 2020.

[133] S. Hashimoto, Y. Ochiai, and K. Aso. Perpendicular magnetic anisotropy and magnetostriction of sputtered Co/Pd and Co/Pt multilayered films. *Journal of Applied Physics*, 66(10):4909–4916, 1989.

[134] P. F. Carcia. Perpendicular magnetic anisotropy in Pd/Co and Pt/Co thin-film layered structures. *Journal of Applied Physics*, 63(10):5066–5073, 1988.

[135] E. Ascher, H. Rieder, H. Schmid, and H. Stössel. Some properties of ferromagnetoelectric nickel-iodine boracite, Ni 3B7O13I. *Journal of Applied Physics*, 37(3): 1404–1405, 1966.

[136] Cheng Song, Bin Cui, Fan Li, Xiangjun Zhou, and Feng Pan. Recent progress in voltage control of magnetism: Materials, mechanisms, and performance. *Progress in Materials Science*, 87:33–82, 2017.

[137] Chun Gang Duan, Julian P. Velev, R. F. Sabirianov, Ziqiang Zhu, Junhao Chu, S. S. Jaswal, and E. Y. Tsymbal. Surface magnetoelectric effect in ferromagnetic metal films. *Physical Review Letters*, 101(13):137201, 2008.

[138] Daichi Chiba. Electric field effect on magnetism in metallic ultra-thin films. *Frontiers in Physics*, 3(OCT):83, 2015.

[139] Fumihiro Matsukura, Yoshinori Tokura, and Hideo Ohno. Control of magnetism by electric fields. *Nature Nanotechnology*, 10(3):209–220, 2015.

[140] Shufeng Zhang. Spin-dependent surface screening in ferromagnets and magnetic tunnel junctions. *Physical Review Letters*, 83(3):640, 1999.

[141] L. Fallarino, A. Oelschlägel, J. A. Arregi, A. Bashkatov, F. Samad, B. Böhm, K. Chesnel, and O. Hellwig. Control of domain structure and magnetization reversal in thick Co/Pt multilayers. *Physical Review B*, 99(2):024431, 2019.

[142] O. Hellwig, G. P. Denbeaux, J. B. Kortright, and Eric E. Fullerton. X-ray studies of aligned magnetic stripe domains in perpendicular multilayers. *Physica B: Condensed Matter*, 336(1,2):136–144, 2003.

[143] M. J. Benitez, A. Hrabec, A. P. Mihai, T. A. Moore, G. Burnell, D. Mcgrouther, C. H. Marrows, and S. McVitie. Magnetic microscopy and topological stability of homochiral Néel domain walls in a Pt/Co/AlO x trilayer. *Nature Communications*, 6:8957, 2015.

[144] Vikas Kashid, Timo Schena, Bernd Zimmermann, Yuriy Mokrousov, Stefan Blügel, Vaishali Shah, and H. G. Salunke. Dzyaloshinskii-Moriya interaction and chiral magnetism in 3d-5d zigzag chains: Tight-binding model and ab initio calculations. *Physical Review B - Condensed Matter and Materials Physics*, 90 (5):054412, 2014.

[145] Andre Thiaville, Stanislas Rohart, Emilie Jué, Vincent Cros, and Albert Fert. Dynamics of Dzyaloshinskii domain walls in ultrathin magnetic films. *Europhysics Letters*, 100(5):57002, 2012.

[146] R. Lavrijsen, D. M.F. Hartmann, A. Van Den Brink, Y. Yin, B. Barcones, R. A. Duine, M. A. Verheijen, H. J.M. Swagten, and B. Koopmans. Asymmetric magnetic bubble expansion under in-plane field in Pt/Co/Pt: Effect of interface engineering. *Physical Review B - Condensed Matter and Materials Physics*, 91(10): 104414, 2015.

[147] Jaehun Cho, Nam Hui Kim, Sukmock Lee, June Seo Kim, Reinoud Lavrijsen, Aurelie Solignac, Yuxiang Yin, Dong Soo Han, Niels J.J. Van Hoof, Henk J.M. Swagten, Bert Koopmans, and Chun Yeol You. Thickness dependence of the interfacial Dzyaloshinskii-Moriya interaction in inversion symmetry broken systems. *Nature Communications*, 6:7635, 2015.

[148] R. M. Rowan-Robinson, A. A. Stashkevich, Y. Roussigné, M. Belmeguenai, S. M. Chérif, A. Thiaville, T. P.A. Hase, A. T. Hindmarch, and D. Atkinson. The

interfacial nature of proximity-induced magnetism and the Dzyaloshinskii-Moriya interaction at the Pt/Co interface. *Scientific Reports*, 7(1):16835, 2017.

[149] Serban Lepadatu. Effect of inter-layer spin diffusion on skyrmion motion in magnetic multilayers. *Scientific Reports*, 9(1):9592, 2019.

[150] Voicu O. Dolocan. Domain wall pinning and interaction in rough cylindrical nanowires. *Applied Physics Letters*, 105(16):162401, 2014.

[151] Kyoung Woong Moon, Jae Chul Lee, Sug Bong Choe, and Kyung Ho Shin. Determination of perpendicular magnetic anisotropy in ultrathin ferromagnetic films by extraordinary Hall voltage measurement. *Review of Scientific Instruments*, 80 (11):113904, 2009.

[152] Joseph Barker. Bloch's Law Derivations. Technical report, University of Leeds, Leeds, 6 2020.

[153] M. Kona, P. Spišák, P. Kollár, P. Sovák, O. Duša, and T. Reininger. Temperature Dependence of the Magnetization and of the other Physical Properties of Rapidly Quenched Amorphous CoB Alloys. *IEEE Transactions on Magnetics*, 30(2):524 – 526, 1994.

[154] M. D. Kuzmin, K. P. Skokov, L. V.B. Diop, I. A. Radulov, and O. Gutfleisch. Exchange stiffness of ferromagnets. *European Physical Journal Plus*, 135(3):301, 2020.

[155] Soong Geun Je, Duck Ho Kim, Sang Cheol Yoo, Byoung Chul Min, Kyung Jin Lee, and Sug Bong Choe. Asymmetric magnetic domain-wall motion by the Dzyaloshinskii-Moriya interaction. *Physical Review B - Condensed Matter and Materials Physics*, 88(21):214401, 2013.

[156] Philippa M Shepley. Dataset associated with ”Magnetic properties, domain-wall creep motion, and the Dzyaloshinskii-Moriya interaction in Pt/Co/Ir thin films”. *Physical Review B*, 97(13):134417, 2018.

[157] Philippa M. Shepley, Harry Tunnicliffe, Kowsar Shahbazi, Gavin Burnell, and Thomas A. Moore. Magnetic properties, domain-wall creep motion, and the Dzyaloshinskii-Moriya interaction in Pt/Co/Ir thin films. *Physical Review B*, 97 (13):134417, 2018.

[158] Pascal Chauve, Thierry Giamarchi, and Pierre Le Doussal. Creep and depinning in disordered media. *Physical Review B - Condensed Matter and Materials Physics*, 62(10):6241, 2000.

[159] Juriaan Lucassen, Marielle J. Meijer, Mark C.H. De Jong, Rembert A. Duine, Henk J.M. Swagten, Bert Koopmans, and Reinoud Lavrijsen. Stabilizing chiral spin structures via an alternating Dzyaloshinskii-Moriya interaction. *Physical Review B*, 102(1):014451, 2020.

[160] Rohit Pachat, Djoudi Ourdani, Maria Andromachi Syskaki, Alessio Lamperti, Subhajit Roy, Song Chen, Adriano Di Pietro, Ludovic Largeau, Romeo Juge, Maryam Massouras, Cristina Balan, Johannes Wilhelmus van der Jagt, Guillaume Agnus, Yves Roussigné, Mihai Gabor, Salim Mourad Chérif, Gianfranco Durin, Shimpei Ono, Jurgen Langer, Damien Querlioz, Dafine Ravelosona, Mohamed Belmeguenai, and Liza Herrera Diez. Magneto-Ionics in Annealed W/CoFeB/HfO2 Thin Films. *Advanced Materials Interfaces*, 9(36):2200690, 2022.

[161] Martin Nichterwitz, Sabine Neitsch, Stefan Röher, Daniel Wolf, Kornelius Nielsch, and Karin Leistner. Voltage-controlled on switching and manipulation of magnetization via the redox transformation of β-FeOOH nanoplatelets. *Journal of Physics D: Applied Physics*, 53(8):084001, 2020.

[162] Di Yi, Yujia Wang, Olaf M.J. vant Erve, Liubin Xu, Hongtao Yuan, Michael J. Veit, Purnima P. Balakrishnan, Yongseong Choi, Alpha T. N Diaye, Padraic Shafer, Elke Arenholz, Alexander Grutter, Haixuan Xu, Pu Yu, Berend T. Jonker, and Yuri Suzuki. Emergent electric field control of phase transformation in oxide superlattices. *Nature Communications*, 11(1):902, 2020.

[163] Shuai Ning, Qiqi Zhang, Connor Occhialini, Riccardo Comin, Xiaoyan Zhong, and Caroline A. Ross. Voltage Control of Magnetism above Room Temperature in Epitaxial SrCo1- xFexO3-δ. *ACS Nano*, 14(7):8949–8957, 2020.

[164] M. Nichterwitz, S. Honnali, M. Kutuzau, S. Guo, J. Zehner, K. Nielsch, and K. Leistner. Advances in magneto-ionic materials and perspectives for their application. *APL Materials*, 9(3):030903, 2021.

[165] Felix Büttner, C. Moutafis, M. Schneider, B. Krüger, C. M. Günther, J. Geilhufe, C. V.Korff Schmising, J. Mohanty, B. Pfau, S. Schaffert, A. Bisig, M. Foerster, T. Schulz, C. A.F. Vaz, J. H. Franken, H. J.M. Swagten, M. Kläui, and S. Eisebitt. Dynamics and inertia of skyrmionic spin structures. *Nature Physics*, 11(3):225–228, 2015.

[166] R. Lavrijsen, G. Malinowski, J. H. Franken, J. T. Kohlhepp, H. J.M. Swagten, B. Koopmans, M. Czapkiewicz, and T. Stobiecki. Reduced domain wall pinning in ultrathin Pt/ Co100-x B x /Pt with perpendicular magnetic anisotropy. *Applied Physics Letters*, 96(2), 2010. ISSN 00036951. doi: 10.1063/1.3280373.

[167] Uwe Bauer, Satoru Emori, and Geoffrey S.D. Beach. Voltage-controlled domain wall traps in ferromagnetic nanowires. *Nature Nanotechnology*, 8(6):411–416, 2013.

[168] S. Ono, S. Seki, R. Hirahara, Y. Tominari, and J. Takeya. High-mobility, low-power, and fast-switching organic field-effect transistors with ionic liquids. *Applied Physics Letters*, 92(10):103313, 2008.

[169] Chris Leighton. Electrolyte-based ionic control of functional oxides. *Nature Materials*, 18(1):13–18, 2019.

[170] Youdi Gu, Cheng Song, Qian Wang, Weijin Hu, Wei Liu, Feng Pan, and Zhidong Zhang. Emerging opportunities for voltage-driven magneto-ionic control in ferroic heterostructures, 4 2021.

[171] Cristina Balan, Jose Peña Garcia, Aymen Fassatoui, Jan Vogel, Dayane De Souza Chaves, Marlio Bonfim, Jean Pascal Rueff, Laurent Ranno, and Stefania Pizzini. Tuning the Dynamics of Chiral Domain Walls of Ferrimagnetic Films by Magnetoionic Effects. *Physical Review Applied*, 18(3):034065, 9 2022.

[172] Hao Bo Li, Nianpeng Lu, Qinghua Zhang, Yujia Wang, Deqiang Feng, Tianzhe Chen, Shuzhen Yang, Zheng Duan, Zhuolu Li, Yujun Shi, Weichao Wang, Wei Hua Wang, Kui Jin, Hui Liu, Jing Ma, Lin Gu, Cewen Nan, and Pu Yu. Electric-field control of ferromagnetism through oxygen ion gating. *Nature Communications*, 8(1):2156, 2017.

[173] Xiangjun Zhou, Yinuo Yan, Miao Jiang, Bin Cui, Feng Pan, and Cheng Song. Role of oxygen ion migration in the electrical control of magnetism in Pt/Co/Ni/HfO2 films. *Journal of Physical Chemistry C*, 120(3):1633–1639, 2016.

[174] Chong Bi, Yaohua Liu, T. Newhouse-Illige, M. Xu, M. Rosales, J. W. Freeland, Oleg Mryasov, Shufeng Zhang, S. G.E. Te Velthuis, and W. G. Wang. Reversible control of Co magnetism by voltage-induced oxidation. *Physical Review Letters*, 113(26):267202, 2014.

[175] Dustin A. Gilbert, Alexander J. Grutter, Elke Arenholz, Kai Liu, B. J. Kirby, Julie A. Borchers, and Brian B. Maranville. Structural and magnetic depth profiles of magneto-ionic heterostructures beyond the interface limit. *Nature Communications*, 7:12264, 2016.

[176] Jiwan Acharya, Balasubramaniam Gnana Sundara Raj, Tae Hoon Ko, Myung Seob Khil, Hak Yong Kim, and Byoung Suhk Kim. Facile one pot sonochemical synthesis of CoFe2O4/MWCNTs hybrids with well-dispersed MWCNTs for asymmetric hybrid supercapacitor applications. *International Journal of Hydrogen Energy*, 45(4):3073–3085, 1 2020.

[177] Mark C. Biesinger, Brad P. Payne, Andrew P. Grosvenor, Leo W.M. Lau, Andrea R. Gerson, and Roger St C. Smart. Resolving surface chemical states in XPS analysis of first row transition metals, oxides and hydroxides: Cr, Mn, Fe, Co and Ni. *Applied Surface Science*, 257(7):2717–2730, 2011.

[178] M. Behazin, M. C. Biesinger, J. J. Noël, and J. C. Wren. Comparative study of film formation on high-purity Co and Stellite-6: Probing the roles of a chromium oxide layer and gamma-radiation. *Corrosion Science*, 63:40–50, 2012.

[179] Mark C. Biesinger, Brad P. Payne, Leo W.M. Lau, Andrea Gerson, and Roger St C. Smart. X-ray photoelectron spectroscopic chemical state Quantification of mixed nickel metal, oxide and hydroxide systems. *Surface and Interface Analysis*, 41(4):324–332, 2009.

[180] J. M. Wood, C. I. Oseghale, O. Cespedes, M. Grell, and D. A. Allwood. Control of ferromagnetic properties of Ni80Fe20 thin films by voltage-induced oxidation. *Journal of Applied Physics*, 124(8):085304, 2018.

[181] Jing Yang, Hongwei Liu, Wayde N. Martens, and Ray L. Frost. Synthesis and characterization of Cobalt hydroxide, cobalt oxyhydroxide, and cobalt oxide nanodiscs. *Journal of Physical Chemistry C*, 114(1):111–119, 2010.

[182] John F Moulder, William F Stickle, Peter E Sobol, and Kenneth D Bomben. *Handbook of X-ray Photoelectron Spectroscopy: A Reference Book of Standard Spectra for Identification and Interpretation of XPS Data.* Physical Electronics, Inc., Minnesota, 1992.

[183] Andrew P. Grosvenor, Stephen D. Wik, Ronald G. Cavell, and Arthur Mar. Examination of the bonding in binary transition-metal monophosphides MP (M = Cr, Mn, Fe, Co) by X-ray photoelectron spectroscopy. *Inorganic Chemistry*, 44(24):8988–8998, 2005.

[184] Kwok Feng Chong Eslam A.A. Aboelazm, Gomaa A.M. Ali. Cobalt Oxide Supercapacitor Electrode Recovered from Spent Lithium-Ion Battery. *Chemistry of Advanced Materials*, 3(4):67–74, 2018.

[185] Md Abu Sayeed, Tenille Herd, and Anthony P. O'Mullane. Direct electrochemical formation of nanostructured amorphous Co(OH)2 on gold electrodes with enhanced activity for the oxygen evolution reaction. *Journal of Materials Chemistry A*, 4(3):991–999, 2016.

[186] Enxian Yuan, Meixia Zhou, Mingqing Gu, Panming Jian, Lin Xia, and Jingran Xiao. Boosting Creation of Oxygen Vacancies in Co-Co3O4 Homogeneous Hybrids for Aerobic Oxidation of Cyclohexane. *Catalysis Letters*, 152(1):282–298, 2022.

[187] Zakaria Azdad, Laurent Marot, Lucas Moser, Roland Steiner, and Ernst Meyer. Valence band behaviour of zirconium oxide, Photoelectron and Auger spectroscopy study. *Scientific Reports*, 8(1):16251, 2018.

[188] Y. Popat, M. Orlandi, S. Gupta, N. Bazzanella, S. Pillai, M. K. Patel, A. Miotello, and N. Patel. Morphological and Elemental Investigations on Coâ€“Feâ€“Bâ€“O Thin Films Deposited by Pulsed Laser Deposition for Alkaline Water Oxidation: Charge Exchange Efficiency as the Prevailing Factor in Comparison with the Adsorption Process. *Catalysis Letters*, 152(2):438–451, 2022.

[189] Yang Zhao, Min Luo, Shufen Chu, Ming Peng, Boyang Liu, Qiuli Wu, Pan Liu, Frank M.F. de Groot, and Yongwen Tan. 3D nanoporous iridium-based alloy microwires for efficient oxygen evolution in acidic media. *Nano Energy*, 59:146–153, 2019.

[190] Neil G. Farr and Hans J. Griesser. XPS excitation dependence of measured cobalt 2p3 2 peak intensity due to auger peak interference. *Journal of Electron Spectroscopy and Related Phenomena*, 49(3):293–302, 1989.

[191] Agustin R. González-Elipe and Francisco Yubero. SPECTROSCOPIC CHARACTERIZATION OF OXIDE/OXIDE INTERFACES. In *Handbook of Surfaces and Interfaces of Materials*. Academic Press, 2001.

[192] Yu Jin Park, Jooyoung Lee, Yoo Sei Park, Juchan Yang, Myeong Je Jang, Jaehoon Jeong, Seunghoe Choe, Jung Woo Lee, Jung Dae Kwon, and Sung Mook Choi. Electrodeposition of High-Surface-Area IrO2 Films on Ti Felt as an Efficient Catalyst for the Oxygen Evolution Reaction. *Frontiers in Chemistry*, 8:593272, 2020.

[193] Seunghoe Choe, Byung Seok Lee, Min Kyung Cho, Hyoung Juhn Kim, Dirk Henkensmeier, Sung Jong Yoo, Jin Young Kim, So Young Lee, Hyun S. Park, and Jong Hyun Jang. Electrodeposited IrO2/Ti electrodes as durable and cost-effective anodes in high-temperature polymer-membrane-electrolyte water electrolyzers. *Applied Catalysis B: Environmental*, 226:289–294, 2018.

[194] Dmytro S. Kozak, Ruslan A. Sergiienko, Etsuro Shibata, Atsushi Iizuka, and Takashi Nakamura. Non-electrolytic synthesis of copper oxide/carbon nanocomposite by surface plasma in super-dehydrated ethanol. *Scientific Reports*, 6:21178, 2016.

[195] Biljana Šljukić, Craig E. Banks, Alison Crossley, and Richard G. Compton. Copper oxide - Graphite composite electrodes: Application to nitrite sensing. *Electroanalysis*, 19(1):79–84, 2007.

[196] T. M. Ivanova, K. I. Maslakov, A. A. Sidorov, M. A. Kiskin, R. V. Linko, S. V. Savilov, V. V. Lunin, and I. L. Eremenko. XPS detection of unusual Cu(II) to Cu(I) transition on the surface of complexes with redox-active ligands. *Journal of Electron Spectroscopy and Related Phenomena*, 238:146878, 2020.

[197] I. A. Safo, M. Werheid, C. Dosche, and M. Oezaslan. The role of polyvinylpyrrolidone (PVP) as a capping and structure-directing agent in the formation of Pt nanocubes. *Nanoscale Advances*, 1(8):3095–3106, 2019.

[198] Fatih Şen and GÜlsÜn G\"Okagaç. Different sized platinum nanoparticles supported on carbon: An XPS study on these methanol oxidation catalysts. *Journal of Physical Chemistry C*, 111(15):5715–5720, 2007.

[199] N. Satchell, T. Mitchell, P. M. Shepley, E. Darwin, B. J. Hickey, and G. Burnell. Pt and CoB trilayer Josephson π junctions with perpendicular magnetic anisotropy. *Scientific Reports*, 11(1):11173, 2021.

[200] R. Lavrijsen, G. Malinowski, J. H. Franken, J. T. Kohlhepp, H. J.M. Swagten, B. Koopmans, M. Czapkiewicz, and T. Stobiecki. Reduced domain wall pinning in ultrathin Pt/ Co100-x B x /Pt with perpendicular magnetic anisotropy. *Applied Physics Letters*, 96(2):022501, 2010.

[201] H. K. Tan, Royston J.J. Lim, H. L. Seng, J. Shanmugam, H. Y.Y. Ko, X. M. Cheng, V. Putra, Z. X. Xing, Anjan Soumyanarayanan, and Pin Ho. Intermixing induced anisotropy variations in CoB-based chiral multilayer films. *Journal of Physics D: Applied Physics*, 54(35):354003, 2021.

[202] Fei Wang, Yang Zhang, Zhijie Wang, Haoxiong Zhang, Xi Wu, Changhua Bao, Jia Li, Pu Yu, and Shuyun Zhou. Ionic liquid gating induced self-intercalation of transition metal chalcogenides. *Nature Communications*, 14(1):4945, 2023.

[203] J. Iijima, J. W. Lim, S. H. Hong, S. Suzuki, K. Mimura, and M. Isshiki. Native oxidation of ultra high purity Cu bulk and thin films. *Applied Surface Science*, 253(5):2825–2829, 2006.

[204] Ilia Platzman, Reuven Brener, Hossam Haick, and Rina Tannenbaum. Oxidation of polycrystalline copper thin films at ambient conditions. *Journal of Physical Chemistry C*, 112(4):1101–1108, 2008.

[205] Junxiao Feng, Eva Grimaldi, Can Onur Avci, Manuel Baumgartner, Giovanni Cossu, Antonella Rossi, and Pietro Gambardella. Effects of Oxidation of Top and Bottom Interfaces on the Electric, Magnetic, and Spin-Orbit Torque Properties of Pt / Co / Al Ox Trilayers. *Physical Review Applied*, 13(4):044029, 2020.

[206] Zeyu Zhang, Zhipeng Li, Kangkang Meng, Yong Wu, Jikun Chen, Xiaoguang Xu, and Yong Jiang. Perpendicular magnetic anisotropy in SrTiO3/Co/Pt films induced by oxygen diffusion from CaTiO3 spacer layer. *Applied Physics Letters*, 116(23):232402, 2020.

[207] Hyung Keun Gweon, Seok Jin Yun, and Sang Ho Lim. A very large perpendicular magnetic anisotropy in Pt/Co/MgO trilayers fabricated by controlling the MgO sputtering power and its thickness. *Scientific Reports*, 8(1):1266, 2018.

[208] Hyung Suk Oh, Hong Nhan Nong, Tobias Reier, Arno Bergmann, Manuel Gliech, Jorge Ferreira De Araújo, Elena Willinger, Robert Schlögl, Detre Teschner, and Peter Strasser. Electrochemical Catalyst-Support Effects and Their Stabilizing Role for IrOx Nanoparticle Catalysts during the Oxygen Evolution Reaction. *Journal of the American Chemical Society*, 138(38):12552–12563, 9 2016.

[209] Wei Sun, Ji Yuan Liu, Xue Qing Gong, Waqas Qamar Zaman, Li Mei Cao, and Ji Yang. OER activity manipulated by IrO 6 coordination geometry: An insight from pyrochlore iridates. *Scientific Reports*, 6:38429, 2016.

[210] Masahiro Watanabe, Makoto Uchida, and Satoshi Motoo. Preparation of highly dispersed Pt + Ru alloy clusters and the activity for the electrooxidation of methanol. *Journal of Electroanalytical Chemistry*, 229(1-2):395–406, 1987.

[211] Aicheng Chen and Peter Holt-Hindle. Platinum-based nanostructured materials: Synthesis, properties, and applications. *Chemical Reviews*, 110(6):3767–3804, 2010.

[212] Zheng Ma, Laura Fuentes-Rodriguez, Zhengwei Tan, Eva Pellicer, Llibertat Abad, Javier Herrero-Martín, Enric Menéndez, Nieves Casan-Pastor, and Jordi Sort. Wireless magneto-ionics: voltage control of magnetism by bipolar electrochemistry. *Nature Communications*, 14(1):6486, 2023.

[213] K. Rode, R. Mattana, A. Anane, V. Cros, E. Jacquet, J. P. Contour, F. Petroff, A. Fert, M. A. Arrio, Ph Sainctavit, P. Bencok, F. Wilhelm, N. B. Brookes, and A. Rogalev. Magnetism of (Zn,Co)O thin films probed by x-ray absorption spectroscopies. *Applied Physics Letters*, 92(1):012509, 2008.

[214] Tetsuro Ueno, Jaivardhan Sinha, Nobuhito Inami, Yasuo Takeichi, Seiji Mitani, Kanta Ono, and Masamitsu Hayashi. Enhanced orbital magnetic moments in magnetic heterostructures with interface perpendicular magnetic anisotropy. *Scientific Reports*, 5:14858, 2015.

[215] C. T. Chen, Y. U. Idzerda, H. J. Lin, N. V. Smith, G. Meigs, E. Chaban, G. H. Ho, E. Pellegrin, and F. Sette. Experimental confirmation of the x-ray magnetic circular dichroism sum rules for iron and cobalt. *Physical Review Letters*, 75(1): 152, 1995.

[216] P. Gambardella, S. Rusponi, M. Veronese, S. S. Dhesi, C. Grazioli, A. Dallmeyer, I. Cabria, R. Zeller, P. H. Dederichs, K. Kern, C. Carbone, and H. Brune. Giant magnetic anisotropy of single cobalt atoms and nanoparticles. *Science*, 300(5622): 1130–1133, 2003.

[217] Hari Babu Vasili, Matheus Gamino, Jaume Gàzquez, Florencio Sánchez, Manuel Valvidares, Pierluigi Gargiani, Eric Pellegrin, and Josep Fontcuberta. Magnetoresistance in Hybrid Pt/CoFe2O4 Bilayers Controlled by Competing Spin Accumulation and Interfacial Chemical Reconstruction. *ACS Applied Materials and Interfaces*, 10(14):12031–12041, 2018.

[218] I. Benguettat-El Mokhtari, D. Ourdani, Y. Roussigné, R. B. Mos, M. Nasui, F. Kail, L. Chahed, S. M. Chérif, A. Stashkevich, M. Gabor, and M. Belmeguenai. Perpendicular magnetic anisotropy and interfacial Dzyaloshinskii-Moriya interaction in as grown and annealed X/Co/Y ultrathin systems. *Journal of Physics Condensed Matter*, 32(49):495802, 2020.

[219] M. Tokaç, S. A. Bunyaev, G. N. Kakazei, D. S. Schmool, D. Atkinson, and A. T. Hindmarch. Interfacial Structure Dependent Spin Mixing Conductance in Cobalt Thin Films. *Physical Review Letters*, 115(5):056601, 2015.

[220] M. B. Salamon and Eiji Kita. Aperiodical oscillation of interlayer coupling in epitaxial co/ir(001) superlattices. *Physical Review B - Condensed Matter and Materials Physics*, 60(18):12957, 1999.

[221] S. Colis, A. Dinia, C. Mény, P. Panissod, C. Ulhaq-Bouillet, and G. Schmerber. Magnetic, transport, and structural properties of Fe/Co/Cu/[Co/Ir/Co]

sandwiches and Fe/Co/Cu/[Co/Ir] multilayers prepared by ion-beam sputtering. *Physical Review B - Condensed Matter and Materials Physics*, 62(17):11709, 2000.

[222] D. Ourdani, Y. Roussigné, S. M. Chérif, M. S. Gabor, and M. Belmeguenai. Dependence of the interfacial Dzyaloshinskii-Moriya interaction, perpendicular magnetic anisotropy, and damping in Co-based systems on the thickness of Pt and Ir layers. *Physical Review B*, 104(10):104421, 2021.

[223] Runze Chen, Xinran Wang, Houyi Cheng, Kyu Joon Lee, Danrong Xiong, Jun Young Kim, Sai Li, Hongxin Yang, Hongchao Zhang, Kaihua Cao, Mathias Kläui, Shouzhong Peng, Xueying Zhang, and Weisheng Zhao. Large Dzyaloshinskii-Moriya interaction and room-temperature nanoscale skyrmions in CoFeB/MgO heterostructures. *Cell Reports Physical Science*, 2(11):100618, 2021.

[224] Gong Chen, Alpha T. N'Diaye, Yizheng Wu, and Andreas K. Schmid. Ternary superlattice boosting interface-stabilized magnetic chirality. *Applied Physics Letters*, 106(6):062402, 2015.

[225] Fabian Kloodt-Twesten, Susanne Kuhrau, Hans Peter Oepen, and Robert Frömter. Measuring the Dzyaloshinskii-Moriya interaction of the epitaxial Co/Ir(111) interface. *Physical Review B*, 100(10):100402, 2019.

[226] M. Belmeguenai, Y. Roussigné, S. M. Chérif, A. Stashkevich, T. Petrisor, M. Nasui, and M. S. Gabor. Influence of the capping layer material on the interfacial Dzyaloshinskii-Moriya interaction in Pt/Co/capping layer structures probed by Brillouin light scattering. *Journal of Physics D: Applied Physics*, 52(12):125002, 2019.

[227] Arne Vansteenkiste, Jonathan Leliaert, Mykola Dvornik, Mathias Helsen, Felipe Garcia-Sanchez, and Bartel Van Waeyenberge. The design and verification of MuMax3. *AIP Advances*, 4(10):107133, 2014.

[228] Jeroen Mulkers, Bartel Van Waeyenberge, and Milorad V. Milošević. Effects of spatially engineered Dzyaloshinskii-Moriya interaction in ferromagnetic films. *Physical Review B*, 95(14):144401, 2017.

[229] J. Sampaio, V. Cros, S. Rohart, A. Thiaville, and A. Fert. Nucleation, stability and current-induced motion of isolated magnetic skyrmions in nanostructures. *Nature Nanotechnology*, 8(11):839–844, 2013.

[230] Satoru Hayami. Skyrmion crystal and spiral phases in centrosymmetric bilayer magnets with staggered Dzyaloshinskii-Moriya interaction. *Physical Review B*, 105(1):014408, 2022.

[231] Y. Zhou, E. Iacocca, A. A. Awad, R. K. Dumas, F. C. Zhang, H. B. Braun, and J. Åkerman. Dynamically stabilized magnetic skyrmions. *Nature Communications*, 6:8193, 2015.

[232] Shijiang Luo and Long You. Skyrmion devices for memory and logic applications. *APL Materials*, 9(5):050901, 2021.

[233] Xin Ma, Guoqiang Yu, Chi Tang, Xiang Li, Congli He, Jing Shi, Kang L. Wang, and Xiaoqin Li. Interfacial Dzyaloshinskii-Moriya Interaction: Effect of 5d Band Filling and Correlation with Spin Mixing Conductance. *Physical Review Letters*, 120(15):157204, 2018.